Numerical modelling of landfast sea ice

Thesis submitted in accordance with the requirements of
the University of Liverpool for the degree of Doctor in Philosophy

by

Nuala Carson

June 2014

Abstract

Landfast sea ice is a recurring seasonal feature along many coastlines in the polar regions. It is characterised by a lack of horizontal motion, for at least 20 days, and its attachment to the coast or seabed. It can form as a result of restrictive geometry, such as channels or embayments, or through the grounding of thick ice ridges which add lateral stability to the ice cover. Due to its stationary and persistent nature, landfast ice fundamentally modifies the exchange of heat and momentum between the atmosphere and ocean, compared with more mobile pack ice.

The current generation of sea ice models is not capable of reproducing certain aspects of landfast ice formation and breakup. In this work two landfast ice parameterisations were developed, which describe the formation and breakup of landfast ice through the grounding of thick ice ridges. The parameterisations assume the sub-grid scale distribution of ice draft and ocean depth, the two parameters important in determining the occurrence of grounded ridges. The sub-grid scale distribution of grounded ice is firstly defined by assuming that ice draft and ocean depth are independent. This parameterisation allowed ice of any thickness to occur and ground at any depth. Advancing from this the sub-grid scale distribution of the grounded ice was restricted in an effort to make it more realistic. Based on Arctic ice scour observations ice was prevented from grounding in regions where the draft thickness was much larger than the ocean depth. Both parameterisations were incorporated into a commonly used sea ice model, the Los Alamos Sea Ice Model (CICE), to which a multi-category ocean depth distribution from high resolution global bathymetry data (ETOPO1) was included. The parameterisations were tested in global standalone format (i.e. no active ocean) with realistic atmospheric forcing. Both parameterisa-

tions were found to improve the spatial distribution and the seasonal cycle of landfast ice compared to the control (i.e. no landfast ice parameterisation) in the Arctic and Antarctic. However, the grounded ridges produced by the parameterisations were very stable, and tended to become multiyear leading to the production of multiyear landfast ice, which was particularly widespread in the Antarctic.

It was found that tides have a significant impact on both grounded and landfast ice. In some polar locations tides were found to increase the occurrence of landfast ice, by increasing the production of thick ridges which were able to ground. Conversely, in some regions, tides were found to decrease the occurrence of landfast ice, as strong tidal and residual currents increased the mobility of the grounded ridges and landfast ice.

This thesis finishes by considering whether a sea ice model could be used to further our understanding of the physical landfast ice system. Analytically derived characteristic numbers, which describe the ability of landfast ice to form, were found to fully describe the formation of landfast ice within the sea ice model CICE during idealised 1D scenarios. For these scenarios the key parameters controlling ice motion were found to be the external forcing component, the width of the ice cover, the internal ice strength, and the thickness of the ice. However, an exact characteristic variable able to describe the occurrence of landfast ice in an idealised 2D scenario could not be found analytically, nor could it be inferred numerically, and this remains an area for further research.

This thesis examines different methods of modelling landfast sea ice and provides the sea ice modelling community with a means to parametrise landfast ice formation as a result of grounded ridges without having to work at very fine resolution, as this is computationally inefficient.

Contents

List of Figures

List of Tables

Acknowledgements

Firstly, I want to thank all three of my supervisors, Dr Miguel Angel Morales Maqueda (National Oceanography Centre, Liverpool), Dr Clare Postlethwaite (British Oceanographic Data Centre) and Dr Harry Leach (University of Liverpool), to whom I owe a great debt. Their encouragement, advice, endless hours of discussion and problem solving have been essential to the completion of this thesis. I hope each of you understand how much you have helped.

The Los Alamos National Laboratory provided the Los Alamos Sea Ice code (CICE), which was essential to this research. I owe a massive thank you to everyone who helped me get to grips with this code, develop my own scripts and teach me to use the NOCL cluster. This includes all 3 of my supervisors, but also Dr Vassil Roussenov from the University of Liverpool and Mark Birmingham from the NOCL IT help desk. Thank you for not laughing when I asked stupid questions or made silly mistakes.

I owe a massive thank you to all my fellow students at the University of Liverpool and the National Oceanography Centre Liverpool, and in particular my office mates. Without their help, reassurance, support, and friendship, I do not think I would have survived.

My last thanks is for my friends and family, in particular my partner Simon, who have helped me through the last 4 years. It hasn't been easy, and I am in awe of the apparently unlimited amount of patience you had for me, and your ability to help me put things in perspective. Thank you.

Chapter 1

Introduction

1.1 Sea ice

Sea ice is a fundamental component of the cryosphere, and an integral part of our global climate system. It modifies the exchange of heat, gas and momentum between the atmosphere and polar oceans, it affects the fresh water budget and alters the albedo of the high latitudes. Most sea ice is part of the mobile pack ice, which is free to circulate under the influence of winds and oceanic currents. Pack ice is extremely inhomogeneous with differences in concentration, thickness, age and snow cover occurring over a range of spatial scales. Landfast ice is a distinct type of sea ice which is attached to the coast, remains motionless for long periods of time, and is generally homogeneous in properties.

In recent years, satellite observations have shown a significant decline in Arctic sea ice extent in all seasons, but most markedly in summer (Stroeve et al., 2012). The record minimum Arctic ice extent (since 1979) was reached in September 2012, as reported by the National Snow and Ice Data Centre (NSIDC). This decline in extent has been accompanied by a reduction in ice thickness (Rothrock et al., 2003; Schweiger et al., 2011; Laxon et al., 2013). Similar observations in the Antarctic have not revealed a significantly consistent trend. In order to fully understand the impacts of the observed and future changes in polar sea ice, it is essential to understand all components of the sea ice system, including landfast ice, and accurately represent

them in global models.

1.2 Landfast sea ice definition

There is no one standard definition consistently applied to landfast sea ice. Some definitions are based on physical understanding of the landfast ice system while others are based more generally on observations and trends. The applied definition, and how stringent it is, will have implications on the resultant estimates of landfast ice occurrence. Although definitions can vary significantly, most agree on two fundamental characteristics, that landfast ice is stationary, and that it is attached to the coast or seabed at some point. The World Meteorological Organisation (WMO, 1970) defines landfast ice as "sea ice which forms and remains fast along the coast, where it is attached to the shore, to an ice wall, to an ice front, between shoals and grounded icebergs". This definition was further refined by Mahoney et al. (2005), who attached a minimum time constraint of 20 days which the ice must remain stationary for in order to be considered landfast. This time period is long enough to preclude transient events such as pack ice being temporarily driven shoreward by oceanic or atmospheric forcing, but short enough to resolve intra-annual events, such as seasonal growth and breakup of landfast ice. Recent research into landfast ice has widely adopted the definition proposed by Mahoney et al. (2005) in both observational and modelling studies, and is the one applied in this research.

1.3 Background

Landfast sea ice, as shown in Fig 1.1, is a recurring feature along many coastlines in the polar regions. Most landfast ice is seasonal, with only a small proportion becoming multiyear. The multiyear landfast ice which does occur usually forms as a result of highly restrictive geometry, such as in the Canadian Arctic Archipelago (CAA). A prominent example of the semi-permanent landfast ice is the Norske Øer ice barrier which occurs off NE Greenland (Hughes et al., 2011). The landfast ice

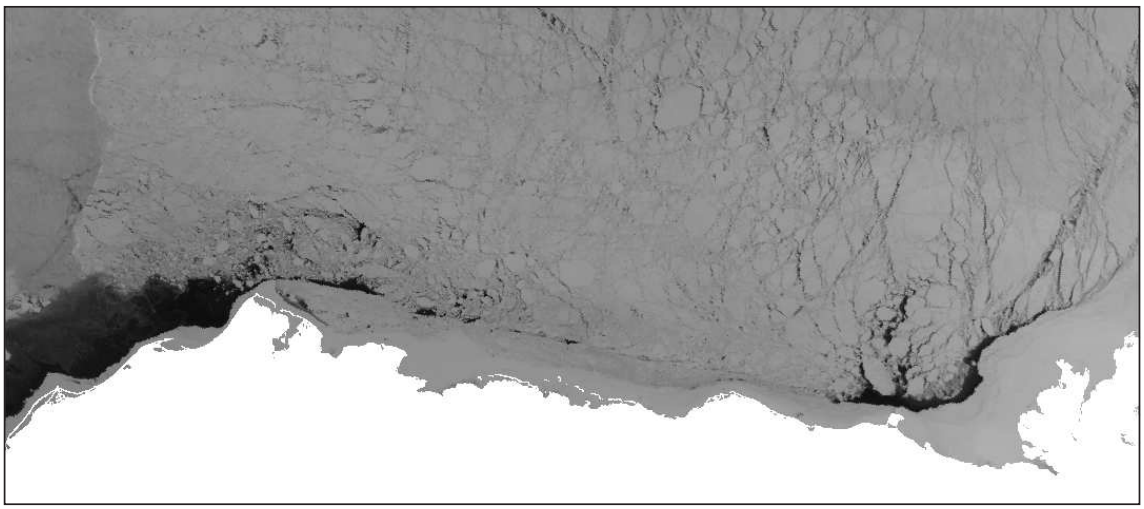

Figure 1.1: A Visible Band Image of Beaufort Sea for 04 May 2004 (Eicken et al., 2009). Leads appear dark, sea ice appears grey, and the Alaskan coast is white. The landfast ice is that shoreward of the lead.

cover is separated into 3 distinct sections: undeformed ice grown in coastal regions which is subdivided into bottomfast or floating, and a section of highly deformed shear and pressure ridges located near the landfast ice edge, known as the stamukhi zone (Fig.1.2) (Reimnitz, 2000; Mahoney et al., 2007b). The word stamukhi is a historical Russian term that describes an area of grounded ice (Weeks, 2010). The stamukhi zone at the edge of the landfast ice cover is discontinuous, meaning that there are sections of the landfast ice edge which are not dominated by grounded pressure ridges. The floating section of the landfast ice cover (i.e. ignoring the stamukhi zone) generally has a homogeneous thickness, as its growth is dominated by thermodynamics. Tidal cracks are a common occurrence between the bottomfast and floating sections. They accommodate differential motion between the two sections caused by changes in sea level (Kovacs and Mellor, 1974b; Reimnitz and Barnes, 1974; Reimnitz, 2000). The tide cracks are assumed to have negligible tensile strength, meaning that it is unlikely that bottomfast ice plays a significant role in attaching the floating landfast ice section to the coast.

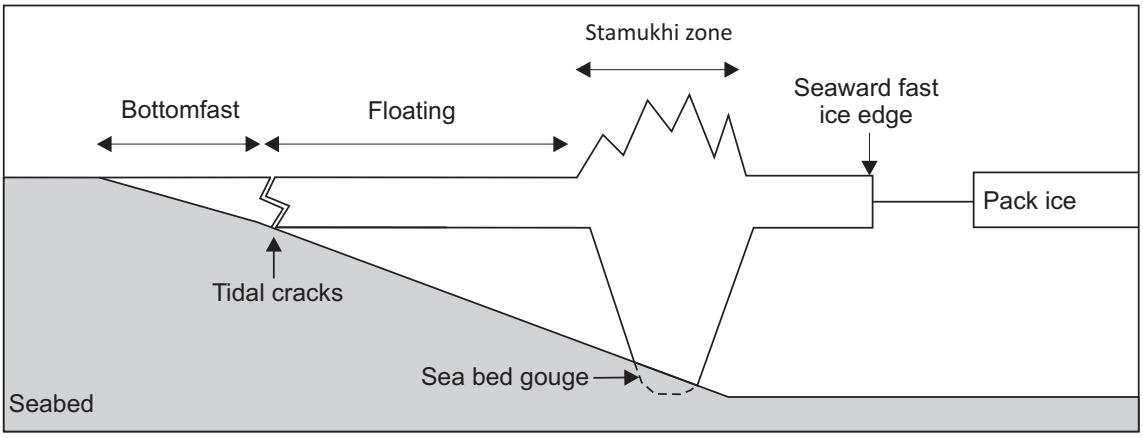

Figure 1.2: A generalized cross-section of landfast ice extending offshore showing a grounded pressure ridge (part of the stamukhi zone) at the landfast ice edge. However, the grounded ice ridges do not occur continuously along the landfast ice edge.

1.4 Formation

Sea ice forms when the sea water is cooled to the freezing point. The freezing point of sea water is depressed in comparison to that of fresh water due to the addition of salt. Typically, in polar regions (with a salinity of 35 ppt) the sea water freezes at $-1.8°$C. Sea ice begins by forming small crystals which join together to form needle like structures, which are typically 3-4 mm in diameter known as frazil ice. The frazil ice crystals coalesce to form larger structures. If the ice formation occurs in calm conditions then smooth, thin, homogeneous sheets of ice develop, known as nilas or grease ice. If the weather conditions are not calm then the frazil ice turns into circular disks of ice, known as pancake ice. Eventually, the individual 'pancakes' consolidate into a coherent sheet of sea ice. The thin sheets of ice thicken through rafting and ridging processes, and continue to grow in winter through congelation to form first year ice. Congelation is when water molecules freeze onto the underside of the existing ice cover (Wadhams, 2000). Sea ice which survives one or more summer melt season is known as multiyear, or perennial ice.

The strength of sea ice depends primarily on its thickness, but also on its brine

content, temperature and density. Thin ice fails or breaks more easily under stress. It is widely accepted that a consolidated sheet of ice is strongest in compression, then shear, and weakest in tension (Hibler, 1979), with the tensile strength generally accepted to be around $^{1}/_{20}{}^{\text{th}}$ of the compressive strength (Hibler and Schulson, 2000; Wang, 2007). As sea ice is highly fractured at fine scales it is generally assumed to have no, or negligible, tensile strength at most model resolutions (Lepparanta, 1998). Recently, there has been some discussion as to whether landfast ice, unlike pack ice, does in fact contain a significant degree of tensile strength which would allow it to remain attached along an unrestricted coastline, over relatively deep water, and under the influence of offshore winds as these conditions mean that it is unlikely that restrictive geometry plays a significant role in landfast ice creation. Tremblay and Hakakian (2006) reported that sea ice exhibits tensile strength when subjected to offshore winds, particularly in the East Siberian Sea. However, to date no definitive modelling work in support of this theory has been proposed (König Beatty and Holland, 2010; Ólason, 2012).

Landfast ice forms through a number of different processes. Probably the most well understood is that of restrictive geometry, where ice is held stationary through resistive shear or compressional stress imparted on the ice as it interacts with narrow channels or embayments, such as in the CAA. Landfast ice is also observed to occur along unrestricted coastlines and under the influence of offshore winds. Both of these factors act to prevent the formation, or encourage the breakup of landfast ice, raising the question of how it can form under these conditions. Discontinuous grounded ridges along the landfast ice edge add stability to the fast ice sheet acting to limit lateral motion. The grounded ridges usually form through offshore deformation of pack ice but can also form through *in situ* deformation of the landfast ice itself. The ridges which form offshore drift inshore under the influence of oceanic and atmospheric stresses, and ground on shallowing bathymetry. The ridges gouge the seabed to a given depth until the resistive frictional force imparted by the seabed is large enough to fully arrest the ice ridge, as shown in Figure 1.2. The depth of

the gouge depends on the strength of the keel, how strongly the ice sheet and ridge are coupled, and the strength of the seabed sediments (Kovacs and Mellor, 1974a). The anchoring strength provided by the ridge is limited by either the strength of the ridge's keel or its coupling with the seabed i.e. the gouge depth. Grounded ridges which form *in situ* are thought to provide significantly lower anchoring strengths than those which form offshore as they typically only reach thicknesses just equal to the local ocean depth, and so are not strongly coupled with the seabed (Mahoney et al., 2007b; Phillips et al., 2005).

Landfast ice begins to form at the coast, gradually advancing offshore until a stable extent is reached, the location of which is primarily determined by the coastline and bathymetry (Mahoney et al., 2007a). This occurs in early winter once the thick ridges have assimilated into the shallow coastal regions. Once the stable extent is reached, the landfast ice is persistent, generally remaining unchanged until the summer melt season. Episodic breakout events do occur, where the fast ice edge temporally extends beyond the stable width, but these are generally short lived. In late spring, with the onset of thawing temperatures, the landfast cover breaks-up and drifts offshore. The floating section is thinned thermodynamically and weakened. Once the grounded ridges uncouple from the seabed the landfast ice sheet breaks-up and drifts offshore rather than melting *in situ*. This process is much quicker than the formation, and in many cases the landfast ice is completely removed within a few days. Recent observations have shown a reduction in landfast sea ice in the Arctic (Mahoney et al., 2007a). This reduction has been attributed to the earlier onset of thawing temperatures in spring and the later inclusion of the ice ridges into shallow coastal waters in winter due to an increased northward retreat of the perennial ice edge (Serreze et al., 2003; Stroeve et al., 2005).

In general, Arctic landfast ice is observed to reach its stable extent around the 20 m isobath (Kovacs and Mellor, 1974b; Reimnitz and Barnes, 1974; Stringer, 1974; Stringer et al., 1980; Mahoney et al., 2007a), but this can differ between regions. In the western Kara Sea the landfast ice reaches its maximum extent around the

10 m isobath, while in the eastern Kara sea the landfast ice edge can stabilise around the 100 m isobath (Divine et al., 2004). These variations occur for a number of reasons. For example, the occurrence of offshore islands can allow landfast ice to form in regions which are much deeper than 20 m. Also, if local ice deformation results in ridges which are relatively shallow (less than 20 m), then the landfast ice edge can only extend to regions which are shallower than the 20 m isobath. Strong variations in landfast ice width are also observed due to differences in the slope of the continental shelf, as this determines how far offshore the ridges will ground. Landfast ice is observed to extend hundreds of kilometres from the coast in the Siberian Arctic (Barnett, 1991; Eicken et al., 2005), while along the Alaskan coastline it generally reaches stable widths of $\leq$ 50 km (Stringer et al., 1980). The strong correlation between the stable landfast ice edge and the 20 m isobath suggests the importance of grounded ridges in landfast ice formation and retention. Ice ridges, which are formed through the convergence of the sea ice cover, commonly reach thicknesses of 20 m in the Arctic, although thicker ice ridges have been observed (e.g. Barnes et al., 1984; Timco and Burden, 1997). The maximum thickness of an ice ridge is limited, as once a ridge has reached a certain vertical length, the pack ice which surrounds the ice is too weak to penetrate the ridge under deformation to allow it to grow thicker. At this point, the ice cover will break in front of the ridge, and the ridge will grow laterally (Lepparanta, 2011; Hopkins et al., 1991). This maximum thickness limit is primarily controlled by the thickness of the parent ice cover, while also being dependent on the strength of the convergent stresses acting on the ice cover and the duration over which the convergent stresses act. The thicker the starting ice cover, the stronger the convergent stresses, and the longer these stresses occur, the thicker the resultant ice ridge will become. Much of Arctic sea ice does not commonly exceed thermodynamically driven thickness of 2-3 m (Rothrock et al., 2003; Schweiger et al., 2011; Laxon et al., 2013). As such, the maximum thickness of the pressure ridges will be capped by this (along with the strength of the convergent stresses and the timescale over which these are applied). In the Arctic, this results in ridges which do not generally exceed 20m.

The occurrence of landfast ice in the Antarctic is controlled by the same processes as in the Arctic but significant differences in the physical environment have resulted in notable differences in the resultant landfast ice. Much of the continental shelf surrounding the Antarctic continent is generally much deeper than in the Arctic, beyond depths which sea ice ridges would be able to ground in. The lack of grounded ridges will act to limit landfast ice formation. However, the occurrence of very thick icebergs, up to $\approx$ 400m (Massom et al., 2001), provide anchoring points for the landfast ice in very deep water. The occurrence of extensive ice sheets over the available continental shelf, and strong katabatic winds, both act to limit the grounding of ridges and the formation of landfast ice. Limited studies of Antarctic fast ice have meant that long term or large spatial scale records of landfast ice are significantly lacking. Along the east Antarctic coast landfast ice is known to form in narrow bands of varying widths rarely exceeding 150 km (Giles et al., 2008).

1.5 Importance

Landfast ice is an important component of the cryosphere, influencing a wide range of local and global processes. Due to its persistence and lack of mobility, landfast ice acts as an extension of the coast over the continental shelf, fundamentally modifying the exchange of heat, gas, and momentum between the atmosphere and ocean. This is unlike pack ice which has the ability to move, allowing the ocean and atmosphere to intermittently interact with one another.

Latent heat polynyas form offshore of many coastlines in the polar regions. The large negative ocean to atmosphere heat fluxes (up to several hundred Wm^{-2}) affect mesoscale atmospheric motion (Dethleff, 1994) and ocean circulation (e.g. Morales-Maqueda et al., 2004). High rates of ice production caused by the negative heat flux result in high levels of brine rejection, altering the local ocean salinity. This process sets up vertical mixing and convection which can result in the formation and cascading of intermediate and deep water masses. The properties of the dense water formed in polynyas, and the depth to which it cascades, depends on the location of

the formation polynya. The occurrence of landfast ice moves the effective coastline, and the location of the flaw polynyas, offshore. The dense water then has a reduced distance to travel before reaching the shelf break, undergoing less mixing with the fresher ambient shelf water. This allows the water to retain a density close to its original maximum and cascade to great depths, forming deep water (Schauer and Fahrbach, 1999).

Landfast ice is the form of sea ice which people have most frequent and direct contact with. The landfast ice edge is an essential habitat and feeding ground for Arctic mammals and the Inuit who depend on them for subsistence (Druckenmiller et al., 2000). It also affects economic activities such as shipping and offshore oil and gas exploration. With increased shipping and mineral exploration interest in Arctic coastal waters, understanding the landfast ice system and being able to accurately model it is becoming increasingly important.

1.6 Research aims

Despite the important and wide ranging effects of landfast sea ice, there has been limited work into its accurate inclusion in dynamical models. Landfast ice modelling studies originally concentrated on thermodynamic models. These thermodynamic studies considered ice to be landfast when the ice thickness would reach, or exceed, a given percentage of the local ocean depth (usually 10%) (Flato and Brown, 1996; Dumas et al., 2006; Lieser, 2004). More recently, work has focused on producing a dynamic representation of landfast sea ice. However, to date, dynamic sea ice models have not been able to reproduce landfast sea ice in a realistic setting. König Beatty and Holland (2010) showed that by adding tensile strength into a commonly used sea ice model they were able to produce landfast sea ice features in idealised scenarios. Tensile strength allows the ice to remain attached to an unrestricted coastline, under forcing conditions acting to set the ice into motion. It is commonly accepted that, in general, sea ice has no, or a very little, tensile strength as it is highly fractured on the scales typically used for sea ice modelling. However, there is still uncertainty

as to whether landfast ice contains a degree of tensile strength. König Beatty and Holland (2010) found that the magnitude of tensile strength required to simulate landfast ice was equal to the compressive strength of the ice, which contradicts what is known about the strength of sea ice; that ice is strongest in compression, then shear, and weakest in tension (Hibler, 1979). König Beatty and Holland (2010) were also unable to reproduce landfast ice features under realistic conditions.

Landfast ice research has generally focused on regional scales, due to the increases in model resolution that can be gained. One region which has been studied in detail, with respect to landfast sea ice is the Kara Sea, building up a good understanding of the seasonal progression of the landfast ice and the processes involved in its formation (Volkov et al., 2002; Divine et al., 2004, 2005). As such, the Kara Sea has become a good case study for testing modelling concepts. Ólason (2012) followed a similar method to that proposed by König Beatty and Holland (2010), modelling landfast ice in the Kara Sea by allowing the sea ice to contain a degree of tensile strength. The spatial distribution of the modelled landfast ice compared well with observations, but the model was not able to realistically represent the duration of the fast ice cover, despite modelling at relatively fine resolutions.

In this study we consider the inability of sea ice models to produce realistic landfast sea ice along unrestricted coastlines and under offshore winds, when it is observed to occur in reality. In contrast to recent landfast ice studies carried out by König Beatty and Holland (2010) and Ólason (2012) we propose that it is not tensile strength within the landfast ice which allows it to remain fast under offshore winds and along unrestricted coastlines. Instead, we consider the hypothesis that the grounded ridges within the stamukhi zone (at the offshore edge of the landfast ice cover) provide enough lateral stability to keep the ice fast.

The formation and properties of thick ice ridges has been widely studied over the years (Lepparanta and Hakala, 1992; Lepparanta et al., 1995; Timco and Burden, 1997). The impact of these ice ridges on the seabed, i.e. seabed gouging, has also been of significant interest, particularly in relation to the location and depth of oil and gas pipe lines (e.g. Palmer et al., 2005; Barrette, 2011; Palmer and Tung, 2012).

The impact of the thick ice ridges on the formation and maintenance of landfast ice formation and maintenance has not been widely investigated.

This study begins with a discussion of how ridges help to form landfast ice, and important aspects relating to this process. Chapter 2 considers two separate methods of parameterising grounded ridges, and their impact on the ice cover, in a sea ice model. We then test the ability of the parameterisations to reproduce the formation, maintenance and breakup of landfast sea ice in the Arctic and Antarctic. We investigate the impact of tides on grounded ridges, and consider the sensitivity of the modelled landfast ice to realistic tidal forcing in Chapter 3. We finish by considering some open questions remaining in landfast ice research, and consider whether we can use a model representation of landfast ice to better understand the sensitivity of the physical landfast ice system. That is, is it possible to use models to better understand the physics of the landfast ice system, such as under what conditions it is likely to form or break up.

Chapter 2

Modelling landfast ice production due to grounded ice

2.1 Introduction

Landfast sea ice is separated into 3 distinct sections; undeformed ice grown in coastal regions which is subdivided into bottomfast or floating, and a section of highly deformed shear and pressure ridges located near the landfast ice edge, known as the stamukhi zone (Fig.1.2). The resultant frictional drag force exerted on the ice due to contact with the sea floor causes the thick ridges to slow, and in some cases completely arrest (Fig.2.1), a process known as grounding. The grounded ridges then act as pinning points within the landfast ice cover, limiting lateral movement of the adjacent ice. The landfast ice sheet begins to form in early winter, once the thick ridges have assimilated into the shallow coastal regions. In spring/summer the landfast ice cover does not typically melt *in situ*. Instead, the grounded ridges uncouple from the seabed due to a combination of thermodynamic melt and offshore wind forcing. This allows the weakened landfast ice to detach from the coast and drift offshore. This process can be quite dramatic, happening over a few days. Grounded ice ridges thus play an integral role in the formation, maintenance and break-up of landfast sea ice.

To model landfast sea ice the area of grounded ice within a grid cell must be

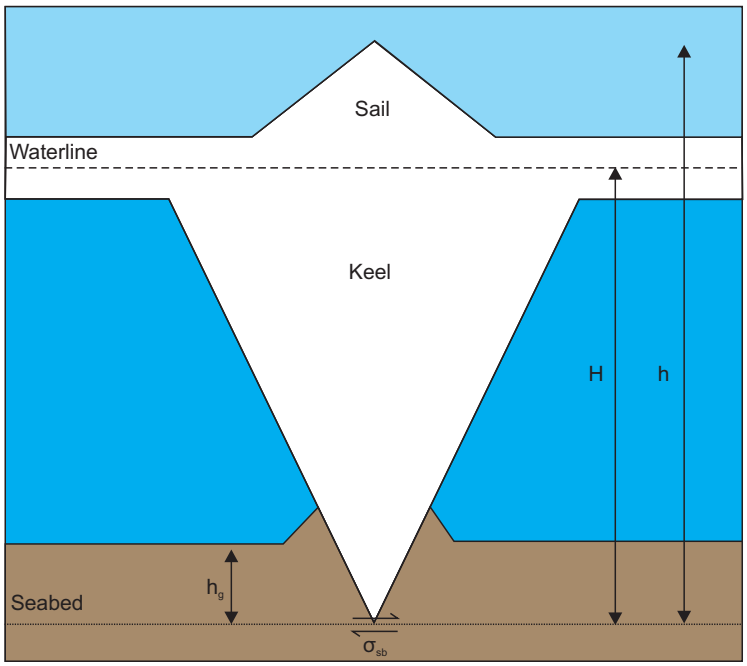

Figure 2.1: An idealized cross-section of a grounded ridge where draft ice thickness (H) is a fraction ($\frac{\rho_i}{\rho_w}$) of the total ice thickness (h). The water and ice densities are given by ρ_w and ρ_i respectively. The ridge has gouged the seabed to a depth of h_g, and exerts a shear stress (σ_{sb}) at the seabed.

determined. The parameters important in determining the amount of ice aground are the draft ice thickness and ocean depth. If the draft ice thickness is greater than the ocean depth then the ice will ground. In this Chapter we explore methods of parameterising the sub-grid scale occurrence of grounded ridges and the anchoring strength it provides to the sea ice cover to produce landfast ice.

2.2 Identifying grounded ice

For a simple idealised scenario, or when the model resolution is fine enough that within each grid cell ice draft and ocean depth are unique, the draft ice thickness and ocean depth are independent. That is, the amount of ice in contact with the seabed will remain unchanged irrespective of how either variable is spatially distributed within the grid cell. As such, the area of grounded ice can be determined logically

and a parameterisation to determine the sub-grid scale area of grounded ice is not required. However, it is generally unrealistic to run models at fine enough resolution such that the variables are unique.

When variables are multi-category and the sub-grid scale distribution of either variable is unknown, as they are in most sea ice modelling studies, then within each grid cell a method of determining the area of ice in contact with the seabed is necessary. Figure 2.2 shows a grid cell with ice thickness and ocean depth of two categories. For this case there are only two possible ways that the ice can be spatially distributed with respect to the bathymetry. Therefore the resultant area of grounded ice can again be logically determined. In the first example (a) the area of grounded ice is equal to the difference between the area of shallow bathymetry and the area of thin ice ($A_g = A_{d1} - A_{h1}$). This is the minimum amount of ice that necessarily must be aground. In the second example (b) the area of grounded ice is equal to the area of shallow bathymetry ($A_g = A_{d1}$). This is the maximum possible area of grounded ice. However, as the number of ice thickness and ocean depth categories increases so too does the complexity of the solution. At resolutions that sea ice is generally modelled at the number of ice and ocean categories within a standard grid cell is such that the solution can not be determined logically. In this case a method, or parameterisation, to determine the sub-grid scale occurrence of grounded ice must be used.

Multi-category draft ice thickness (H) and ocean depth (D) can be considered as continuous random variables, with probability density functions (PDFs) $f(h)$ and $g(d)$ respectively,

$$P(0 \leq H \leq \infty) = \int_0^\infty \mathrm{d}h\, f(h) = 1, \tag{2.1}$$

$$P(0 \leq D \leq \infty) = \int_0^\infty \mathrm{d}d\, g(d) = 1. \tag{2.2}$$

The draft ice thickness (H) is the thickness of ice underwater, where $H = \frac{\rho_i}{\rho_w} h$ and h is the full ice thickness. The PDF of a continuous random variable is a function which can be integrated to obtain the probability that the random variable takes a

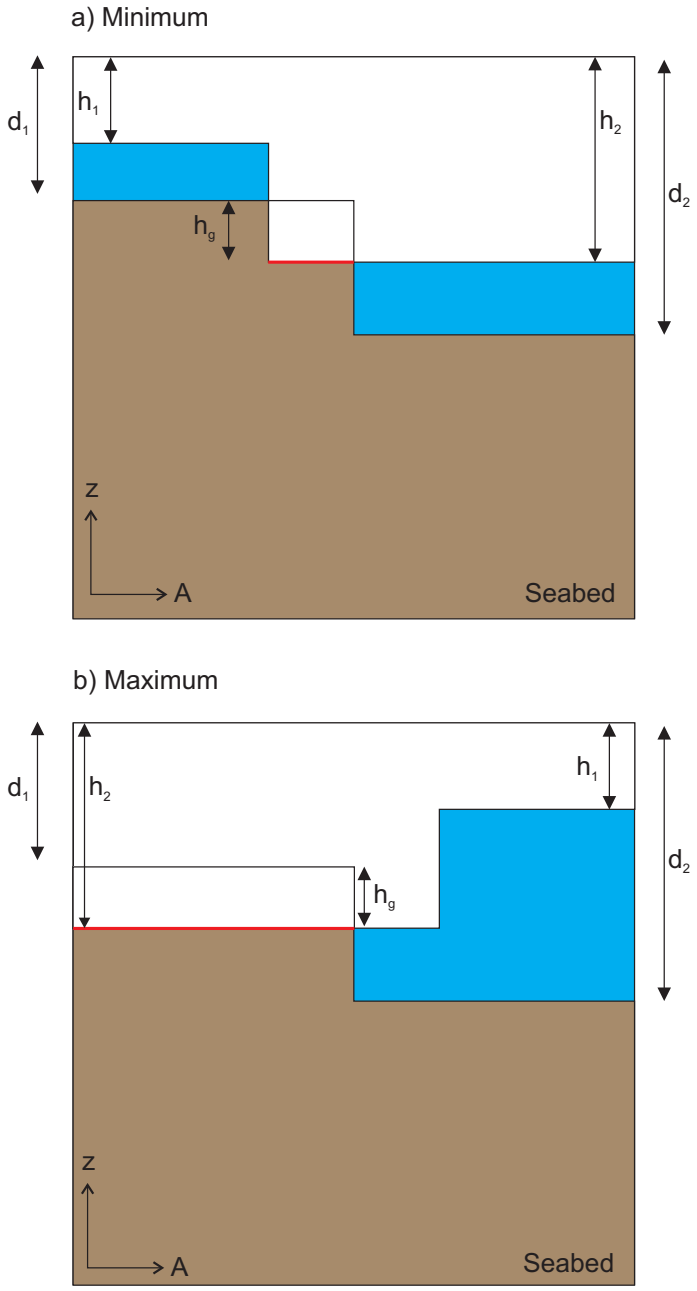

Figure 2.2: Schematic showing ice draft and ocean depth versus cell fractional area (A), where A varies between 0 and 1, for ice thickness ($h_{1,2}$) and ocean depth ($d_{1,2}$) of two categories. The ice can be distributed within the grid cell in two ways ((a) and (b)) which results in different amounts of grounded ice. The red line indicates the area of grounded ice, A_g, and h_g is the depth to which the ice can gouge the seabed.

value in a given interval. In this case the PDFs for ice thickness and ocean depth represent the probability that the ice will be a certain thickness or the ocean will be a certain depth. In Equation (2.2) $g(d)$ is only considered over positive depth ranges, as land values are assumed to be 0. The PDF for ice thickness and ocean depth can then be joined (known as a joint probability density function (JDF)) to find the probability that the ice thickness and ocean depth both take on certain values,

$$P(0 \leq H \leq \infty, 0 \leq D \leq \infty) = \int_0^\infty \mathrm{d}h \int_0^\infty \mathrm{d}d\, j(h,d) = 1. \tag{2.3}$$

The JDF can be used to find the probability that ice will be aground by finding the probability the ice will be thicker than ocean depth. When the JDF is constructed assumptions need to be made about the continuous random variables being joined. These assumptions are important as it will affect the final solution. We do not have sufficient understanding of the physics of the landfast ice system to determine a realistic, dynamically based, joint distribution. It may be useful to mathematically determine the solution bounds by finding the joint distribution which produces the minimum and maximum anchoring strength produced by the grounded ice. The realistic solution must then fall between these extremes. Further details on this are included in the Appendix A.

The simplest approach would be to define a joint distribution based on the assumption that the ice draft and ocean depth are independent, as they are in the single category case discussed earlier. This assumption places no restriction on the sub-grid scale distribution of either variable; within a model grid cell ice can ground anywhere where it is thicker than the ocean depth. The main limitation of this method is that it permits the occurrence, and grounding, of erroneously thick ice on shallow bathymetry. A more restrictive joint distribution could be defined, where the user places restrictions on the sub-grid scale distribution of one, or both, of the variables with the aim of limiting this unrealistic behaviour.

2.3 Landfast ice parameterisation

In this analysis we produce two landfast ice parameterisations which account for the sub-grid scale grounding of thick ice ridges, and the anchoring strength they impart on the landfast ice cover. We begin by producing a JDF from PDF's of ice draft and ocean depth assuming an independent relation between ice draft and ocean depth. Advancing from this an alternative parameterisation is defined which restricts the independently produced joint distribution by limiting the maximum ice draft to ocean depth ratio for grounded ice.

2.3.1 Independent joint density function

As previously discussed, a JDF can be defined from the PDFs of two continuous random variables. If the continuous random variables are independent then the JDF is defined as $j(x, y) = f(x) \times g(y)$. As such, by assuming that ice thickness and ocean depth are independent, the associated JDF is

$$j(h, d) = f(h) \times g(d), \tag{2.4}$$

where $f(h)$ and $g(d)$ are the probability density functions for ice thickness and ocean depth respectively. For example, if a grid cell is completely covered in ice which is uniformly distributed across all thickness categories, that is, there is the same amount of ice within each thickness category,

$$f(h) = \begin{cases} 1/2h_m & \text{if } 0 \leq h \leq 2h_m, \\ 0 & \text{otherwise,} \end{cases}$$

where $2h_m$ is the maximum ice thickness and h_m is the average ice thickness. This is illustrated in Figure 2.3 (a). If that same grid cell also contained bathymetry with a uniform distribution,

$$g(d) = \begin{cases} 1/2d_m & \text{if } 0 \leq d \leq 2d_m, \\ 0 & \text{otherwise,} \end{cases}$$

where $2d_m$ is the maximum ocean depth and d_m is the average ocean depth (illustrated in Figure 2.3 (b)). Assuming that ice thickness and ocean depth are independent the joint distribution, for this example, is therefore

$$j(h,d) = \begin{cases} 1/(2h_m \times 2d_m) & \text{if } 0 \leq h \leq 2h_m \text{ and } 0 \leq d \leq 2d_m, \\ 0 & \text{otherwise.} \end{cases}$$

This is illustrated in Figure 2.3 (c).

The JDF can then be used to define the probability that within a grid cell ice draft is greater than or equal to the ocean depth, and therefore ice can be aground. The fractional area of grounded ice within each grid cell, A_G, is found by integrating the independent JDF over the probability space that represents a draft thickness (H) equal to or larger than the ocean depth (d),

$$A_G = \int_0^\infty \mathrm{d}h \int_0^H \mathrm{d}d\, j(h,d). \tag{2.5}$$

For the example discussed, the area of grounded ice is therefore

$$A_G = \int_0^{2h_m} \mathrm{d}h \int_0^H \mathrm{d}d\, 1/(2h_m \times 2d_m). \tag{2.6}$$

To determine the anchoring strength the grounded ice provides to the landfast sea ice the buoyancy corrected thickness of the grounded ice, H_G, is found. It is determined by multiplying the fractional area of grounded ice by the buoyancy corrected ice thickness, $(h - \frac{\rho_w}{\rho_i} d)$,

$$H_G = \int_0^\infty \mathrm{d}h \int_0^H \mathrm{d}d \left(h - \frac{\rho_w}{\rho_i} d\right) j(h,d). \tag{2.7}$$

For the considered example the thickness of the grounded ice is

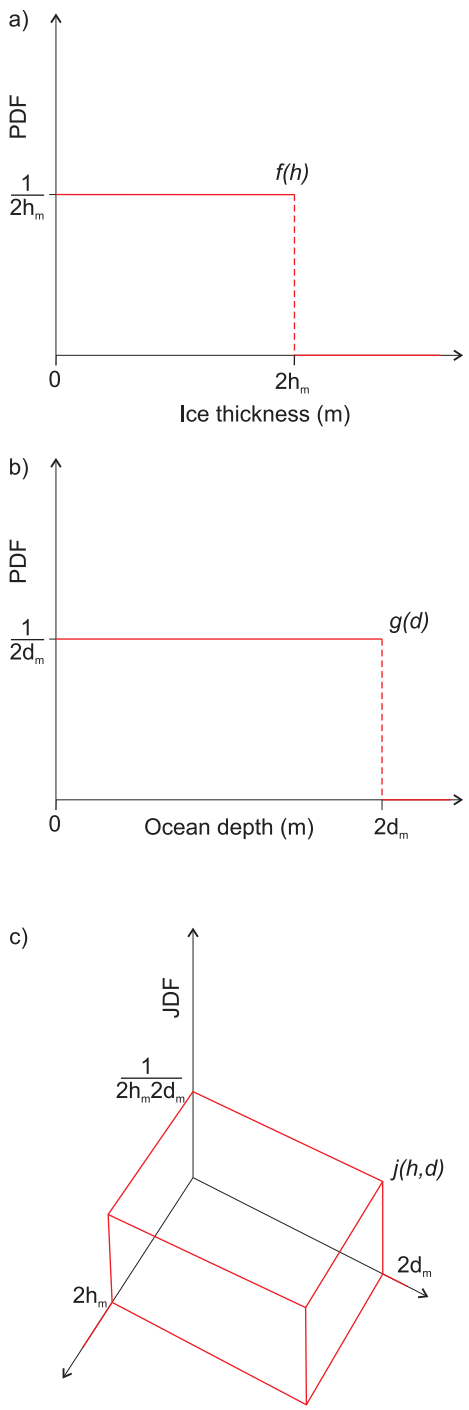

Figure 2.3: Probability density function for (a) ice thickness, $f(h)$, and (b) ocean depth, $g(d)$, which are both uniformly distributed across the thickness/depth categories and (c) the associated joint density function, $j(h, d)$, formulated by assuming ice thickness and ocean depth are independent. Here, $2h_m$ and $2d_m$ are the maximum ice thickness and ocean depth respectively.

$$H_G = \int_0^{2h_m} \mathrm{d}h \int_0^{H} \mathrm{d}d \left(h - \frac{\rho_w}{\rho_i} d\right) {}^{1}\!/_{(2h_m \times 2d_m)}. \tag{2.8}$$

Assuming an independent relation between ice draft and ocean depth means that all ice in contact with the seabed is considered aground. The limitation with this method is that it allows for erroneously thick ice to ground on shallow bathymetry. This is unrealistic and so the production of grounded ice is expected to be positively skewed towards higher values.

2.3.2 Restricted joint density function

Restricting the maximum ice draft to ocean depth ratio of grounded ice will reduce the main limitation of the independent parameterisation, by preventing erroneously thick ice occurring and grounding on shallow bathymetry. A cap on the maximum thickness the grounded ice can reach based on seabed gouging is incorporated into the parameterisation. Seabed gouging is a large-scale coastal process, occurring in both the Arctic and Antarctic, where the keel of an ice ridge comes into contact with the seabed. If the resistive force applied to the ice bottom is not able to overcome the driving forces then the keel will gouge the seabed as shown in Figure 2.1. Gouge dynamics vary according to the physical geometry of both the ice ridge and the seabed, but in general the seabed will be displaced laterally to form side berms, and ahead of the ridge to form a front mount (Barrette, 2011). The depth of the gouge depends on the strength of the keel, how strongly the ice sheet and ridge are coupled, and the strength of the seabed sediments (Kovacs and Mellor, 1974a). Multiyear keels are known to produce the deepest gouges due to the increased strength of the keel. Gouge intensity in the Arctic is greatest around the 20 m isobath, coinciding with the seaward location of the landfast ice edge where 1^{st} year shear and pressure ridges are known to form (Barnes et al., 1984; Hill et al., 1991; Mahoney et al., 2005, 2007b).

Limiting the maximum grounded ice thickness

Ice has the ability to gouge the seabed, and effectively increase the local water depth. The maximum thickness of ice which can ground in a given water depth is therefore controlled by the ability of the ridge to gouge the seabed. This process is parametrised here by introducing a coupling parameter λ. Ice is considered aground if it is thicker than the ocean depth and shallower than λ times the ocean depth,

$$D \leq H \leq \lambda D, \tag{2.9}$$

where D is the ocean depth and

$$\lambda = \frac{D + h_g}{D} = 1 + \frac{h_g}{D}, \tag{2.10}$$

where h_g is the gouge depth. λ was chosen to be a constant factor as observations showed that the gouge depth generally increased proportionally to increasing water depth in the near coastal zone. It is unknown as to why exactly this occurs, but it seems logical that thicker, and stronger, ice will more likely reside in areas of deep water, meaning that the seabed is more likely to be gouged to a greater depth. It is also speculated that reworking by ocean and tidal currents in the shallow water leads to infilling of the gouges (Barnes et al., 1984; Shapiro and Barnes, 1991). In the Arctic, for water depths $\leq 20\,\mathrm{m}$ observed gouge depths are typically $\leq 1\,\mathrm{m}$ relating to an average coupling parameter $\lambda = 1.05$ (Shapiro and Barnes, 1991; Barnes et al., 1984; Reimnitz et al., 1972; Hequette et al., 1995; Conlan et al., 1998). More extreme gouge depths, $2 - 3\,\mathrm{m}$, have been observed in equivalent water depths relating to $1.1 \leq \lambda \leq 1.15$ (Shapiro and Barnes, 1991; Hequette et al., 1995). This parameterisation is likely to be an oversimplification as the gouge depth will depend on a variety of factors including the geology of the seabed, the strength of the ice ridge, the strength to which the ridge is coupled to the surrounding ice cover and the strength of the wind or ocean forcing acting on the ice ridge. For example, if the seabed is made up of relatively loose material then the ridge is likely to gouge the

seabed to a greater depth than if the seabed is made up of tightly packed material. Similarly, the stronger the ice ridge the greater it's ability to gouge the seabed.

The area and buoyancy corrected thickness of the grounded ice, Equations (2.5) and (2.7), were modified accordingly to include this additional grounding restriction:

$$A_G = \int_0^\infty \mathrm{d}h \int_{H/\lambda}^{H} \mathrm{d}d\, j(h,d), \tag{2.11}$$

$$H_G = \int_0^\infty \mathrm{d}h \int_{H/\lambda}^{H} \mathrm{d}d \left(h - \frac{\rho_w}{\rho_i} d\right) j(h,d). \tag{2.12}$$

2.4 Modifying ice motion

In the previous section, a method of identifying the sub-grid scale area and thickness of grounded ice was developed. Here, a mechanism to modify the velocity of the grounded ice is discussed. A reactive grounding force per unit area due to the frictional coupling between grounded ice and the seabed, $\overrightarrow{F_G}$, is introduced into the standard sea ice momentum equation. As a reactive force, it acts to oppose ice motion and cannot act to enhance or excite new ice motion. The simplified momentum equation is

$$m\frac{\mathrm{d}\vec{u}}{\mathrm{d}t} = \overrightarrow{F_A} + \overrightarrow{F_G}, \tag{2.13}$$

where $\overrightarrow{F_A}$ encompasses all original forces acting on the ice (as detailed in Equation (4.1)). The new reactive grounding force, $\overrightarrow{F_G}$, is defined as

$$\overrightarrow{F_G} = -\frac{\overrightarrow{U}}{|\overrightarrow{U}|} min[M, \sigma_{sb}], \tag{2.14}$$

where $\overrightarrow{U}$ is ice velocity, $\sigma_{sb} = \rho_i g H_G c_f$ is the shear stress between the ice and the seabed and $M = \frac{\rho_i h}{T_f}|\overrightarrow{U}|$ is the maximum frictional force needed to fully arrest the ice in a time scale, T_f. Here, ρ_i is the density of the ice, g is gravity, H_G is the thickness of the grounded ice and c_f is the coefficient of friction between the ice and

seabed. In these experiments the coefficient of friction was taken as $c_f = 0.5$ from *in situ* experiments carried out by Shapiro and Metzner (1987) where ice blocks were dragged along the beach to determine the static and kinetic friction between the ice blocks and the ground. Using a constant coefficient of friction is likely to be an oversimplification, as in reality the coefficient of friction will depend on a range of factors including smoothness of the seabed and ice bottom. As such, it would be expected to be variable in space and time.

It should be noted that the definition of $\sigma_{sb} = \rho_i g H_G c_f$ means that its magnitude is large in comparison to the other dominant stresses acting on the ice i.e. wind and ocean stress. Considering a typical wind stress in the Arctic of $0.1\,\mathrm{Nm}^{-2}$ and assuming that the buoyancy corrected thickness of the grounded ice (H_G) is 1 cm and $c_f = 0.5$, then the magnitude of $\sigma_{sb} \sim 50\,\mathrm{Nm}^{-2} >> 0.1\,\mathrm{Nm}^{-2}$. This suggests that once ice is aground it is very stable, and almost impossible to uncouple from the seabed through dynamical processes alone.

2.5 Model description

The Los Alamos Sea Ice Model (CICE) v4.1 was used in this study. The major components of CICE are the horizontal transport routines, the thermodynamics and the dynamics which describe the physical state and motion of the ice cover. The model is fully described by Hunke and Lipscomb (2010), with the key components detailed here.

2.5.1 Ice thickness distribution

Sea ice is a mixture of open water, thin first year, thicker multiyear and thick shear and pressure ridges. Both the thermodynamic and dynamic properties of the ice pack depend the thickness of the ice cover. CICE is a multicategory ice thickness sea ice model. That is, for each model grid cell CICE determines how much ice resides in the discrete ice thickness categories. In these experiments the number of ice thickness categories was increased from the standard of 5 to 15 using the

method of defining interval boundaries employed in the 'original rounded' CICE thickness categories (detailed in Table 2.1) (Hunke and Lipscomb, 2010). Increasing the number and range of the thickness categories allowed thick pressure ridges formed through deformation to be considered by the grounding procedure.

The evolution of the ice thickness distribution in time and space is described by

$$\frac{\partial g}{\partial t} = -\nabla.(g\vec{u}) - \frac{\partial}{\partial h}(fg) + \psi. \tag{2.15}$$

In Equation (2.15) $\vec{u}$ is the horizontal ice velocity, f is the rate of thermodynamic ice growth, h is the ice thickness, ψ is a ridging redistribution function, and $g(x, h, t)$ is the ice thickness distribution function, with gdh defined as the fractional area covered by ice whose thickness lies between h and $h + dh$. The terms on the right-hand side of Equation (2.15) refer to horizontal transport by the velocity field, advection in thickness space by the thermodynamic processes and mechanical redistribution due to ridging and rafting, respectively. Equation (2.15) can be solved taking each component in turn. The component $\frac{\partial g}{\partial t} = -\nabla.(g\vec{u})$ is solved using a two-dimensional transport scheme, $\frac{\partial g}{\partial t} = \frac{\partial}{\partial h}(fg)$ is solved using a remapping scheme and $\frac{\partial g}{\partial t} = \psi$ is solved using a ridging model. The details of these schemes can be found in Hunke and Lipscomb (2010). The redistribution of ice thickness by ridging in CICE follows the work of Rothrock (1975). The ridging redistribution function, ψ, replaces ice with open water when the pack ice is diverging. Under convergence, when ice is entering a grid cell, ψ acts to reduce the area of open water and deforms thin ice into thicker ice ridges. Under convergence enough ridges are formed to ensure that the area of ice does not exceed the area of the grid cell. Under shear, ψ can generate a combination of opening, closing, and ridging.

2.5.2 Dynamics

CICE is based on an elastic-viscous-plastic (EVP) rheology. The EVP model reduces to the viscous-plastic (VP) model at time scales associated with the wind forcing, while at shorter time scales the adjustment process takes place by a numerically more

efficient elastic wave mechanism. While retaining the essential physics, this elastic wave modification leads to a fully explicit numerical scheme which greatly improves the models efficiency.

The two-dimensional momentum equation for sea ice motion is

$$m\frac{\partial \vec{u}}{\partial t} = -mf\vec{k} \times \vec{u} - mg\nabla\zeta + \vec{\tau_a} + \vec{\tau_o} + \vec{\nabla}.\vec{\sigma}, \tag{2.16}$$

where m is the ice mass per unit area of ocean, $\vec{u}$ is the ice velocity, f is the Coriolis parameter, $\vec{k}$ is a unit vector pointing upwards, g is the acceleration due to gravity, ζ is the dynamic topography of the sea surface, $\vec{\tau_a}$ is the wind stress, $\vec{\tau_o}$ is the ocean stress, ∇ is the two dimensional nabla operator, and $\vec{\nabla}.\vec{\sigma}$ is the divergence of the internal ice stress tensor $\vec{\sigma}$. The divergence of the ice stress tensor describes the forces stemming from ice interactions such as rafting, ridging and fracturing. It has been documented that on timescales greater than weeks, the dominant terms are typically atmospheric and oceanic stresses and the internal ice stress (e.g. Steele et al., 1997; Feltham, 2008). The effects of ocean surface tilt and Coriolis have been shown to be of smaller magnitude than the other terms, but can become significant over longer time periods (Hibler, 1986).

The wind and ice-ocean stress terms are given by

$$\vec{\tau_a} = \rho_a C_{da}|\vec{u_a} - \vec{u}|(\vec{u_a} - \vec{u}), \tag{2.17}$$

$$\vec{\tau_o} = \rho_o C_{do}|\vec{u_o} - \vec{u}|(\vec{u_o} - \vec{u}), \tag{2.18}$$

where $\rho_a = 1.3\,\mathrm{kg\,m^{-3}}$ and $\rho_o = 1025\,\mathrm{kg\,m^{-3}}$ are the air and water densities, $C_{da} = 0.001$ and $C_{do} = 0.004$ are the air-ice and ocean-ice drag coefficients, $\vec{u_a}$, $\vec{u_o}$ and $\vec{u}$ are the wind, ocean and ice velocities. There are no ocean currents in this study ($\vec{u_o} = 0$ at all times). The only dynamic impact the ocean has on the ice is through passive ocean drag. The ocean drag term used is thus simplified to

$$\vec{\tau_o} = -\rho_o C_{do}|\vec{u}|(\vec{u}). \tag{2.19}$$

Solving the full momentum equation (Equation (4.1)) for $\vec{u}$ requires a constitutive relation that relates the stress and strain rates. The VP rheology proposed by Hibler (1979) is given by a constitutive law that relates the stress tensor to the strain rate, an internal ice pressure, P, and nonlinear bulk and shear viscosities, ζ and η, such that the principal components of stress lie on an elliptical yield curve,

$$\frac{1}{2\eta}\sigma_{ij} + \frac{\eta - \zeta}{4\eta\zeta}\sigma_{kk}\delta_{ij} + \frac{P}{4\zeta}\delta_{ij} = \dot{\epsilon}_{ij}. \tag{2.20}$$

The strain rate tensor is defined as

$$\dot{\epsilon}_{ij} = \frac{1}{2}\left(\frac{\partial u_i}{\partial x_j} + \frac{\partial u_j}{\partial x_i}\right), \tag{2.21}$$

and P is a measure of ice strength which is related to the thickness of the ice, h and fractional ice area, A. The ice strength is parametrised as

$$P = P^* A h exp^{-20(1-A)}, \tag{2.22}$$

where P^* is the ice strength constant, taken as here as $27500\,\mathrm{N\,m^{-2}}$. The ice strength is parametrised to increase exponentially as $A \to 1$. The nonlinear bulk and shear viscosities are defined in terms of the strain rates,

$$\zeta = \frac{P}{2\Delta}, \tag{2.23}$$

$$\eta = \frac{P}{2\Delta e^2}, \tag{2.24}$$

$$\Delta = [(\dot{\epsilon}_{11}^2 + \dot{\epsilon}_{22}^2)(1 + e^{-2}) + 4e^{-2}\dot{\epsilon}_{12}^2 + 2\dot{\epsilon}_{11}\dot{\epsilon}_{22}(1 - e^{-2})]^{1/2}, \tag{2.25}$$

where the eccentricity, $e = 2$, is the ratio of the major to minor axis of the elliptical yield curve.

An elastic contribution to the strain rate is included in CICE in such a way that the VP and EVP models are identical at steady state (Hunke and Lipscomb, 2010),

$$\frac{1}{E}\frac{\partial \sigma_{ij}}{\partial t} + \frac{1}{2\eta}\sigma_{ij} + \frac{\eta - \zeta}{4\eta\zeta}\sigma_{kk}\delta_{ij} + \frac{P}{4\zeta}\delta_{ij} = \dot{\epsilon}_{ij}. \tag{2.26}$$

2.5.3 Thermodynamics

Ice thermodynamics corresponds to all the processes that involve energy transfer and storage which lead to the potential of growth or melt of ice. CICE utilizes the energy-conserving thermodynamic sea ice model by Bitz and Lipscomb (1999) to compute the growth and melt rates of ice and snow. For each ice thickness category CICE calculates the ice and snow thickness changes and vertical temperature profiles based on vertical radiative, turbulent and conductive heat fluxes. The model considers the effect of brine pockets on specific heat and thermal conductivity due to internal melting and freezing.

Surface fluxes

An energy balance of radiative, turbulent, and conductive heat fluxes in each grid cell determines the temperature profile and thickness changes of ice and snow. The net energy flux from the atmosphere to the surface boundary of the ice or open water (with all fluxes defined as positive downward) is

$$F_0 = F_s + F_l + F_{L\downarrow} + F_{L\uparrow} + (1-\alpha)(1-i_0)F_{sw}. \tag{2.27}$$

Here, F_s and F_l are the sensible and latent heat fluxes which are calculated using a stability based boundary layer parameterisation. $F_{L\downarrow}$ is the incoming longwave flux, $F_{L\uparrow}$ is the outgoing longwave flux, F_{sw} is the incoming shortwave flux which is obtained from observational data. The albedo is denoted by α and i_0 is the fraction of absorbed shortwave flux that penetrates into the ice surface.

Internal fluxes

The rate of temperature change in the ice interior is given by the heat conduction equation defined by Maykut and Untersteiner (1971),

$$\rho_i c_i \frac{\partial T_i}{\partial t} = \frac{\partial}{\partial z}\Big(K_i \frac{\partial T_i}{\partial z}\Big) - \frac{\partial}{\partial z}(I_{pen}(z)), \tag{2.28}$$

where $\rho_i = 917\,\mathrm{kg\,m^{-3}}$ is the ice density (assumed here to be constant), T is the temperature at vertical position z, where z is the vertical coordinate within the ice (defined to be positive downward), S is the salinity of the sea ice, $c_i(T, S)$ is the specific heat of sea ice, $K_i(T, S)$ is the thermal conductivity of sea ice. I_{pen} is the flux of penetrating solar radiation at depth z given by

$$I_{pen}(z) = I_0 \exp(-k_i z). \tag{2.29}$$

Here I_0 is the penetrating solar flux at the top ice surface and k_i is the bulk extinction coefficient for solar radiation. The specific heat of sea ice is approximated by

$$c_i(T, S) = c_0 + \frac{L_0 \mu S}{T^2}, \tag{2.30}$$

where $c_0 = 2106\,\mathrm{J\,kg^{-1}\,deg^{-1}}$ is the specific heat of fresh ice at $0\,^\circ\mathrm{C}$, $L_0 = 3.34 \times 10^5 \mathrm{J\,kg^{-1}}$ is the latent heat of fusion of fresh ice at $0\,^\circ\mathrm{C}$, and $\mu = 0.054\,\mathrm{deg\,ppt^{-1}}$ is the ratio between the freezing temperature and salinity of brine. Following Untersteiner (1964), the thermal conductivity of sea ice is given by

$$K_i(T, S) = k_0 + \frac{\beta S}{T_i}, \tag{2.31}$$

where $k_0 = 2.03\,\mathrm{W\,m^{-1}\,deg^{-1}}$ is the conductivity of fresh ice and $\beta = 0.13\,\mathrm{W\,m^{-1}\,psu^{-1}}$ is an empirical constant. The corresponding equation for the temperature change in snow is

$$\rho_s c_s \frac{\partial T_s}{\partial t} = \frac{\partial}{\partial z}\Big(K_s \frac{\partial T_s}{\partial z}\Big), \tag{2.32}$$

where $\rho_s = 330\,\mathrm{kg\,m^{-3}}$ is the snow density (assumed here to be constant), c_s is the specific heat of snow and $K_s = 0.30\,\mathrm{W\,m^{-1}\,deg^{-1}}$ is the thermal conductivity of snow. The majority of the incoming solar radiation is assumed to be absorbed near the top surface when snow is present.

Bottom and lateral fluxes boundary

Ablation or accretion at the bottom of the ice is governed by

$$q\delta h = (F_{cd} - F_{bot})\Delta t, \tag{2.33}$$

where F_{bot} is the heat flux from the ice bottom to the ocean surface is given by Maykut and McPhee (1995):

$$F_{bot} = -c_o \rho_o c_h u_* (T_o - T_f). \tag{2.34}$$

Here, c_o is the specific heat capacity of the ocean, ρ_o is the ocean density, $c_h = 0.006$ is the Stanton number describing the mixed layer to sea ice turbulent heat transfer, u_* is the frictional velocity between the ice and the mixed layer, T_o is the temperature of the ocean surface (which is equal to the mixed layer temperature in the CICE standard setup used here) and T_f is the salinity dependent freezing temperature at the ice bottom. F_{cd} is the conductive heat flux at the bottom surface,

$$F_{cd} = \frac{K_{i,N+1}}{\Delta h_i}(T_{iN} - T_f). \tag{2.35}$$

If ice is melting at the bottom surface q is the enthalpy of the bottom ice layer. If ice is growing then q is the enthalpy of new ice with temperature T_f and salinity equal to that of the ocean surface.

Lateral heat flux is defined as

$$F_{side} = \frac{R_{side}(q_i V_i + q_s V_s)}{dt}, \tag{2.36}$$

where q_i and q_s are the ice and snow enthalpies respectively and R_{side} is the fraction of ice that can be melted laterally within a given timestep. This is calculated using the formulation defined by Steele (1992),

$$R_{side} = \frac{w_{side}\pi dt}{\alpha_r L_{floe}}, \tag{2.37}$$

where $\alpha_r = 0.66$ is a constant, $L_{floe} = 300$m is the average floe diameter and w_{side} is the lateral melt rate. Ice also forms when snow loading causes the upper ice surface to lie below the surface of the ocean, that is, when

$$h^* = h_s - \Big(\frac{\rho_o - \rho_i}{\rho_s}\Big)h_i > 0. \tag{2.38}$$

When this happens an amount of snow is converted to ice so that the snow-ice interface is brought level with the ocean surface: $\delta h_s = -\rho_i h^*/\rho_o$, $\delta h_i = \rho_s h^*/\rho_o$.

2.5.4 Numerical inclusion of the landfast ice parameterisation

The proposed landfast ice parameterisations can be incorporated into any sea ice model. Here we have considered its inclusion into the Los Alamos Sea Ice Model (CICE). Once the area of grounded ice is found the associated ice velocity is subsequently updated as shown below. The original numerical elastic-viscous-plastic scheme used in CICE produces an updated ice velocity per dynamical timestep (Δt_e) resulting from the combined external and internal forces acting on the ice,

$$u^{t+1} = u^t + F_{A_x}\frac{\Delta t_e}{m}, \tag{2.39}$$

$$v^{t+1} = v^t + F_{A_y}\frac{\Delta t_e}{m}, \tag{2.40}$$

where u^t, v^t are the initial ice velocity components, u^{t+1}, v^{t+1} are the new ice velocity components and F_A encompasses all forces acting on the ice. Updating the original dynamics procedure to account for the new frictional grounding force (f_G) results in the target ice velocity components, $\tilde{u}^{t+1}, \tilde{v}^{t+1}$,

$$\tilde{u}^{t+1} = u^t + \frac{\Delta t_e}{m}(F_{A_x} + F_{G_x}), \tag{2.41}$$

$$\tilde{v}^{t+1} = v^t + \frac{\Delta t_e}{m}(F_{A_y} + F_{G_y}). \tag{2.42}$$

The original ice velocity components were semi-implicitly relaxed to the target over a damping timescale $T_f = C\Delta t_e$. For the simulations detailed in Section 2.5.5 $C = 1$,

$$u^{t+1} = \frac{u^t + \frac{\Delta t_e}{T_f}(\tilde{u}^{t+1} - \alpha u^t)}{\left(1 + \frac{\Delta t_e}{T_f}(1-\alpha)\right)}, \tag{2.43}$$

$$v^{t+1} = \frac{v^t + \frac{\Delta t_e}{T_f}(\tilde{v}^{t+1} - \alpha v^t)}{\left(1 + \frac{\Delta t_e}{T_f}(1-\alpha)\right)}, \tag{2.44}$$

where u^{t+1}/v^{t+1} are the final ice velocities resulting from the new dynamical procedure and α is a constant used to determine whether the equation is solved implicitly or explicitly. If $\alpha = 1$ the solution is fully explicit,

$$u^{t+1} = u^t + \frac{\Delta t_e}{T_f}(\tilde{u}^{t+1} - u^t), \tag{2.45}$$

$$v^{t+1} = v^t + \frac{\Delta t_e}{T_f}(\tilde{v}^{t+1} - v^t). \tag{2.46}$$

It was found that a fully explicit method led to numerical instability. When $\alpha = 0$ the solution is fully implicit,

$$u^{t+1} = \frac{u^t + \frac{\Delta t_e}{T_f}\,\tilde{u}^{t+1}}{\left(1 + \frac{\Delta t_e}{T_f}\right)}, \tag{2.47}$$

$$v^{t+1} = \frac{v^t + \frac{\Delta t_e}{T_f}\,\tilde{v}^{t+1}}{\left(1 + \frac{\Delta t_e}{T_f}\right)}. \tag{2.48}$$

A fully implicit solution allows a longer Δt_e to be used without losing stability. In these experiments a semi-implicit solver, $\alpha = 0.5$, was used. This remained numerically stable at the given model advective and dynamic time-steps. The semi-implicit solution is given by,

$$u^{t+1} = \frac{u^t + \frac{\Delta t_e}{T_f}(\tilde{u}^{t+1} - \frac{1}{2}u^t)}{\left(1 + \frac{1}{2}\frac{\Delta t_e}{T_f}\right)}, \tag{2.49}$$

$$v^{t+1} = \frac{v^t + \frac{\Delta t_e}{T_f}\tilde{v}^{t+1} - \frac{1}{2}v^t}{\left(1 + \frac{1}{2}\frac{\Delta t_e}{T_f}\right)}. \tag{2.50}$$

2.5.5 Setup

CICE was run in standalone format using a displaced pole grid at 3 and 1 degree resolution. This grid centers its north pole on Greenland removing the singularity in the Arctic Ocean and allowing for continuous simulation of the Arctic Ocean. CICE contains a simple mixed layer ocean model with a prognostic ocean temperature. There are no interactive ocean currents, but the impact of upper ocean circulation on sea ice is taken into account through the ice-ocean drag. In this study 15 ice thickness categories, plus open water, each with 4 ice layers and 1 snow layer were used. Unless otherwise stated all sea ice parameters remain as standard. A multi-category bathymetry distribution for each model grid cell was developed from the ETOPO1 dataset, thereby supplementing the bathymetry data with higher resolution information without changing the resolution the model is run at. Further details on the boundary conditions are included in Section 2.6. The model was initialised with no ice and integrated for 11 years (10 year spin up) using repeat NCAR atmospheric forcing from 1997. Results from the last year of integration from the following simulations are presented:

- No landfast ice parameterisation - control experiment,

- Independent landfast ice parameterisation,
- Restricted landfast ice parameterisation using a coupling parameter:
  - $\lambda = 1.05$
  - $\lambda = 1.10$
  - $\lambda = 1.25$

2.6 Boundary conditions

2.6.1 Bathymetry

The high resolution global bathymetry dataset ETOPO1, a 1 arc-minute global relief model of the Earth's surface built from numerous global and regional data sets (Amante and Eakins, 2009), was used to create a high resolution sub-grid scale bathymetry distribution. The total number (N) and area (a_i) of the high resolution ETOPO1 grid cells which reside within each coarser and irregular CICE grid cell was found. The centre point of the ETOPO1 grid cell was used to determine which CICE cell it should be associated with. Once the total ETOPO1 contribution to each CICE grid cell was determined the information was distributed into the depth categories ($Ncat_c$) where $c = 1 : 16$. The boundaries of the depth categories were comparable to the updated ice thickness categories, but with the addition of a land category ($Ncat_1$) (Table 2.1). The fractional concentration of ocean within each depth category was then found by normalising the bathymetry cell area within each category with respect to the total area of the contributing bathymetry cells. For example, if $Ncat = 1$ and there are N number of ETOPO1 cells which contribute to 1 CICE grid cell, of which n contribute to the 1$^{\text{st}}$ depth category, then the fractional concentration in the CICE grid cell of bathymetry which resides within the 1$^{\text{st}}$ is defined as

$$A_{Ncat_1} = \frac{\sum_{k=1}^{n} a_i}{\sum_{k=1}^{N} a_i}. \tag{2.51}$$

Table 2.1: Ice and bathymetry categories

Variable	Ice		Bathymetry	
	Original	New	Original	New
Category no.	Lower thickness bound (m)			
1	0.00	0.00	-	Land
2	0.60	0.60	-	0.00
3	1.40	1.40	-	0.60
4	2.40	2.40	-	1.40
5	3.60	3.60	-	2.40
6	-	5.00	-	3.60
7	-	6.60	-	5.50
8	-	8.40	-	6.60
9	-	10.40	-	8.40
10	-	12.60	-	10.40
11	-	15.00	-	12.60
12	-	17.60	-	15.00
13	-	20.40	-	17.60
14	-	23.40	-	20.40
15	-	26.60	-	23.40
16	-	-	-	26.60

The original ice categories are those used as standard in CICE. The number of ice categories was increased to 15 (new) covering an increased thickness range. In standalone format bathymetry is not included as standard. The newly introduced bathymetry has categories comparable to the new ice categories.

2.6.2 Atmospheric

Surface meteorological forcing was obtained from NCAR. Six hourly fields of air temperature, humidity, density and 10m wind velocity, and monthly precipitation,

shortwave and longwave radiation for the 1st January 1997 - 31st December 1997 were used to calculate bulk surface fluxes. The data is provided in conjunction with the CICE model on the 3 degree grid. The atmospheric fields were interpolated and used for the comparable 1 degree resolution simulations. The NCAR data set is designed for testing the CICE code, and is not necessarily the optimum observational data. However, it was felt that as the focus of this research was on testing the hypothesis of ice grounding leading to landfast ice production, rather than gaining exact global predictions of landfast ice, its use was justifiable.

2.7 Results

In Chapter 1 the range of definitions historically used in landfast ice research was discussed. In this study the definition applied to characterise landfast ice is based on that proposed by Mahoney et al. (2005), where the ice must remain stationary for at least 20 days. In order to implement this definition a maximum allowed velocity for fast ice must be identified. Ice with velocity below this value, for at least 20 days, will therefore be considered landfast. Past landfast ice modelling studies used a critical ice velocity based on observations of average ice flow in the study region, or known model limitations (Ólason, 2012). Here, we inferred the maximum critical fast ice velocity, $0.001\,\mathrm{ms}^{-1}$, directly from model results by considering histograms of ice velocity across the considered regions. The ice flow must therefore remain below $0.001\,\mathrm{ms}^{-1}$ for at least 20 days to be characterised as landfast. This prevents ice which intermittently becomes stationary, due to changes in the forcing field or topographic constraints, being classified as landfast.

2.7.1 Arctic

The National Ice Center (NIC) have produced a series of Sea Ice Charts, and comparable gridded data, of sea ice concentration, including information on landfast ice coverage (100% concentration or absent) since 1972. The data set is produced through analyses of available *in situ*, remote sensing, and model data sources and

covers a spatial area of $45°\text{N} - 90°\text{N}$ and $180°\text{W} - 180°\text{E}$. The data is provided on a 361×361 grid, where each cell has a nominal size of $25 \times 25\,\text{km}$ (NIC, 2006, updated 2009).

No explicit definition of landfast ice is provided with this data set, most likely due to the data stemming from multiple sources, and the identification of landfast ice based on the informed judgement of analysts. H. Stern commented that although landfast ice observations were charted continuously, information prior to 1976 is considered unreliable (NIC, 2006, updated 2009). We found that in some of the early years the lack of data caused the minimum landfast ice coverage to be estimated as 0, skewing the data to a lower average estimate.

For reference, most of the Arctic locations mentioned in this section are identified in Figure 2.4.

Control

Figures 2.5 and 2.6 show the Arctic ice volume per unit area in winter (JFM) and summer (JAS) at 3 and 1 degree resolution respectively. In winter the largest ice volume per unit area was observed within the Canadian Arctic Archipelago (CAA) (up to 5 m), along the North Greenland coast and to a lesser extent north of Svalbard ($\approx 3\,\text{m}$). There is a general graduation across the central Arctic to smaller ice volumes along the North Russian coast ($\approx 2\,\text{m}$). In summer the ice cover retreats north. CICE simulates perennial ice coverage over much of the Central Arctic Ocean and CAA. The general patterns are comparable between the 3 and 1 degree simulations, but much of the detail and variation is lost at the coarser 3 degree resolution. In general these patterns compare well to other modelling studies and observations (Laxon et al., 2013; Kwok and Cunningham, 2008; Kwok et al., 2009; Rothrock et al., 2003; Bourke and Garrett, 1987).

However, there are a number of areas where CICE run in standalone format (i.e. without an active ocean) is unable to reproduce a realistic ice cover. For example, CICE underestimates the amount, and thickness, of sea ice along the North Greenland coast in both winter and summer. Observations from ICESat and CryoSat-2

Figure 2.4: Arctic topographic map with bathymetry by Hugo Ahlenius, GRID-Arendal, 2010 ($http://www.grida.no/graphicslib/detail/arctic-topography-and-bathymetry-topographic-map_d003$).

show that the ice in this area is approximately 5 m thick in winter and can extend significant distances offshore. In summer a significant amount of this thick ice is observed to remain (Laxon et al., 2013; Kwok and Cunningham, 2008; Kwok et al., 2009). Experiments where CICE is coupled with and active ocean, or forced with realistic ocean conditions, were better able to represent the temporal and spatial extent of this thick multiyear ice (Hunke, 2010; Rae et al., 2014).

CICE was also found to overestimate the amount of ice in some regions. For example, the Kara Sea is an area of seasonal ice coverage, lasting between 6 - 9 months depending on the location and year (Johannessen et al., 2004; Cheng et al., 2013; Ólason, 2012). Here, CICE simulated much of the Kara Sea to be continuously ice covered. This is also the case for the Laptev Sea, which is known to be dominated by landfast sea ice. Much of the Laptev Sea landfast ice is seasonal resulting in large parts being ice free in summer (Bareiss and Goergen, 2005; Eicken et al., 2005). However, CICE is unable to reproduce this seasonal coverage, and models much of the western Laptev Sea to be dominated by multiyear ice.

These issues result from CICE not including realistic ocean currents or heat fluxes. Ocean currents are an important component of the polar regions, and have a significant impact on ice distribution and thickness (Equation (2.15)). Ocean currents can cause rafting and ridging of the ice cover, resulting in a localised increase in ice thickness. Similarly, divergent ocean currents can produce areas of thin ice and open water. The circulation of relatively warm water under the sea ice can promote melt in summer and prohibit growth in winter (e.g. Vladimir et al., 2012). Also, the absence of river processes, such as river discharge after spring thaw will have an impact on the ice cover. The absence of these processes will affect the growth/melt rate of the sea ice. The inadequacies of CICE run in standalone format to reproduce a realistic ice cover in some regions, as identified here, will inevitably have an impact on the landfast ice parameterisation tested.

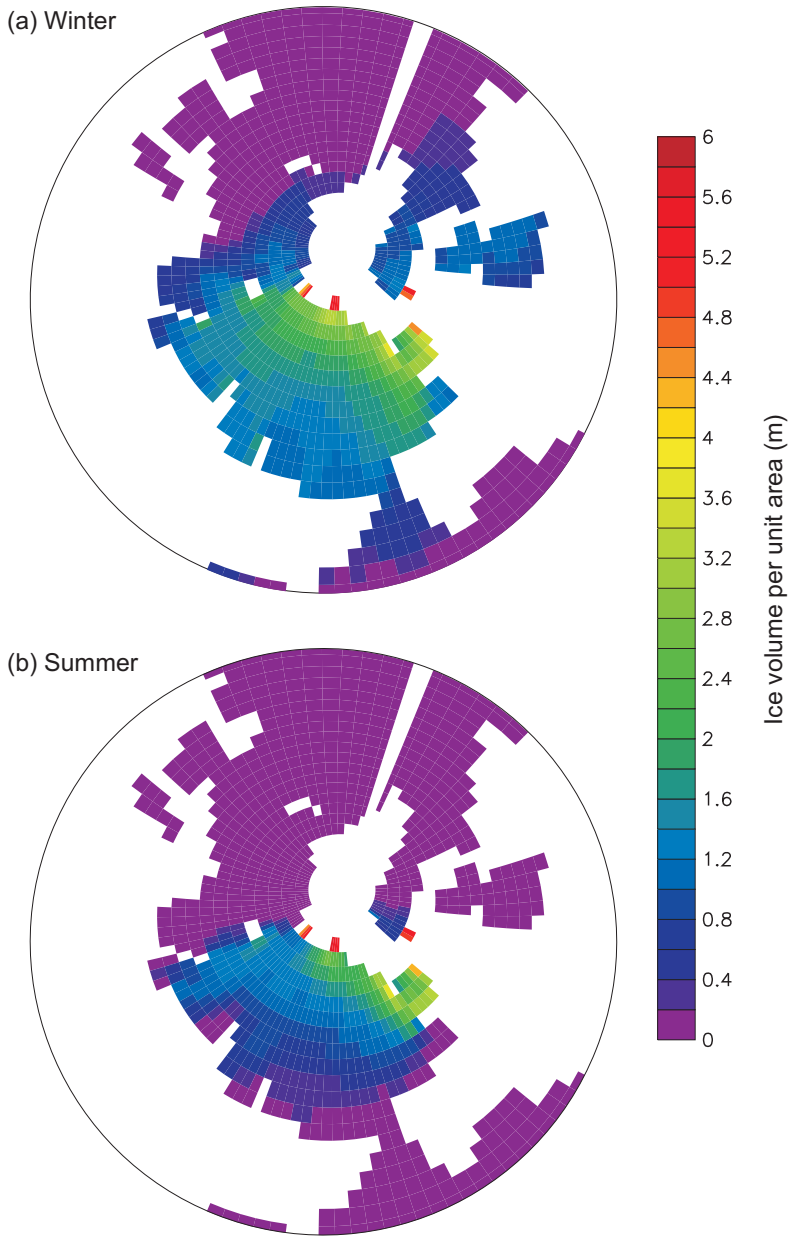

Figure 2.5: Arctic (a) winter (JFM) and (b) summer (JAS) ice volume per unit area (m) for the control simulation (i.e. no landfast ice parameterisation) run at 3 degree resolution.

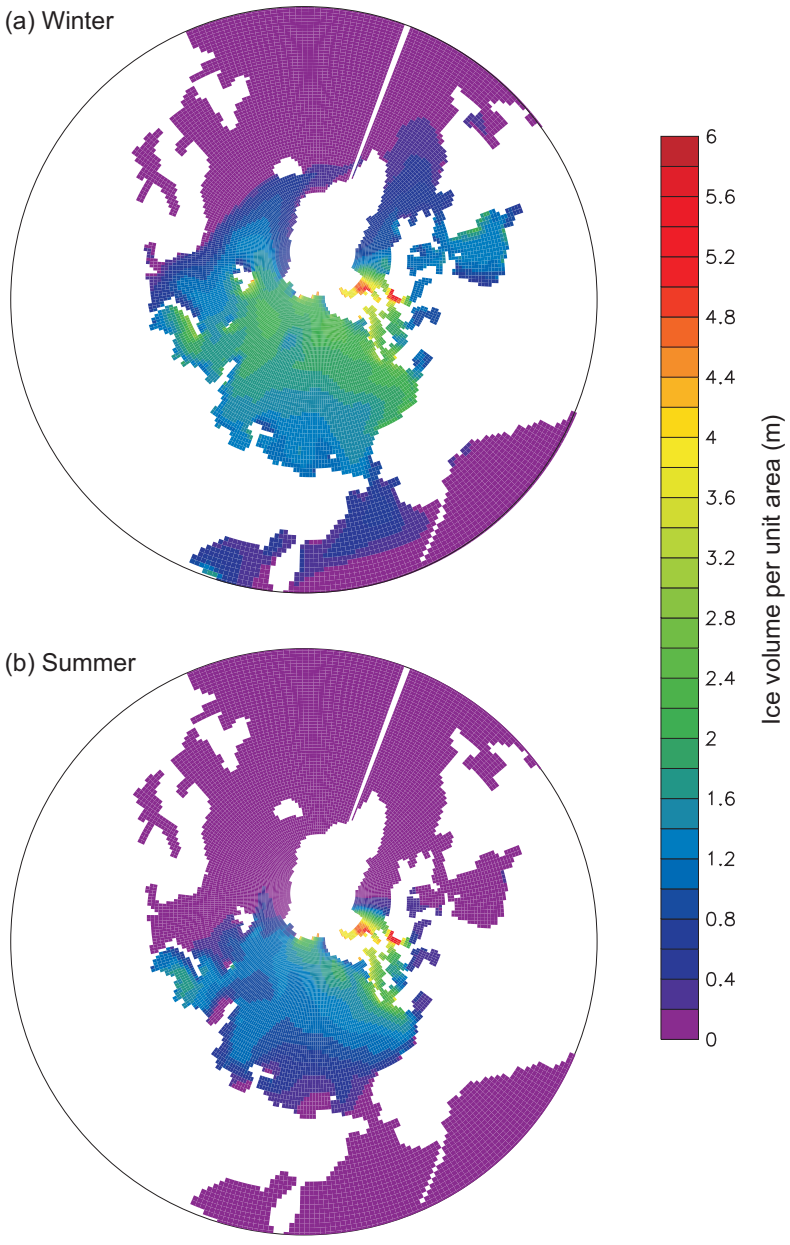

Figure 2.6: Arctic (a) winter (JFM) and (b) summer (JAS) ice volume per unit area (m) for the control simulation (i.e. no landfast ice parameterisation) run at 1 degree resolution.

Area of grounded ice

Both the independent and restricted landfast ice parameterisations reproduced the observed seasonal pattern of grounded ice, progressing steadily from a summer minimum to a winter maximum, Figures 2.7 and 2.8. The restricted landfast ice parameterisation produced significantly less grounded ice than the independent, as it limited the maximum gouge depth at which ice could be considered aground. The seasonal pattern of the grounded ice is comparable between the 3 and 1 degree simulations, but the area of grounded ice is reduced by approximately 50% at finer resolution. The maximum area of grounded ice in winter at 3 degree resolution was $7.52 \times 10^{11}\,\mathrm{m}^2$, compared to $3.75 \times 10^{11}\,\mathrm{m}^2$ at 1 degree resolution. This was due to the increased ability to resolve the complexity of the coastal regions.

At both resolutions, the independent grounding scheme underestimated the removal of grounded ice in summer. This unrealistic behaviour is likely to be a result of the simple definition this parameterisation applied to grounded ice. It allowed any ice to ground if its draft thickness was greater than the local ocean depth. This definition allowed for the possibility of erroneously thick ice to occur and ground on relatively shallow bathymetry. It was previously shown that the grounded ice produced by the landfast ice parameterisations is very stable as the reactive grounding force is much larger than the other dominant forces acting on the ice. As such, it is likely that thermodynamics must play a significant role in ungrounding ice through melt. However, if the grounded ice is much thicker than the local ocean depth, as allowed by the independent parameterisation, then a significant amount of ice may need to be melted before the ridge is uncoupled from the seabed. For example, if an ice ridge with draft thickness of 30 m grounds along the 20 m isobath, then the thermodynamics must melt 10 m of ice for the ridge to uncouple, otherwise it becomes multiyear. Once the transition to multiyear ice occurred, the independent parameterisation was never able to unground the ice. By limiting the maximum possible thickness the grounded ice can be, as the restricted parameterisation does, you limit the amount of ice that must be melted for uncoupling to occur. This effect would be exacerbated by differences in the bathymetry and model resolution. For

example, some grid cells which were considered as open water within the model contained fractional concentrations of land in the bathymetry data, providing unrealistic opportunities for ice to ground, especially for the independent parameterisation.

Other factors which could also contribute to the production of multiyear grounded ice include the absence of relatively warm water circulating under the landfast ice cover in summer months, which will act to destabilise the grounded ice. Also, ocean currents, which are not included here, may act to set the grounded ridges into motion. The absence of river processes, such as the river discharge in spring after thaw may also act to prohibit the summer destabilisation and drift offshore. If ice is aground there is no, or very little, water underneath the ice which can be used to grow basally. The grounded ice may grow laterally, through accumulation of snow on top, or through deformation. The landfast ice parameterisations do not prohibit the basal growth of grounded ice, allowing the ice to undergo unrealistic vertical growth when in contact with the seabed. The rate of this growth is likely to be relatively small due to the thickness of the ice. However, any unrealistic vertical ice growth will add to the proportion of ice that must be melted before the ice can unground.

Location of landfast ice

The spatial and temporal coverage of landfast ice, produced from 5 day averages for the control, independent, and restricted landfast ice parameterisations are shown in Figures 2.9 and 2.10 for the 3 and 1 degree resolution simulations respectively. In the absence of any grounding the model was able to produce landfast ice under the applied definition, persisting for the majority of the year in the CAA and Baffin Bay region, as well as in Foxe Basin, along the North Greenland coast and North Russian coast for shorter periods. This landfast ice occurred due to a combination of restrictive geometry and atmospheric forcing creating conditions favourable to the production of stationary ice.

The landfast ice parameterisation enhanced the occurrence of landfast ice in realistic locations, by allowing its creation and maintenance through grounded pinning points. New landfast ice was produced in Hudson Bay (Galley et al., 2012), along

the South Greenland Coast, the Bering Sea and Bering Strait, and around Svalbard, with enhanced occurrence along the Canadian Coast and Beaufort Sea (Mahoney et al., 2005, 2007b) and the North Russian Coast, specifically in the eastern Kara Sea and Laptev Sea (Divine et al., 2004, 2005; Ólason, 2012). The spatial distribution of the landfast ice produced in these regions in general compared well with observations and previous studies.

There were some locations where the spatial and temporal extent of landfast ice was underestimated. For example, the simulations were unable to realistically reproduce the Norske Øer ice barrier, an extensive region of multiyear landfast ice along the northeast coast of Greenland (Hughes et al., 2011; Holland et al., 1995). However, this failing is not due to the parameterisation, but instead is due to the use of CICE in standalone format. The control simulations (Figures 2.5 and 2.6) show that CICE is unable to reproduce the maximum ice thicknesses in this region.

Some of the landfast ice produced by the parameterisations was unrealistically stable, becoming multiyear. The independent grounding scheme produced multiyear landfast ice between Svalbard and Franz Josef Land due to sub-grid scale shallow bathymetry features and islands in the high resolution bathymerty data producing a line of grounded ice, which acted like a protective barrier to the landfast ice sheet. At this relatively coarse resolution the parameterisations also led to motionless ice in the central Arctic region. As this ice was stationary for more than 20 days it was classified as landfast ice. However, this ice was not held stationary due to the grounding of ice ridges as the central Arctic Ocean is too deep for ice to ground. Instead, it was held stationary by the extensive grounded and landfast ice along the Arctic shelves, reducing the effective region for the atmospheric forcing to act. The control simulation (Figures 2.5 and 2.6) showed that CICE produced an unrealistic multiyear ice cover in the Kara and Laptev Seas. This resulted in unrealistic multiyear landfast ice in these regions. Restricting the maximum thickness of the grounded ice limited the spatial and temporal extent of the landfast ice, with the most restrictive parameterisation comparable to the control results.

In general the coarser resolution simulations overestimated the occurrence of

landfast ice. At finer resolutions, the location and timespan of the landfast ice was much more realistic due to the enhanced ability to resolve more of the intricate geometry of the Arctic Coast and small islands.

Area of landfast ice

The average monthly landfast ice area for the Arctic Region ($\geq 60°$N) produced by the landfast ice parameterisations compared well with NIC climatologies at both tested resolutions, Figure 2.11. In general the independent grounding parameterisation produced the most landfast ice, with the area reducing with increased grounding restriction.

The removal of landfast ice in summer was underestimated by all parameterisations, but most notably by the independent landfast parameterisation. A degree of this multiyear landfast ice, evident in the control simulation, resulted from restrictive geometry of the Canadian Archipelago and surrounding regions. However, in some locations where the grounding scheme was operating, such as the Kara Sea, the Laptev Sea and around Svalbard, the landfast ice grew anomalously thick and became multiyear. This resulted from a combination of unrealistically thick and persistent ice coverage produced by CICE run in standalone format and the landfast ice parameterisations producing unrealistically stable, multiyear, grounded ice. This unrealistic behaviour is discussed further in Section 2.8.

2.7.2 Antarctic

The only landfast ice climatology available for the Antarctic region is that conducted by Fraser et al. (2012). They produced an 8.8 year climatology along the East Antarctic Coast from a Moderate Resolution Imaging Spectroradiometer (MODIS) time series. Fast ice was identified with respect to ice motion and contiguity with the land. The pack ice appeared blurred in the images due to its motion, while landfast ice features remained clearly defined. Unfortunately, due to the short temporal period and limited spatial coverage of this climatology, it is not suitably robust for use here as validation.

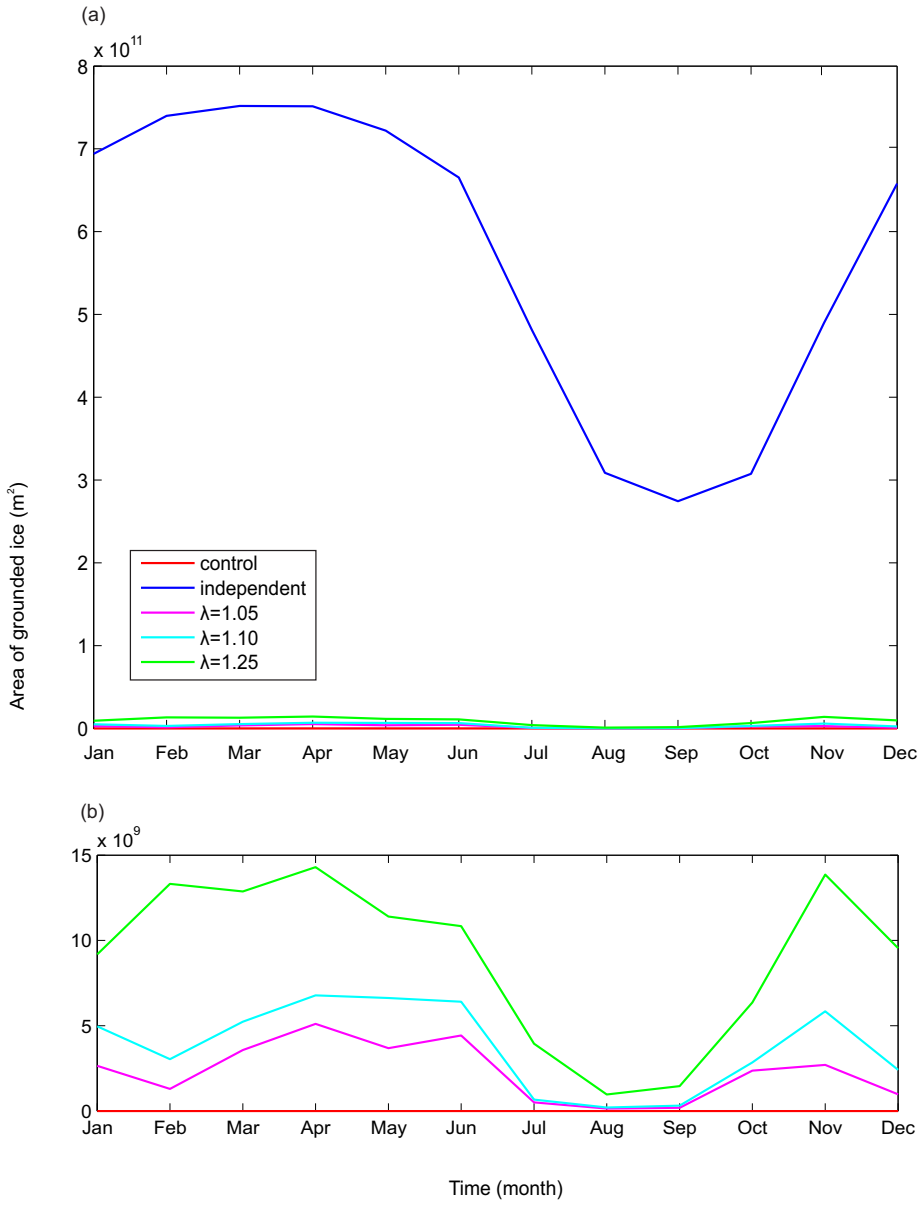

Figure 2.7: Monthly estimates of Arctic grounded ice area at 3 degree resolution for the control (red), independent grounding (blue) and restricted grounding schemes with a coupling parameter $\lambda = 1.25$ (green), 1.10 (cyan) and 1.05 (magenta) for (a) all simulations and (b) magnification of the control and restricted parameterisation.

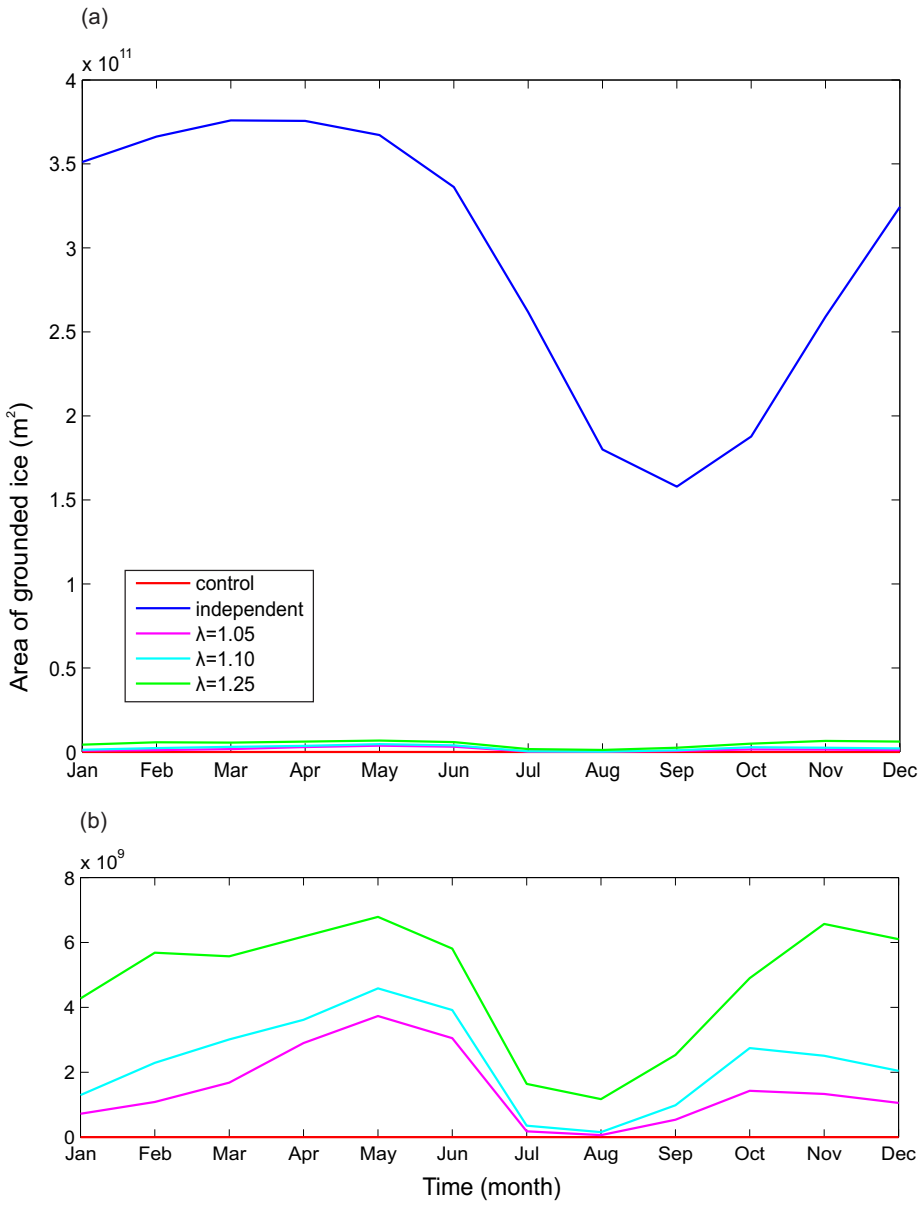

Figure 2.8: Monthly estimates of Arctic grounded ice area at 1 degree resolution for the control (red), independent grounding (blue) and restricted grounding schemes with a coupling parameter $\lambda = 1.25$ (green), 1.10 (cyan) and 1.05 (magenta) for (a) all simulations and (b) magnification of the control and restricted parameterisation.

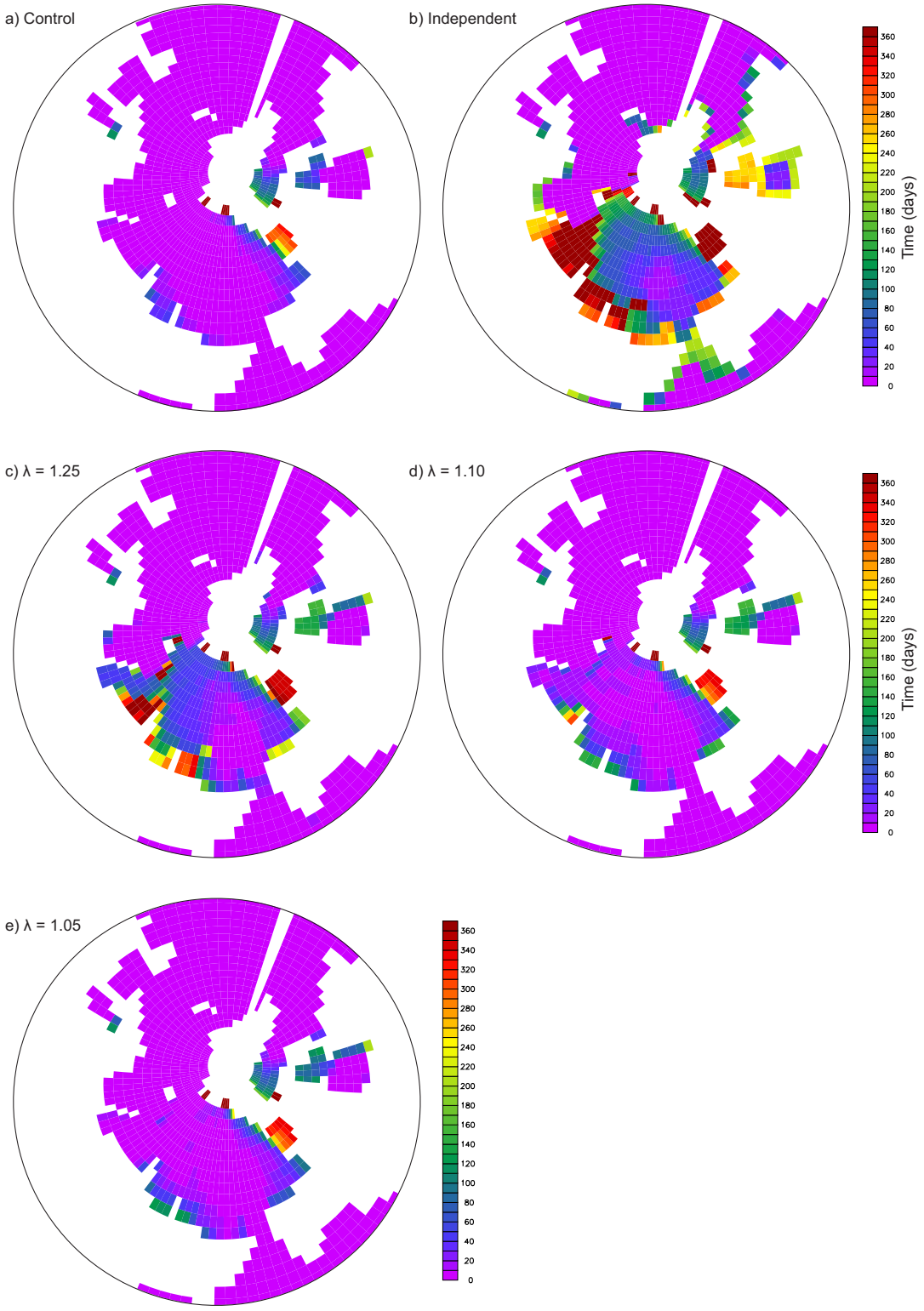

Figure 2.9: Temporal coverage of Arctic landfast ice at 3 degree resolution from 5 day averages for the a) control, b) independent parameterisation, and restricted landfast ice parameterisation using c) $\lambda = 1.25$, d) $\lambda = 1.10$ and e) $\lambda = 1.05$.

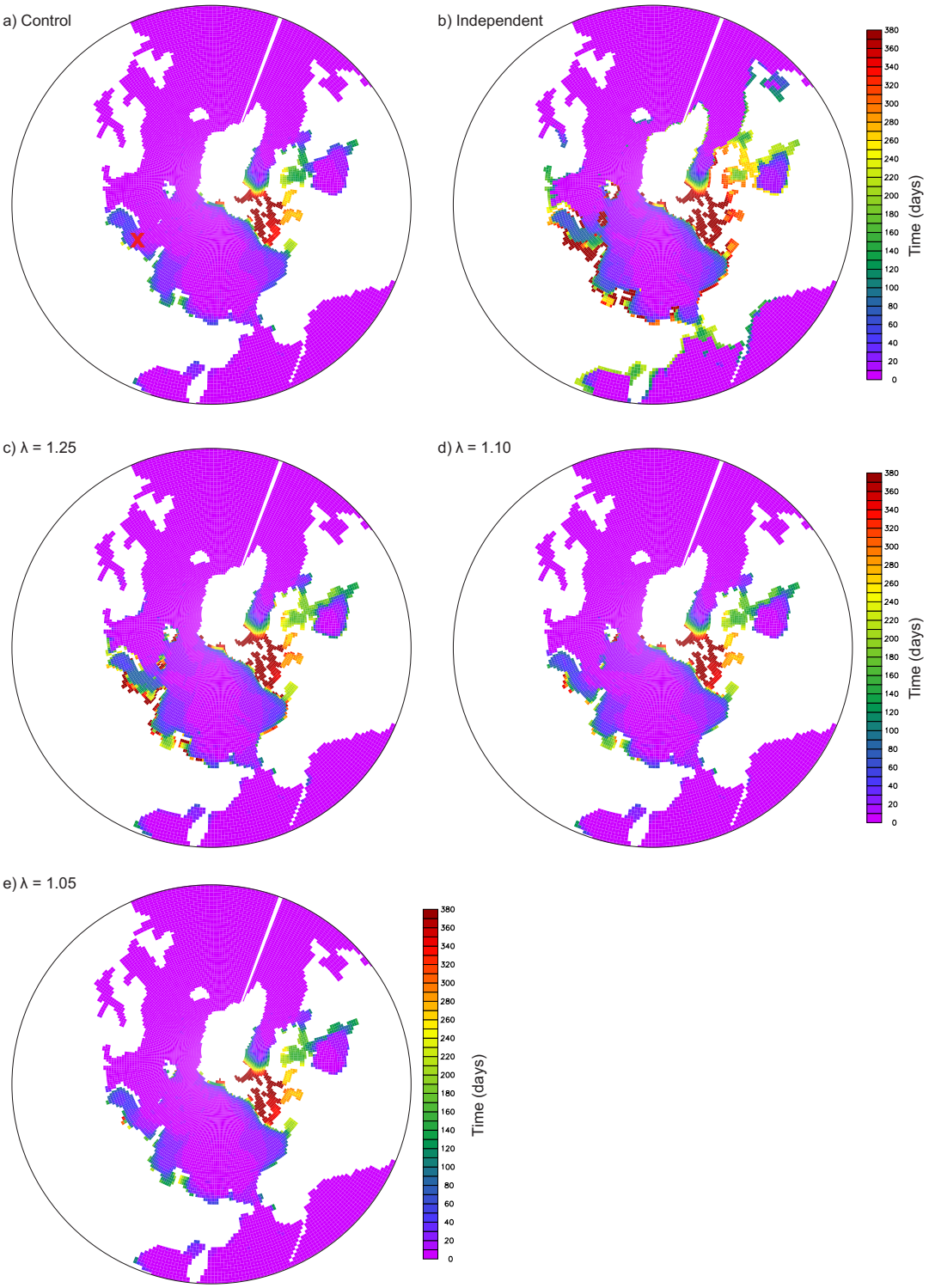

Figure 2.10: Temporal coverage of Arctic landfast ice at 1 degree resolution from 5 day averages for the a) control, b) independent parameterisation, and restricted landfast ice parameterisation using c) $\lambda = 1.25$, d) $\lambda = 1.10$ and e) $\lambda = 1.05$.

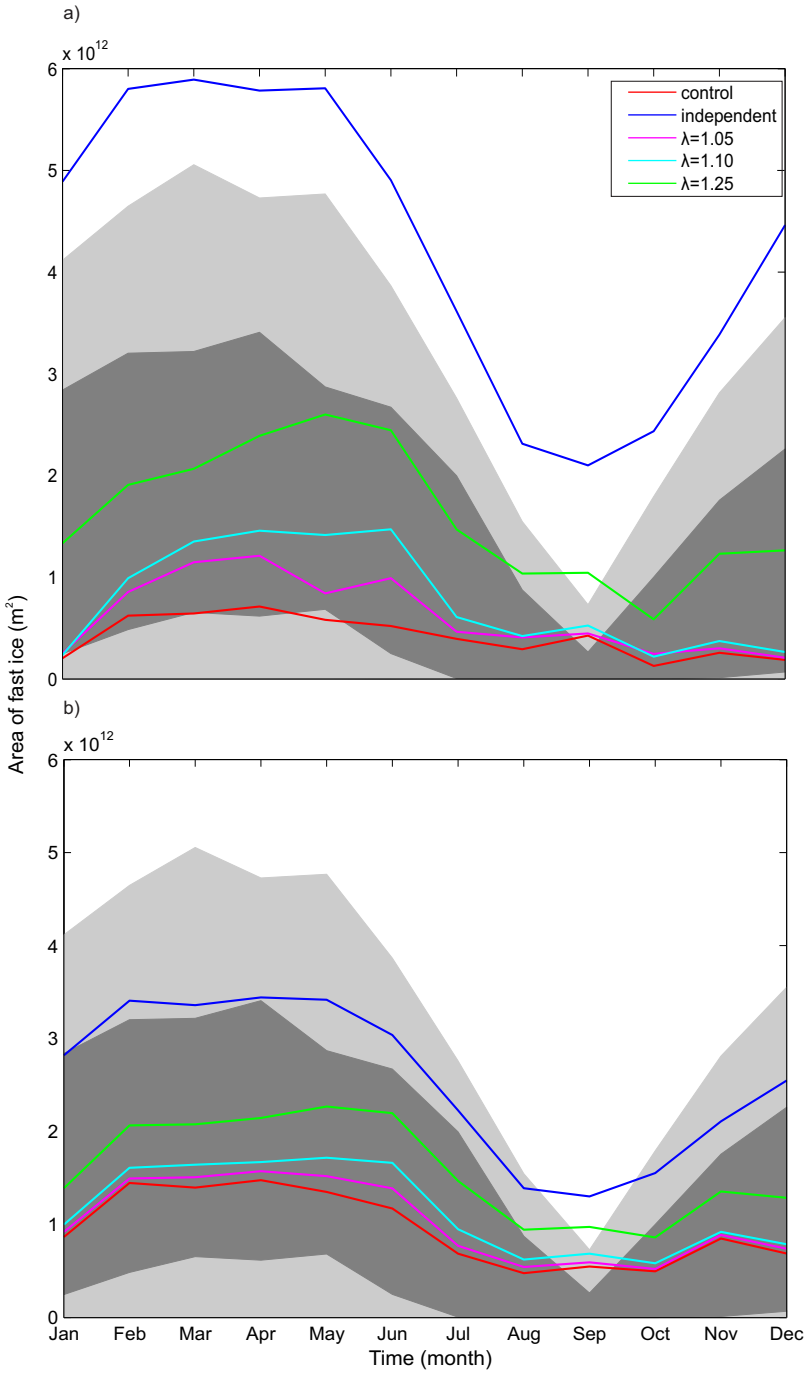

Figure 2.11: Monthly estimates of Arctic landfast ice area at a) 3 degree and b) 1 degree resolution for the control (red), independent grounding (blue) and restricted grounding schemes using a coupling parameter $\lambda = 1.25$ (green), 1.10 (cyan) and 1.05 (magenta). The light and dark grey shaded bands represent the range in landfast ice area estimates from NIC climatology over the time-spans 1972-2007 and 1994-2005 respectively.

For reference, the majority of the Antarctic locations referred to throughout this section are identified in Figure 2.12.

Control

Figures 2.13 and 2.14 show the Antarctic ice volume per unit area in winter (JAS) and summer (JFM) at 3 and 1 degree resolution respectively. In winter, CICE simulates two distinct areas of high ice volume per unit area (up to 2.0 m) in the Weddell Sea and between the Bellingshausen and Ross Sea. Much of the remainder of the Southern Ocean was covered by ice up to 1 m thick. In summer, thermodynamic melt reduced the areal coverage of sea ice, but a significant amount of perennial ice remained. The perennial ice was most abundant eastward between the Ross and Bellinghausen Seas, and in the Weddell Sea. In general these patterns compared well with observed and modelled Antarctic ice thickness (Worby et al., 2008; Kurtz and Markus, 2012; Holland et al., 2014).

However, for some regions CICE failed to reproduce realistic ice thicknesses. For example, along the East Antarctic Peninsula CICE is unable to reproduce the maximum winter ice thicknesses observed in reality (Worby et al., 2008; Kurtz and Markus, 2012). CICE was also unable to reproduce the observed perennial nature of the ice in this region, simulating ice free summers. CICE also simulated the western Ross Sea to be ice free in summer, when in reality it is expected to be ice covered (Kurtz and Markus, 2012). Experiments where CICE is coupled with an active ocean, or forced with realistic oceanic boundary conditions improved its representation of the ice cover along the East Antarctic Peninsula and in the Ross Sea (Rae et al., 2014; Hunke, 2010). This indicates that one of the main reasons for these failings is the absence of a realistic ocean forcing. An additional factor which is important in the Antarctic is that interaction between ice shelves and icebergs with the sea ice cover is not accounted for. The inadequacies of CICE to reproduce a realistic ice cover in some regions when run in standalone format will impact upon the ability of the landfast ice parameterisation to reproduce realistic landfast ice.

Figure 2.12: Antarctic map by www.nationsonline.org.

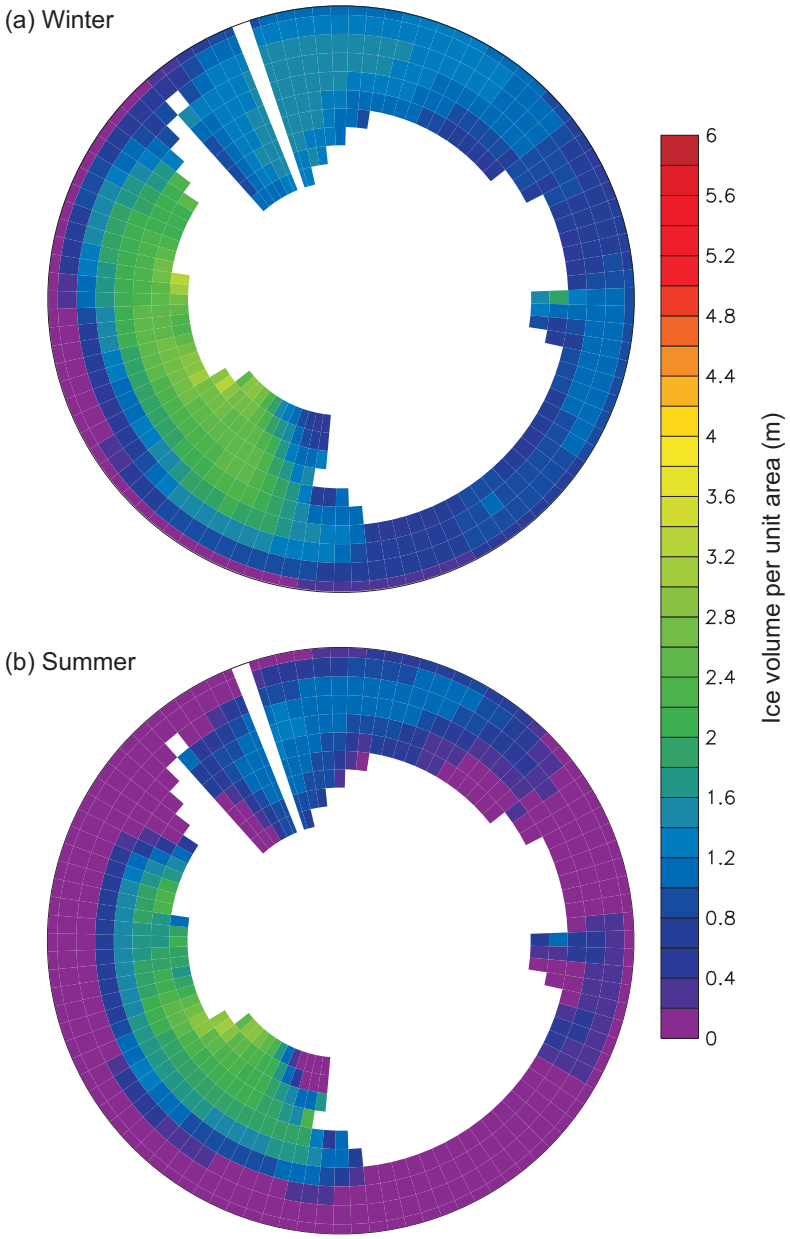

Figure 2.13: Antarctic (a) winter (JAS) and (b) summer (JFM) ice volume per unit area (m) for the control simulation (i.e. no landfast ice parameterisation) run at 3 degree resolution.

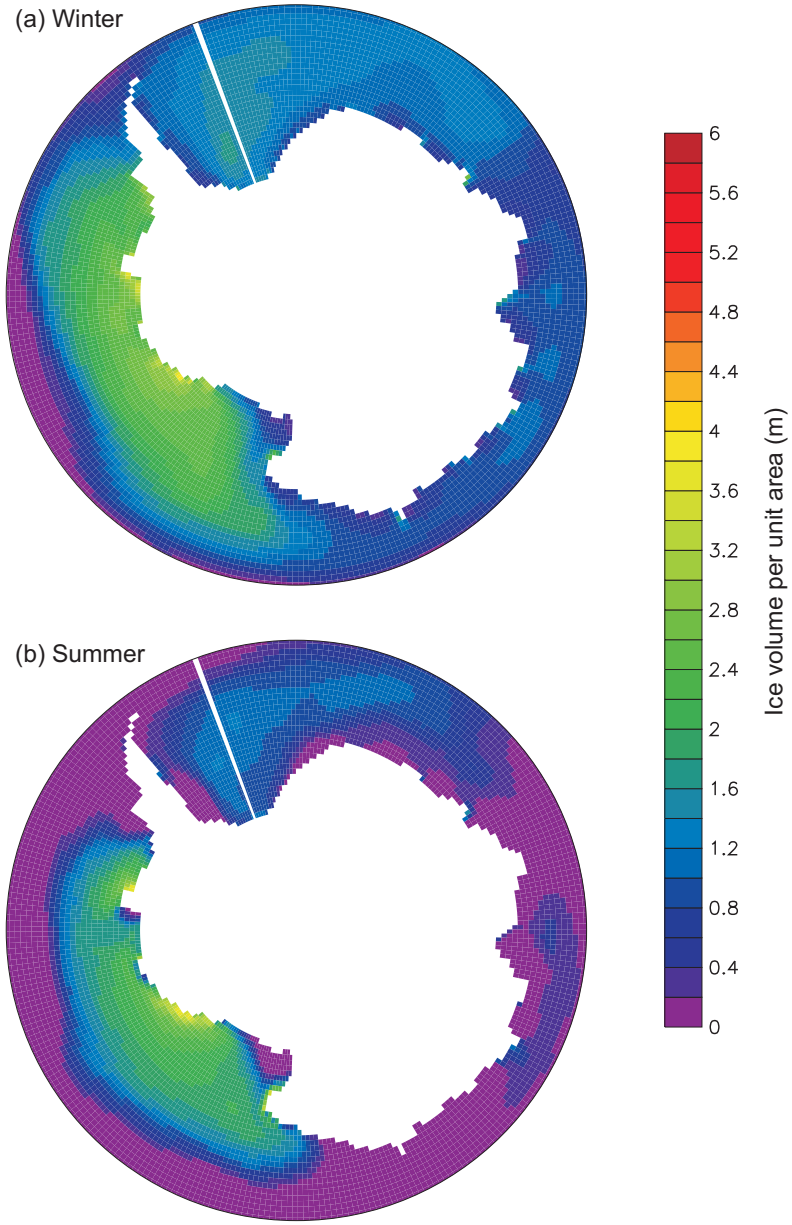

Figure 2.14: Antarctic (a) winter (JAS) and (b) summer (JFM) ice volume per unit area (m) for the control simulation (i.e. no landfast ice parameterisation) run at 1 degree resolution.

Area of grounded ice

The area of grounded ice in the Antarctic produced by the landfast parameterisations are shown in Figures 2.15 and 2.16. The 3 and 1 degree simulations were comparable, with the finer resolution simulations on average producing less grounded ice. The grounded ice coverage remained approximately constant throughout the year when the independent parameterisation was used. As discussed for the Arctic results, the grounded ice produced is very stable and cannot be removed by dynamic processes alone. As such, the lack of any summer removal of grounded ice could be the result of the thermodynamics being unable to sufficiently melt the ice so that it uncouples from the seabed. Other factors which may act to limit the summer removal of this Antarctic grounded ice include the lack of realistic ocean currents or heat fluxes, the absence of river processes and the uncapped basal growth of the grounded ice.

Restricting the maximum thickness the grounded ice can reach significantly reduced the area of grounded ice. When the restricted parameterisation was used the grounded ice also exhibited more seasonality. It would be expected that the maximum area of grounded ice would occur around September, and the minimum around March / April. However, the maximum area of grounded ice, for all tested simulations using the restricted landfast ice parameterisation occurred in March. This may be due to CICE underestimating the maximum thickness and coverage of sea ice in the Weddell Sea and along the East Antarctic Peninsula (as shown in the control simulations in Figures 2.13 and 2.14) subsequently leading to an underestimation of the winter grounded ice in that region.

There are stark differences in the geography of the Arctic and the Antarctic, and as such, the landfast ice systems are notably different. While thick ice ridges which ground on the extensive continental shelves of the Arctic dominate the production of landfast ice there, the Antarctic continental shelf is relatively narrow with significant portions covered by ice shelves. This means that the grounding of ice ridges may not be as important a formation method in the Antarctic compared to its northern counterpart. The Antarctic is also influenced by icebergs which have the ability to ground in deep water. These grounded icebergs act in the same way as grounded sea

ice, anchoring the landfast ice (Fraser et al., 2012). However, CICE does not include icebergs so this process is not accounted for in these simulations.

Location of landfast ice

As previously discussed the landfast ice systems in the Arctic and Antarctic are notably different. The continental shelf that surrounds the Antarctic continent is relatively deep and narrow with significant portions covered by ice shelves. Both of these factors act to limit the formation of landfast ice through the grounding of thick ice ridges. In the Antarctic, landfast ice is observed to form near coastal promontories and ice tongues, in embayments and through the grounding of thick sea ice (although limited) and the grounding of icebergs (Giles et al., 2008; Fraser et al., 2012). As already noted, these experiments do not include icebergs. Antarctic landfast ice tends to form in relatively small discrete sections, rather than covering large spatial extents as seen in the Arctic. This means that at the resolutions used in these experiments it will be difficult to reproduce the detail of the coastal geometry necessary to realistically reproduce Antarctic landfast ice.

The spatial and temporal coverage of landfast ice for the control, independent, and restricted landfast ice parameterisations produced by restrictive geometry and grounded ice ridges are shown in Figures 2.17 and 2.18 for the simulations run at 3 and 1 degree resolution respectively. The standard control simulation produced minimal landfast ice, with limited coverage from the Bellingshausen Sea westward to the eastern edge of the Ross Sea, and a small amount formed near the Amery Ice Shelf. This inherent landfast ice was generally short lived, with the majority occurring for 30 days or less.

The independent landfast ice parameterisation led to the occurrence of persistent landfast ice along the majority of the Antarctic coast, with the exception of the Ross Sea. This extensive landfast ice resulted from the persistent grounded ice, preventing breakup of the landfast ice cover. Restricting the grounding significantly reduced the occurrence of landfast ice, with the most restrictive coupling ($\lambda = 1.05$) producing results comparable to the control. The parameterisations appeared to underestimate

the production of landfast ice along the eastern edge of the Antarctic Peninsula. This was not due to the parameterisations themselves, but was instead the result of CICE underestimating the thickness and temporal coverage of ice in this region (as shown in Figures 2.13 and 2.14).

Area of landfast ice

The annual cycle of Antarctic landfast ice area (Figure 2.19) was closely related to the annual cycle in grounded ice (Figures 2.15 and 2.16). When the independent landfast ice parameterisation was used the landfast ice did not exhibit a seasonal cycle. The landfast ice grew anomalously thick and became multiyear, due to the persistent grounded ridges holding it stationary. The independent landfast ice parameterisation produced the most landfast ice, with the area reducing with increased grounding restriction. When the restricted landfast ice parameterisation was used the landfast ice exhibited more seasonality. However, the maximum areal coverage of landfast ice occurred in March / April, as it did with the grounded ice.

2.8 Unrealistic multiyear landfast ice

As noted in Section 2.7 the main limitation of the independent landfast ice parameterisation, evident in some parts of the Arctic Region and along much of the Antarctic coast, was the production of anomalously thick and persistent multiyear landfast ice. Two study areas, the Kara Sea and the Amundsen Bay area, are considered in detail to further investigate the causes of this multiyear landfast ice.

The independent parameterisation did not limit the maximum ice draft to ocean depth ratio. This allowed for the possibility of unrealistically thick ice to ground on shallow bathymetry. As the grounded ridges produced by the parameterisations were very stable, and could not be uncoupled by dynamic forces alone, thermodynamic melt was important in uncoupling the ice from the seabed. When the independent parameterisation was used the thermodynamics were not able to sufficiently melt the erroneously thick grounded ridges, and so they remained coupled with the seabed,

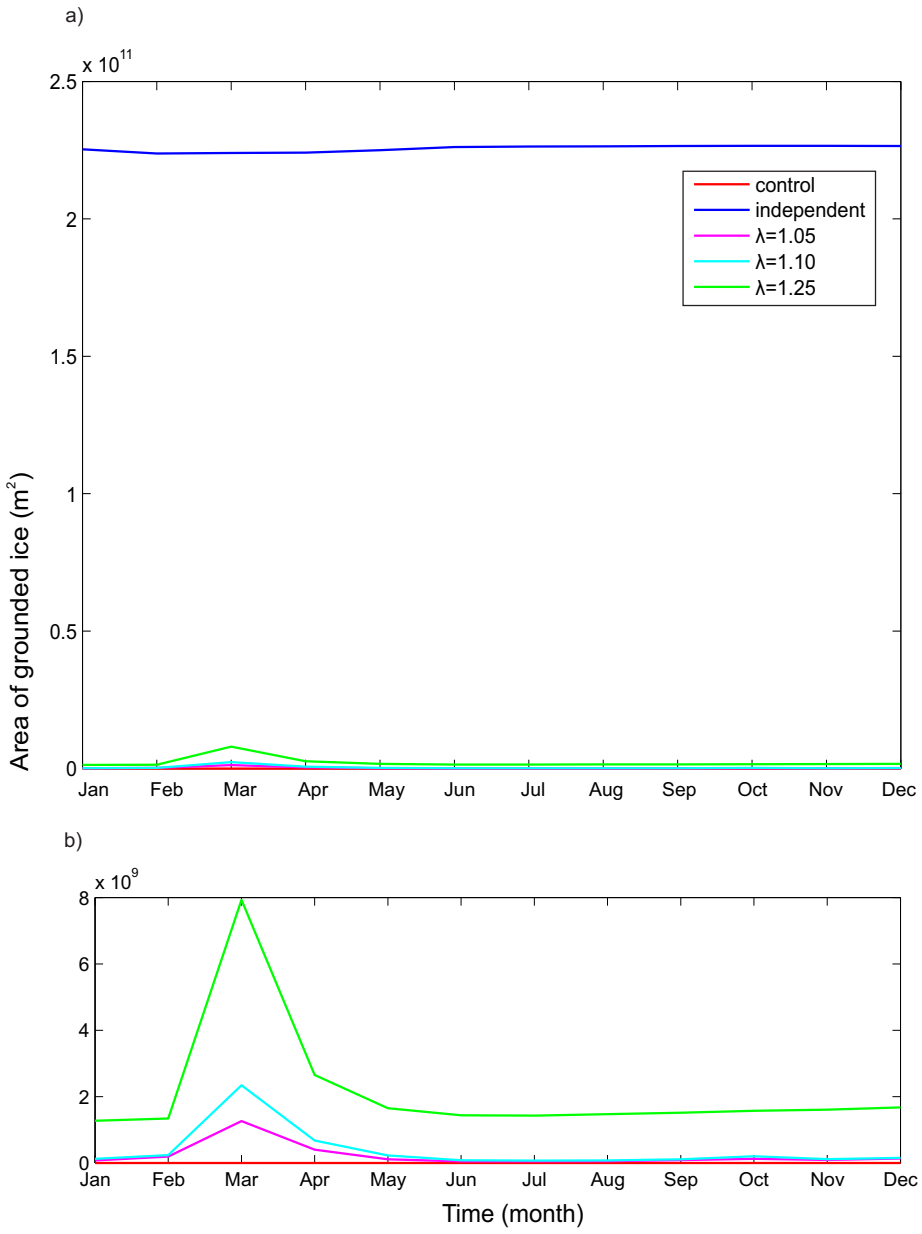

Figure 2.15: Monthly estimates of Antarctic grounded ice area at 3 degree resolution for the control (red), independent grounding (blue) and restricted grounding schemes with a coupling parameter $\lambda = 1.25$ (green), 1.10 (cyan) and 1.05 (magenta) for (a) all simulations and (b) magnification of the control and restricted parameterisation.

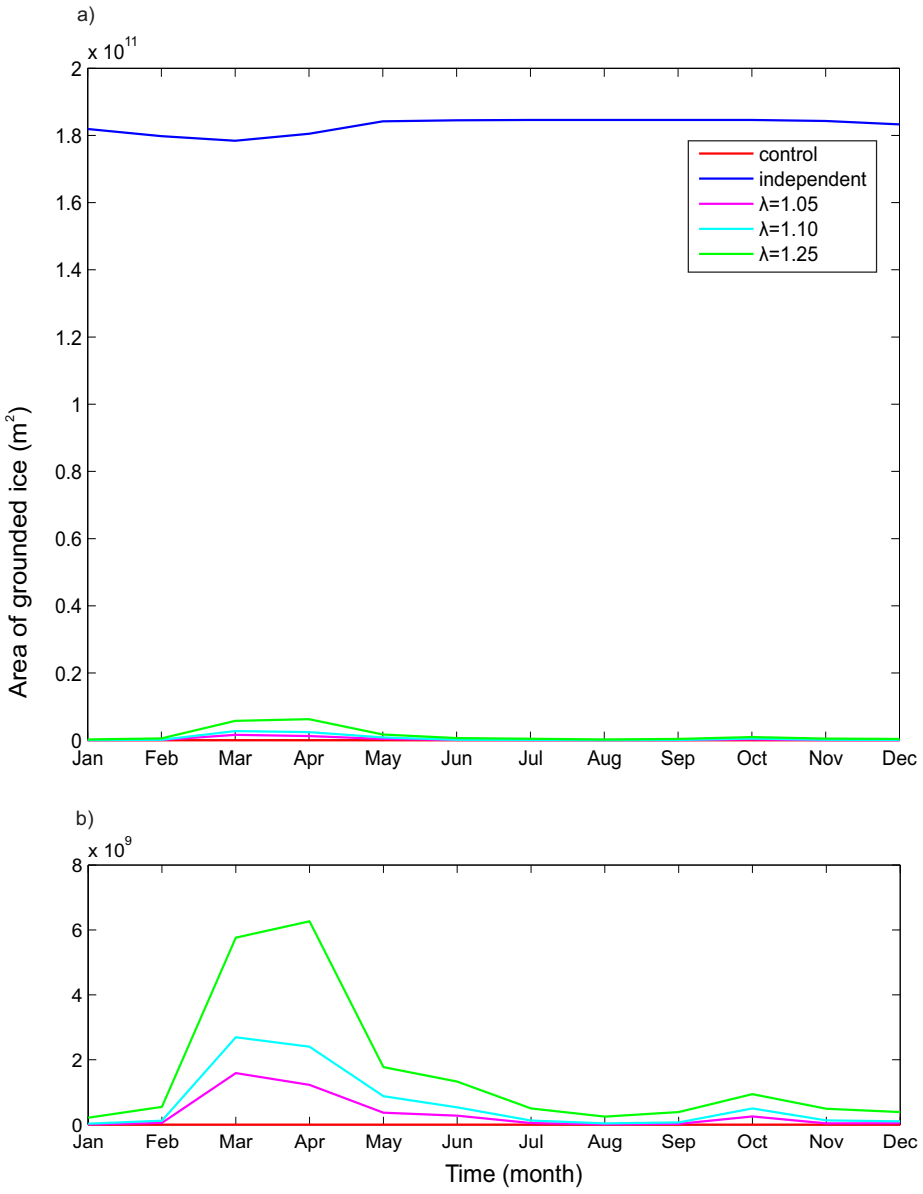

Figure 2.16: Monthly estimates of Antarctic grounded ice area at 1 degree resolution for the control (red), independent grounding (blue) and restricted grounding schemes with a coupling parameter $\lambda = 1.25$ (green), 1.10 (cyan) and 1.05 (magenta) for (a) all simulations and (b) magnification of the control and restricted parameterisation.

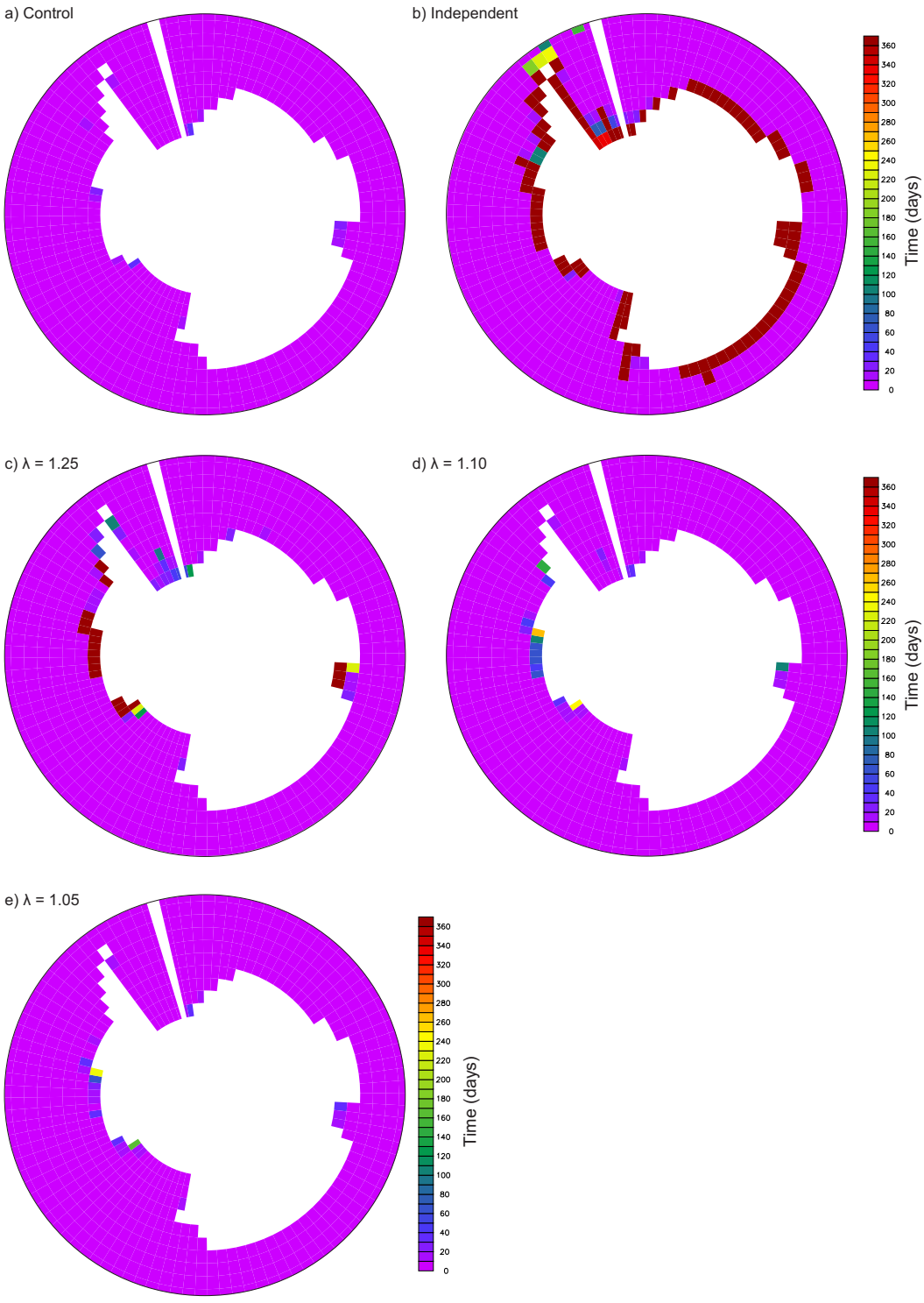

Figure 2.17: Temporal coverage of Antarctic landfast ice at 3 degree resolution from 5 day averages for the a) control, b) independent parameterisation, and restricted landfast ice parameterisation using c) $\lambda = 1.25$, d) $\lambda = 1.10$ and e) $\lambda = 1.05$.

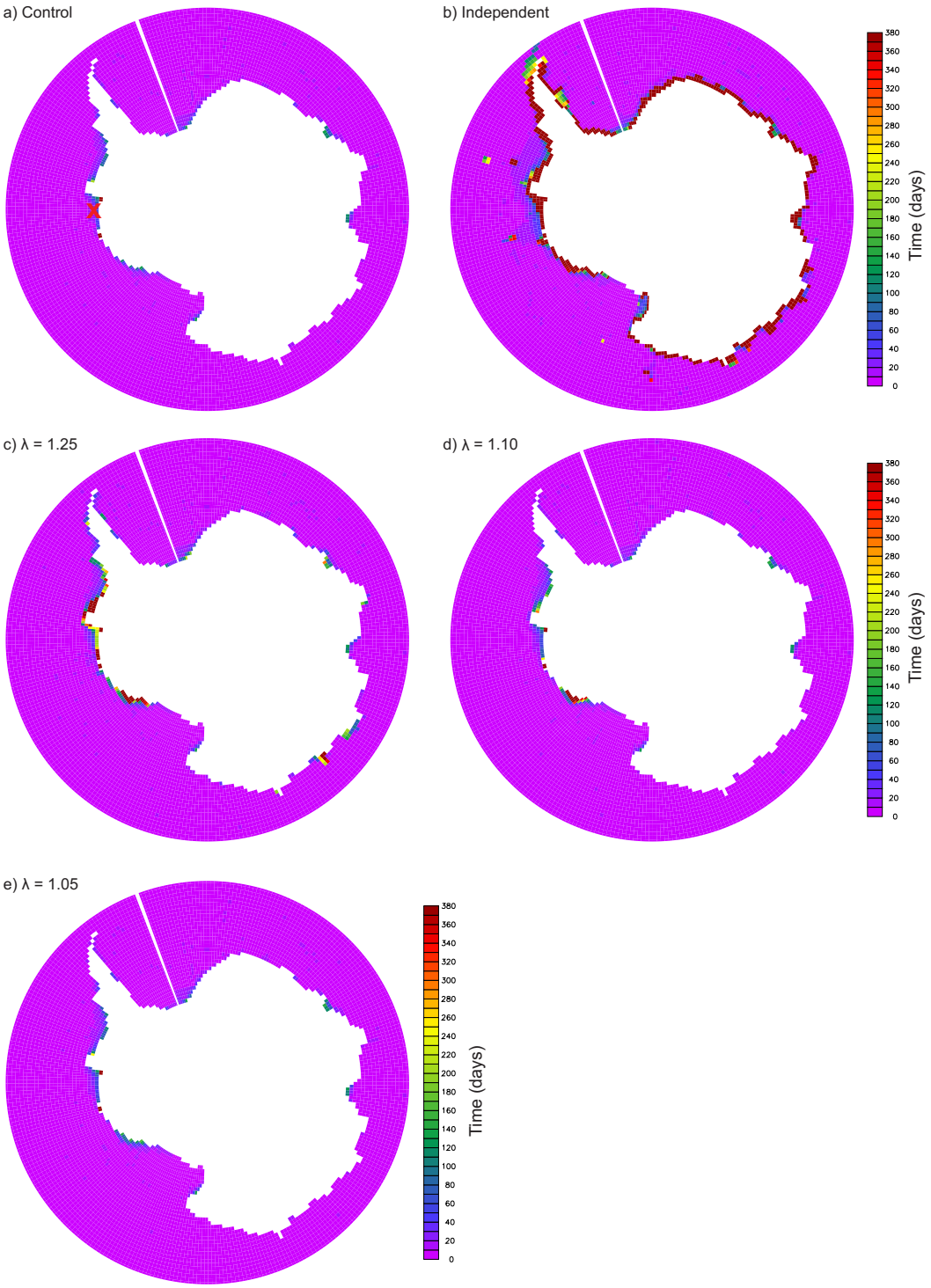

Figure 2.18: Temporal coverage of Antarctic landfast ice at 1 degree resolution from 5 day averages for the a) control, b) independent parameterisation, and restricted landfast ice parameterisation using c) $\lambda = 1.25$, d) $\lambda = 1.10$ and e) $\lambda = 1.05$.

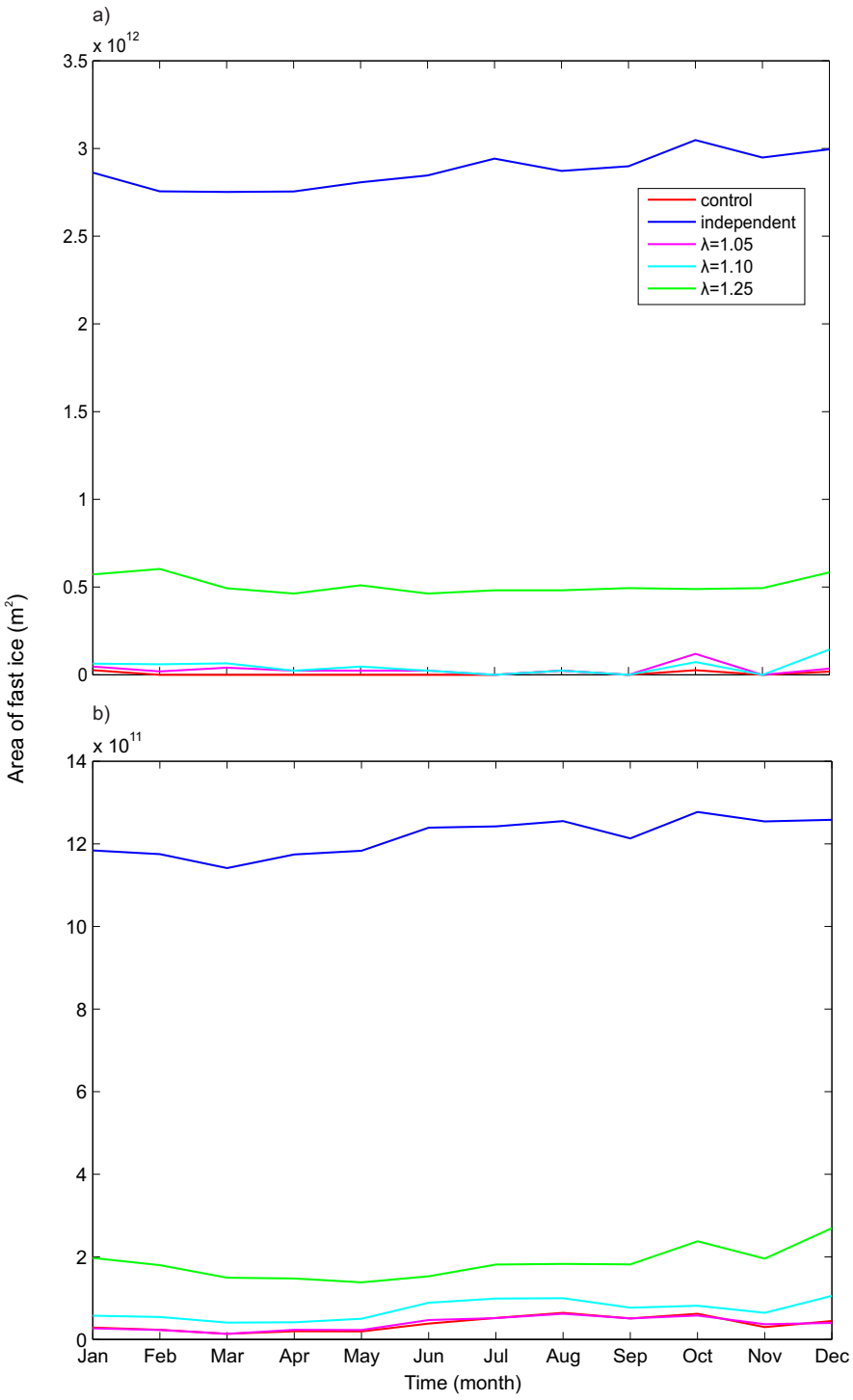

Figure 2.19: Monthly estimates of Antarctic landfast ice area at a) 3 degree and b) 1 degree resolution for the control (red), independent grounding (blue) and restricted grounding schemes using a coupling parameter $\lambda = 1.25$ (green), 1.10 (cyan) and 1.05 (magenta).

becoming multiyear.

The persistence of these grounded pinning points prohibited the breakup and retreat of the landfast ice in early summer, resulting in a transition to multiyear ice. The multiyear landfast ice was then able to reach unrealistic thicknesses through thermodynamic growth, enhanced by the accumulation of snow. In winter, snow has an insulating effect, slowing the rate of ice growth, however, in summer the increased albedo of the snow compared to bare ice significantly reduced the melt rate.

This issue was further complicated by the absence of ocean currents and realistic ocean heat fluxes, which play an important role in the melt and redistribution of ice in summer. The circulation of relatively warm water under the landfast ice cover in summer months acts to destabilise and initiate breakup of the landfast ice cover (Mahoney et al., 2007a,b; Cole et al., 2004). River discharge has also been shown to reduce the stability of landfast ice, promoting melt and breakup (Dmitrenko et al., 1999; Dean et al., 1994; O'Brien et al., 2006). Many rivers in the polar regions are frozen in winter, and thaw in spring. Thawing rivers flood the coastal landfast ice, causing increased absorption of solar radiation as the flood waters have a reduced albedo compared to the landfast ice, initiating melt. The river discharge also deposits sediments and transports heat from the terrestrial to the marine environment, warming the coastal waters (Dean et al., 1994; O'Brien et al., 2006). In the case of the Mackenzie River, Dean et al. (1994) reported that landfast ice was removed two weeks earlier than along surrounding coasts where river discharge was minimal. The impact of river runoff is not only immediate, Dmitrenko et al. (1999) found that intensity of spring-summer river run off from rivers along the Russian Arctic Shelf was negatively correlated with the width of the landfast ice cover in the subsequent winter.

2.8.1 Kara Sea

Monthly ice thickness estimates of landfast ice, over 10 years, for a grid cell in the Kara Sea (denoted by marker X in Figure 2.10) for the control, independent parameterisation, the independent parameterisation without snow, and the restricted

parameterisation using $\lambda = 1.05$ are shown in Figure 2.20. The landfast ice grows erroneously thick when the independent landfast ice parameterisation was applied (b), far surpassing the comparable maximum ice thickness in the control simulation (a), while the restricted parameterisation (d) produces an annual growth/melt cycle comparable to the control.

The removal of snow limits the maximum attained ice thickness, inferring that the occurrence of snow enhanced the unrealistic vertical ice growth, but did not cause the initial transition to multiyear ice. Once the landfast ice became multiyear, the snow readily accumulates, Figure 2.21, while in the control and restricted grounding schemes the snow is completely melted annually.

2.8.2 Amundsen Sea

Monthly ice thickness estimates, over 10 years, for a grid cell in the Amundsen Sea (denoted by a marker X in Figure 2.18) for the control, the independent parameterisation, the independent parameterisation without snow, and the restricted parameterisation using a $\lambda = 1.05$ are shown in Figure 2.22. When the independent parameterisation was used (b) the ice grew erroneously thick, becoming multiyear within the first forcing cycle. Restricting the grounding of thick ice by capping the maximum allowed thickness of the grounded ice (d), produced thickness profiles comparable with the control simulation (a).

Removing snow reduced the maximum attained landfast ice thickness, but did not prevent it from becoming multiyear. Similar to the results from the Kara Sea example, snow readily accumulated on the multiyear landfast ice produced by the independent landfast ice parameterisation (Figure 2.23) enhancing its vertical ice growth.

2.9 Grounded ridge stability

The persistence of grounded ridges produced by the parameterisation through the summer period suggests that the grounded ridges are too stable. The standard

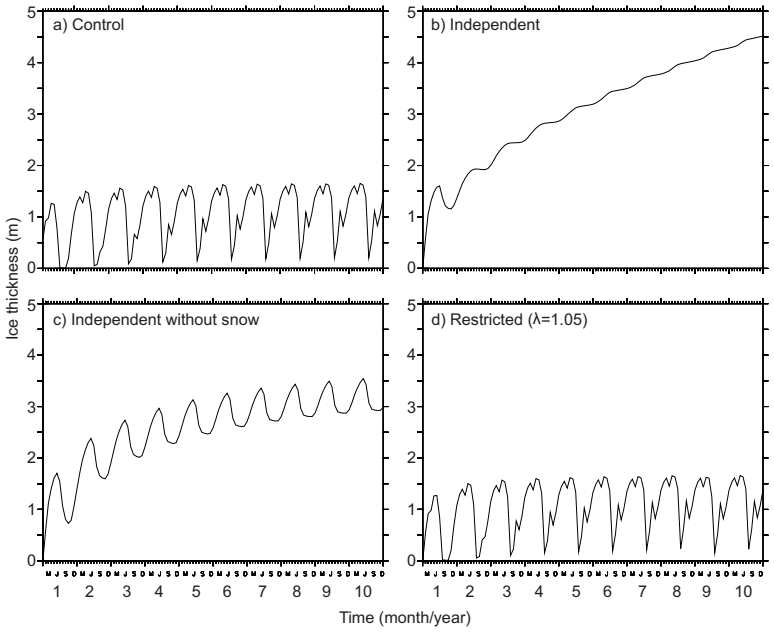

Figure 2.20: Ice thickness for a grid cell in the Kara Sea (denoted by marker X in Fig.2.10) for a) control b) independent c) independent without snow and d) restricted grounding with $\lambda = 1.05$ using repeat forcing from 1997.

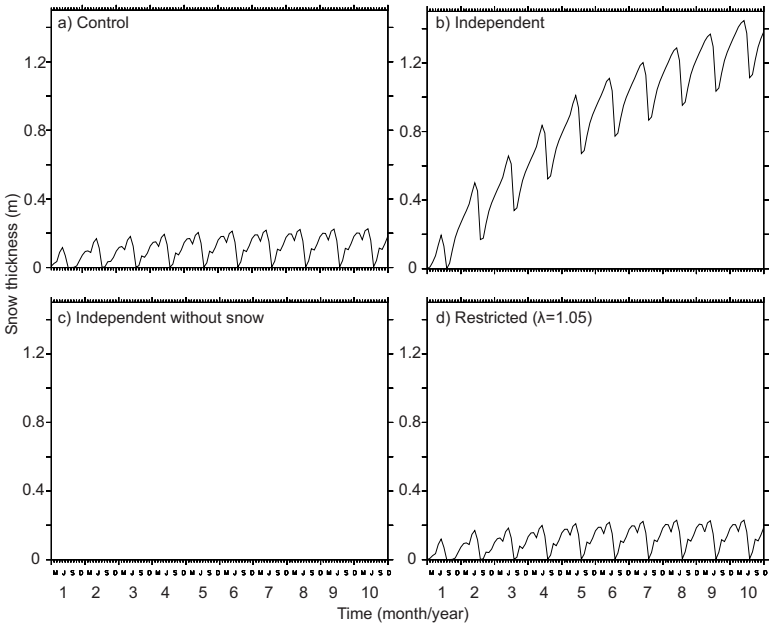

Figure 2.21: Snow thickness for a grid cell in the Kara Sea (denoted by marker X in Fig.2.10) a) control b) independent c) independent without snow and d) restricted grounding with $\lambda = 1.05$ using repeat forcing from 1997.

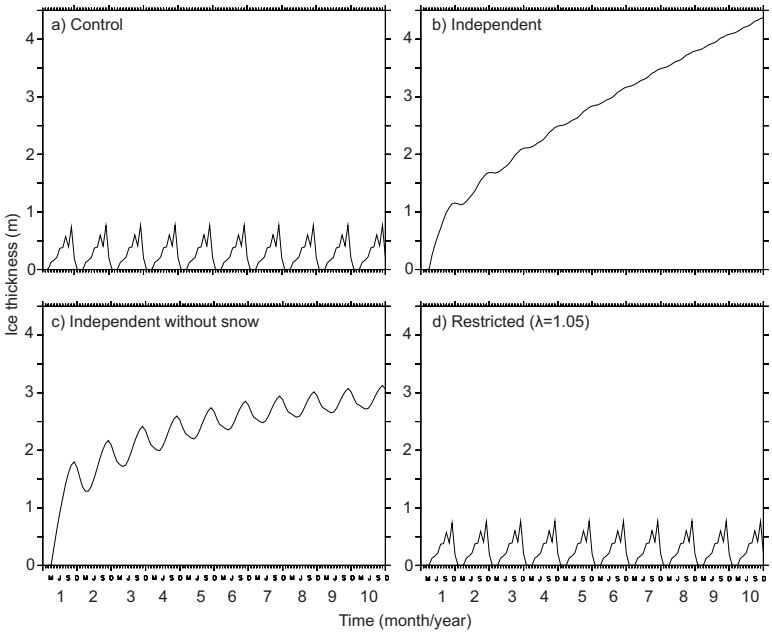

Figure 2.22: Ice thickness for a grid cell in the Amundsen Sea (denoted by a marker X in Fig.2.18) for a) control b) independent c) independent without snow and d) restricted grounding with $\lambda = 1.05$ using repeat forcing from 1997.

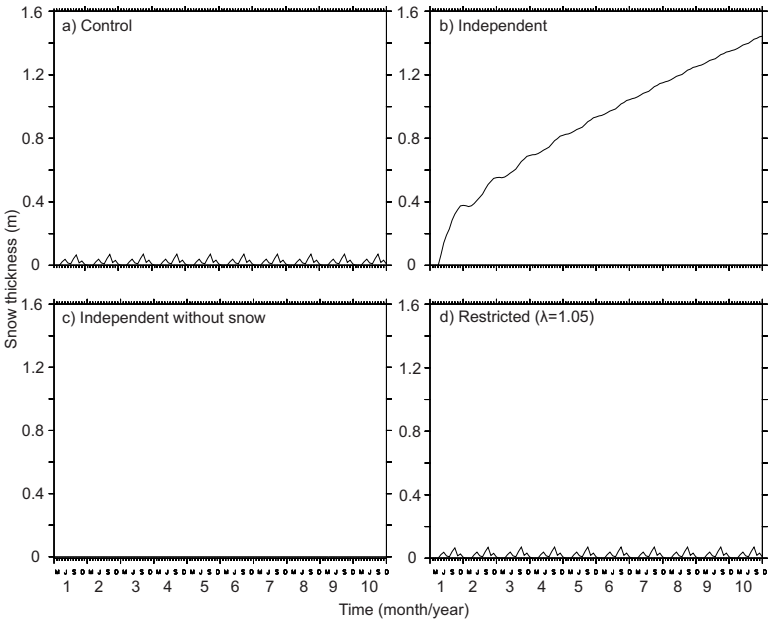

Figure 2.23: Snow thickness for a grid cell in the Amundsen Sea (denoted by a marker X in Fig.2.18) a) control b) independent c) independent without snow and d) restricted grounding with $\lambda = 1.05$ using repeat forcing from 1997.

coefficient of friction between the ice bottom and the seabed, $c_f = 0.5$, was taken from Shapiro and Metzner (1987). As previously discussed, this is dependent on a wide range of factors and parametrising it as a constant is likely to be an oversimplification. This frictional coefficient may be too large to allow the atmospheric wind stress in spring/summer to uncouple the grounded ice, and allow the breakup of the landfast ice cover. A sensitivity analysis of the area of landfast ice produced depending on the chosen frictional coefficient was carried out considering values $c_f = 0.5$, 0.05 and 0.005.

Reducing the magnitude of the frictional grounding coefficient reduced the area of landfast ice across the entire seasonal cycle in both polar regions. In the Arctic (Figure 2.24 (a)) reductions to the frictional coefficient of 1 ($cf = 0.05$) and 2 ($cf = 0.005$) orders of magnitude from the standard value ($cf = 0.5$) resulted in a reduction of the landfast ice area of $1.8 - 5.9\%$ and $8.8 - 21.6\%$ respectively. In the Antarctic (Figure 2.24 (b)) the reductions in the area of landfast ice are slightly larger than the Arctic, with ranges of $7.6 - 12.7\%$ and $21.0 - 27.6\%$ for reductions in the frictional coefficient of 1 and 2 orders of magnitude respectively. The resultant reduction in landfast ice occurs at a constant magnitude throughout the year, with no enhanced summer removal in the Arctic or Antarctic (Figs.2.25 (a) and (b)). These results suggest that it is not the stability of the grounded ice that is the dominant factor in the persistence of landfast ice in summer. Instead it is the unrestricted ratio of ice draft to ocean depth of the grounded ice, resulting in erroneously thick grounded ice which must be melted for the ridge to unground.

2.10 Discussion

The lack of high spatial and temporal resolution observations of landfast sea ice on large scales (e.g. Arctic or Antarctic wide) is a limiting factor for this work. In order to quantitatively validate these results one would need an appropriate climatology. There are some small scale landfast ice climatologies with high spatial resolution, but these tend to be localised and also suffer from low temporal resolution and/or

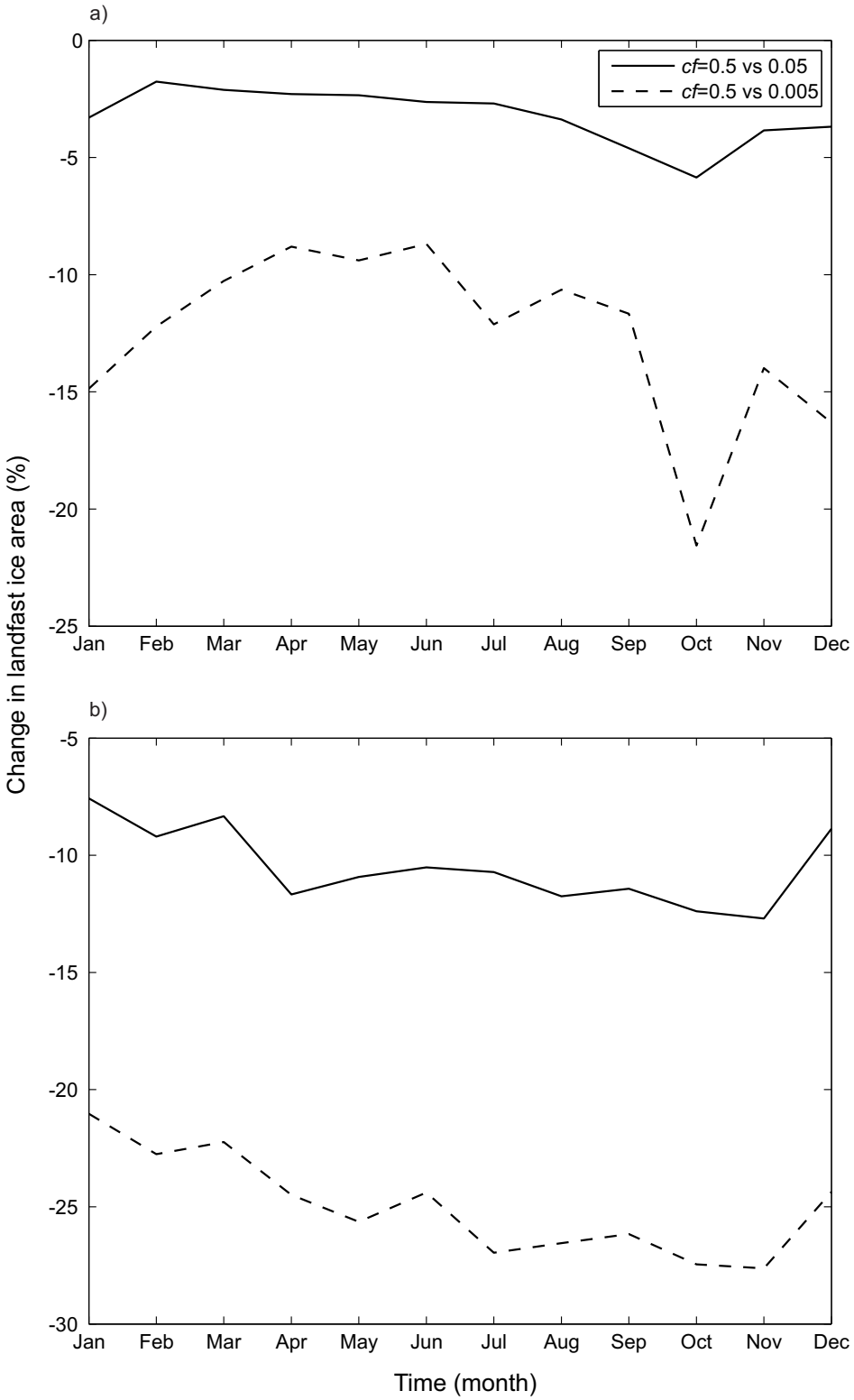

Figure 2.24: Difference in landfast ice area (%) in the (a) Arctic and (b) Antarctic for $cf = 0.05$ (solid black line) and 0.005 (dashed black line) compared to the standard value $cf = 0.5$.

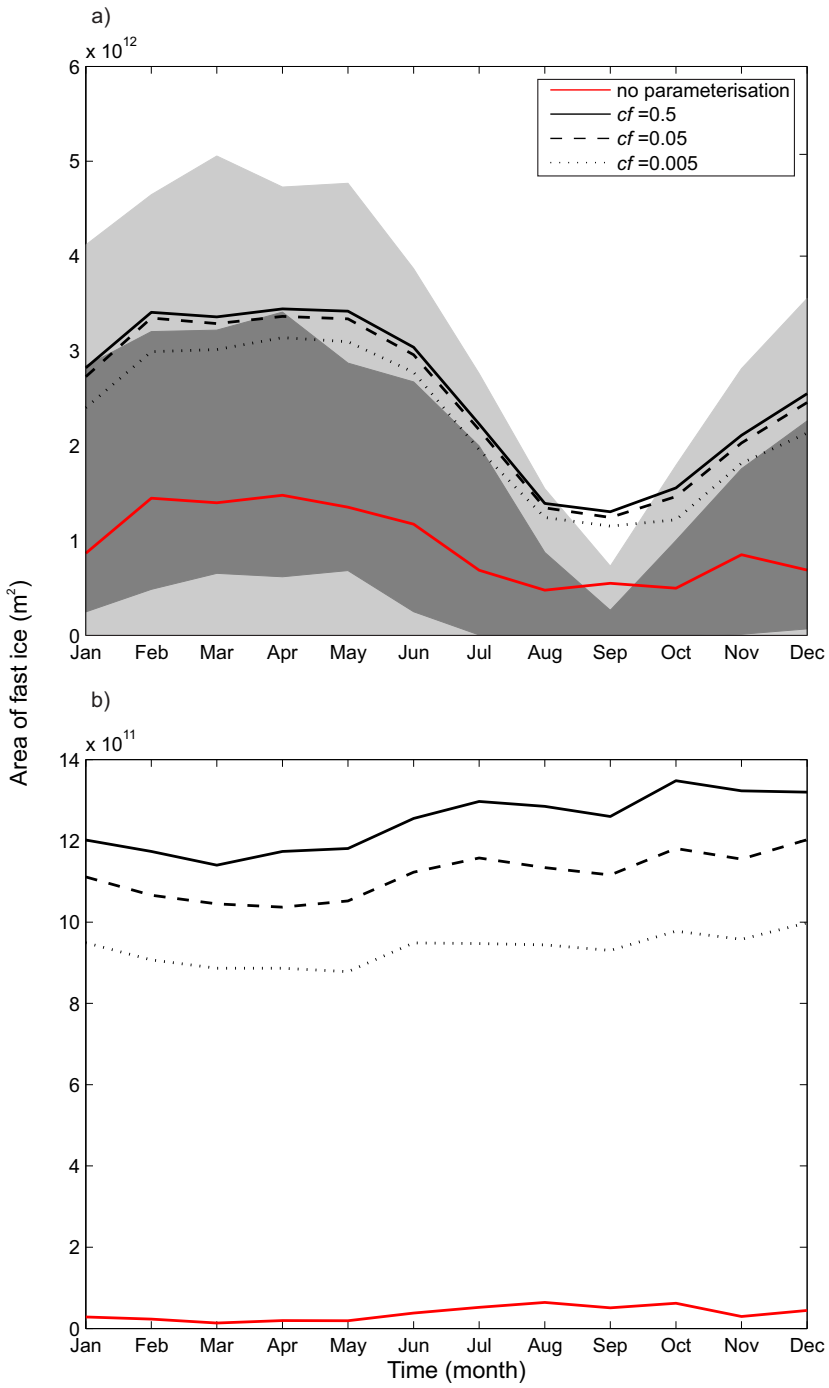

Figure 2.25: Area of landfast ice (ms^{-2}) in the (a) Arctic and (b) Antarctic for $cf = 0.5$ (solid black line), $cf = 0.05$ (dashed black line) and $cf = 0.005$ (dotted black line) compared to the control i.e. no landfast ice parameterisation included (solid red line). Arctic results are plotted against NIC climatologies of landfast ice area over the time periods 1972-2007 and 1994-2005 in light and dark grey respectively.

significant gaps in the data. Here we have compared results for the Arctic against the NIC landfast ice climatology which has good spatial and temporal coverage (1972 - present). A limitation of the NIC climatology, is that no definition for landfast ice is provided in conjunction with the data, and so may differ from the one we have imposed. Also, the climatology does not include information on landfast ice concentration, only occurrence (i.e. present or absent). Validation for the Antarctic results is even harder, with no appropriate climatology currently available. The most appropriate is that developed by Fraser et al. (2012), but this only covers a section along the Eastern Antarctic coast over an 8.8 year time period. As a result, much of our validation is qualitative, based on the representation of realistic seasonal patterns and locations of landfast ice rather than absolute values of area.

The landfast ice parameterisations developed generate grounded ice, the magnitudes of which is dependent on the level of restriction placed on the maximum thickness of ice which is able to ground in a given ocean depth. The grounded ice leads to the production of landfast ice by adding lateral stability to the ice cover. Despite the noted limitation of the independent landfast ice parameterisation (producing multiyear landfast ice), it is able to produce landfast ice on spatial and temporal scales which compare well with available observations. The restricted parameterisations do not necessarily perform better in comparison; they limit the production of multiyear landfast ice, but they produce much less grounded ice, and also introduce an additional unconstrained coupling parameter (λ). The model performs particularly well in the Arctic, simulating grounded and landfast ice in-line with the observed seasonal spatial and temporal patterns, comparing well with NIC climatologies. The 1 degree simulations perform significantly better than the 3 degree due to the improved ability to resolve the intricate coastal geometry, known to be important in landfast ice formation. Due to the differences of the landfast ice system in the Antarctic; that the limited available continental shelf limits the grounding of thick sea ice ridges, the potential for very thick icebergs to ground, and landfast ice forming along coastal protrusions and ice tongues, the landfast ice parameterisations tested here may not be best suited to reproduce Antarctic landfast ice. However, the technique to ac-

count for the grounding of thick sea ice could also be applied to the grounding of icebergs.

The independent landfast ice parameterisation is able to represent the formation, growth, and breakup of landfast ice relatively well, despite the relatively simplistic assumption that ice and bathymetry are independent, because the ice has an approximately homogeneous thickness distribution in the shallow coastal regions of interest in landfast ice modelling. In these regions the ice is dominated by a small number of thin ice categories in comparison to central Arctic Regions, where the ice spans a wider range of thickness categories as shown in Table 2.2. In the Barents Sea $> 85\%$ of the ice was contained within the 1^{st} thickness category, while in the Laptev Sea and Foxe Basin the majority of ice resided within the 2^{nd} category during the winter maximum. In the Central Arctic the ice distribution had a greater range, distributed between the 1^{st} and 6^{th} categories. This means that the ice distribution in the regions of interest in landfast ice modelling can be thought of as broadly independent to the bathymetry.

The main limitation of the landfast ice parameterisations is the development of anomalously thick and persistent grounded ice, which results in multiyear landfast ice in a number of regions in the Arctic and Antarctic. This is primarily due to the ridges being very stable once in contact with the seabed and cannot be uncoupled by dynamic processes alone. As such, the ridges must be thermodynamically melted to promote ungrounding. The amount of ice that must be melted for the ridge to uncouple from the seabed is controlled by the level of restriction placed on the ice draft to ocean depth ratio. The independent parameterisation allowed for unrealistically thick ice to ground on relatively shallow bathymtery. The grounded ice was then generally too thick to be sufficiently melted, resulting in a proportion of the grounded ice becoming multiyear. The restricted parameterisation limited the ice draft to ocean depth ratio which minimised this unrealistic behaviour, but did not completely prevent it. It should also be noted that CICE used in standalone format was found to produced unrealistic distributions of sea ice in some regions of the Arctic and Antarctic. This negatively impacted on the ability of the parameterisations

to realistically reproduce landfast sea ice in these regions.

The temporal occurrence of the grounded and landfast ice could be improved by the inclusion of realistic high resolution ocean boundary conditions. Accurate oceanic currents and heat fluxes would have a significant effect on the strength of the coupling between the thick grounded ridges and the seabed, potentially promoting summer removal. Atmospheric wind stresses are also a dominant force in determining the temporal occurrence of grounded ridges in coastal regions, both in terms of causing the initial drift inshore in early winter allowing the ridges to ground initially, but also the offshore removal in spring/summer. In these experiments 6 hourly average wind stress values where used. It should be noted that averaging the atmospheric velocity components over any time period (6 hours in our case) may result in the loss of peak values, which may be important for the accurate removal of the grounded ridges. The removal of grounded ice ridges usually requires persistent forcing, and not of intermittent pulses, but the peaks in wind stress may help to weaken the coupling between the ridges and the landfast ice, aiding the breakup of the landfast ice cover in summer. Wind speed values taken from an Antarctic weather station, on 8/01/2000, over a 6 hourly period (Stroeve and Shuman, 2004) show that the average value masks approximately 34% of the variation (Fig.2.26).

As previously identified, there are a number of ways in which landfast or grounded ice can be distributed within a grid cell in a coarse resolution model. The different methods of distributing the sub-grid scale ice will lead to different amounts of ice becoming aground and varying anchoring strengths available to the landfast ice. We do not have a sufficient understanding of the physics of the landfast ice system to determine a realistic, dynamically based, distribution. In this analysis we assumed an independent relation between ice thickness and ocean depth to produce one possible distribution, and then placed restrictions upon this independent distribution to produce a second possible distribution. However, neither of these may be the optimum sub-grid scale distribution to produce the most realistic representation of landfast ice. For completion it would be beneficial to test a range of sub-grid scale

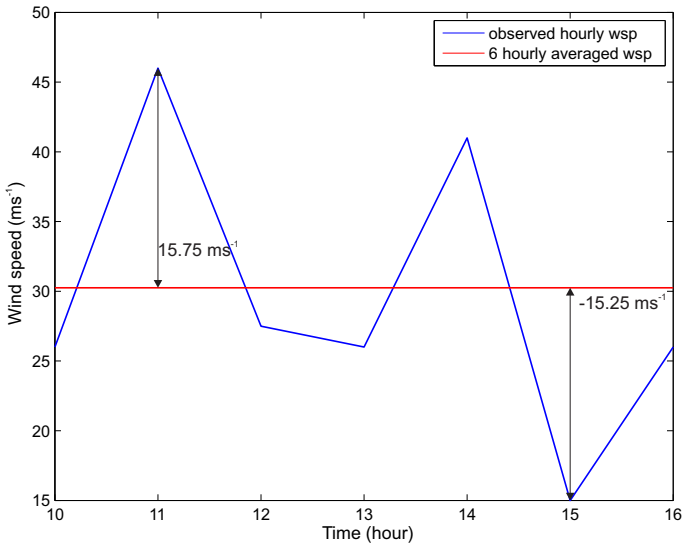

Figure 2.26: Observed hourly and averaged 6 hourly wind speed ms^{-1} at Antarctic weather station (043166) Lat = 65.5800 N, Lon = 37.1500 W, for hours 10-15 on 08/01/2000 obtained from the Historic Arctic and Antarctic Surface Observational Data, NSIDC (Stroeve and Shuman, 2004).

distributions.

2.11 Implications

Landfast ice acts as an extension of the coast over the continental shelf, operating as a constant barrier between the atmosphere and ocean. This is unlike pack ice, which has the ability to move, allowing the ocean and atmosphere to intermittently exchange heat and momentum. As such, accurately representing the seasonal landfast ice cycle is essential for the realistic representation of many atmospheric and oceanic processes.

Latent heat polynyas form offshore of many coastlines in the Arctic and Antarctic (e.g. Morales-Maqueda et al., 2004). The large negative ocean to atmosphere heat fluxes (up to several hundred Wm^2) affect mesoscale atmospheric motions (Dethleff, 1994) and ocean circulation (e.g. Morales-Maqueda et al., 2004). High rates of ice

production caused by the negative heat fluxes result in high levels of brine rejection, altering the local ocean salinity. This process sets up vertical mixing and convection, which can result in the formation and cascading of intermediate and deep water masses. In the Arctic, lateral advection of the cold dense water formed on the continental shelf is also thought to help maintain the cold halocline layer (Winsor and Bjork, 2000), which insulates the cold surface water from the underlying warmer, more saline Atlantic Water. Steele and Boyd (2012) found that in recent years the cold halocline layer in the Arctic has retreated to cover a significantly smaller area than previously. Since the cold halocline layer insulates the surface layer (and thus the overlying sea ice) from the heat contained in the Atlantic Water layer, this retreat could have a significant impact on the surface energy and mass balance of sea ice. The cause of the cold halocline retreat is thought to be due to a shift in the wind forcing, resulting in a shift in the motion of the sea ice. This could then impact on the location and timing of the fresh shelf waters flow into the deeper basins of the Arctic Ocean.

The properties of the dense water formed in polynyas, and to what depth it cascades once at the shelf break, depends on the location of the formation polynya. The occurrence of landfast ice moves the effective coastline, and the location of the flaw polynya, offshore. The dense water then has a reduced distance to travel before reaching the shelf break, undergoing less mixing with the fresher ambient shelf water. This may allow the water to maintain its original high density, and cascade to greater depths than that formed closer to the coast (Schauer and Fahrbach, 1999).

Even at 1 degree resolution, we are unable to resolve polynyas, as would most ocean general circulation models, but we do simulate landfast ice in locations known to be dominated by polynyas and important areas of dense water formation. The landfast ice simulations completed in this research were run in standalone format, meaning that there is no ocean in which to directly evaluate the effect of landfast ice. Therefore, ice production is used here as a proxy for deep water formation. Figure 2.27 shows the annual average ice production for the control, the independent parameterisation and the anomaly. Despite its simplicity the independent param-

eterisation was able reproduced many of the key aspects of the landfast ice cycle. As such, the impact of the restricted parameterisations on ice production will be comparable to that of the independent parameterisation shown in Figure 2.27. The independent landfast ice parameterisation resulted in the production of landfast ice in coastal regions which led to a subsequent decrease in ice production where the landfast ice cover was located (comparing to Fig.2.10(b) for landfast ice coverage). An increase in ice production occurred directly offshore of the landfast ice edge, closer to the shelf break, where the ocean is able to interact with the atmosphere. This suggests that at both polynya-resolving and coarser resolution models, the introduction of this landfast ice parameterisation would result in significant changes to deep water formation, and subsequently ocean circulation.

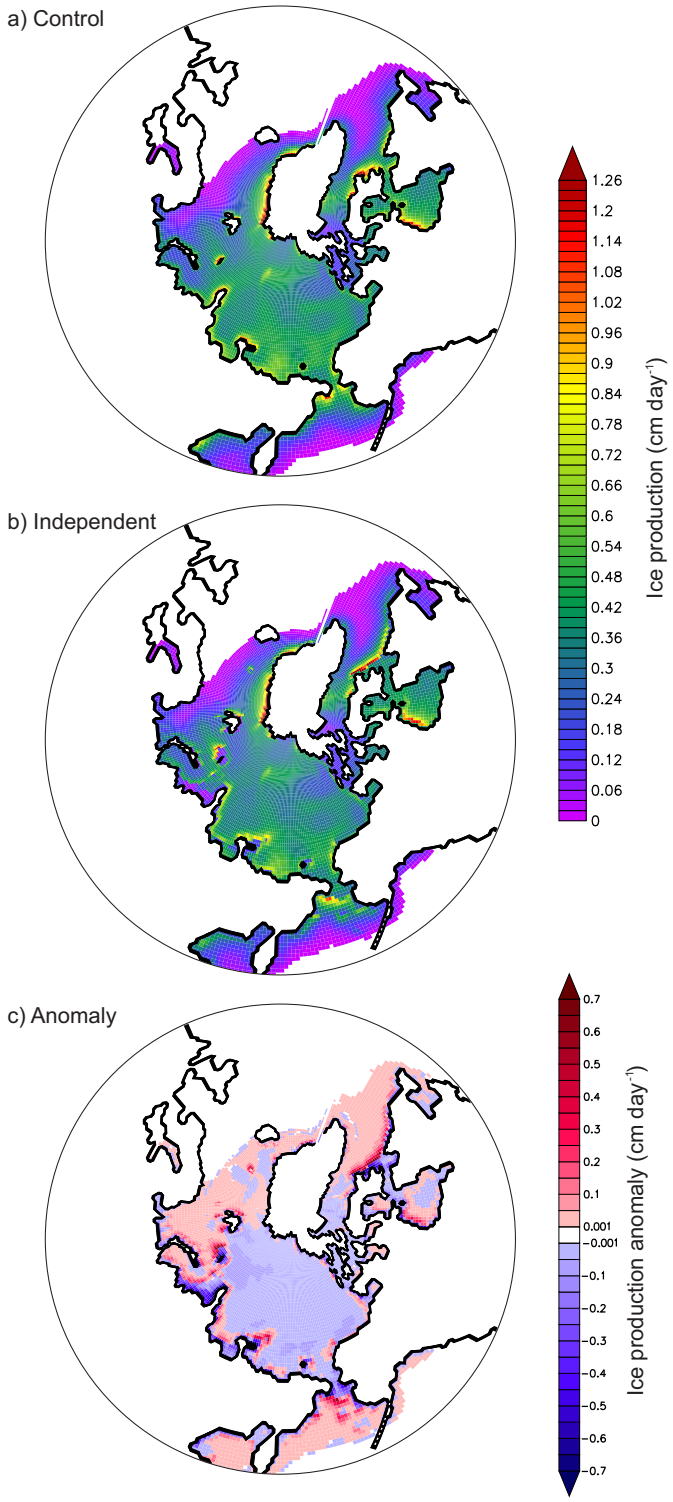

Figure 2.27: Arctic annual average ice production (cm day^{-1}) for the a) control (i.e no parameterisation, b) independent parameterisation and c) anomaly (independent - control) at 1 degree resolution. Ice production smaller than 0.001 cm day^{-1} has been masked to white.

Table 2.2: Ice thickness density and cumulative distributions

Thickness category	Type	Barents Sea	Laptev Sea	Foxe Basin	Central Arctic
1	PDF	0.8678	0.2234	0.0016	0.0137
	CDF	0.8678	0.2234	0.0016	0.0137
2	PDF	0.0583	0.5204	0.7430	0.2081
	CDF	0.9261	0.7438	0.7446	0.2218
3	PDF	0.0152	0.1679	0.2465	0.6666
	CDF	0.9412	0.9117	0.9911	0.8884
4	PDF	0.0188	0.0211	0.0032	0.0225
	CDF	0.9600	0.9328	0.9942	0.9109
5	PDF	0.0135	0.0249	0.0029	0.0332
	CDF	0.9736	0.9577	0.9972	0.9441
6	PDF	0.0002	0.0173	0.0018	0.0229
	CDF	0.9738	0.9750	0.9990	0.9670
7	PDF	0.0000	0.0097	0.0005	0.0193
	CDF	0.9738	0.9847	0.9995	0.9863
8	PDF	0.0000	0.0059	0.0003	0.0125
	CDF	0.9738	0.9906	0.9998	0.9988
9	PDF	0.0000	0.0000	0.0000	0.0008
	CDF	0.9738	0.9906	0.9998	0.9996
10	PDF	0.0000	0.0000	0.0000	0.0000
	CDF	0.9738	0.9906	0.9998	0.9996

The probability density (PDF) and cumulative distribution (CDF) of the fractional ice concentration [0,1] within the first 10 thickness categories. The intervals of the depth categories are detailed in Table. 2.1.

Chapter 3

Impact of tides

3.1 Introduction

Ocean tides are the response of the ocean to the gravitational attraction of the Moon and Sun. The gravitational force between the Earth, Moon, and Sun provides the driving force of the tides, but it is nonastronomical factors such as local water depth, ocean bathymetry, and coastal geometry and topography which determine the magnitude and frequency of the tide at a particular location. In shallow water the tidal wave slows, increasing the tidal range and current velocity. This process results in enhanced tidal forcing globally over the continental shelf. The tidal force can be broken down into a number of harmonic constituents, which are mathematically modelled as sine waves. Each harmonic constituent has a specific period which corresponds to a particular astronomical motion such as the diurnal constituents O1 and K1 (one peak and trough per day) or the semi-diurnal M2 and S2 (two peaks and troughs per day). The spring-neap cycle is a 14.8 day cycle which results from the Sun and Moon reinforcing one another to produce exceptionally large amplitude tides (spring tide), or partially cancelling one another out to produce an exceptionally small amplitude tide (neap tide) (Pugh, 1996; Simpson and Sharples, 2012). There are other tidal cycles which have much longer periods. For example, the lunar nodal (cycle of 18.6 years) is known to have measurable impact on climate, especially in the Arctic (Yndestad, 2006).

3.1.1 Polar tides

Arctic

The shallow water magnification of tidal forcing is important in the Arctic, due to the extensive continental shelves. Approximately $1/3^{rd}$ of the Arctic Ocean is covered by shallow continental shelves with depths typically less than 100 m. The East Siberian Shelf, with water depths shallower than 50 m, is the widest continental shelf in the world extending up to 600 km offshore (Wadhams, 2000).

The largest tidal amplitudes in the Arctic Ocean occur in the Barents Sea, at the entrance to the White Sea, the Labrador Sea, the Northern edge of Baffin Bay and over much of the Canadian Arctic Archipelago (CAA). In Ungava Bay the semi-diurnal tidal range can exceed 12 m (Saucier et al., 2004). In the Arctic, changes in elevation are dominated by the semi-diurnal M2 and S2 tides which propagate from the Atlantic Ocean (Gjevik and Straume, 1989; Proshutinsky, 1991). The largest tidal current speeds, exceeding $0.8\,\mathrm{ms}^{-1}$, occur in similar locations to the largest amplitude tides but are dominated by the diurnal constituents (Padman and Erofeeva, 2004; Kowalik, 1994; Kowalik and Proshutinsky, 1995; Postlethwaite et al., 2011). These diurnal tides are formed directly in the Arctic Ocean by astronomical forces (Defant, 1924; Gjevik and Straume, 1989; Proshutinsky, 1991; Kowalik and Proshutinsky, 1994).

Antarctic

In the Antarctic, the area of ocean dominated by shallow continental shelf is much smaller than in the Arctic, as the shelf break generally occurs close to the coast. Although the Weddell and Ross Seas do contain wide continental shelves, much of them are covered by ice shelves. As such, the effective area where tidal forcing becomes significant is diminished.

In general, tidal forcing is relatively constant around Antarctica, but enhanced tidal forcing does occur in the Weddell and Ross Seas, and to a lesser magnitude the Bellingshausen Sea. The strong tidal forcing in these areas results in an increased

lead fraction, enhancing dense water formation (Koentopp et al., 2005).

One important impact of Antarctic tides is their effect on mass loss of ice shelves through calving and basal melt. Tidally induced vertical displacement of Antarctic ice shelves is generally $1 - 2\,\mathrm{m}$, but in the Weddell Sea and under the Larsen Ice Shelf it can be greater than $3\,\mathrm{m}$, not accounting for the spring tide $\times 2$ amplification factor (Jacobs et al., 1992).

3.1.2 Importance of tides

Tides are an important component of sea-surface height (SSH) and ocean current variability, impacting upon the sea ice cover through both dynamic and thermodynamic processes. The periodic divergent and convergent tidal motion over the tidal cycle causes the ice to undergo mechanical redistribution as the currents exert a stress on the underside of the ice cover. Divergent flows cause the opening of leads and polynyas in the ice cover, enhancing the exchange of heat between the ocean and atmosphere, resulting in a greater net rate of ice production in winter. Kowalik and Proshutinsky (1994) showed that the increased lead fraction in the Arctic sea ice cover caused by tidal forcing alone was responsible for local ice growth of between 10 - 100 cm per year. However, the reduced albedo of the open water compared to ice or snow means that in summer the tidally produced areas of open water absorb higher levels of incoming solar radiation.

Over time periods longer than a tidal period or the spring neap cycle, ice drift can be affected by non-linear residual tidal motion. Residual currents occur from the distortion of the idealized tidal ellipse by factors such as the shape of coastlines, bottom topography and local weather conditions. Residual currents produce a long-term net movement of water (and ice) in a defined direction. The magnitudes of residual currents tend to be small in comparison to the oscillatory tidal flow, but over longer temporal periods they can significantly alter the drift of sea ice (Proshutinsky, 1988). Residual currents tend to be most prominent in shallow coastal regions where landfast ice occurs.

Tidally induced mixing between surface water and warmer deeper water increases

the temperature of the water in contact with the underside of the ice cover, leading to increased melting or a decreased freeze potential. Tidal mixing over Arctic seamounts has been observed to transfer heat from the warm Atlantic water layer to the surface, thinning the ice pack (Proshutinsky, 1988). The upwelling of heat also has the potential to create sensible heat polynyas (Morales-Maqueda et al., 2004). Most latent heat polynyas which occur in the CAA result from tide-induced mixing in the shallow channels which bring warm Atlantic water to the surface (Melling et al., 1984).

Just as tides affect the sea ice cover, sea ice too has an important effect on the amplitude and phase of the tides. Sea ice acts as a flexible cover, weakly damping the vertical tidal motion and restricting horizontal motion. This effect is relatively small in deep water, but in shallow coastal water this process can significantly alter the tidal flow (Murty, 1985). Prinsenberg (1986) and Saucier et al. (2004) found that the presence of ice could reduce tidal currents by about 20 % due to the friction at the ice-ocean boundary.

3.1.3 Impact on landfast ice

The effect of tides on sea ice is amplified in shallow coastal regions, due to increased tidal amplitude and current speed. Proximity to the coast can also result in the reinforcement of incident tidal waves by reflections, producing a much greater tidal range (e.g. Simpson and Sharples, 2012). As landfast ice mainly occurs in shallow coastal regions the effect of tides needs to be considered in any realistic landfast ice modelling study.

Tide cracks are a persistent feature of the landfast ice cover produced by tidal forcing (Figure 1.2). They form parallel to the coast between the bottom-fast and floating sections of landfast ice and allow the floating section of the landfast ice to fluctuate vertically and horizontally with oscillatory tidal motion (Kovacs and Mellor, 1974a; Reimnitz and Barnes, 1974; Mahoney et al., 2007b). Residual tidal currents may also act to initiate horizontal motion of the landfast ice cover. Tidal mixing can cause warm water to upwell onto the continental shelf, spreading under

the landfast ice, altering the freeze/melt potential and stability of the landfast ice cover.

The occurrence of grounded ice is highly sensitive to fluctuations in sea level, especially if the grounded ice is resting within relatively shallow gouges (Mahoney et al., 2007b). A fluctuation in sea level, such as that caused by tides, will cause the ice cover (including the grounded ridges) to be lifted or lowered accordingly, as illustrated in Figure 3.1. If the ridge resides within a gouge with a depth smaller than the experienced rise in sea level then the ridge can be completely uncoupled from the seabed. Tidal currents can then act on the floating ice causing it to be redistributed into water of a different depth. The area of grounded ice will then increase or decrease depending on the ocean depth of the new ridge location. It would be expected that the maximum distance the ridges can be distributed is controlled by the tidal excursion, i.e. the net horizontal distance over which a water particle moves during one tidal cycle. If the gouge depth is greater than the experienced change in sea level then, although the ridge will be lifted up, the walls of the gouge can prevent any horizontal motion by currents, unless the ridge is forced in the direction of its original gouge track. As grounded ridges help to stabilise the landfast ice (Mahoney et al., 2005) it would be assumed that any alteration to the extent or location of grounded ridges, in this case caused by tidal redistribution, will alter the formation and retention of landfast ice.

In this Chapter we consider the impact of tidal forcing on the landfast ice cover, and the ability of thick ice ridges to ground. This is done by using a multi-category sea ice model which has been updated to parameterise the grounding of thick sea ice ridges and the formation of landfast ice. Tidal forcing is then included in the stand alone sea ice model simulations to look at the impact of the tides on the ability of the landfast ice parameterisation to reproduce realistic landfast ice.

3.2 Landfast ice parameterisation

The inclusion of tides as boundary conditions to the sea ice model affects the entire ice cover, as discussed in Section 3.1.2, but we are primarily interested in how tides affect the grounding of thick ice ridges which are known to be important in determining the spatial and temporal occurrence of landfast ice.

Improving the representation of sea surface height in a sea ice model, so that it accounts for tidal elevation, directly affects the grounding of these thick ridges. Positive tidal elevations increase the minimum necessary draft thickness the ridges must reach to ground. Similarly, negative tidal elevations will reduce the minimum necessary draft thickness. This implies that the periodic oscillations in tidal elevation will result in a comparable periodic increase and decrease in the area of grounded ice.

The fractional area of grounded ice, A_G, and its average buoyancy corrected thickness, H_G, are defined by the method fully described in Chapter 2. We first assume an independent relation between ice thickness, h, and ocean depth, d, which allows us to define a joint distribution function (JDF), $j(h,d) = f(h) \times g(d)$ where $f(h)$ is the ice thickness distribution and $g(d)$ is the ocean depth distribution. The JDF is then integrated over the ice draft ocean depth space which represents a draft thickness greater than or equal to the ocean depth. The only difference between the definition of A_G and H_G here, compared to that described in Chapter 2, is that the ocean depth is now time dependent to account for tidally induced elevation changes, but this is not explicitly seen in the equations,

$$A_G = \int_0^\infty \mathrm{d}h \int_0^H \mathrm{d}d\, j(h,d), \tag{3.1}$$

$$H_G = \int_0^\infty \mathrm{d}h \int_0^H \mathrm{d}d \left(h - \frac{\rho_w}{\rho_i} d\right) j(h,d). \tag{3.2}$$

In Equations (3.1) and (3.2) ρ_i and ρ_w are the ice and water density respectively, $H = \frac{\rho_i}{\rho_w} h$ is the draft ice thickness and $(h - \frac{\rho_w}{\rho_i} d)$ is the buoyancy corrected ice

thickness. The effective weight of ice which is aground is $H_G \times \rho_i$.

As detailed in Chapter 2, the A_G and H_G calculated using the formulation detailed by Equations (3.1) and (3.2)) are unrealistic, in that it is not entirely reasonable to postulate that the ice thickness and ocean depth are independent. In reality, ice will generally ground in water depths that are comparable to its draft thickness. To account for this we proposed a second approach to estimate A_G and H_G, whereby the development of grounded ice is restricted by limiting the occurrence of erroneously thick ice grounding on shallow bathymetry. This is done by capping the maximum possible draft thickness of the grounded ice, dependent on the ocean depth, by introducing a coupling parameter, λ. Here, the coupling parameter also accounts for tidally induced changes in sea surface height,

$$\lambda = \frac{d + h_{go}}{d}, \tag{3.3}$$

where d is the ocean depth and h_{go} is the gouge depth. λ was chosen to be a constant factor as h_g was proportional to the water depth, as observations show that the gouge depth generally increases with increasing water depth (Barnes et al., 1984; Shapiro and Barnes, 1991). In the Arctic, for water depths less than or equal to 20 m, observed gouge depths are typically less than or equal to 1m, relating to an average coupling parameter $\lambda = 1.05$ (Barnes et al., 1984; Shapiro and Barnes, 1991; Hequette et al., 1995; Conlan et al., 1998). More extreme gouge depths, $2 - 3\,\mathrm{m}$, have been observed in equivalent water depths (Shapiro and Barnes, 1991; Hequette et al., 1995), relating to $1.1 \leq \lambda \leq 1.15$. Equations (3.1) and (3.2) are thus modified,

$$A_G = \int_0^\infty \mathrm{d}h \int_{H/\lambda}^{H} \mathrm{d}d\, j(h,d), \tag{3.4}$$

$$H_G = \int_0^\infty \mathrm{d}h \int_{H/\lambda}^{H} \mathrm{d}d \left(h - \frac{\rho_w}{\rho_i} d\right) j(h,d). \tag{3.5}$$

3.3 Tidal Model

The Oregon State University (OSU) TPXO7.2 Global Inverse Model (here on referred to as TPXO7.2) is a medium-resolution, $1/4^\circ \times 1/4^\circ$, global inverse tide model. A detailed description of the model is provided in Egbert et al. (1994) and further in Egbert and Erofeeva (2002), and so not be repeated here. The TPXO7.2 tidal model was chosen here as it assimilates TOPEX/Poseidon and TOPEX Tandem satellite radar altimetry (available for the ice-free ocean between $+/-66^\circ$ latitude), and *in situ* coastal and benthic tide gauge data from the polar regions, making it one of the most accurate global tidal solutions. The TPXO7.2 model is particularly accurate for polar regions (our area of interest in this investigation), due to the assimilation of tide gauge data and its utilisation of the most recent Antarctic grounding line information (Egbert and Erofeeva, 2002). The basic global solution (obtained at $1/4^\circ$ resolution) is combined with high resolution local solutions, e.g. The Bering Sea at $1/30^\circ$, which are averaged onto the coarser global grid. However, it should also be noted that as with the majority of tidal models TPXO7.2 does not directly simulate sea ice. Therefore, the tides produced from TPXO7.2 are not modulated by the sea ice cover and will consequently not be as realistic as those tides accounting for this interaction. To ensure that the impact of the tides on landfast sea ice was as realistic as possible we accounted for the eight major harmonic constituents (M2, S2, N2, K2, K1, O1, P1, Q1), two long period (Mf, Mm) and 3 non-linear (M4, MS4, MN4) constituents. These are the standard harmonic constituents used to calculate tidal forcing in TPXO7.2.

3.4 Model setup

The Los Alamos Sea Ice Model (CICE) v4.1 (Hunke and Lipscomb, 2010) was used to carry out the simulations discussed here. CICE is described in detail in Chapter 2 and so not repeated here. It should be noted that the CICE model was setup and run so that all variables, apart from the inclusion of tidal boundary conditions, were identical to the previous global simulations discussed in Chapter 2, i.e. the model

was run in standalone format using a displaced pole grid at 1 degree resolution with 15 ice thickness categories. It was initialised with no ice and integrated for 11 years (10 year spin up) using repeat NCAR atmospheric forcing from 1997 and bathymetry boundary conditions obtained from ETOPO1. Tides were included in the standalone CICE code by forcing the code with sea surface height and ocean velocity output from the TPXO7.2 tidal model. Hourly tidal elevation and currents from 1997 were obtained from TPXO7.2 at each CICE grid cell through a weighted interpolation of the 4 closest TPXO7.2 points. No other ocean currents are included in these simulations. Results from the last year of integration from the following simulations are presented:

- No landfast ice parameterisation with tidal forcing (control tidal),
- Independent landfast ice parameterisation with tidal forcing (independent tidal),
- Restricted landfast ice parameterisation with tidal forcing (restricted tidal), using a coupling parameter:
  - $\lambda = 1.05$
  - $\lambda = 1.10$
  - $\lambda = 1.25$

3.5 Results

3.5.1 Arctic

Impact on ice distribution

Before looking at the impact of tides on grounded and landfast ice, it is important to investigate the effect of tidally induced thermodynamic and dynamic processes, as detailed in Section 3.1.2, more generally on the ice cover. We consider the effect of tides on the monthly mean ice extent, the mean winter (JFM) and summer (JAS)

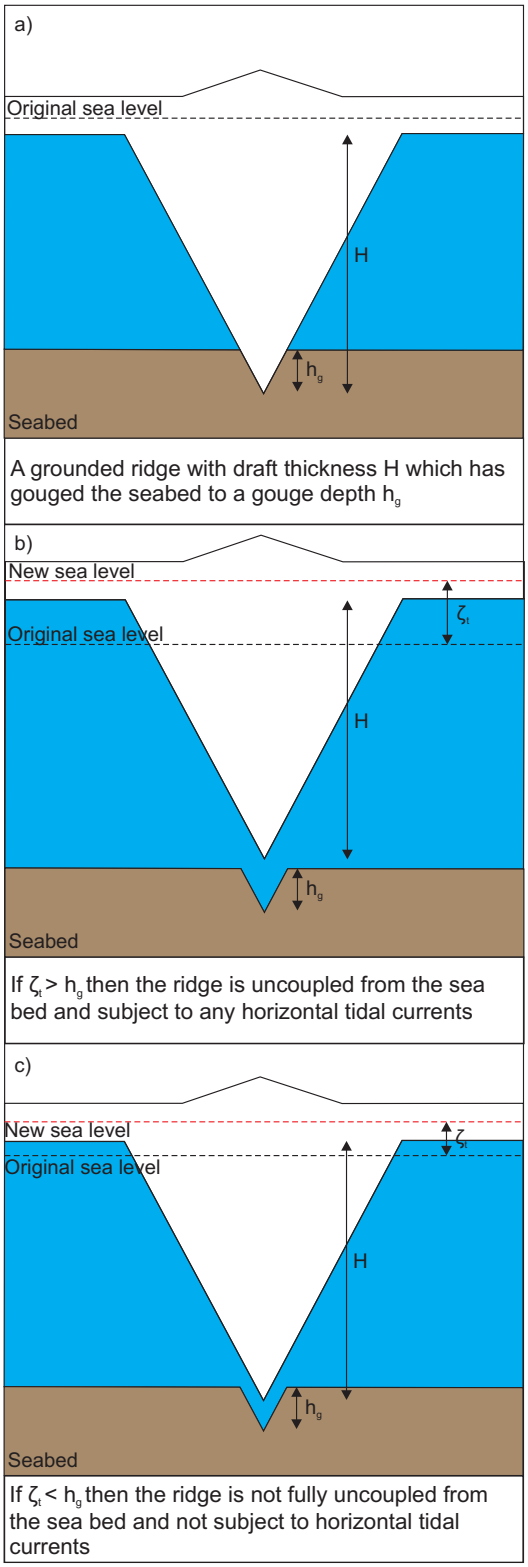

Figure 3.1: Effect of tidally induced fluctuations in sea surface height on grounded ridges where H is draft thickness, h_g is the gouge depth and ζ_t is the change in sea surface height.

ice volume, and ice thickness distribution for the control (i.e. no landfast ice parameterisation). For reference, most of the Arctic locations mentioned in this section are identified in Figure 2.4.

Ice extent

The Arctic winter maximum and summer minimum ice extents, with and without tidal forcing for the control simulation (i.e. no landfast ice parameterisation) are shown in Figure 3.2 (a). The introduction of tidal forcing did not change the time the maximum ice extent was reached but did result in a small temporal shift in the absolute minimum extent from the 3rd September to the 29th of August. However, for consistency we compare September ice extents.

The edge of the maximum ice extent underwent minor modification with the introduction of tides. A relatively small northward shift was observed in the Norwegian Sea, the Bering Sea and Gulf of Alaska. Similarly the edge of the September ice extent underwent little modification with tidal forcing. A small southward advance occurred between Svalbard and Novaya Zemlya, with a northward retreat between Svalbard and Greenland. Slight differences were also observed in the Kara and Laptev Seas as well as the CAA and Hudson Bay (HB) region.

Qualitative comparison with observations (Fig. 3.3(a)) shows that CICE generally overestimated the summer and winter ice extent, both with and without tidal forcing, most likely due to the lack of realistic ocean heat fluxes and currents.

Ice volume

The Arctic winter (JFM) and summer (JAS) mean ice volume per unit area without tides, with tides, and the anomaly (tides - no tides) for the control simulation are shown in Figures 3.4 and 3.5 respectively. In winter the largest ice volume per unit area was observed within the CAA and along the north Greenland coast (up to 5.6 m), and to a lesser extent north of Svalbard ($\approx$ 3 m). There was a graduation to smaller ice volume per unit area along the north Russian coast ($\approx$ 2 m). This pattern compares well to observed and modelled Arctic ice thickness, and more

recently satellite observation from CryoSat-2 and ICESat (Laxon et al., 2013; Kwok and Cunningham, 2008; Kwok et al., 2009; Rothrock et al., 2003; Bourke and Garrett, 1987). CICE was found to produce higher than expected ice volume in the Kara Sea, evident in both the non tidal and tidal simulations.

Over much of the Arctic the winter mean ice volume underwent changes on the order of $+/-10\%$ due to the introduction of tides. However, a number of regions underwent significant localised changes. The CAA, HB, Foxe Basin, and along the north Russian coast were the regions most notably affected by tides. Most areas which experienced these strong changes in ice volume were also influenced by strong residual tidal currents (Figure 3.6(a)), which caused significant modifications to ice motion (Figure 3.7). In the CAA the ice volume changes were approximately 50%, with large sections undergoing a reduction in ice volume due to the residual currents acting to force ice out from the CAA into Baffin Bay. In Foxe Basin changes in ice volume were found to exceed 100%, with significant increases to the north and east of Foxe Basin. the residual tidal currents in Foxe Basin resulted in a long term southwesterly flow of water, causing the ice to pile up along the northeast coastline. In HB ice volume increased in the east and decreased in the west as the residual tidal currents resulted in a long term westerly flow of water and ice. The patterns observed in the CAA, HB and Foxe Basin were not unrealistic (Saucier et al., 2004) but the magnitudes of the changes were. Along the north Russian coast the introduction of tides resulted in an alternating increase and decrease in ice volume. The residual tidal currents tended to force the ice from west to east but northerly protruding landmasses acted as barriers to this ice flow. Novaya Zemlya separates the Barents and Kara Seas, while North Land (between the Kara and Laptev Seas) and the New Siberian Islands (between the Laptev and East Siberian Seas) were modelled as being attached to the coast in these simulations due to the relatively coarse model resolution. As such, the ice piled up on the western side of these boundaries. The ice volume was also altered due to modification of the ice production rate through the opening (increase) and closing (decrease) of leads caused by tides.

In summer, due to thermodynamic melt, the areal coverage of sea ice is reduced,

but a fraction of perennial ice remained in the CAA, where the highest mean ice volume was experienced, and in the central Arctic Ocean. CICE also produced multiyear ice in the Kara and Laptev Seas, which is generally reported to be ice free (or have minimal ice cover) in summer months (Fetterer et al., 2002, updated 2009; Bourke and Garrett, 1987; Divine et al., 2004). This over estimation of perennial ice may contribute to the production of multiyear landfast ice in these regions. Similar patterns in the ice volume anomaly were observed in summer as winter (for the areas containing ice). Additionally, an increase in ice was found in the southern Barents Sea caused by residual tidal currents altering the mean ice motion, transporting ice from the northern Barents Sea, and surrounding areas, south.

Throughout the year, tides modified ice transport and the rate of ice production, resulting in subtle changes to ice distribution over much of the Arctic, with larger localised changes in some regions. These changes led to a small net increase in ice volume in each month (compared to no tides), up to a maximum of 3 %, except in August and September which experienced a small net decrease ($\leq$ 2 %) as shown in Figure 3.8 (a). Amplification of the seasonal cycle due to tidal forcing is to be expected, as there will be more ice production in winter and more melt in summer, both associated with a larger lead area. This trend is comparable to Kowalik and Proshutinsky (1994) who showed that the increased lead fraction in the Arctic sea ice cover caused by tidal forcing alone was responsible for a net increase in ice production in winter.

Ice thickness distribution

The impact of tides on Arctic annual, winter, and summer mean ice thickness distribution is detailed in Table 3.1 for the control simulation (i.e. no parameterisation). The annual mean area of ice within each thickness category, with and without tides, for all simulations is shown in Figure 3.9. A consistent pattern is observed across the winter, summer, and annual means for the simulations employing no landfast ice parameterisation (control), the independent parameterisation and restricted pa-

rameterisation. In all cases there is a consistent redistribution of ice from thinner to thicker ice categories due to dynamical deformation (such as ridging and rafting). This process was most active within the first 7 thickness categories (which relates to ice up to 8.40 m thick), as it is increasingly more difficult to deform thicker ice.

Thickness category 1 relates to thin ice (up to 0.6 m), and changes of ice area within this category can be used as a proxy for ice production (as CICE will place any new ice within this category). CICE can redistribute ice into thicker categories but cannot mechanically redistribute it into thinner ice categories. Ice can only be redistributed into thinner categories through thermodynamic melt. An increase in the area of ice within the thinnest category is consistently observed with the inclusion of tides. This effect is strongest in winter (Table 3.1), while summer melting of this thin ice results in the increase in ice production in the annual mean appearing relatively insignificant in comparison to the redistribution of ice into thicker ice categories (Figure 3.9). As an increase in ice within the thinnest category was observed in winter, as well as summer, when ice will not be subject to thermodynamic melt, this suggests that tides caused an increase in ice production due to an increased lead fraction.

In general, over the Arctic, tides were found to increase the lead area (Figure 3.10), although localised differences were observed. The locations which underwent the strongest increases in lead area were comparable to those locations influenced by the strongest tides and residual currents (Figure 3.6(a)). Under the influence of tides the lead area in Foxe Basin and Hudson Bay increased by approximately 20%, while in the CAA, Baffin Bay and south of Svalbard the lead fraction increased by around 10%. Due to the westerly flow of ice along the north Russian coast driven by the residual currents which were interrupted by the northerly landmass protrusions the lead fraction alternated between increasing in the west and decreasing is the east of the Barents, Kara and Laptev Seas by approximately 10%. Modifications to the lead area resulted in comparable changes in the rate of ice production, Figure 3.11. A higher lead area in winter resulted in increased ice production, as the cold overlying atmosphere was able to cool and freeze the increased area of open water.

In summer, an increased lead fraction meant that the water was able to absorb more heat from the comparatively warm atmosphere resulting in increased melt of the remaining ice. These factors combine to give an amplification of the seasonal cycle of ice production, Figure 3.8(a).

A note on residual tidal currents

The location of the residual tidal currents produced by TPXO 7.2 compared well with observations and other modelling studies (Kowalik and Proshutinsky, 1994, 1995; Gjevik et al., 1994; Hannah et al., 2009), but in some cases the magnitude far exceeded previously reported values. In the East Siberian and Laptev Sea Kowalik and Proshutinsky (1994) reported M_2 residual tidal currents up to $1\,\mathrm{cm\,s^{-1}}$ in a barotropic tidal model at 14 km resolution. For the same location, but at coarser resolution, we found the residual currents, due to all harmonic constituents, to be comparable at approximately $4\,\mathrm{cm\,s^{-1}}$.

Erroneously strong residual currents in the tidal forcing occurred at a number of Arctic locations including the HB region. This region is a unique tidal system due to its relatively shallow mean depth and intricate coastal geometry. Observations show this area to be dominated by some of the world's strongest tidal currents (semi-diurnial tidal current velocity up to $0.9\,\mathrm{m\,s^{-1}}$ (Prinsenberg, 1987)) and greatest tidal elevations (the semi-diurnal tidal range exceeding 12 m in Ungava Bay (Saucier et al., 2004)). These tidal current velocities and ranges are represented well in the TPXO7.2 tidal model, but the magnitudes of the residual currents in the HB region were unrealistically strong, on the order of $0.5\,\mathrm{m\,s^{-1}}$. In some cases, the direction of the residual current was also unrealistic, such as those flowing into the closed coastal boundary in NE Foxe Basin. Erroneously strong residual currents in TPXO7.2 were also apparent in other Arctic regions e.g. between Svalbard and Norway, and in the Bering Sea, but not to the magnitude experienced in the HB system. It should be noted that these currents will adversely alter the ice drift, potentially leading to an unrealistic ice distribution.

The failings of the TPXO7.2 tidal model to realistically resolve the residual tidal

currents in these regions may be due to the differences in the landmasks used in the relatively coarse resolution CICE ($1^\circ \times 1^\circ$) and the finer resolution TPXO7.2 code ($1/4^\circ \times 1/4^\circ$). If the same landmask was used in both codes then it would be expected that much of the spurious convergence and divergence in coastal regions would be removed. For future work it would be suggested that the TPXO7.2 code is run using the CICE landmask to improve consistency. Similarly, any disparities between the bathymetry used in the TPXO7.2 and the ETOPO1 derived CICE bathymetry could be a source of error.

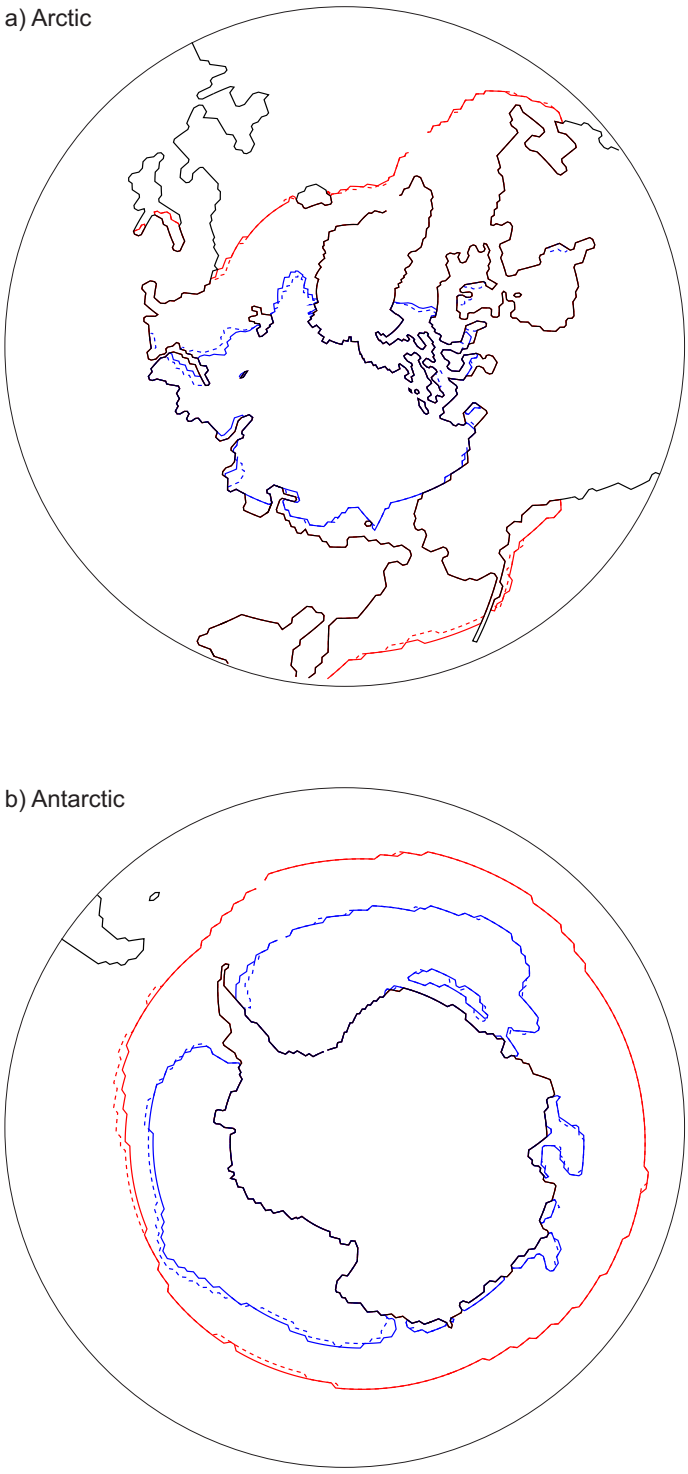

Figure 3.2: The monthly maximum (red) and minimum (blue) sea ice extent without tides (solid line) and with tides (dashed line) for the control simulation in (a) the Arctic and (b) the Antarctic. In the Arctic the September extent is used for the minimum in both simulations.

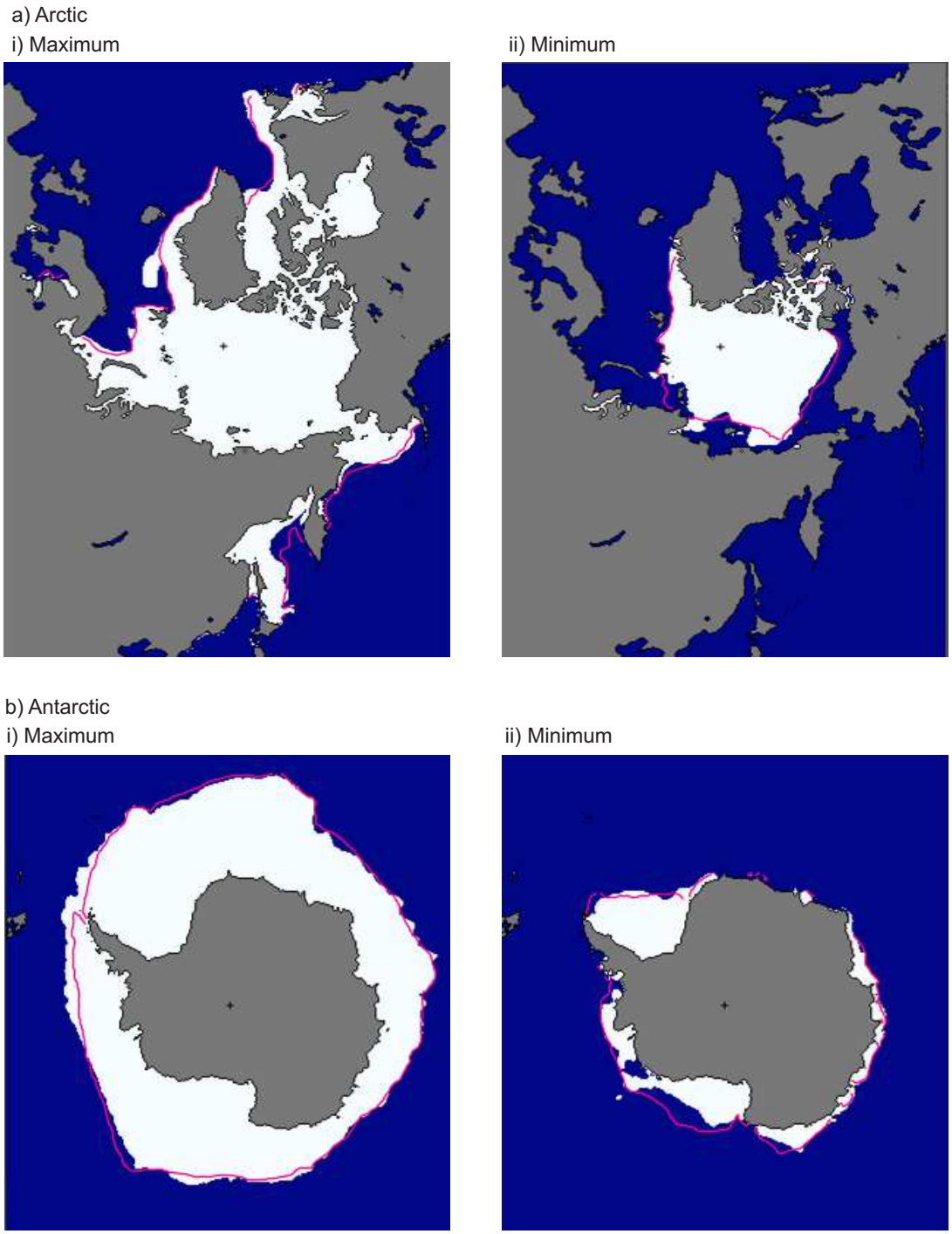

Figure 3.3: (a) Arctic and (b) Antarctic (i) maximum and (ii) minimum 1997 ice extent from the NSIDC Sea Ice Index (Fetterer et al., 2002, updated 2009). The pink line represents the monthly median ice extent over 1981 - 2010.

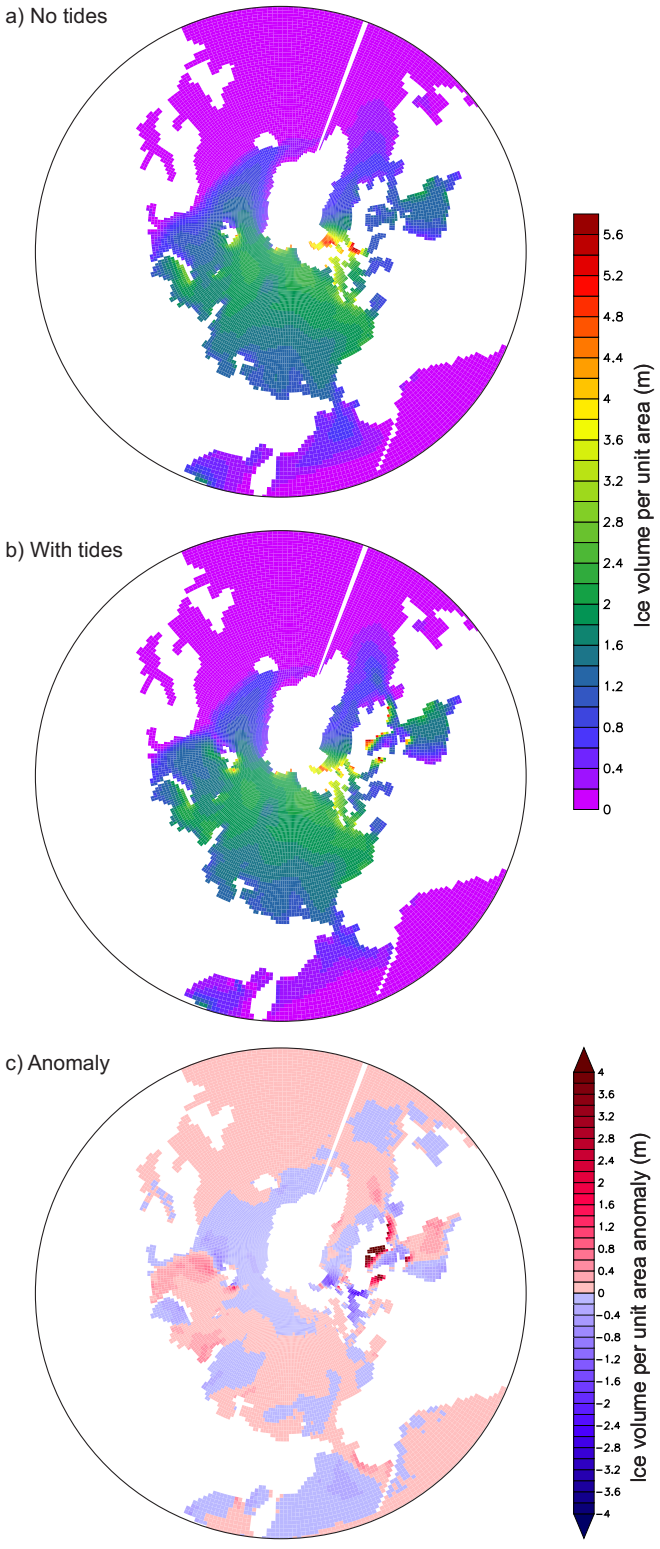

Figure 3.4: Arctic winter (JFM) ice volume per unit area (m) (a) without tides, (b) with tides, and (c) anomaly (tides-no tides) for the control simulation (i.e. no landfast ice parameterisation).

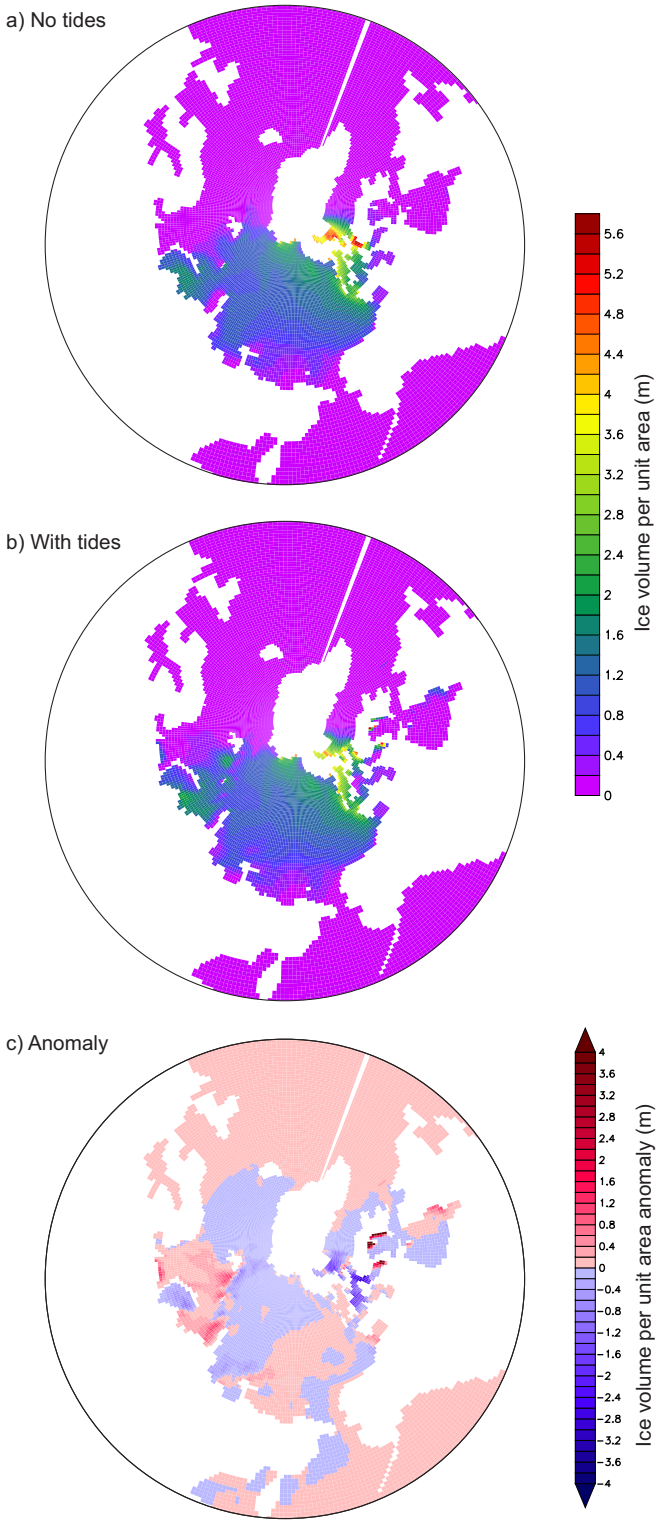

Figure 3.5: Arctic summer (JAS) ice volume per unit area (m) (a) without tides, (b) with tides, and (c) anomaly (tides-no tides) for the control simulation (i.e. no landfast ice parameterisation).

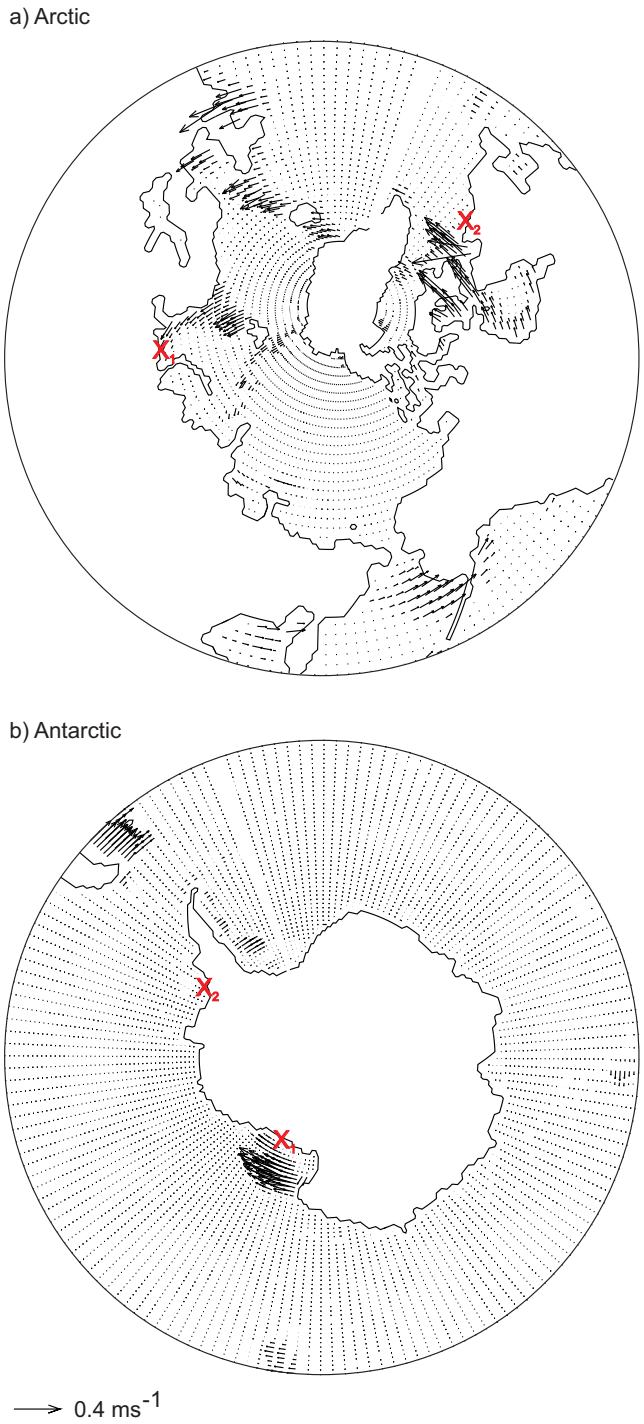

Figure 3.6: Annual mean residual tidal currents ($\mathrm{m\,s^{-1}}$) for the control simulation (i.e. no landfast ice parameterisation) at every second grid cell in the x and y direction (a) the Arctic, and at every second cell in the x direction only in (b) the Antarctic. The markers X1 and X2 relate to locations where tidal time series are considered in Figures 3.12, 3.13, 3.26, 3.27.

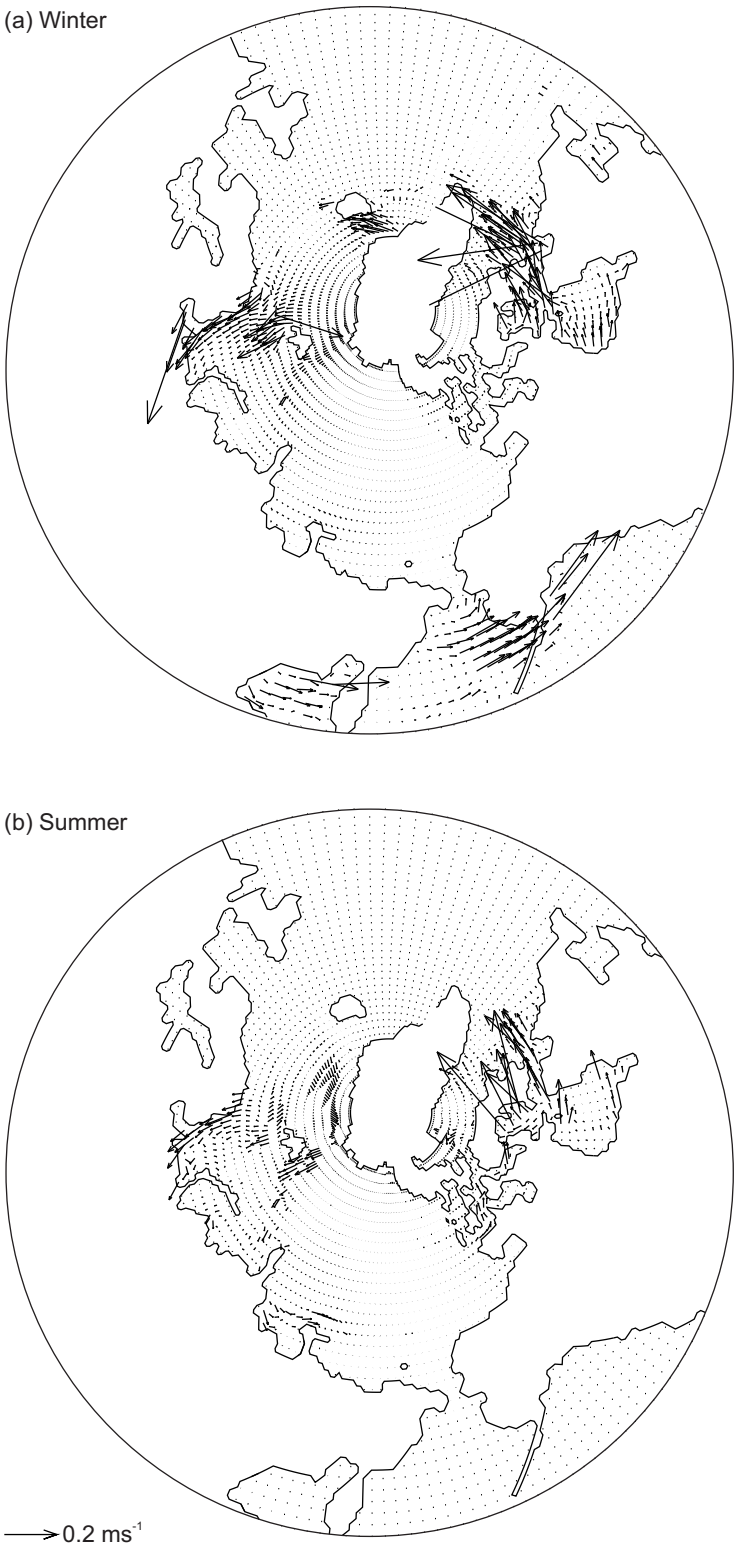

Figure 3.7: Arctic mean ice velocity anomaly (tides - no tides) ($\mathrm{m\,s^{-1}}$) for the control simulation (i.e. no landfast ice parameterisation) at every second grid cell in the x and y direction for (a) the winter (JFM) and (b) the summer (JAS).

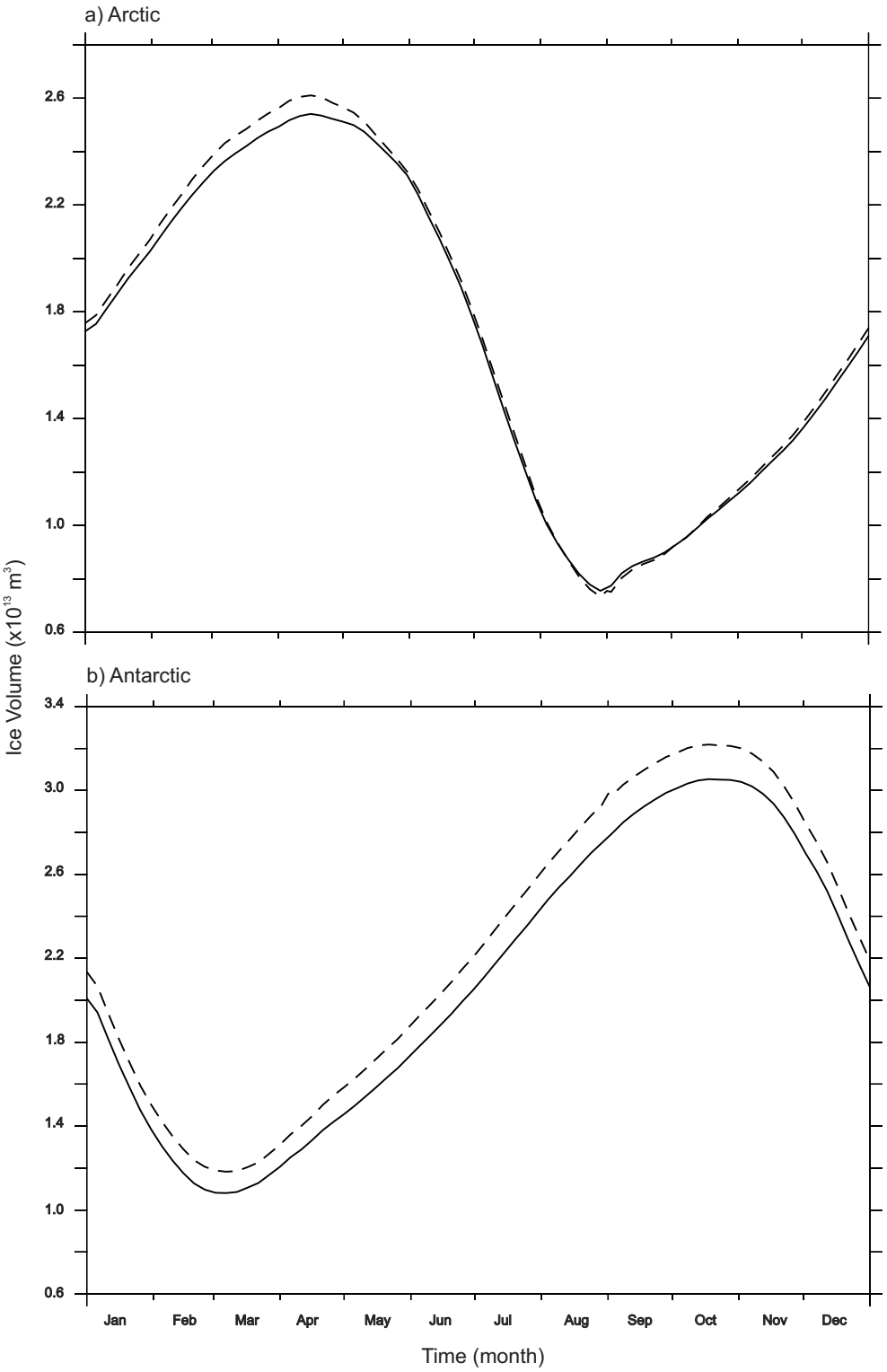

Figure 3.8: 5 day mean ice volume (m^3) for the control simulation (i.e. no landfast ice parameterisation) without tides (solid black line) and with tides (dashed black line) for (a) the Arctic and (b) the Antarctic.

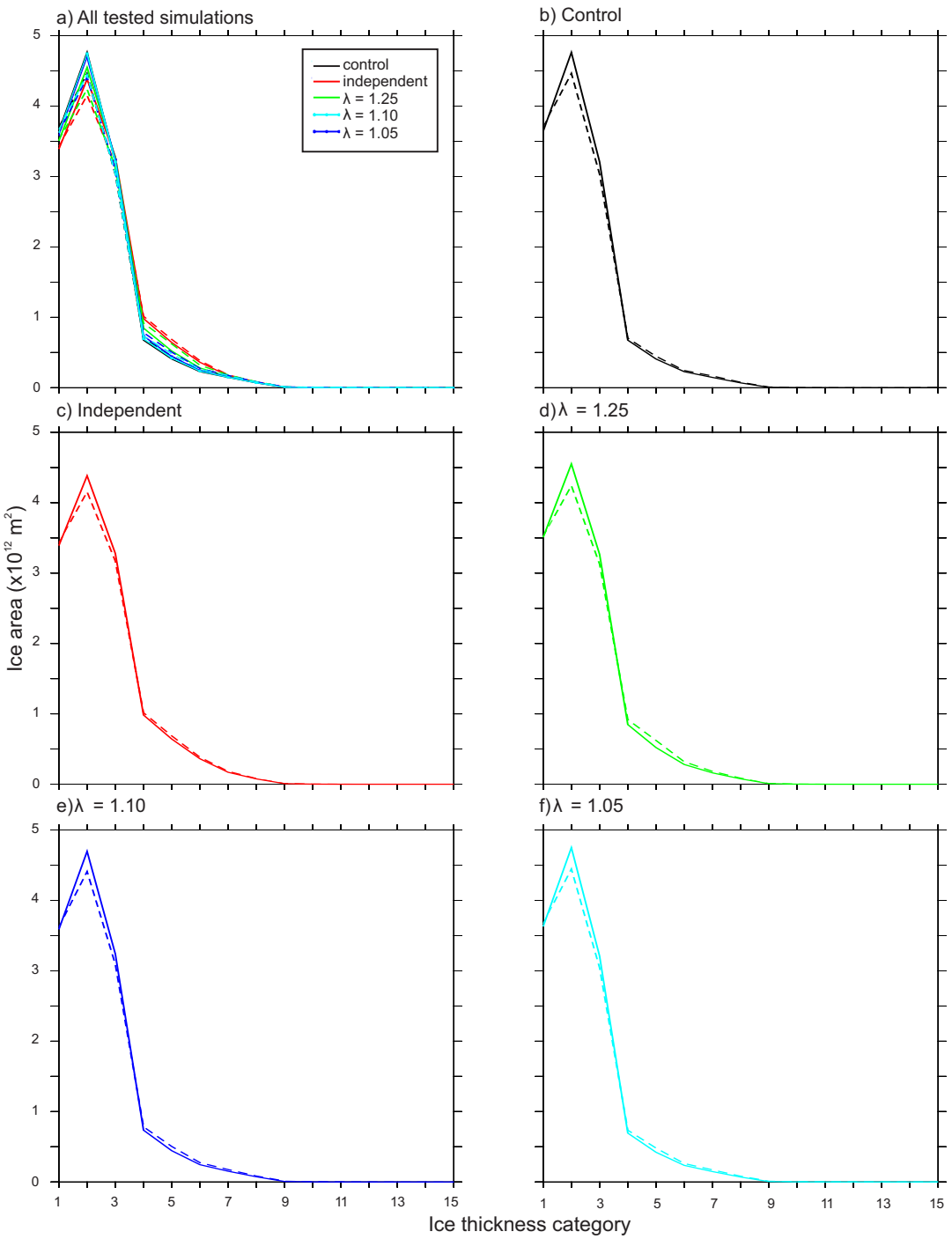

Figure 3.9: Arctic mean annual ice thickness distribution per thickness category without tides (solid line) and with tides (dashed line) for (a) all tested scenarios, (b) the control, (c) the independent parameterisation, and the restricted parameterisations for (d) $\lambda = 1.25$, (e) $\lambda = 1.10$ and (f) $\lambda = 1.05$. Details of thickness category limits can be found in Table 3.1

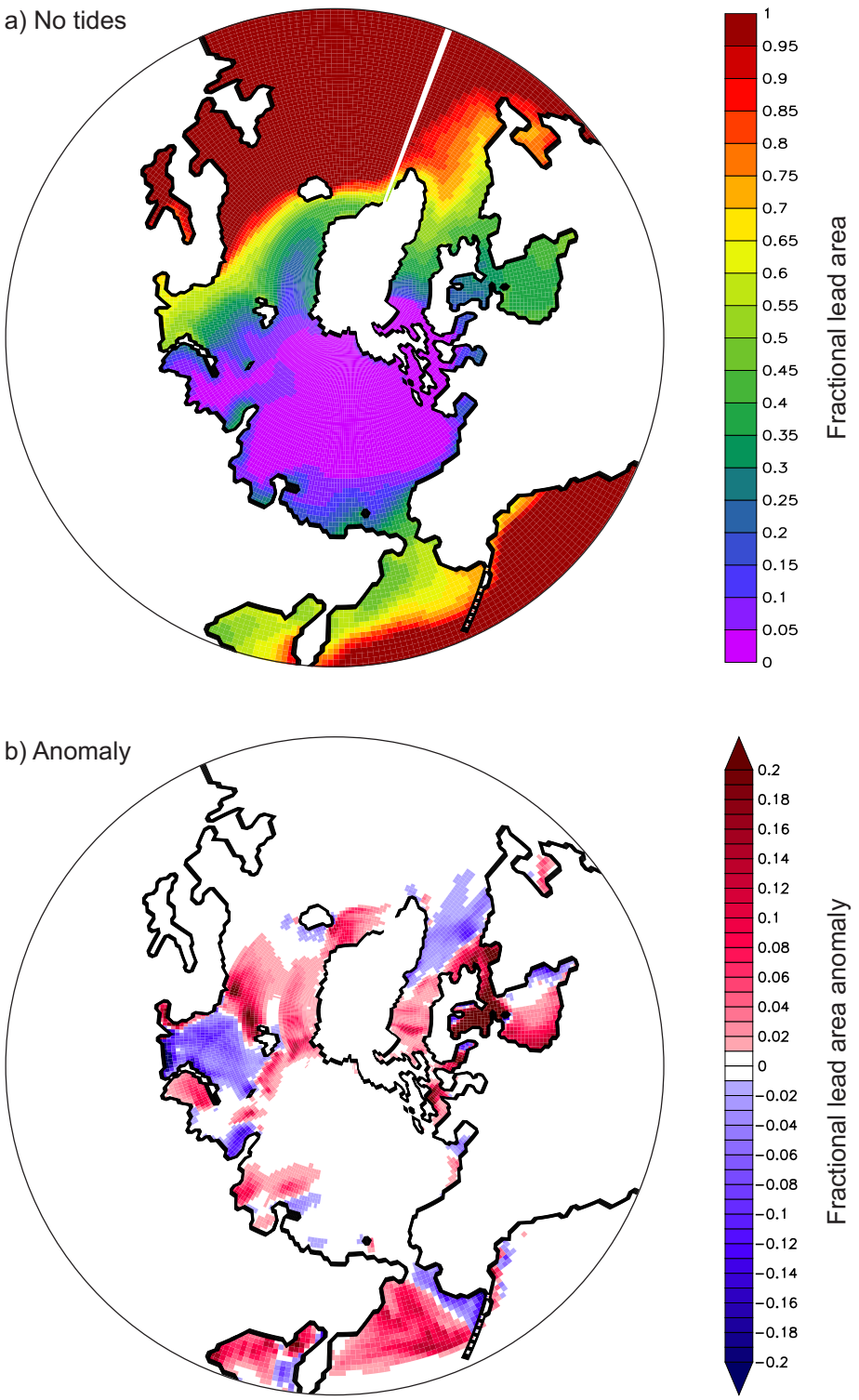

Figure 3.10: Annual mean Arctic fractional lead area (0−1) for the control simulation (i.e. no landfast ice parameterisation) (a) without tides and (b) the anomaly (tides-no tides). Any anomaly less than 0.01 is masked to white to remove noise.

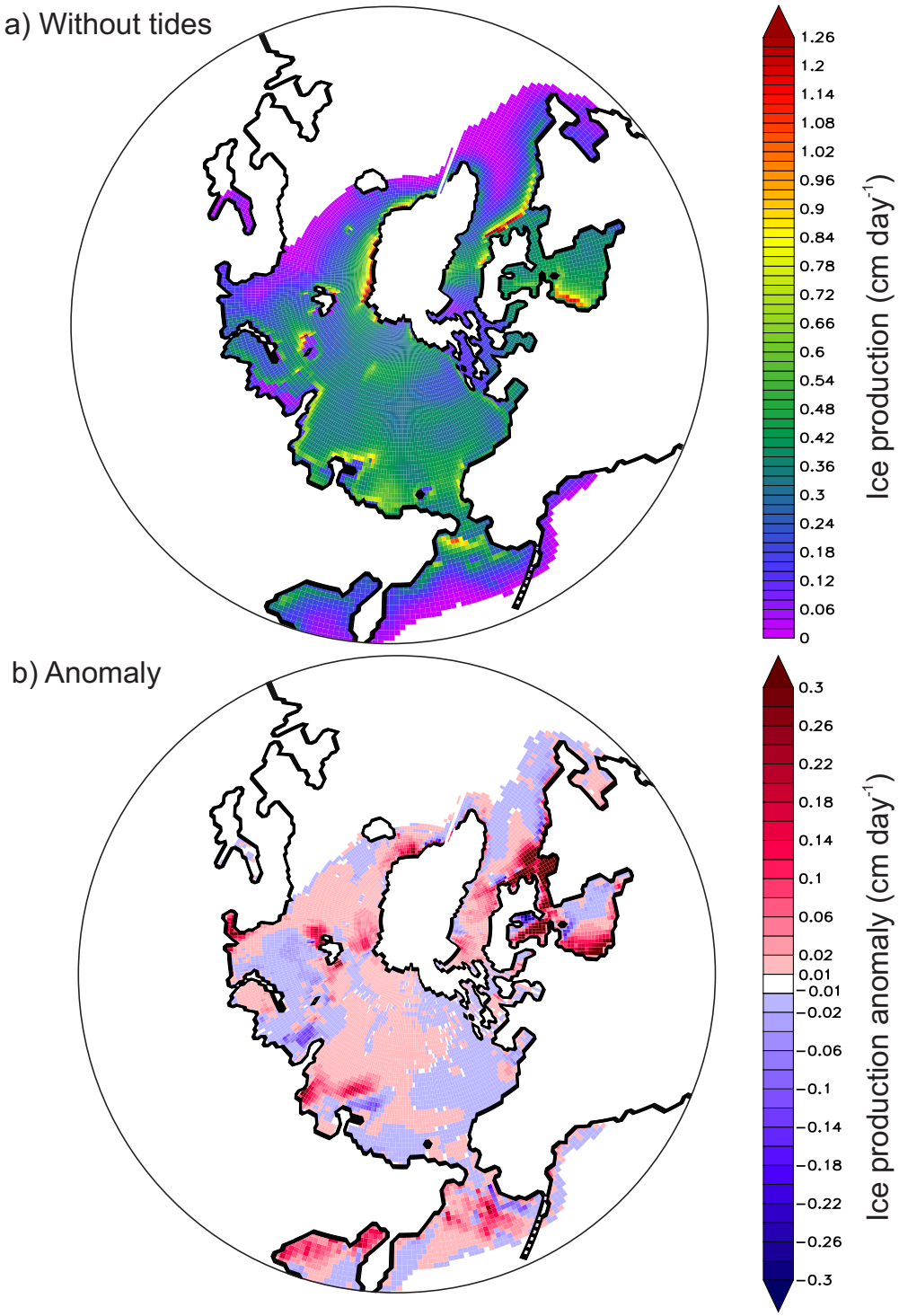

Figure 3.11: Arctic annual mean ice production (cm day^{-1}) a) without tides and b) tidal induced anomaly (tides - no tides) using the independent landfast ice parameterisation. Ice production smaller than 0.001 mm day^{-1} have been masked to white.

Grounded ice

In Chapter 2 the ability of the independent and restricted landfast parameterisations to reproduce landfast sea ice is documented in detail. Despite its simplicity, the independent parameterisation reproduced many of the key aspects of the landfast ice cycle, although it did lead to an overestimation of multi-year landfast ice. For simplicity and consistency, only results from the independent parameterisation are considered in the following sections looking at the impact of tides on grounded ice.

Tidal cycle

Tidally induced oscillations in sea surface height directly alter the ability of ice to ground. Positive sea surface elevations increase the necessary minimum draft thickness the ice must reach in order to ground, decreasing the occurrence of grounded ice, while negative sea surface elevations reduce the necessary minimum draft thickness, increasing the occurrence of grounded ice. These effects were observed throughout the Arctic in the simulations, but specific examples are shown for coastal grid cells in the Barents Sea and Hudson Strait in Figures 3.12 and 3.13 respectively. The exact location of these test areas are indicated by the markers X_1 and X_2 respectively in Figure 3.6(a). Both the Barents Sea and Hudson Strait were dominated by regular semi-diurnal tides, producing twice daily peaks and troughs in sea-surface height. The area of grounded ice was observed to fluctuate in line with these peaks and troughs. The magnitude of the change in grounded ice area at a particular grid cell is controlled by the magnitude of the tidal elevation; areas experiencing a large tidal range showed large fluctuations in grounded ice area over the tidal cycle, while those experiencing a reduced tidal range underwent smaller changes in the grounded ice area.

Spring-Neap cycle

The spring-neap cycle describes the strongest (spring) and weakest (neap) tides which occur on a 14.8 day cycle. At grid cell X_2 in the Hudson Strait the range in tidal

elevation is shown to reach two maxima and minima over 28 days in March (Figure 3.14). A response to this spring-neap cycle is identified in the grounded ice. The largest range in grounded ice area over a tidal cycle was obtained during the spring tide, and the smallest range during the neap tide. Although the spring-neap range in the maximum sea surface height was large (up to 4 m) the induced fluctuation in grounded ice area was comparatively small. During the neap tide ($\approx$ day 4) the area of grounded ice reached a maximum of approximately 37% of the grid cell. This maximum decreased to 34% during the spring tide ($\approx$ day 11).

Horizontal transport of grounded ice

Over the tidal cycle the tidally induced vertical oscillations in grounded ice, which alters the area of the grounded ice, would average to a zero net change if no other forces acted upon the grounded ice when uncoupled from the seabed. If additional horizontal forces, such as tidal currents or residual currents, are present, then the grounded ridges may be horizontally redistributed into regions of a different ocean depth when uncoupled. If the ridges are redistributed into an area which is shallower than the original location, then all ice which was previously aground, and potentially new ice, will reground. If the ridges are redistributed into a region which is deeper than the original location then the amount of ice that grounds could be less, the exact value will depend on the relation between the draft ice thickness and the new ocean depth accounting for the new tidal range.

The change in the area of grounded ice within a given grid cell will be controlled by an *in situ* source or sink from thermodynamic growth or melt S_{therm}, a mechanical sink due to exporting of grounded ice through divergence S_{exp} and a mechanical source due to importing and grounding ice through convergence S_{imp},

$$\frac{\partial A_g}{\partial t} = S_{therm} + S_{exp} + S_{imp}. \tag{3.6}$$

To build a complete theory of grounded ice dynamics these terms must be defined. In this parameterisation we diagnose the total amount of ice aground within each

grid cell at each timestep and can therefore calculate $^{\partial A_g}/_{\partial t}$. However, this means we do not have an understanding of the contributions of each of these terms individually to $^{\partial A_g}/_{\partial t}$.

We are interested in the impact of tides on the motion of the grounded ice, and as such we do not consider the effect of S_{therm}. We assume that S_{therm} is consistent between the non tidal and tidal runs (as the same thermodynamic forcing was used) and therefore any change in the grounded ice location when tides are introduced is caused by dynamic processes only. We are unable to reconstruct the terms S_{exp} and S_{imp} from the model output, but we are able to examine the transport of grounded ice, namely $A_g\vec{u}$. In Figure 3.15 we show the annual mean transport of grounded ice for the independent landfast ice parameterisation without tides and the anomaly (tides - no tides). In general, the grounded ice is being transported on the order of 1×10^{-4} to 1×10^{-5} ms^{-1} by winds alone. This is much slower than the transport of pack ice due to winds, as the frictional stress between the ice bottom and the seabed will act to slow any ice motion. When tides are introduced the transport of the grounded ice is altered as shown in Figure 3.15(b). The impact of tides appears to be relatively localised, with no consistent hemispheric trend. In some regions (e.g. HB, White Sea and Bering Sea) tides appear to cause increased divergence of grounded ice, while in other regions (e.g. Barents Sea and Northern Kara Sea) the tides caused increased convergence. The strongest changes occur where the strongest residual currents are found (Fig. 3.6(a)). This suggests that the tides are acting to redistribute the grounded ridges once uncoupled from the seabed.

Total area of grounded ice

Monthly estimates of grounded ice area, produced with and without tides, are shown in Figure 3.16. As observed in the simulations with no tides, the model experiments with tides produced a seasonal cycle of grounded ice which progressed steadily from a summer minimum to a winter maximum. The independent parameterisation produced significantly more grounded ice than the restricted parameterisations, with the total area decreasing with increasing level of restriction. For the tidal simulations,

over the year, the independent parameterisation produced between $1637 - 4007\,\%$ more grounded ice than the restricted parameterisation using a coupling parameter $\lambda = 1.25$. Increasing the level of restriction on the grounding parameterisation means that the ridges are only allowed to ground in water which is just shallower than the draft ice thickness, removing the occurrence of erroneously thick grounded ice. This is comparable to the results for the non tidal simulations

It has already been found that tides increased the rate of new ice production and the occurrence of thicker ridged ice through mechanical deformation, Figure 3.9. Both of these factors will lead to an increased ability of ice to ground. However, oscillations in sea surface height, tidal currents, and residual tidal currents which mobilise the ice pack will act to prevent ice from grounding. The area of grounded ice in simulations which employed a restricted grounding parameterisation was found to increase with the inclusion of tides as the effect of more, and thicker, pack ice dominated. However, simulations which employed an independent parameterisation underwent a reduction in the level of grounded ice when tides were introduced. This may be because in the simulations with and without tides, the grounded ice produced by the independent parameterisation is much more extensive, occurring in areas which are influenced by strong oscillations in sea surface height, tidal currents, and especially residual tidal currents, and is therefore more susceptible to removal.

In all cases, the magnitude of the change in grounded ice was greater in winter than summer. This is due to the remaining summer grounded ice being relatively thick and stable, and thus less susceptible to tidally induced motion.

The magnitude of the change in grounded ice area when tides are included for the independent parameterisation is greater than the changes observed for any of the tested restricted parameterisations. This is likely to be due to simulations which used the independent parameterisation without tidal forcing producing much more grounded ice than simulations which used the restricted parameterisations, and therefore there is a larger area of grounded ice which can be acted upon, and removed, by tides.

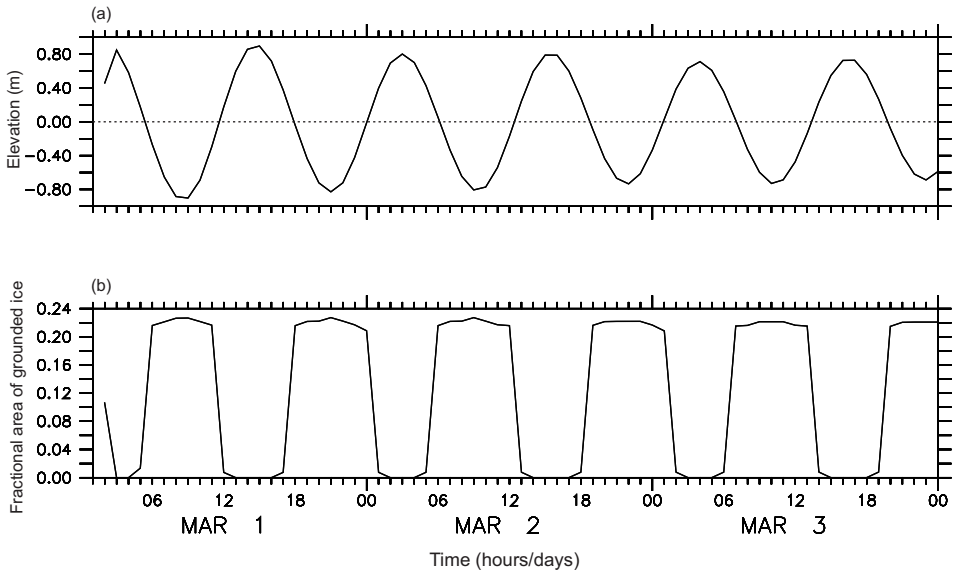

Figure 3.12: (a) Tidal elevation (m) and (b) fractional area of grounded ice at a coastal point in the Barents Sea (X_1 in Fig. 3.6(a)) for the 1st-3rd March from Year 11 in the independent parameterisation model run forced with 1997 atmospheric data.

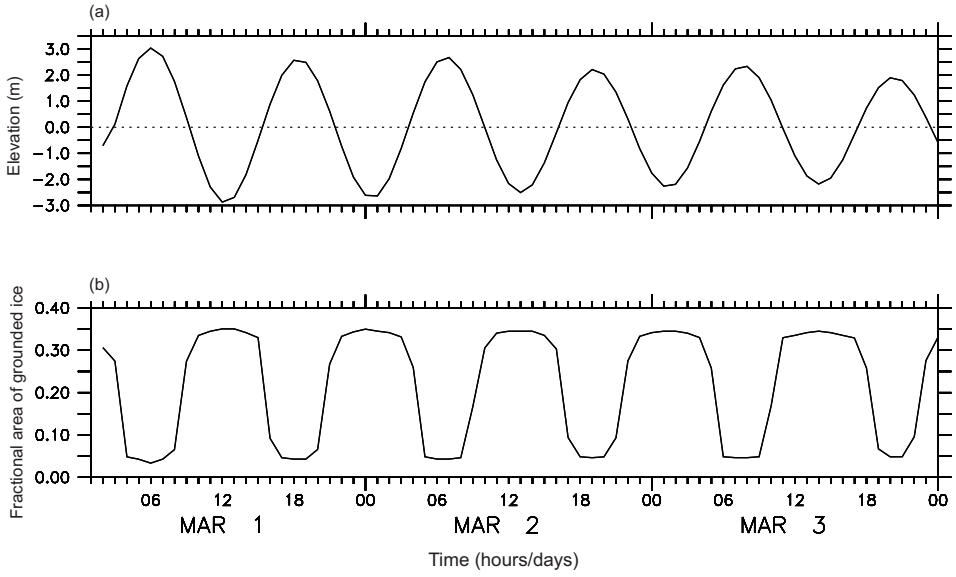

Figure 3.13: (a) Tidal elevation (m) and (b) fractional area of grounded ice at a coastal point in the Hudson Strait (X_2 in Fig. 3.6(a)) for the 1st-3rd March from Year 11 in the independent parameterisation model run forced with 1997 atmospheric data.

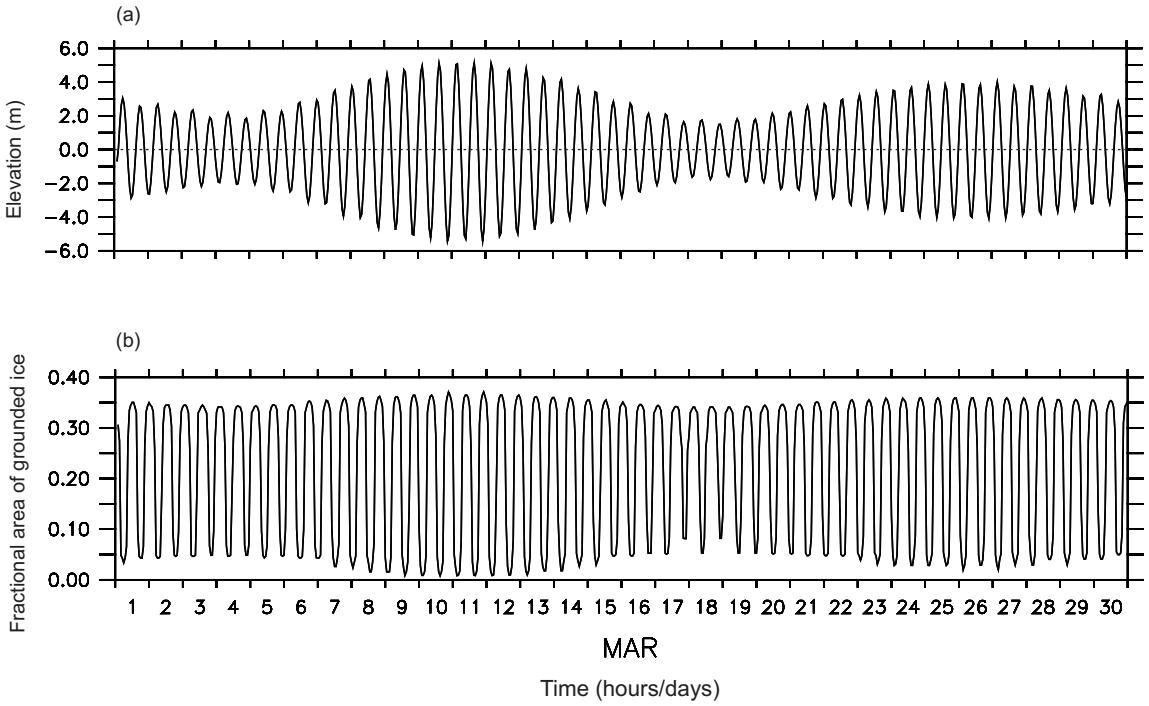

Figure 3.14: (a) Tidal elevation (m) and (b) fractional area of grounded ice at a coastal point in the Hudson Strait (X_2 in Fig. 3.6(a)) for March from Year 11 in the independent parameterisation model run forced with 1997 atmospheric data.

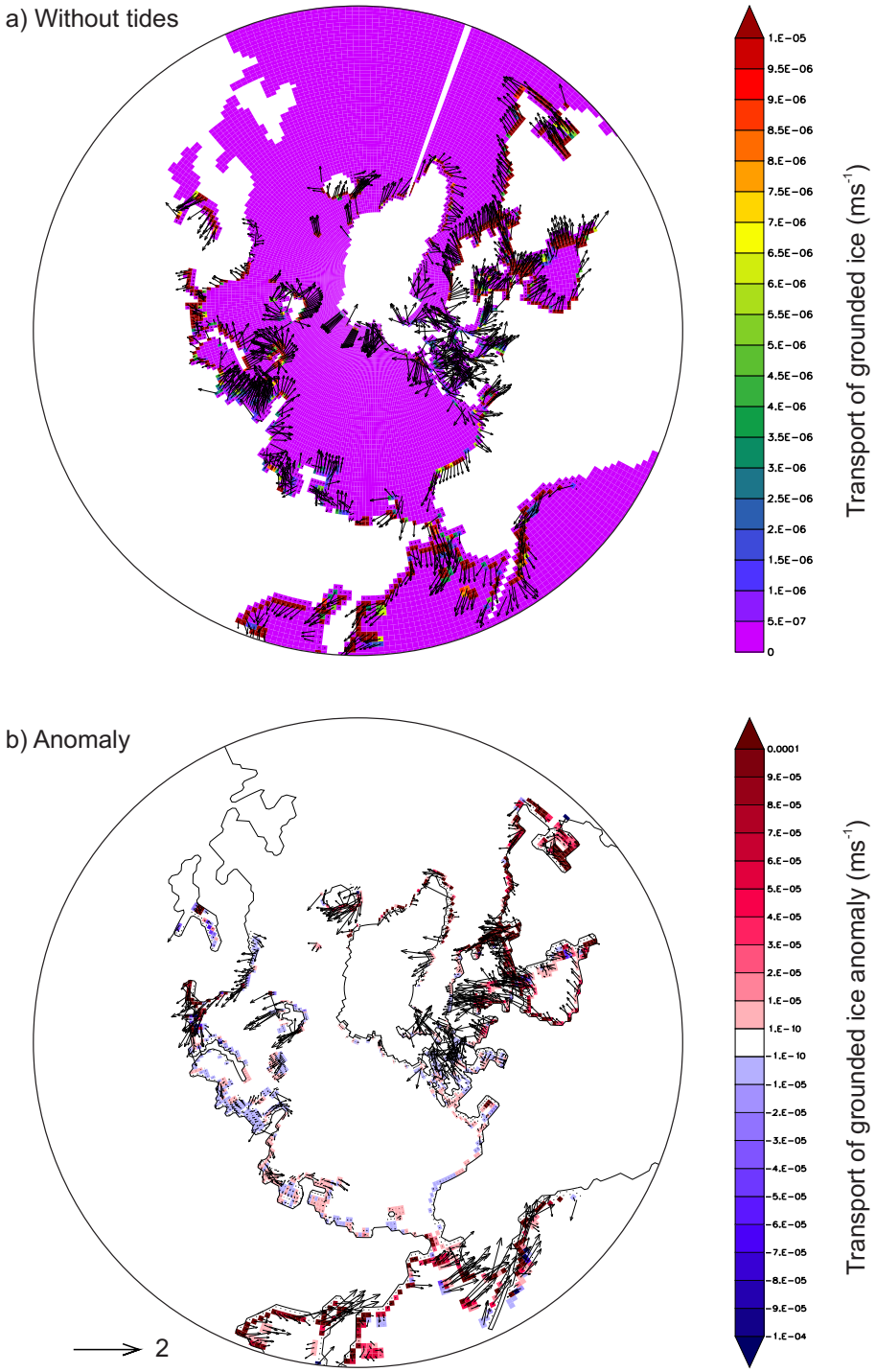

Figure 3.15: Arctic annual mean transport of grounded ice (ms^{-1}) and normalised unit vector for the independent parameterisation for a) simulation without tides and b) anomaly (tides - no tides). In the anomaly tidal induced changes less than 1×10^{-10} ms^{-1} are masked white.

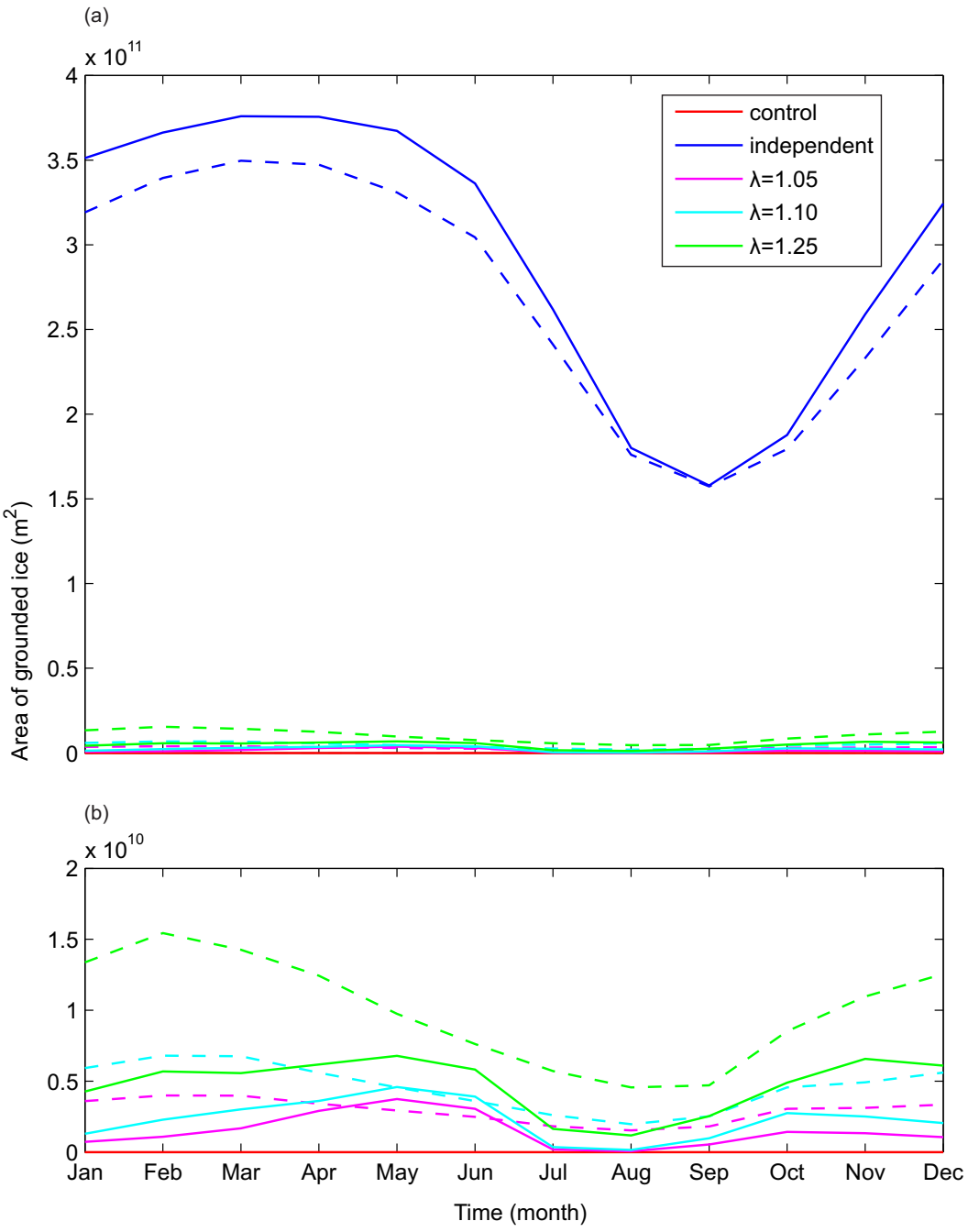

Figure 3.16: Monthly estimates of Arctic grounded ice area without tidal forcing (solid) and including tidal forcing (dashed) for model experiments run at 1 degree resolution for the control (red), independent grounding (blue), and restricted grounding schemes with a coupling parameter $\lambda = 1.25$ (green), 1.10 (cyan) and 1.05 (magenta) for (a) all simulations and (b) magnification of the control and restricted parameterisation.

Landfast ice area

The spatial and temporal coverage of landfast ice produced from 5 day averages for the control (no landfast ice parameterisation), independent, and restricted parameterisations with tides are shown in Figure 3.18. The associated anomalies (tides - no tides) are shown in Figure 3.19 and the comparative results without tides can be found in Chapter 2.

The monthly mean Arctic landfast ice area produced by the landfast ice parameterisations when tides were included reproduced the observed seasonal cycle, reaching a minimum coverage around September, and a maximum coverage around March. The magnitude and pattern of the landfast ice coverage compared well with NIC climatologies (Figure 3.17). In general, the independent landfast ice parameterisation produced the most landfast ice, with the area reducing with increased grounding restriction. This was comparable to the non tidal simulations (discussed in Chapter 2). All parameterisation schemes including tides failed to fully remove summer landfast ice, for the same reasons as the non tidal runs as detailed in Chapter 2.

The inclusion of tides resulted in a consistent reduction in landfast ice in all tested cases, except for the restricted parameterisation using $\lambda = 1.10, 1.25$ in October-December. This is in contrast to the effect of tides on grounded ice, where the occurrence of grounded ice increased under tidal forcing for the restricted parameterisation, but decreased under the independent parameterisation. The tides act to increase the horizontal and vertical mobility of sea ice, reducing its ability to remain stationary, and thus become landfast. A major contribution to the consistent reduction was the removal of a significant area of stationary ice in the CAA and HB region. This removal occurred as strong residual tidal currents initiated an outflow of ice from these regions into open areas, where the ice was not held stationary by restrictive geometry. The magnitude of the change in landfast ice area caused by tides was greatest in the winter months, as observed in the grounded ice, due to the residual summer landfast ice being erroneously thick and stable, and thus less susceptible to modification by the tides.

Landfast ice distribution

The spatial distribution of the landfast ice when tidal forcing was included was comparable to observations, and the recorded results without tides found in Chapter 2. However, the length of time the ice remained fast was altered. The impact of tides on the duration of landfast ice was generally regional, with some regions, such as the Northern Kara Sea and East Siberian Sea, undergoing increased landfast ice duration, and other regions, such as the CAA and Western Laptev Sea, undergoing decreased landfast ice duration (Figure 3.19). Tidal induced changes in sea surface height, tidal currents and residual currents will all act to decrease the stability of the landfast ice itself, as well as the grounded ridges which act to keep it in place. While increased production of thick grounded ridges will act to increase the occurrence of landfast ice.

The strongest anomalies were observed in the CAA, HB region and Baffin Bay, where landfast ice duration was altered by up to 80 days. Significant modifications were also observed along the north Russian Coast, namely in the Kara and Laptev Seas, and to a lesser extent the Sea of Okhotsk. Although the pattern of tidal impact was generally consistent across the tested scenarios those which included a grounding parameterisation, of any restriction, also underwent a significant increase in landfast ice duration in NE Foxe Basin which was not apparent in the control. This increase was due to a significant pile up of ice against the coast resulting from unrealistic residual currents as discussed previously.

Much of the observed anomaly pattern in landfast ice duration was comparable to the observed patterns in the ice volume anomalies (Figures 3.4 and 3.5) which primarily resulted from the strong residual currents. The changes in ice volume, and the residual currents which caused them, will initiate the same response in the landfast ice; that is a reduction in ice volume in a given region will subsequently lead to a reduction in landfast ice.

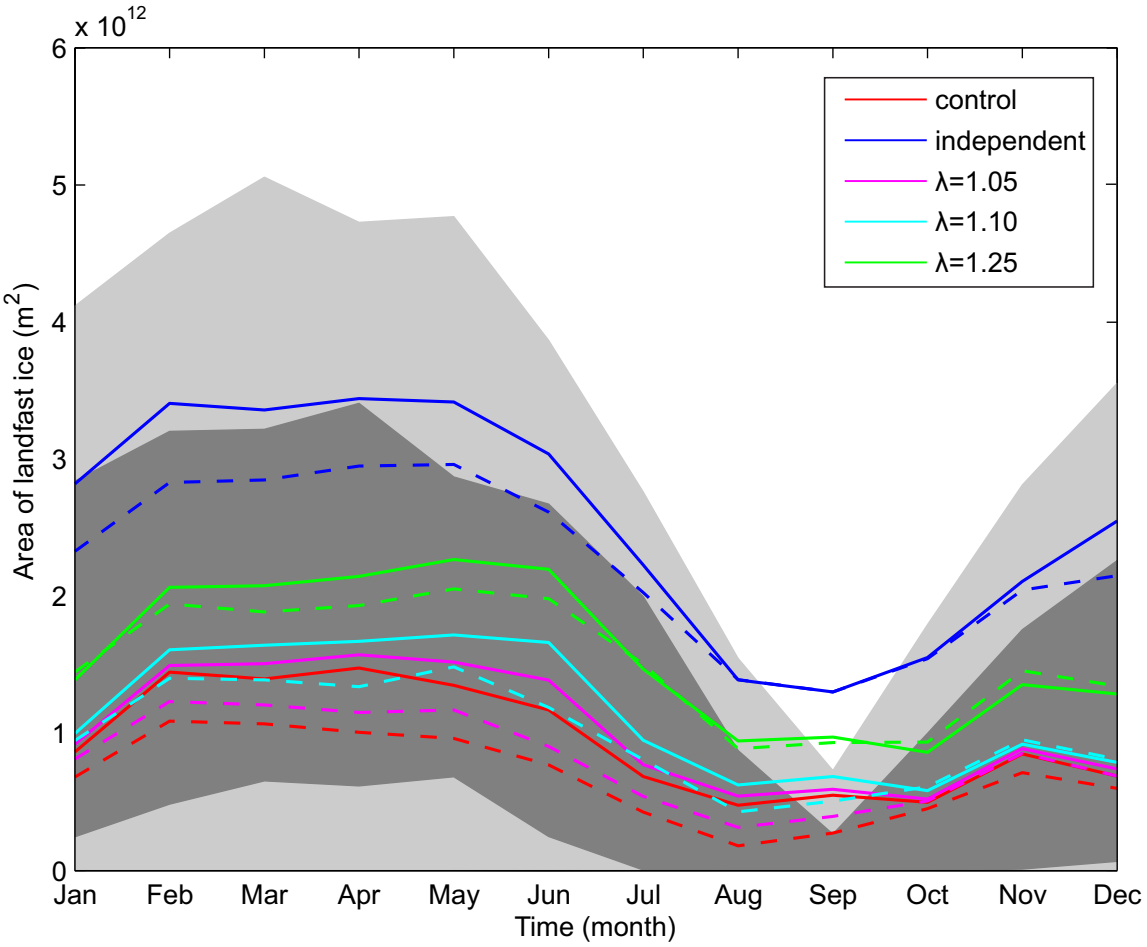

Figure 3.17: Monthly estimates of Arctic landfast ice area without tides (solid line) and with tides (dashed line) for model experiments run at 1 degree resolution for the control (red), independent grounding (blue), and restricted grounding schemes using a coupling parameter $\lambda = 1.25$ (green), 1.10 (cyan), and 1.05 (magenta). The light and dark grey shaded bands represent the range in landfast ice area estimated from NIC climatology over 1972-2007 and 1994-2005 respectively.

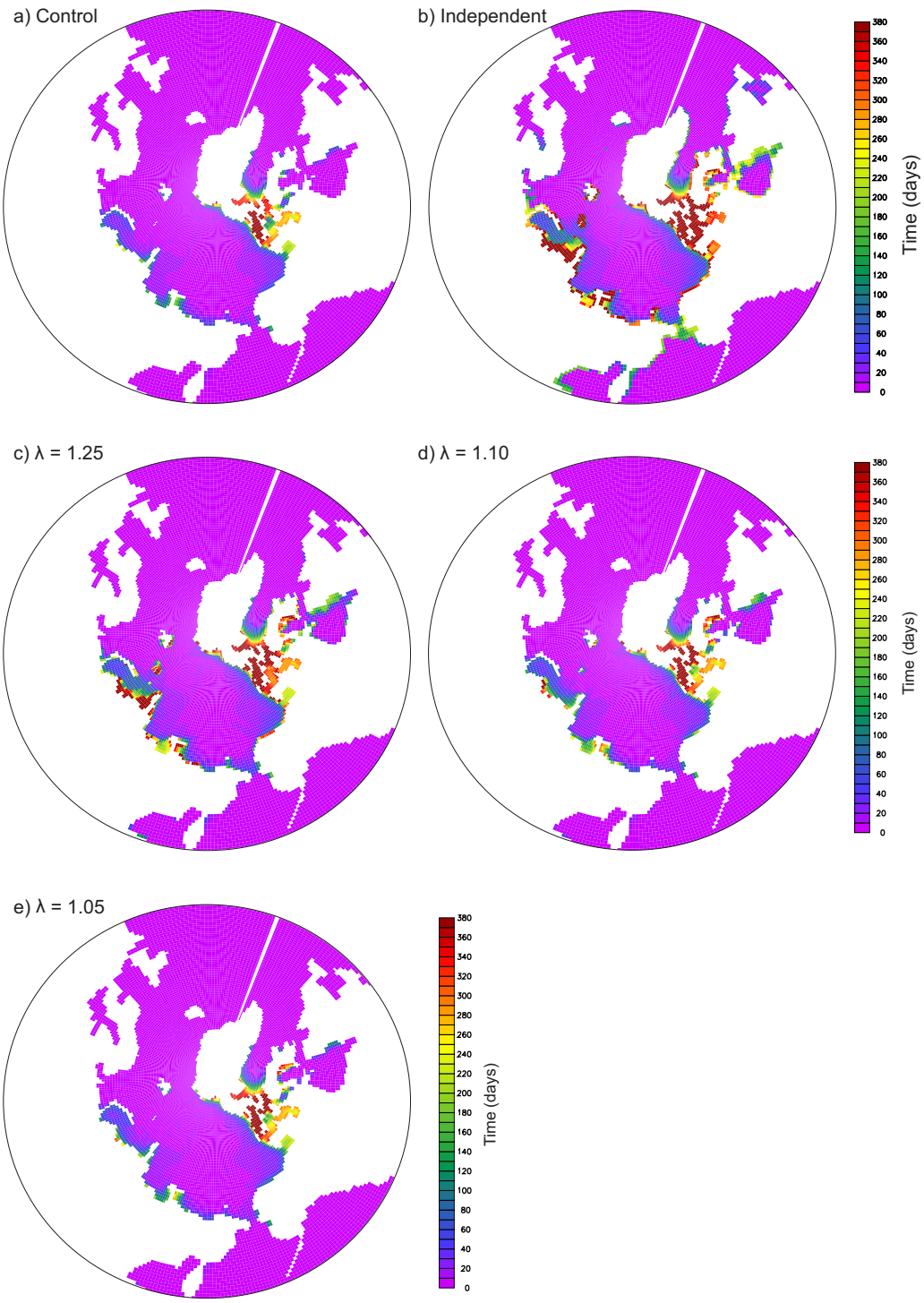

Figure 3.18: Arctic landfast ice duration from 5 day averages for model experiments run at 1 degree resolution including tidal forcing for the (a) control, (b) independent parameterisation, and restricted parameterisation using (c) $\lambda = 1.25$, (d) $\lambda = 1.10$, and (e) $\lambda = 1.05$.

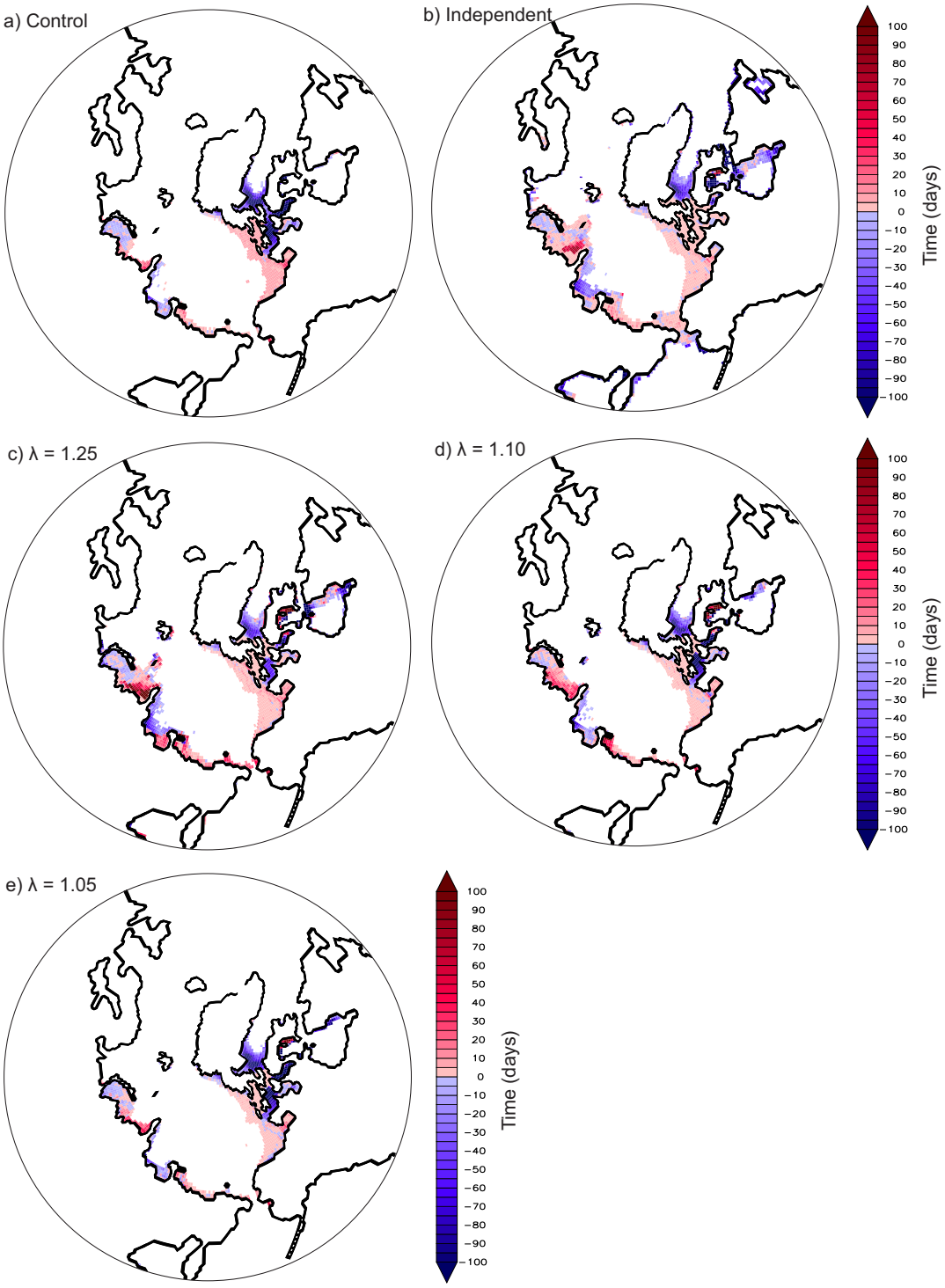

Figure 3.19: Arctic landfast ice duration anomaly (tides - no tides) from 5 day averages for model experiments run at 1 degree resolution for the (a) control, (b) independent parameterisation, and restricted parameterisation using (c) $\lambda = 1.25$, (d) $\lambda = 1.10$ and (e) $\lambda = 1.05$. Red = increase, blue = decrease, white = no change.

Table 3.1: Difference in total ice area per thickness category (tides - no tides)

Region	Arctic			Antarctic		
Thickness Cat.	Annual	Winter	Summer	Annual	Winter	Summer
1	6.363E+10	2.306E+11	2.374E+10	7.762E+10	8.276E+10	-2.144E+10
2	-2.965E+11	-4.329E+11	-1.553E+11	-1.125E+11	-3.251E+10	-2.208E+11
3	-1.754E+11	-1.813E+11	-1.036E+11	-3.072E+11	-3.181E+11	-2.902E+11
4	2.749E+10	5.377E+10	1.246E+10	-2.222E+10	-3.845E+10	1.654E+10
5	3.872E+10	6.517E+10	8.150E+09	1.640E+11	1.932E+11	1.287E+11
6	1.649E+10	2.235E+10	9.770E+09	5.904E+10	6.477E+10	5.238E+10
7	2.088E+10	2.178E+10	1.762E+10	6.639E+10	6.712E+10	6.813E+10
8	8.933E+09	1.039E+10	5.166E+09	5.043E+10	5.397E+10	4.594E+10
9	4.403E+09	5.042E+09	3.474E+09	1.508E+10	1.550E+10	1.467E+10
10	3.548E+09	4.412E+09	2.587E+09	6.536E+09	6.983E+09	5.951E+09
11	2.397E+09	3.101E+09	1.503E+09	7.822E+08	8.433E+08	7.271E+08
12	1.384E+09	1.637E+09	8.175E+08	1.111E+08	1.184E+08	9.521E+07
13	9.959E+08	9.329E+08	7.539E+08	1.133E+06	1.164E+06	1.026E+06
14	2.004E+09	1.781E+09	1.897E+09	6.463E+04	6.814E+04	5.217E+04
15	8.295E+09	6.707E+09	8.739E+09	1.828E+03	1.811E+03	1.590E+03

The difference in the total ice area (m^2) within each ice thickness category when tides are included for the Arctic and Antarctic. Winter is defined as (JFM) and summer as (JAS) for the Arctic, and the opposite for the Antarctic. The thickness bounds for the thickness categories are detailed in Table. 2.1.

3.5.2 Antarctic

Impact on ice distribution

Before the impact of tides on grounded and landfast ice are considered, we first study the effect of tides on the mean Antarctic winter (JAS) and summer (JFM) ice volumes. The influence of tides on the ice thickness distribution and the maximum and minimum ice extent are also considered. For reference, the majority of the Antarctic locations referred to throughout this section are identified in Figure 2.12.

Ice extent

The Antarctic winter maximum and summer minimum ice extent, with and without tides, for the control simulation (i.e. no landfast ice parameterisation) are shown in Figure 3.2 (b). The temporal occurrence of the maximum and minimum ice extents were not modified by the introduction of tides, consistently occurring in October and March respectively.

Spatially, the location of the maximum and minimum ice extent edges underwent little change with the introduction of tides. A slight northward shift of the minimum extent occurred from the Bellingshausen Sea westward to the eastern Ross Sea, with a minor southward retreat across the eastern Ross Sea and western Weddell Sea region. The maximum extent edge underwent a slight northward shift in the Bellingshausen and Amundsen Seas with a small southward retreat in the eastern Ross Sea.

Ice volume

The Antarctic winter (JAS) and summer (JFM) mean ice volume per unit area without tides, with tides, and the anomaly (tides - no tides) for the control simulation (i.e. no landfast ice parameterisation) are shown in Figures 3.20 and 3.21 respectively. When tides are not included, the pattern of winter ice volume per unit area shows two distinct areas of high ice volume per unit area ($> 2.0\,\mathrm{m}$) in the Weddell Sea and between the Bellingshausen and Ross Sea. The remainder of the Southern Ocean, which contained sea ice, was found to have an ice volume per unit area approximately

less than 1.0 m. These results compare well with observed and modelled Antarctic ice thickness (Worby et al., 2008; Kurtz and Markus, 2012).

In winter, the effect of tides was relatively small over much of the Southern Ocean, with the mean ice volume generally undergoing changes within $+/-10\%$ of the original (no tides). However, in the Ross and Weddell Seas the tides were observed to have a significant localised impact on ice volume. In the Ross Sea, a distinct dipole effect was observed, with the western Ross Sea experiencing a 100% reduction in ice volume and the eastern Ross Sea experiencing a similar magnitude increase. A comparable pattern, of similar magnitude, occurred in the Weddell Sea when tides were included. Both of these anomalies can be explained by the strong residual tidal currents (Figure 3.6(b)) which resulted in a westerly flow of ice in the Weddell and Ross Seas (Figure 3.22). As noted in the Arctic results, the 1 degree standalone CICE model forced with tidal velocities from TPXO7.2, and atmospheric forcing from NCAR, generated large localised residual currents. It should be noted that there is no ocean heat flux or circulation, so the Antarctic Circumpolar Current is not represented here.

In summer, thermodynamic melt reduced the areal coverage of sea ice, but a significant amount of perennial ice remained. The perennial ice was most abundant eastward between the Ross and Bellinghausen Seas, and in the Weddell Sea. This coverage compared well with observations, but CICE appeared under-represented the summer sea ice thickness directly adjacent to the East Antarctic coast (Worby et al., 2008; Kurtz and Markus, 2012). The effect of tides on the summer ice volume distribution was comparable to that observed in winter, with a dipole effect observed in the Ross and Weddell Seas.

Throughout the year, around the Antarctic coast, the introduction of tides led to subtle changes over much of the region, with larger localised modifications in ice volume in the Ross and Weddell Seas, resulting from modification to ice transport and changes to the rate of ice production through changing lead fraction. These changes led to a small consistent net increase in ice volume in each month up to a maximum of 11.5 % as shown in Figure 3.8(b).

Ice thickness distribution

The impact of tides on the Antarctic annual, winter, and summer mean ice thickness distribution is detailed in Table 3.1 for the control simulation (i.e. no landfast ice parameterisation). The annual mean area of ice within each thickness category, with and without tides, for all simulations is shown in Figure 3.23. A consistent pattern is observed across the winter, summer, and annual means for the simulations employing no landfast ice parameterisation (control), an independent and restricted landfast ice parameterisation.

In all tested cases there was a consistent redistribution of ice from thinner to thicker ice categories due to dynamical deformation (such as ridging and rafting) of the thinner ice when tides were included. This process was most active within the first 5 thickness categories (ice with a thickness up to 5 m), as it is increasingly more difficult to deform thicker ice.

As CICE can not mechanically redistribute ice into thinner categories, any increase in the thinnest category observed in winter is due to an increase in ice production (as there will be no thermodynamic melt). This increase in thin ice occurs as tides act to increase the lead fraction (area of open water) in the sea ice cover. Ice is then able to form in these open water areas due to thermodynamic cooling from the cold overlying atmosphere. In general, over the Antarctic, tides were found to increase the lead area (Figure 3.24), although localised differences were observed. The lead fraction over much of the near coastal Southern Ocean was not significantly modified. However, in the Eastern Ross and Weddell Seas the lead area was observed to increase by approximately 20%. The locations which underwent the strongest changes, the Ross Sea and Weddell Sea, were comparable to those locations influenced by the strongest tides and residual currents (Figure 3.6(b)). Increased lead area will result in increased ice production in winter, and increased melt in summer, and therefore an amplification of the seasonal cycle of ice production. In general, the Antarctic tides were found to increase ice production by 0.37 cm day^{-1} annually (Figure 3.25). The patterns of the changes in ice production compared well with the tidal induced changes to the lead area.

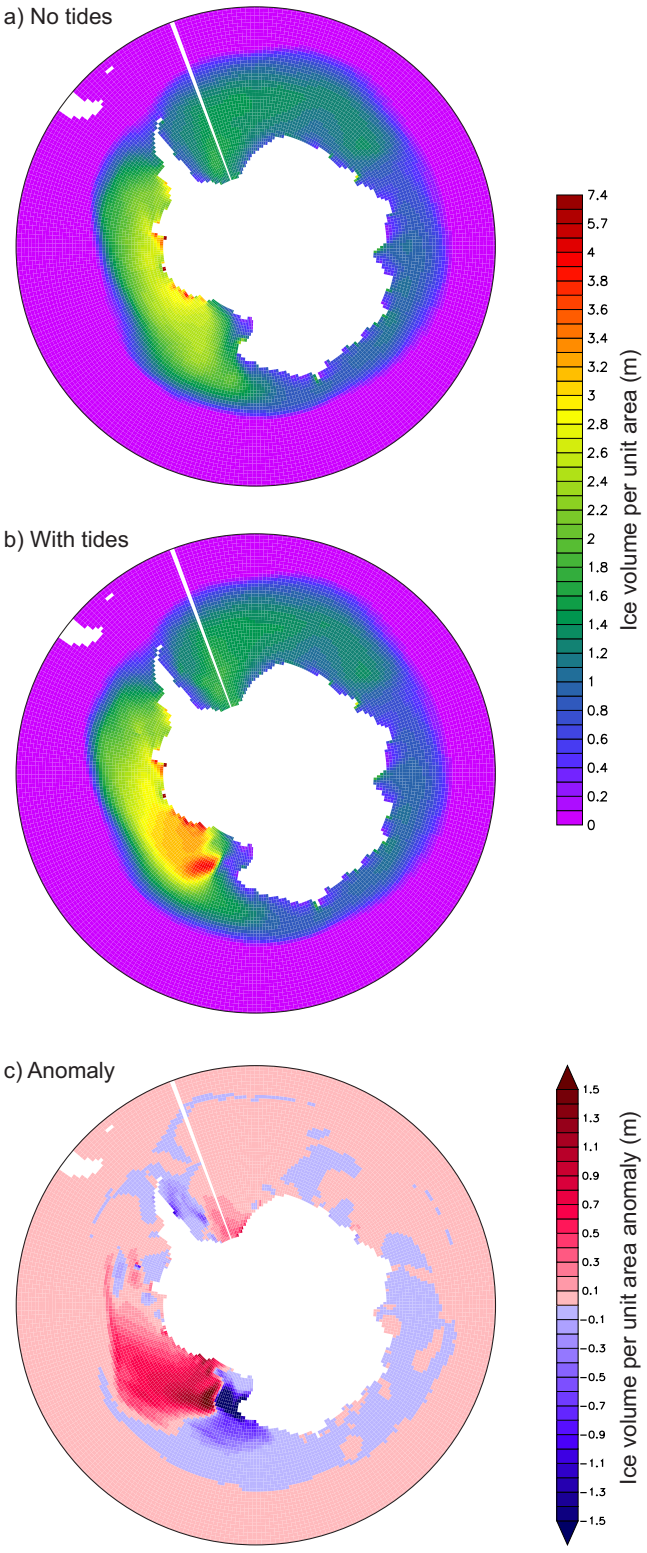

Figure 3.20: Antarctic winter (JAS) ice volume per unit area (m) (a) without tides, (b) with tides, and (c) anomaly (tides - no tides) for the control simulation (i.e. no landfast ice parameterisation).

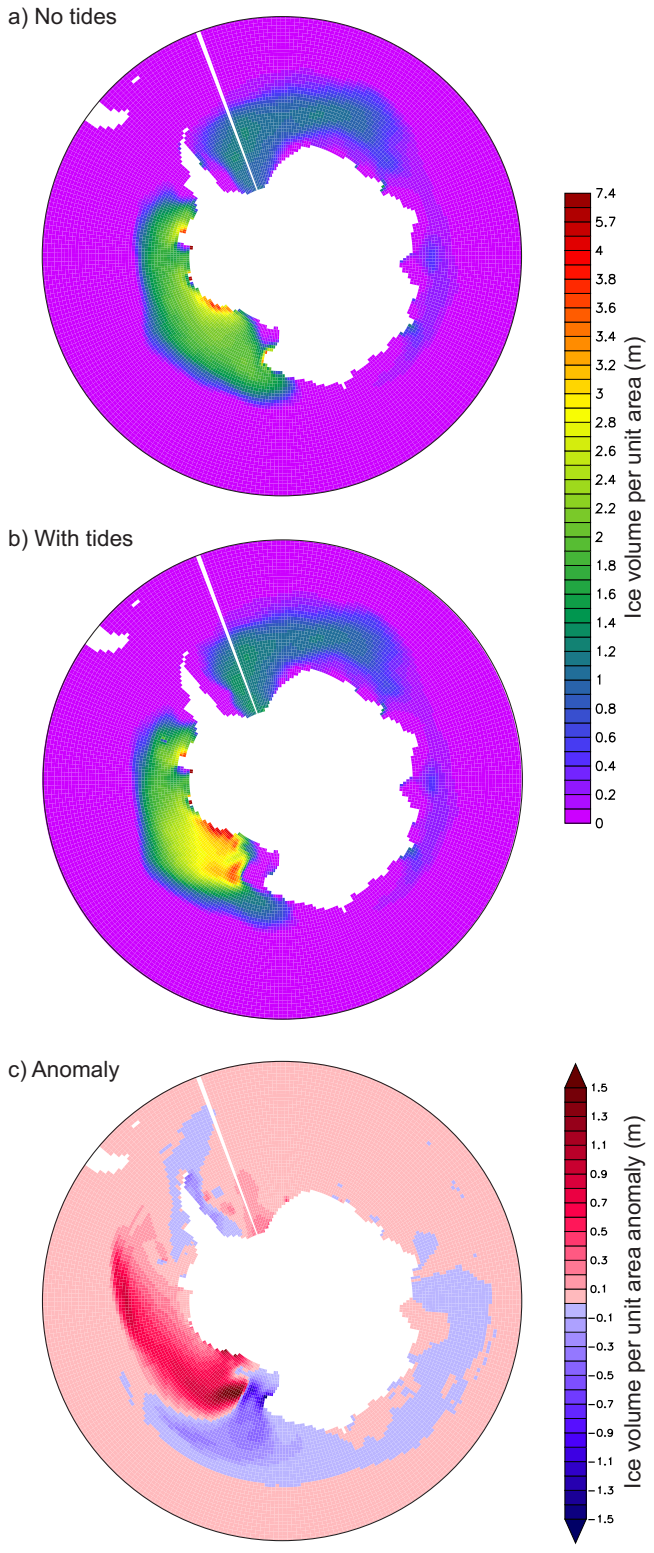

Figure 3.21: Antarctic summer (JFM) ice volume per unit area (m) (a) without tides, (b) with tides, and (c) anomaly (tides - no tides) for the control simulation (i.e. no landfast ice parameterisation).

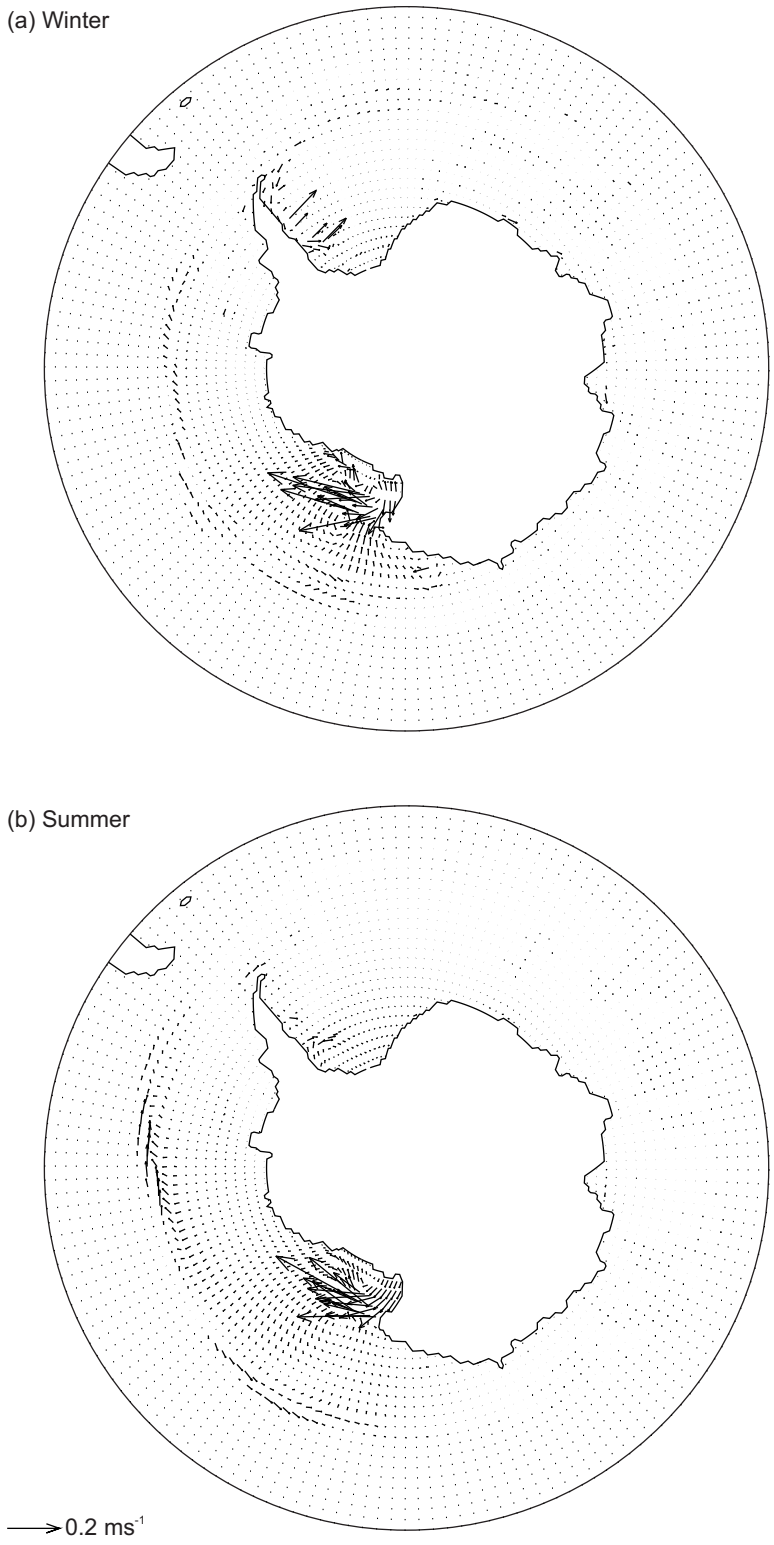

Figure 3.22: Antarctic annual mean ice velocity anomaly (tides - no tides) for (a) the winter (JAS), and (b) the summer (JFM) for the control simulation (i.e. no landfast ice parameterisation).

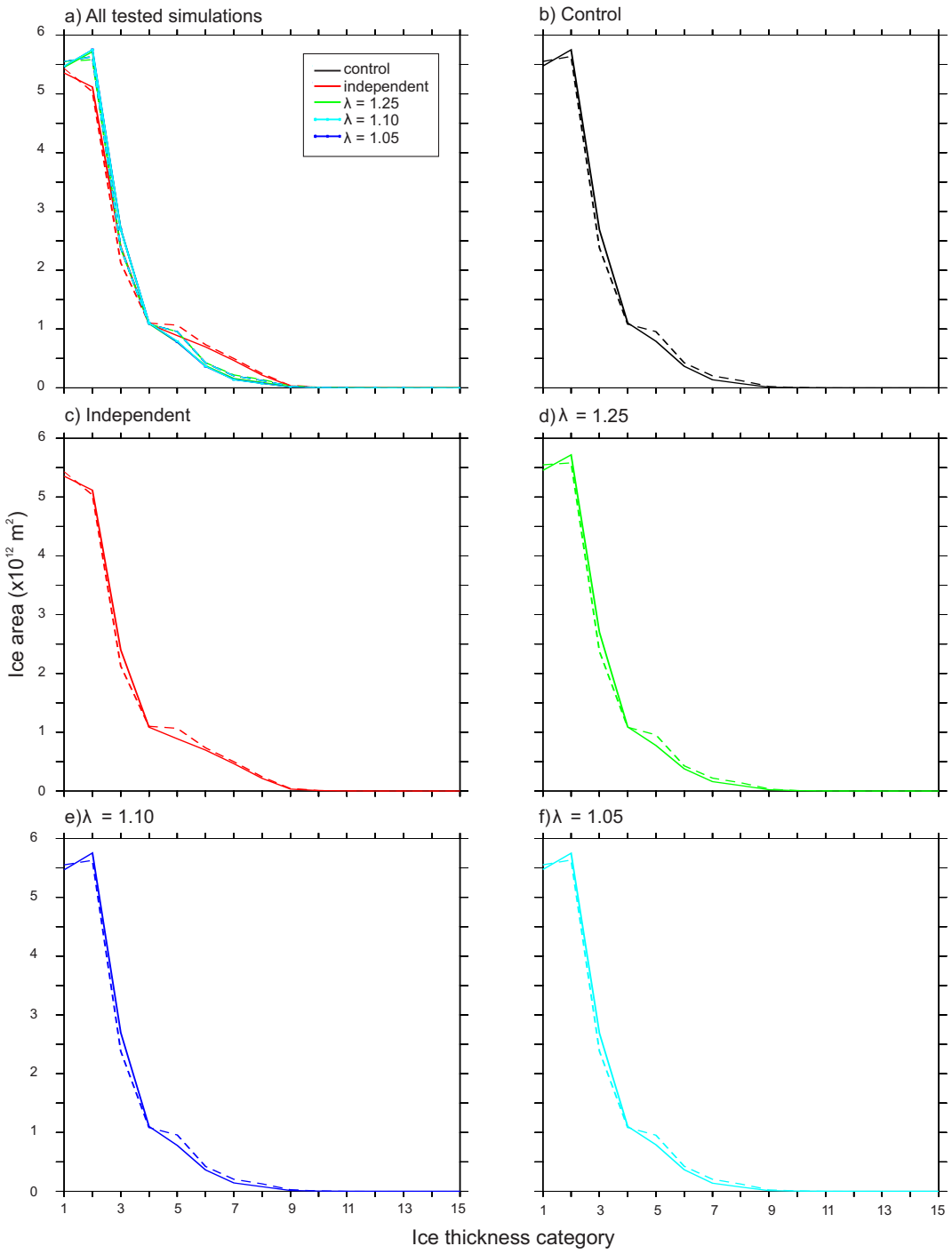

Figure 3.23: Antarctic mean annual ice thickness distribution per thickness category for (a) all tested scenarios, (b) the control, (c) the independent parameterisation and the restricted parameterisations for (d) $\lambda = 1.25$, (e) $\lambda = 1.10$, and (f) $\lambda = 1.05$ without tides (solid line) and with tides (dashed line). Details of thickness category limits can be found in Table 3.1

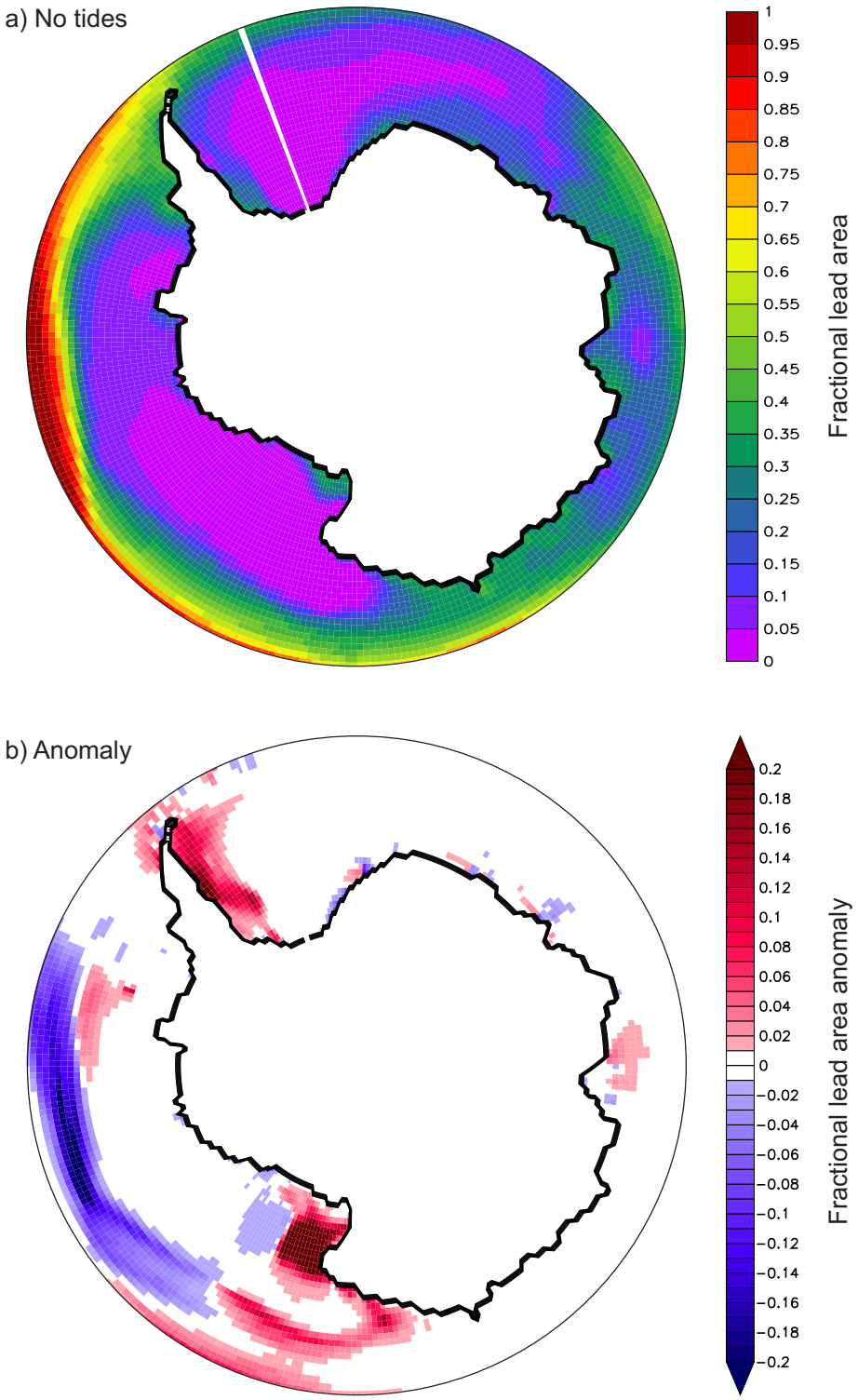

Figure 3.24: Annual mean Antarctic fractional lead area $(0-1)$ for (a) without tides and (b) the anomaly (tides-no tides) for the control simulation (i.e. no landfast ice parameterisation). Any anomaly less than 0.01 is masked to white to remove noise.

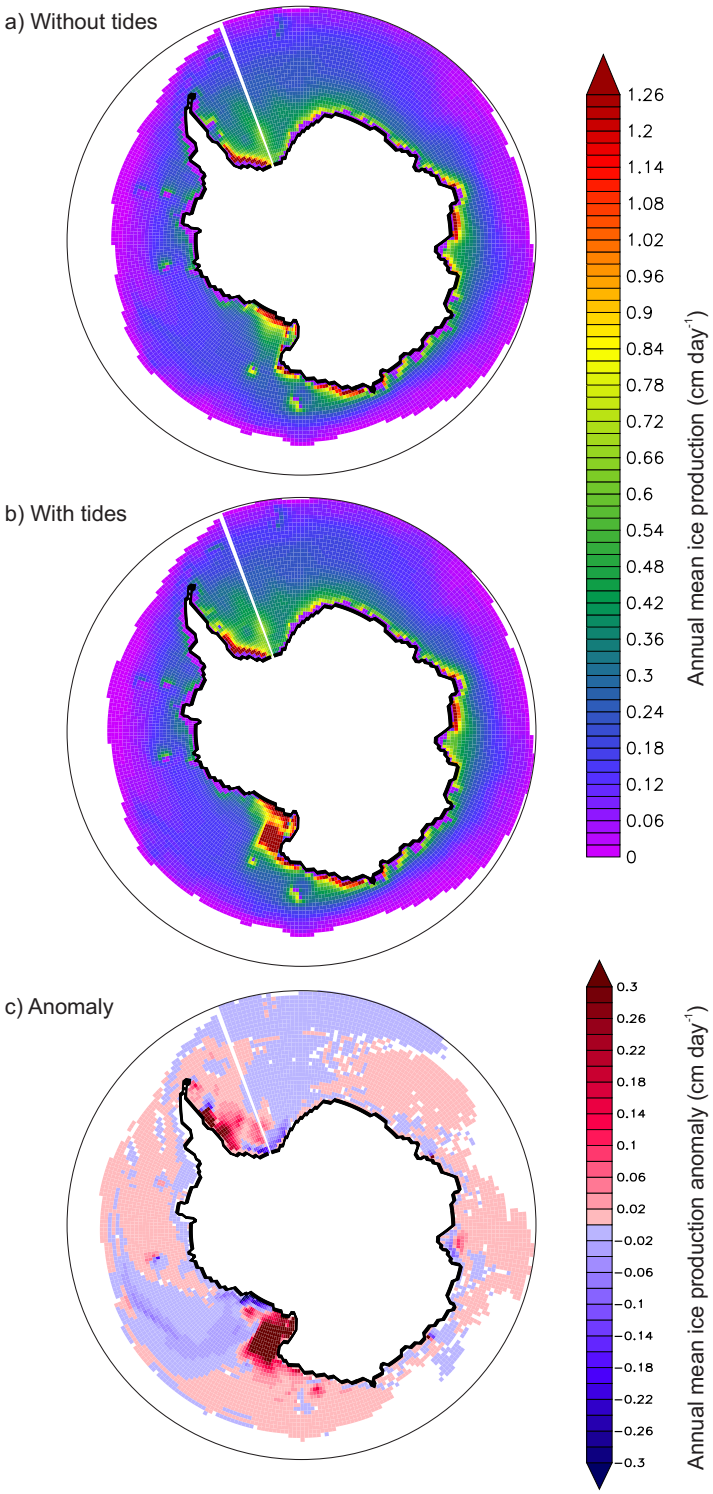

Figure 3.25: Antarctic annual mean ice production (cm day^{-1}) a) without tides, b) with tide and c) anomaly (tides - no tides) for the independent landfast ice parameterisation. Ice production smaller than 0.001 mm day^{-1} have been masked to white.

Grounded ice

As with the Arctic results, for simplicity and consistency only results from the independent parameterisation are considered in the following sections looking at the impact of tides on grounded ice.

Tidal cycle

A time series of sea surface height for the $1^{st} - 3^{3rd}$ September 1997 in the Ross Sea and Bellingshausen Sea for the simulation using the independent parameterisation, are shown in Figures 3.26 and 3.27 respectively. The location of these test areas are shown by the markers X_1 and X_2 in Figure 3.6(b). The chosen location in the Ross Sea is dominated by a regular diurnal tide, resulting in a once daily peak and trough in sea surface height, while the Bellingshausen Sea location is dominated by a mixed tide. In the mixed tide, the diurnal and semi-diurnal oscillations are both important contributions, and the tide is characterized by a large asymmetry in the high and low sea surface heights. The area of grounded ice was observed to fluctuate in line with these oscillations in sea surface height as the ridges were set into vertical motion. The range in the area of grounded ice in these Antarctic test locations was generally smaller than those observed in the Arctic due to comparatively smaller tidal ranges.

Due to the differences in the type of tide dominating each area, the ridges are aground or afloat for differing periods of time over the tidal cycle. In the Ross Sea, the period of minimum ice grounding (i.e. when the ridges were uncoupled from the seabed due to an increase in sea surface height) occurred for approximately 5 hours, while in the Bellingshausen Sea it occurred for as little as 1 hour. Subsequently, the ridges in the Ross Sea were more likely to be horizontally redistributed greater distances by tidal and residual currents than those in the Bellingshausen Sea.

Spring-Neap cycle

Over the $1^{st} - 30^{th}$ September the range in tidally induced sea surface elevation in the Bellingshausen Sea obtained 2 maxima (spring) and 2 minima (neap) (Figure 3.28).

A clear response to this spring-neap cycle was identified in the grounded ice. The largest range in grounded ice area was obtained during the spring tide and the smallest range during the neap tide. As observed in the Arctic, the change in the area of grounded ice was relatively small between the spring and neap tides when compared to the range in sea level.

Horizontal transport of grounded ice

If a ridge is uncoupled from the seabed through tidally induced changes in sea surface height, it has the potential to be redistributed by tidal currents, residual tidal currents, other oceanic currents (not included in this model) as well as atmospheric forcing. If a once grounded ridge is transported into an area which has a different ocean depth, or significantly different tidal range, to its starting location then that ridge may or may not reground at low tide. Whether the ridge will reground depends on the ratio of the new ocean depth to the ridge draft, accounting for the new tidal range.

Applying the method described in Section 3.5.1, the transport of grounded ice due to dynamical processes only is illustrated by considering $A_g\vec{u}$ (Figure 3.29). Around much of the coast of Antarctica the grounded ice is being transported on order of $1 \times 10^{-5} - 1 \times 10^{-6}$ ms^{-1} by winds alone (i.e no tidal forcing) (Figure 3.29(a)). This is much slower than transport of the freely moving pack ice, as the frictional stress between the ice bottom of the grounded ice and the seabed will act to slow any ice motion. When tides are introduced, the transport of the grounded ice is updated as shown in Figure 3.29(b). The impact of tides appeared relatively localised, with no consistent hemispheric trend. The strongest changes occurred in the same regions dominated by strong residual currents (Figure 3.6(a)).

Total area of grounded ice

Monthly estimates of the area of grounded ice, produced with and without the inclusion of tides, is shown in Figure 3.30. The independent parameterisation produced significantly more grounded ice than the restricted paramaterisations as it did not

prevent the grounding of erroneously thick ice on shallow bathymetry. The total area of grounded ice decreased with increasing level of restriction between the maximum allowed thickness of the grounded ice (i.e. reduction in λ). For simulations which included tides, over the year the independent parameterisation produced between $1761 - 13289\,\%$ more grounded ice than the restricted parameterisation which used a coupling parameter $\lambda = 1.25$. This is comparable to the results observed in the Arctic.

The impact of tides on the production of grounded ice is comparable to that observed in the Arctic; increasing when a restricted parameterisation was used, while decreasing when the independent parameterisation was used. This is for the same reasons as stated in Section 3.5.1. The magnitude of the change in grounded ice produced when tides were included was greater under the independent parametrisation compared to the restricted parameterisation. This is due to the independent parameterisation producing much more grounded ice than the restricted, and therefore has a much larger amount that can be removed by tidal action.

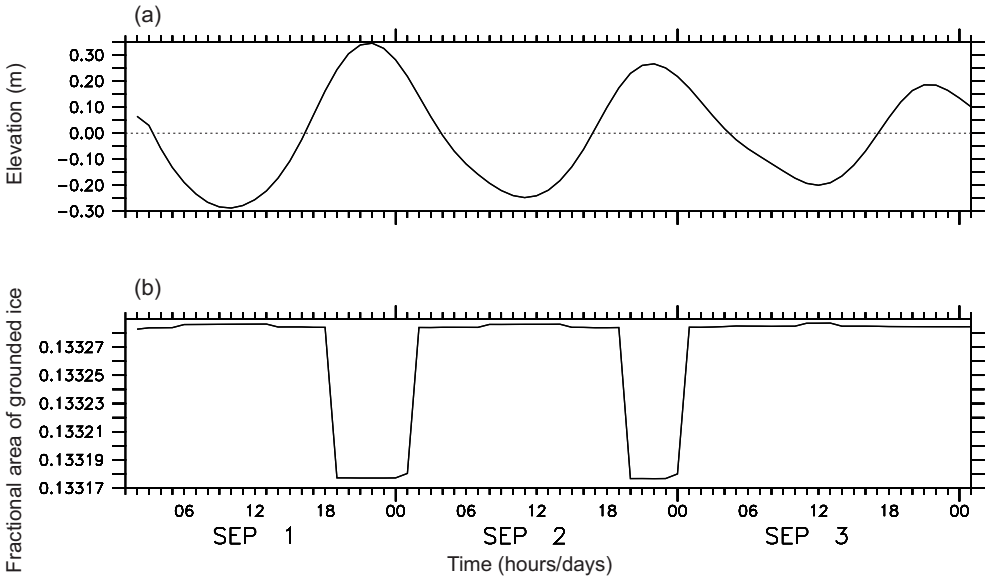

Figure 3.26: (a) Tidal elevation (m) and (b) fractional area of grounded ice at a coastal point in the Ross Sea (X_1 in Figure 3.6(b)) for the 1st-3rd September from Year 11 in the independent parameterisation model run forced with 1997 atmospheric data.

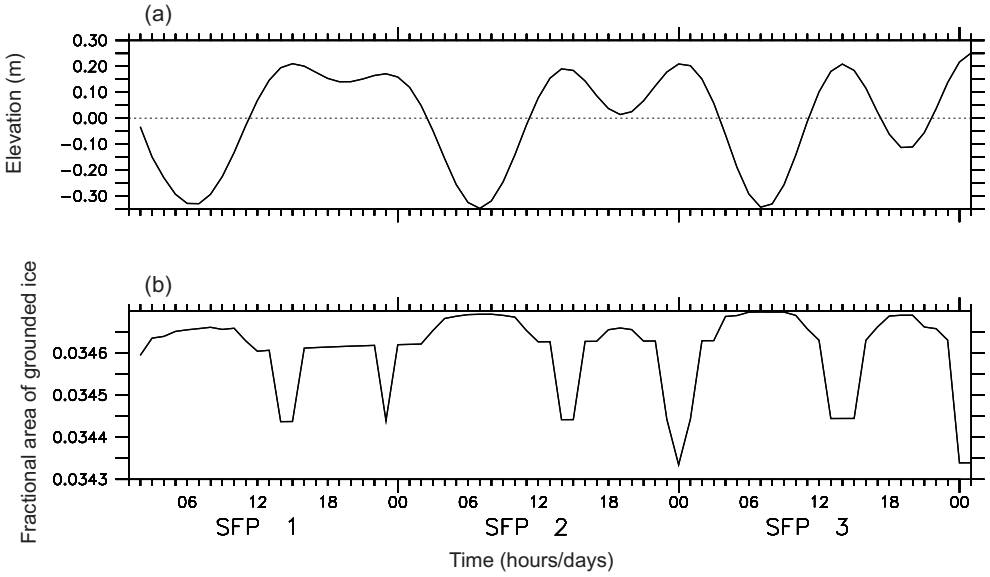

Figure 3.27: (a) Tidal elevation (m) and (b) fractional area of grounded ice at a coastal point in the Bellingshausen Sea (X_2 in Figure 3.6(b)) for the 1st-3rd September from Year 11 in the independent parameterisation model run forced with 1997 atmospheric data.

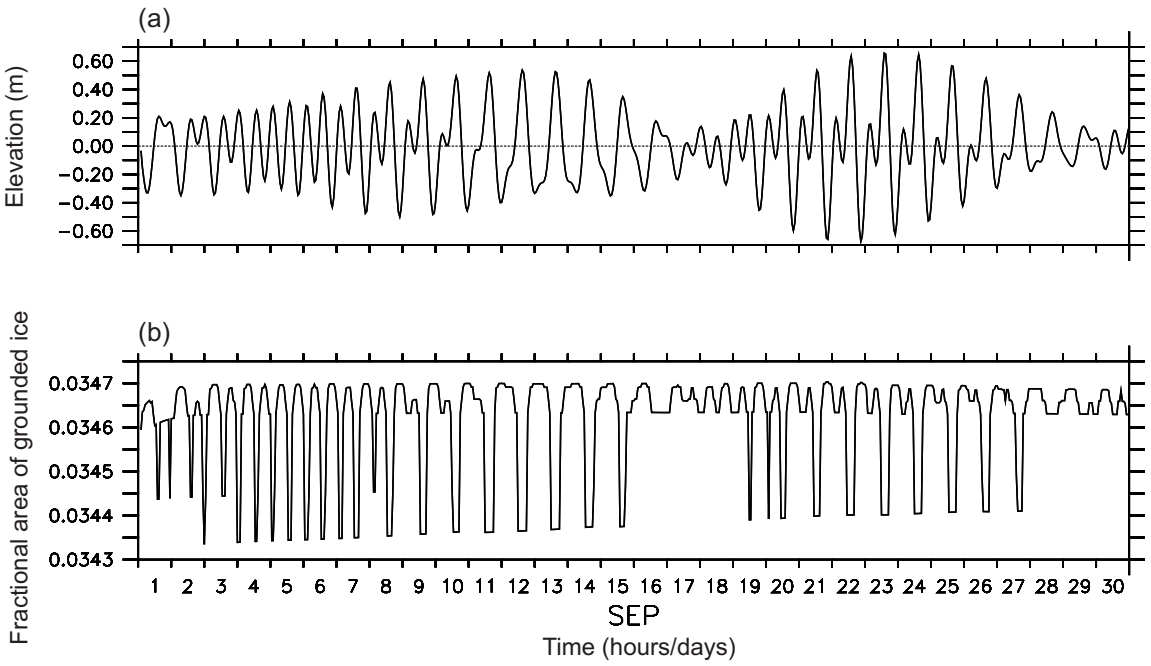

Figure 3.28: (a) Tidal elevation (m) and (b) fractional area of grounded ice at a coastal point in the Bellingshausen Sea (X_2 in Figure 3.6(b)) for September from Year 11 in the independent parameterisation model run forced with 1997 atmospheric data.

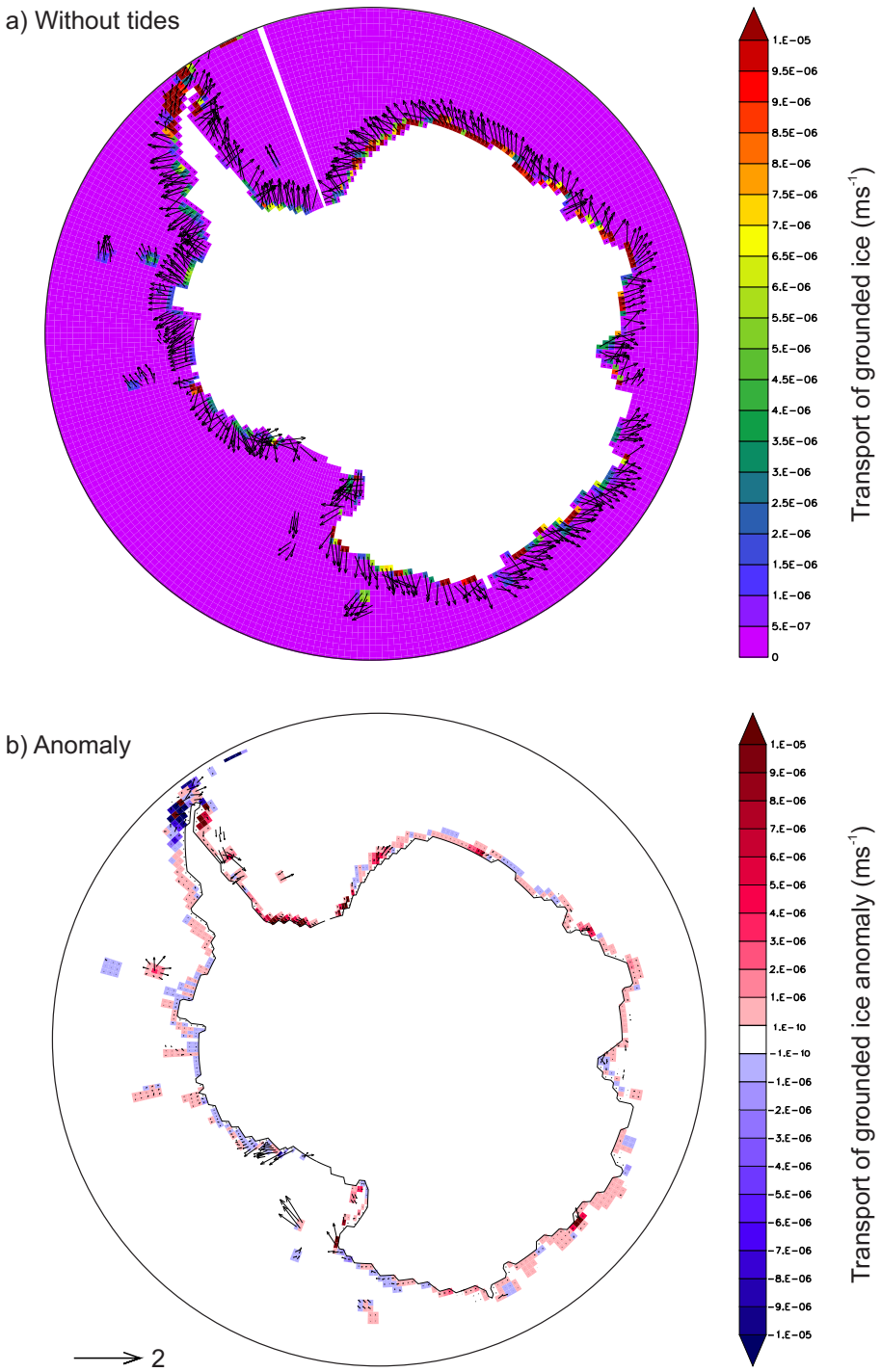

Figure 3.29: Antarctic annual mean transport of grounded ice (ms^{-1}) and normalised unit vector for the independent parameterisation for a) simulation without tides and b) anomaly (tides - no tides). In the anomaly changes less than 1×10^{-10} ms^{-1} are masked white.

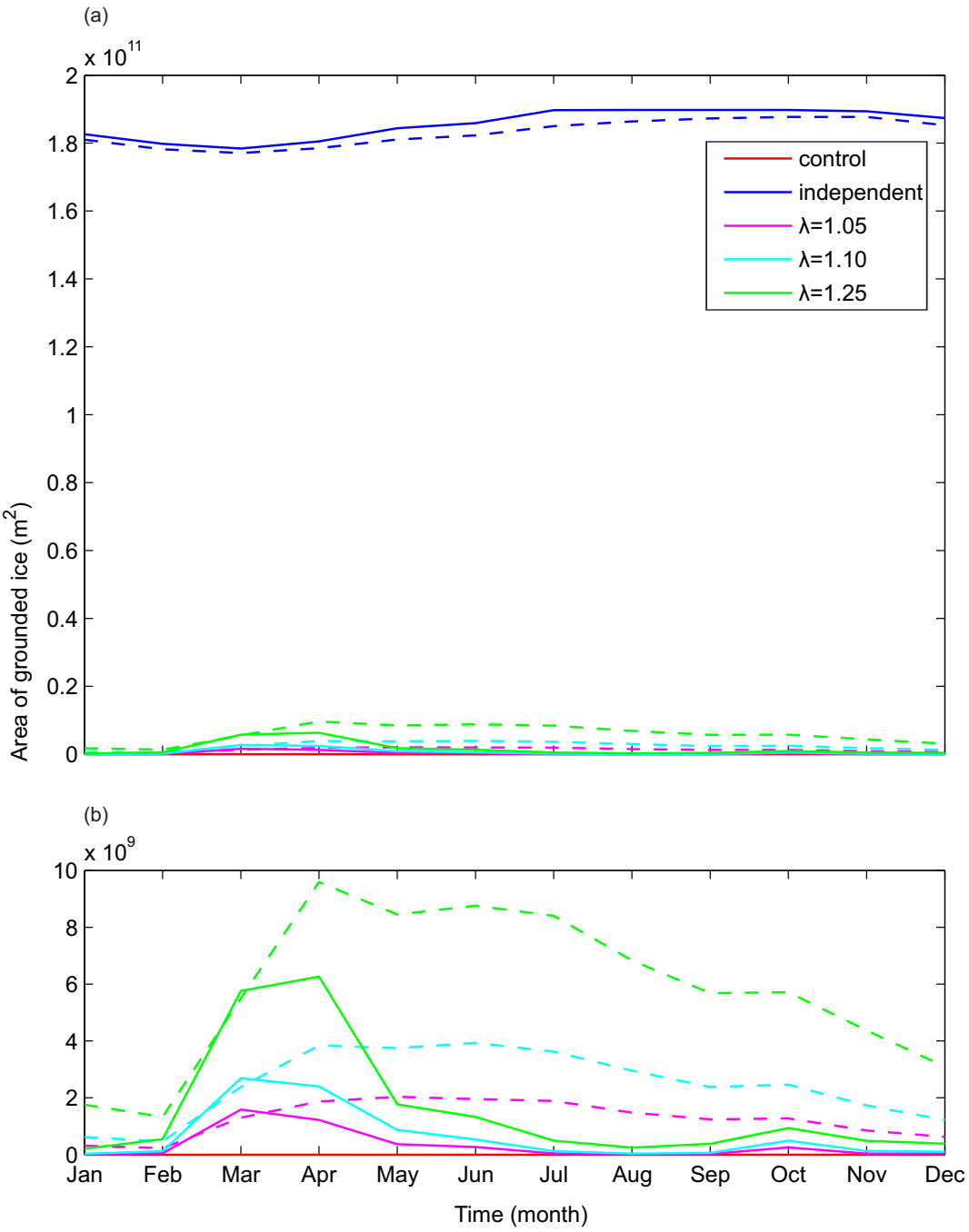

Figure 3.30: Monthly estimates of Antarctic grounded ice area without tides (solid) and with tides (dashed) for model experiments run at 1 degree resolution for the control (red), independent grounding (blue), and restricted grounding schemes with a coupling parameter $\lambda = 1.25$ (green), 1.10 (cyan), and 1.05 (magenta) for (a) all simulations and (b) magnification of the control and restricted parameterisation.

Landfast ice area

The spatial and temporal coverage of landfast ice produced from 5 day averages for the control (i.e. no landfast ice parameterisation), independent, and restricted landfast ice parameterisations with tides are shown in Figure 3.32. The associated anomalies (tides - no tides) are shown in Figure 3.33 and the comparative results without tides can be found in Section 2.7.2.

The monthly mean area of landfast ice produced by the tested landfast ice parameterisations when tides were included produced similar seasonal cycles to those simulations which did not include tides, Figure 3.31. The same issues previously discussed in Chapter 2 were apparent. A lack of seasonal variation in the landfast ice coverage was still evident under tidal forcing, indicating that the majority of the landfast ice produced by the landfast ice parameterisations was multiyear (and therefore remained throughout the summer melt season). In general, the independent landfast ice parameterisation produced the most landfast ice as widespread stable grounded ice anchored the landfast ice cover. The area of landfast ice reduced with increasing restriction on the maximum thickness of ice which is able to ground in a given depth (decreasing λ), as the occurrence of the stabilising grounded ice produced is reduced.

The observed impact of tides on the landfast ice was comparable to the observed impact of tides on the grounded ice (Figure 3.30). The area of landfast ice was found to increase with the introduction of tides for the restricted parameterisation, and decrease under the influence of tides when the independent parameterisations was employed. This is because the grounded ice stabilises the landfast ice sheet, allowing it to remain motionless and attached to the coast. An increase (or decrease) in the area of grounded ice will therefore lead to a comparable increase (or decrease) in the area of landfast ice.

Landfast ice distribution

The spatial distribution of the landfast ice under tidal forcing compared well with observations, and the results of simulations without tides (detailed in Chapter 2).

Very little landfast ice was produced in the control simulation (i.e. no parameterisation). The independent parameterisation produced the most landfast ice, with the restricted parameterisations producing gradually less landfast ice as the maximum allowed thickness of the grounded ice is made increasingly small (decreasing λ).

Tides are observed to modify the duration that landfast ice was present (Figure 3.32). In the control simulation (i.e. no landfast ice parameterisation) the impact of tides was minimal. When a landfast ice parameterisation was included, the landfast ice was found to undergo a reduction in duration in the Weddell Sea and western Ross Sea, with increased duration in the Bellingshausen, Amundsen, and eastern Ross Seas and near the Amery Ice Shelf. The magnitude of these changes varied depending on the level of restriction placed on the landfast ice parameterisation. There does not appear to be an observable link between magnitude of applied grounding restriction and the landfast ice duration anomaly.

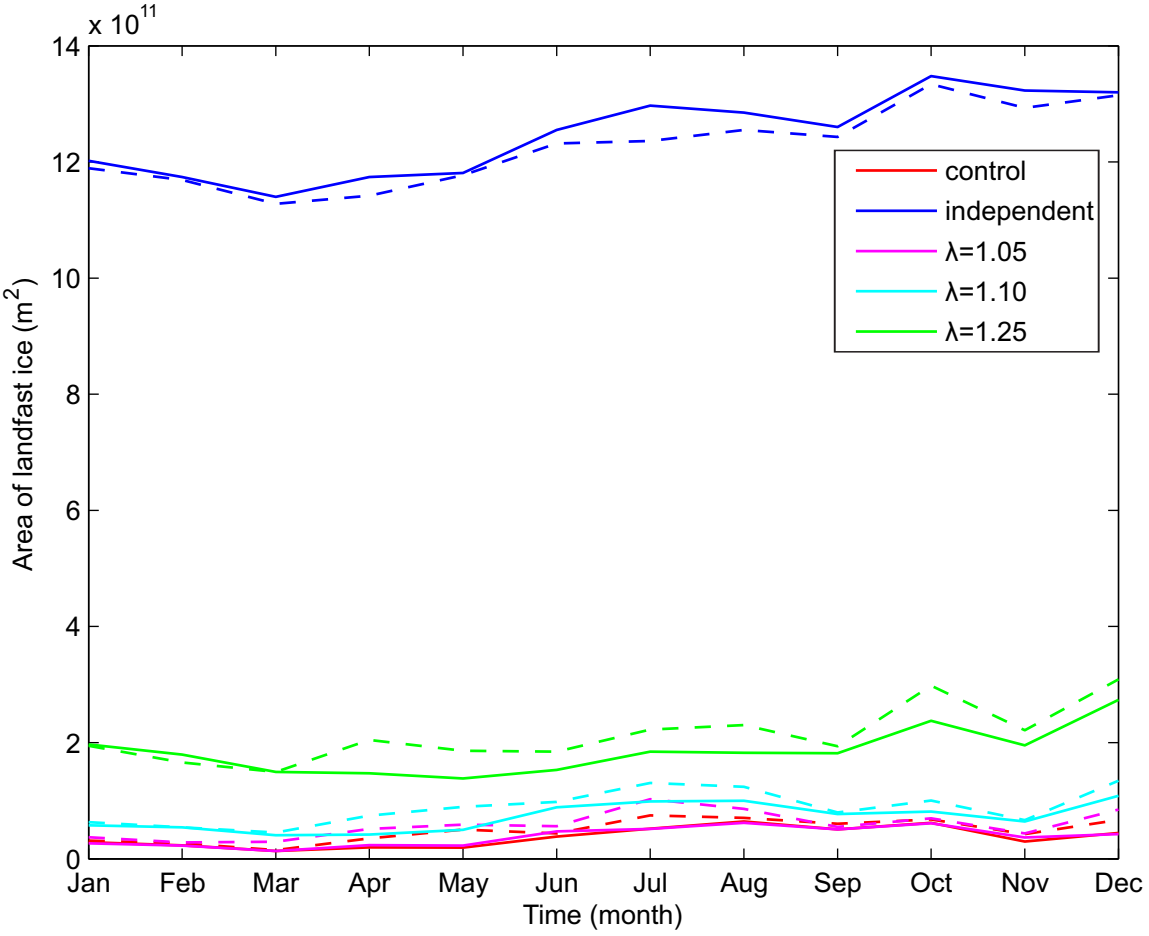

Figure 3.31: Monthly estimates of Antarctic landfast ice area without tides (solid line) and with tides (dashed line) for model experiments run at 1 degree resolution for the control (red), independent grounding (blue), and restricted grounding schemes using a coupling parameter $\lambda = 1.25$ (green), 1.10 (cyan), and 1.05 (magenta).

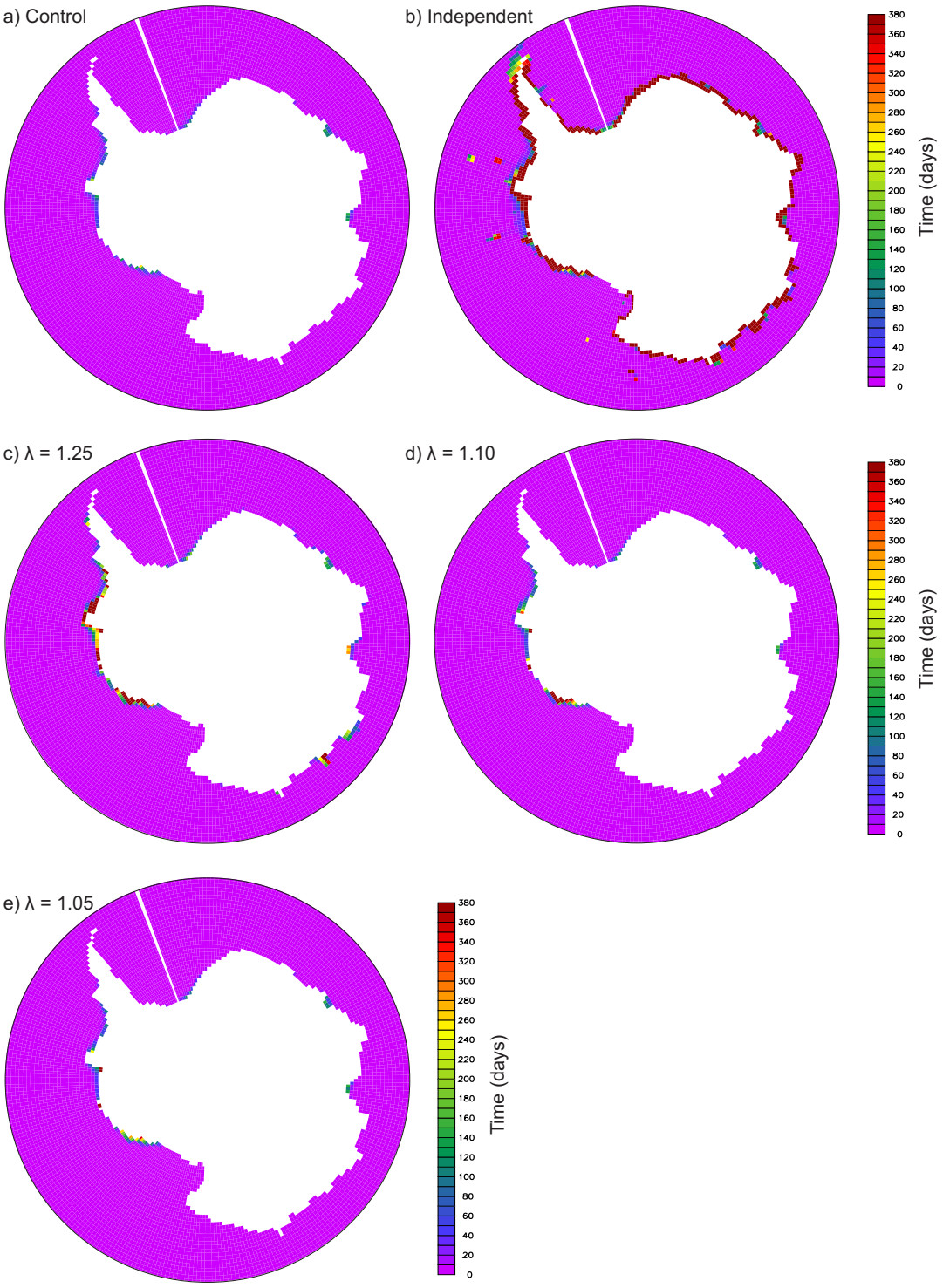

Figure 3.32: Antarctic landfast ice duration from 5 day averages for model simulations run at 1 degree resolution including tidal forcing for the (a) control, (b) independent parameterisation, and restricted parameterisation using (c) $\lambda = 1.25$, (d) $\lambda = 1.10$ and (e) $\lambda = 1.05$.

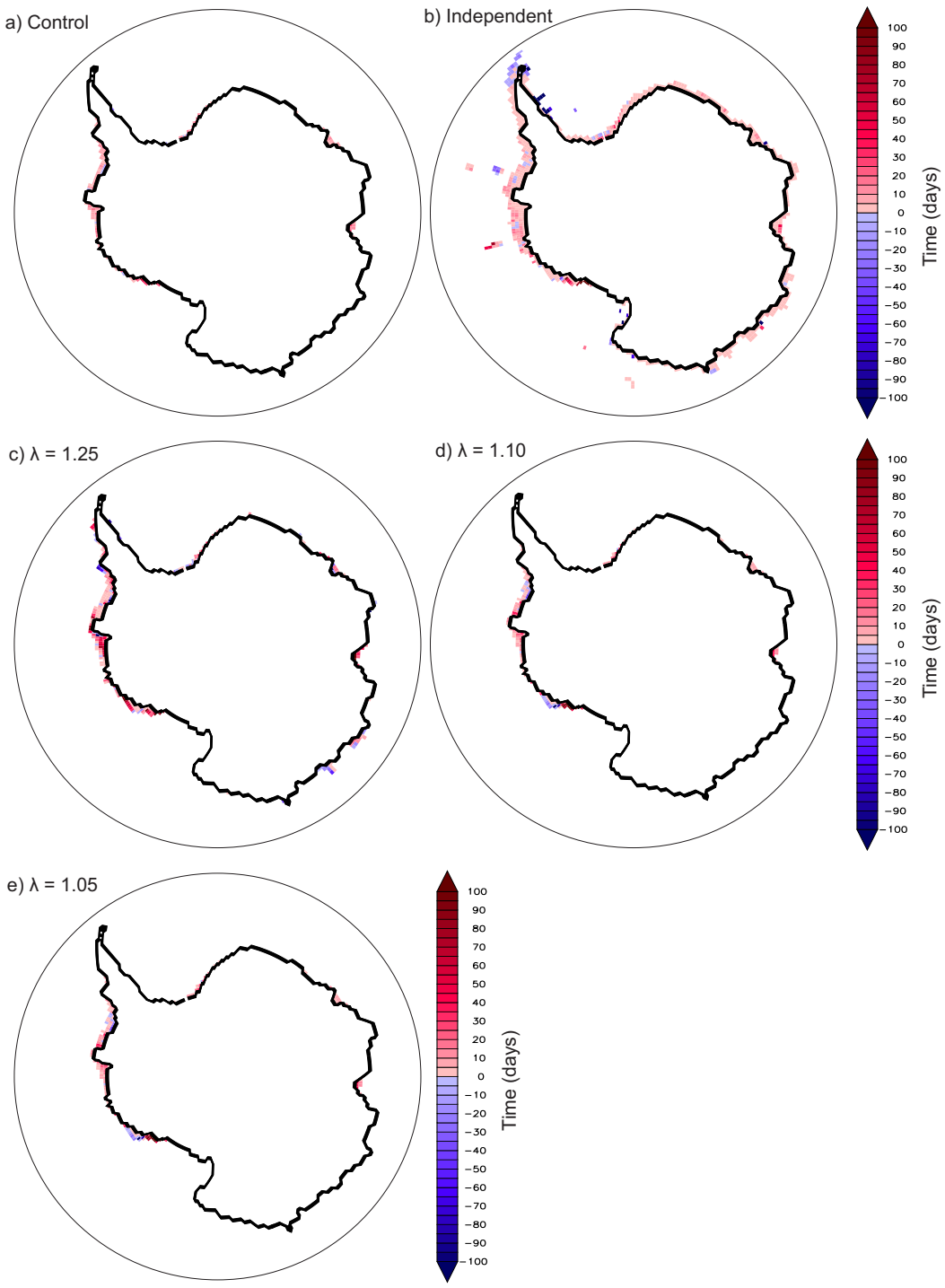

Figure 3.33: Antarctic landfast ice duration anomaly (tides - no tides) from 5 day averages for model simulations run at 1 degree resolution for the (a) control, (b) independent parameterisation, and restricted parameterisation using (c) $\lambda = 1.25$, (d) $\lambda = 1.10$ and (e) $\lambda = 1.05$. Red = increase, blue = decrease, white = no change.

3.6 Conclusions

Tides are an important component of sea surface height and ocean current variability, affecting sea ice through thermodynamic and dynamic processes. Using CICE, we have isolated the tidal component by comparing two sets of global model experiments with identical set-up and initial conditions, except that one ignores the effect of tides while the second includes tidal boundary conditions obtained from the TPXO7.2 tidal model. This has allowed us to identify the impact of tides on grounded ridges and landfast ice.

Tides were found to have a significant effect on the spatial and temporal occurrence of both grounded ridges and landfast sea ice. Tidally induced fluctuations in sea surface height initiated comparable vertical oscillations in the grounded ice, periodically uncoupling the thick ridges from the seabed. The tidal range was found to be important for determining the area of grounded ice within a grid cell. Model grid cells which experienced a large tidal range induced a comparably large fluctuation in the amount of ice aground over the tidal cycle. The type of tide which dominated an area (diurnal, semi-diurnal or mixed) was also found to be important, initiating a different response in the grounded ice. Asymmetric tides, with longer duration peaks than troughs caused the grounded ridges to be uncoupled from the seabed for longer periods of time, and therefore be more susceptible to horizontal redistribution by tidal and residual currents. The horizontal tidal currents associated with the rise and fall of the sea surface, and the non linear residual currents, both acted to redistribute the sea ice horizontally. When the ridges were aground, a strong frictional stress at the seabed acted to prohibit any horizontal movement, but when the ridges were afloat they were free to be transported with the rest of the floating ice cover. When the ridges were transported to a new region, they would reground if the draft thickness of the ice was greater than the new ocean depth accounting for the new tidal range. This horizontal redistribution was found to alter the extent and pattern of grounded ridges.

Tides were also found to alter the occurrence of grounded ice by changing the

thickness distribution of the sea ice cover. The tides redistributed ice through mechanical deformation into thicker ice categories, increasing the occurrence of thick ridges. This also meant that the lead fraction increased, and so too did the rate of new ice production. Both of these factors increased the potential for thick ice to ground. Simulations which employed the independent landfast ice parametrisation experienced a competing effect, as the tides acted to mobilise the erroneously thick grounded ice ridges which occurred in shallow coastal waters, minimising one of the noted limitations of the independent parameterisation to over estimate grounded ice. The tides did not however remove the perennial grounded ice produced by all parameterisations, as it was too stable to be mobilised by the vertical and horizontal tidal forcing.

As shown in Chapter 2, grounded ridges act to stabilise the sea ice, allowing landfast ice to form. Changing the extent and location of these grounded ridges inevitably impacted upon the formation and maintenance of landfast ice. The effect of tides on the landfast ice cover was not simple. In some simulations the tides were found to increase the area of landfast ice, because the area of grounded ice had increased. However, tides were also observed to decrease the occurrence of landfast ice as they increased the mobility, and therefore decreased the stability of the ice cover by introducing oscillations in sea level, tidal currents and residual currents. In the Arctic the second process tended to dominate these results as the landfast ice occurred in locations which were influenced by unrealistically strong residual tidal currents.

It is pertinent to note that the results presented here were based on the comparison of two sets of model runs with identical set-up and boundary conditions apart from the addition of tides from TPXO 7.2 in the second set of simulations. The non tidal runs were essentially taken as the 'control' against which the impact of tides was measured. In both cases, results were taken from the last year of integration after a 10 year spin up. However, this means that the sea ice distribution was different at the beginning of the presented results year, as the tidal runs had 10 years of tidal forcing which modified the concentration and thickness distribution of the

ice cover. In most regions the difference was found to be minimal, but there were a number of localised regions where the impact of tides was significantly larger. This discrepancy has the potential to introduce a bias in the final results.

One shortcoming of this work is the unrealistic residual tidal currents obtained from the TPXO7.2 tidal model. Potential reasons for their occurrence have been discussed in Section 3.5. These unrealistic currents inevitably altered the general sea ice cover, and affected the production of grounded and landfast ice, but their occurrence did not affect our ability to investigate the sensitivity of the grounded and landfast ice to tides.

3.7 Discussion

It has long been accepted that tides have an important impact on sea ice (Kowalik and Proshutinsky, 1994; Proshutinsky, 1988; Melling et al., 1984; Holloway and Proshutinsky, 2007; Koentopp et al., 2005), and they are widely included in current sea ice modelling studies. However, there is a limited body of work looking at modelling landfast sea ice, and even less considering the impact of tides on landfast ice. This analysis found that even at relatively coarse model resolution (1°) the impact of tides on grounded ridges and landfast ice is important. In the Arctic the introduction of tides was found to improve the prediction of landfast ice location and duration across the tested landfast ice parameterisations. A lack of observational data in the Antarctic prohibits a conclusion being drawn on whether the inclusion of tides improved the reproduction of the landfast ice here. From these results, we argue that tides are an important component of ocean variability that should be included in landfast ice modelling studies, in the Arctic at least, in order to accurately represent its seasonal cycle. Many studies which aim to realistically model the seasonal progression of landfast ice do not include tides, and so the important impacts identified in this analysis will not be included. The effect of tides is likely to be even more pertinent at finer resolution or regional studies, like those which the majority of the landfast ice modelling studies are performed at. At finer resolution, greater

variability in the tidal range, tidal currents and residual currents will be represented. Higher resolution bathymetry, known to be an important factor in determining the strength of tides, will alter the prediction of tides in the coastal regions where landfast ice forms. To further this work, and fully ascertain the sensitivity of landfast ice to tidal motion, a high resolution study could be completed.

There are a number of important implications which can be inferred from this analysis. Although we cannot directly investigate the oceanographic impacts of a tidally altered landfast ice cover with this model, in Chapter 2 it was found that the introduction of landfast ice altered the location of leads of polynyas, moving them offshore. It was then suggested that this process would alter the properties of the dense water cascading at the shelf break. In this analysis it has been noted that tides had a significant effect on landfast ice location and duration, which will impact on the location of the offshore polynyas and leads. Tides were also found to increase the lead fraction by mechanically redistributing thin ice into thicker ice. By increasing the lead fraction the net ice production was also found to increase (Figures 3.11 and 3.25). Annually, over the Arctic the net increase in ice production caused by tides when the independent landfast ice parameterisation was employed was $0.41\,\mathrm{cm\,day^{-1}}$, with strong increases in ice production observed in the HB region, Baffin Bay, around Svalbard and Greenland, in the White and Laptev Seas, in the Bering Sea and the Sea of Okhotsk. Similarly in the Antarctic the tides were found to increase the net rate of ice production by $0.37\,\mathrm{cm\,day^{-1}}$, with the largest effects seen in the Ross and Weddell Seas. Climate models which do not include landfast ice and tides will misrepresent the location and rate of ice production, and the ice thickness distribution of the pack ice - two crucial characteristics of the sea ice cover.

By combining the results of this tidal analysis with recent research looking at the impact of a changing climate on the sea ice system, inferences on the future state of the landfast ice system can be made. It has been shown that the extent and thickness of the Arctic sea ice cover, especially in summer, has been significantly declining in recent years (Stroeve et al., 2012; Rothrock et al., 2003; Schweiger et al., 2011; Laxon

et al., 2013). In line with these general changes it would then be expected that the number, and maximum thickness, of ice ridges which stabilise the landfast ice sheet will also decrease. The likely result of fewer, and thinner, ridges would be a landfast ice cover which is less stable, and that reaches its stable extent closer to the coast (in shallower water). Monitoring of landfast ice in some Arctic regions has not provided a definitive answer to the long term spatial and temporal landfast ice trend. Some regions have been observed to have undergone significant thinning of landfast ice, while other areas have experienced no change (Mahoney et al., 2007a; Druckenmiller et al., 2000; Gerland et al., 2008; Dumas et al., 2006). However, it was found that in Barrow Alaska, the temporal duration of the landfast ice season was significantly reduced compared to earlier records (Mahoney et al., 2007a; Barry et al., 1979) due to the combined effect of later inclusion of the ice ridges in coastal regions, and earlier onset of thawing temperatures. If the landfast ice system responds to a warming climate, as we suggest, then the impact of tides on the area of open water just offshore of the landfast ice edge (flaw lead or flaw polynya) would be more pronounced, as the new landfast ice edge would be located in a more tidally active region than if the landfast ice edge were to occur further offshore, in deeper water. Enhanced tidal mixing would act to increase the ocean heat flux to the surface waters, which may act prohibit new ice production, keeping the area ice free. As open water has a lower albedo than the 'bright' snow or sea ice, the increased area of open water in summer will lead to increased absorption of radiation. Again this may act to inhibit sea ice formation in winter. However, in winter, if the water is shallow enough, or the heat loss to the cold overlaying atmosphere is sufficient enough, the water may become sufficiently cooled to allow ice production. From this study, we cannot speculate on which process would dominate, only that the impact of tides on the landfast ice edge will increase as the edge moves into more tidally active regions.

This work is particularly useful to those who interact with landfast ice, and need to predict short and long term changes in the landfast ice such as hunters, the shipping industry, and mineral exploitation industries. For example, the shipping industry

need to be able to accurately predict the date of freeze-up and break-off of landfast ice, so that they know when channels will be ice free and therefore passable. This analysis has shown that tides alter the duration and location of landfast ice, and therefore need to be included to accurately predict when shipping passages will be open.

Chapter 4

Understanding the landfast ice system

4.1 Representing landfast sea ice in sea ice models

4.1.1 Background

The majority of sea ice models, from regional to global scales, do not explicitly include landfast sea ice. However, most models are able to represent ice which becomes landfast due to lateral constraints, such as restrictive geometry, such as in the Canadian Arctic Archipelago (CAA) and other narrow channels or embayments, which can impart a horizontal resistive stress on the ice which is sufficient to resist lateral motion. However, models fail to include landfast ice along unrestricted coastlines or under offshore winds which is formed due to the grounding of thick ice ridges. The grounded ridges anchor the ice cover to the seabed preventing lateral motion. In order to model landfast ice, both these lateral and vertical constraints need to be represented. At fine enough resolution these processes could be directly represented, which may allow us to learn more about how to properly parameterise landfast ice in coarser resolution models. However, it is generally not feasible to run simulations at the resolutions necessary to capture the small scale features of landfast ice, and therefore realistic landfast ice parameterisations need to be developed.

4.1.2 Summary of proposed landfast ice parameterisation

The analysis in this thesis so far (Chapters 2 and 3) has considered how grounded ridges add lateral stability to sea ice, allowing landfast ice to form. Two distinct landfast ice parameterisations were developed and tested in a commonly used sea ice model. The parameterisations accounted for the sub-grid scale grounding of thick ice ridges, which added lateral stability to the ice cover. The important parameters which determine the amount of ice aground at any given point are the draft ice thickness and ocean depth. The 'independent parameterisation' allowed ice of any thickness to occur and ground on bathymetry of any depth. However, as ice generally grounds in water just shallower than its draft thickness the 'restricted parameterisation' limited the maximum thickness of ice which could ground in a given ocean depth using Arctic observations of ice gouge depth.

In the Arctic, both the independent and restricted parameterisations reproduced the seasonal cycle of landfast ice area, comparing well with NIC observations. Both parameterisations were also able to reproduce the spatial occurrence of landfast ice. However, a major limitation, evident in both parameterisations, was the production of multiyear grounded ridges and landfast ice. Overall the parameterisations did not perform as well in the Antarctic. Generally the spatial distribution of the landfast ice was reasonable, but widespread perennial landfast ice was produced. It was shown that the production of the multiyear grounded ice occurred because the basal growth of the ice ridges was not capped once the ridges were in contact with the seabed, allowing the ridges to reach thicknesses beyond that which could be thermodynamically melted in summer. The ridges then remained coupled to the seabed, anchoring the landfast ice throughout the summer period. Improving this aspect of the parameterisations would greatly improve the temporal representation of the landfast ice cover. There are a number of additional factors, not included in these simulations, which could also help to improve the results. For example, inclusion of realistic ocean currents and heat fluxes (Mahoney et al., 2007a,b; Cole et al., 2004) as well as river processes (Dmitrenko et al., 1999; Dean et al., 1994; O'Brien et al.,

2006) would be expected to improve the representation of the landfast ice seasonal cycle.

The effect of tides on landfast ice was considered in Chapter 3. It was found that tides did not have a simple impact on the landfast ice. In some cases tides increased the area of landfast ice, by increasing the production of thick ridges which were able to ground on the seabed. The tides mechanically redistributed thin ice into thick ice, resulting in a greater proportion of thick ice, but also a higher lead fraction. The increased lead fraction in winter led to an increased rate of new ice production. Both of these processes acted to increase the occurrence of thick grounded ridges. However, in some cases the tides were found to decrease the occurrence of landfast ice, as strong tidal and residual currents increased the mobility of the ice pack, decreasing the stability of both the grounded ridges and landfast ice. The spatial distribution of the grounded ridges was also altered by tidal action. Tidally induced vertical fluctuations in sea surface height, twinned with the horizontal tidal currents, and the non linear residual currents, caused the thick ice ridges to be vertically and horizontally redistributed.

4.2 Open questions

There are a number of open questions remaining in landfast ice research. Here we discuss a few of them in more detail. Related to the work presented in this thesis so far, one area which would benefit from further research is the impact of different sub-grid scale distributions of grounded ice used within a parameterisation on the production of landfast ice. Different sub-grid scale distributions of ice draft and ocean depth will lead to varying amounts of ice becoming aground, and subsequently varying degrees of landfast ice being produced. Currently our understanding of the landfast ice system is not sufficient to determine realistic, dynamically based, variable distributions. In the analysis presented so far, it was assumed that there was an independent relation between draft thickness and ocean depth to produce one possible sub-grid scale distribution. We also placed restrictions upon this independent distribution

to produce a second possible distribution. However, neither of these may be the optimum sub-grid scale distribution to produce the most realistic representation of landfast ice. For completion, it would be beneficial to test a range of sub-grid scale distributions, such as those which result in the maximum and minimum amount of grounded ice (discussed in Appendix A).

A major driver for understanding, and realistically modelling, the formation of landfast ice is the impact of landfast ice on ice-ocean interactions. The work presented in this thesis cannot directly investigate the oceanographic impacts of the landfast ice, as a standalone sea ice model was used. By not including realistic ocean currents or heat fluxes a significant part of the landfast ice system was ignored. For example, the break-up of landfast ice is found to be earlier along coasts with recurring springtime polynyas than along those without, as increased solar energy is absorbed by the open water. This energy can be transferred to the landfast ice through pulses of warm water entering the shelf area (Mahoney et al., 2007b). Landfast ice also impacts upon the ocean system in a number of ways. The occurrence of landfast ice moves the effective coastline, and the location of flaw polynyas that form adjacent to the effective coastline, offshore. The dense water formed in the polynyas then has a reduced distance to travel before reaching the shelf break, undergoing less mixing with the fresher ambient shelf water. This may allow the water to maintain its original high density, and cascade to greater depths once at the shelf break (Schauer and Fahrbach, 1999). Landfast ice has also been observed to modify the under ice flow. The thick grounded ridges, which are prevelant at the seaward edge of landfast ice, have been observed to disrupt ocean currents, and even trap pockets of freshwater under the ice (Macdonald et al., 1995). Ultimately, in order to fully test the developed landfast ice parameterisations these, and many more, ice-ocean interactions need to be included.

Landfast ice formation as a result of restrictive geometry is well documented and understood by the science community, while the other processes which lead to the formation of landfast ice are less well understood. Thick ice ridges which ground on the sea floor are known to add lateral stability to the sea ice, anchoring

it in place. The grounded ridges then allow the sea ice to remain fast to the coast under conditions which would act to prevent landfast ice formation, such as along unrestricted coastlines and under offshore winds. Ridges which gouge the seabed offer significantly larger anchoring strengths than those which are only just in contact with the seabed (Mahoney et al., 2007b). The distribution of the grounded ridges also alters the anchoring strength available to the landfast ice (Mahoney et al., 2007b). However, the details of the interaction between ridges and landfast ice have not yet been fully explored. For example, questions remain over the minimum level of anchoring needed to form landfast ice. Another open question is the role of tensile strength in landfast ice formation. Recent landfast ice modelling studies have focused on the inclusion of tensile strength into the landfast ice cover (e.g. König Beatty and Holland, 2010), but it has not been confirmed if landfast ice does in fact contain tensile strength, let alone agreement on the level needed to form landfast ice. These questions are confounded by the lack of long term or wide spatial scale observations.

4.3 Using sea ice models to further our understanding of the landfast ice system

The work presented so far in this thesis has focused on parameterising landfast ice in a standalone thermodynamic-dynamic sea ice model, forced with realistic high resolution bathymetry, and atmospheric and tidal boundary conditions, based on our current understanding of the landfast ice system. However, there is still uncertainty surrounding the key parameters of the ice cover and the physical environment which control the formation of landfast ice. It is known that coastal geometry is an important factor, as it can cause ice to become fast if it is restrictive, such as a narrow channel or embayment (Mahoney et al., 2007a). The depth of the water the ice resides in is also an important factor in determining the width of the landfast ice cover, as the ridges important in stabilising the landfast ice cover typically ground at ocean depths less than 20 m (e.g. Mahoney et al., 2007a). It is also known that the occurrence of landfast ice is dependent on external forcing, such as atmospheric

winds and ocean currents (Divine et al., 2004, 2005). The direction and strength of the atmospheric and oceanic forcing helps to determine the width of the landfast ice. For example, strong winds tend to result in landfast ice extending reduced distances offshore (Divine et al., 2005). Modelling the landfast ice environment at fine enough resolution, so that the landfast ice does not need to parameterised, but can be directly represented, would allow us to learn more about the landfast ice system. This would then help to identify the optimum method of parameterising landfast ice as a sub-grid scale process in coarser resolution models. We consider here whether it is possible to use a sea ice model to further our understanding of the landfast ice system, by identifying the parameters which are important in determining whether ice will become landfast or not.

4.3.1 Method

In this Chapter we attempt to define the principal parameters of the landfast ice system, including the sea ice itself and the physical environment in which it resides, that are necessary to determine whether the ice will be in motion or not. We then combine these parameters into a 'characteristic variable' which can be used to calculate whether the ice will be landfast or not under given conditions. We firstly considered two idealised one dimensional scenarios, which can be solved analytically: ice acting under pure compression and ice acting under pure shear. For these examples, the analytical solution identifies the key parameters which determine whether the ice will be landfast or not. The numerical solutions are then compared against the analytical, to test if the analytically proposed characteristic variables are able to fully describe ice motion in the model.

We then consider an idealised two dimensional scenario which is more akin to that found in reality (although still idealised) which cannot be solved analytically. From a range of sensitivity experiments we attempt to determine which parameters, and the relationship between those parameters, necessary to define whether landfast ice will form or not within the model.

Model description

For continuity the Los Alamos Sea Ice Model (CICE), used previously in the global landfast ice simulations in Chapters 2 and 3, is also used for this analysis. The CICE model is described in detail by in Chapter 1 and so not repeated here. For these experiments the model was run in standalone format with no thermodynamic processes. As such, any variations in ice thickness or concentration will be caused by dynamically driven convergent or divergent flow only. There are no interactive ocean currents, but the impact of upper ocean circulation on sea ice is taken into account through the ice-ocean drag and all other ice-ocean-atmosphere interactions are also removed. A regular Cartesian rectangular grid was used to create the two 1D, and the 2D domains, as illustrated in Figures 4.1, 4.2 and 4.5 respectively. The default model specifications for the 1D and 2D domains are listed in Tables 4.1 and 4.2 respectively. For each simulation one ice thickness category plus open water was used.

The ice concentration, A, is the fraction of the area in a grid cell covered by ice (from 0 to 1). If the concentration is 1, then the grid cell is completely covered by ice. If the concentration is less than 1 then the grid cell contains some proportion $(1-A)$ of open water. For each simulation the model was run for 5 days, after which point the ice was considered in motion if the ice concentration in one or more of the grid cells along the central transect (from the southern to the northern boundary), underwent a change greater than or equal to 20% from the initial state. Ice concentration was used as a proxy for ice motion, instead of ice velocity, to prevent misclassification of moving ice. It was noted that in a number of simulations a positive ice velocity was recorded for a short period of time, before the velocity returned to zero (or near zero due to ice creep). This velocity 'jolt' was not significant enough to result in ice motion across a grid cell, and therefore the ice remained 'stationary'. Results from the following simulations are presented:

- Idealised one dimensional pure compression;
- Idealised one dimensional pure shear; and

- Idealised two dimensional domain.

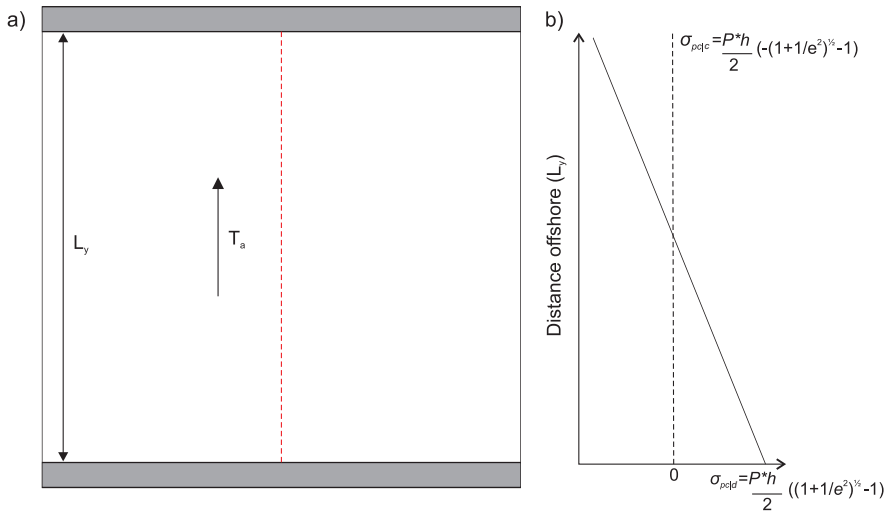

Figure 4.1: Schematic showing a) the model domain for the 1D pure compression scenario and b) the sign and magnitude of the internal ice stress (σ_{pc}) along the central transect (indicated by the dashed red line in (a)). Here, $P^* = 27500\,\mathrm{Nm}^{-2}$ is the internal ice strength constant (Equation (4.6)), $e = 2$ is the eccentricity of the yield curve and h is the ice thickness.

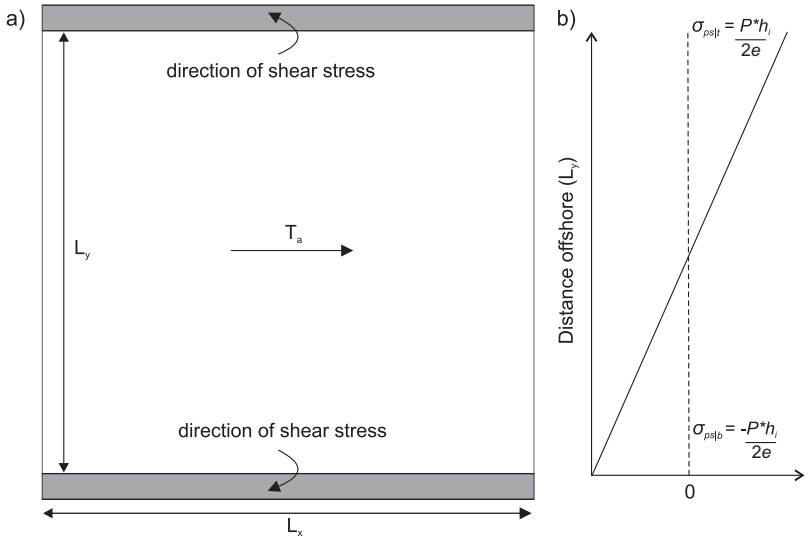

Figure 4.2: Schematic showing a) the model domain for the 1D pure shear scenario and b) the sign and magnitude of the internal ice stress (σ_{ps}) along the central transect (indicated by the dashed red line in (a)). Here, $P^* = 27500\,\mathrm{Nm}^{-2}$ is the internal ice strength constant (Equation (4.6)), $e = 2$ is the eccentricity of the yield curve and h is the ice thickness.

Table 4.1: Model specifications for the one dimensional idealised model domains.

Parameter	Symbol	Value (units)
Right domain boundary		Periodic
Left domain boundary		Periodic
Top domain boundary		Closed
Bottom domain boundary		Closed
Resolution		10 km
Initial width of the ice cover	L_y	150 : 350 km in 50 km intervals
Initial ice thickness	h	1 m
Initial ice concentration	A	1
Initial ice velocity	U_i	$0\,\mathrm{m\,s^{-1}}$
Ocean velocity	U_o	$0\,\mathrm{m\,s^{-1}}$
Wind stress	τ_a	- $\mathrm{N\,m^{-2}}$
Empirical ice strength parameter	P^*	$27500\,\mathrm{N\,m^{-2}}$
Yield curve eccentricity	e	2
Coriolis	f	$0\,\mathrm{rad\,s^{-2}}$

Pure Compression

A homogeneous strip of landfast ice which is attached between two closed boundaries (coastlines), as illustrated in Figure 4.1, is set-up in CICE using the default model specifications listed in Table 4.1. A constant offshore wind stress (τ_{ay}) is applied over the whole domain. If the wind stress is sufficiently large to overcome the resistive internal ice stress, the ice will detach from the bottom coastline and move offshore, piling up along the closed top boundary. As such, it will not be considered landfast. Under this scenario, the ice deformation at the top boundary will eventually be sufficient for the ice to resist the wind stress and become stationary once more. If the wind stress is not sufficiently large to overcome the resistive internal ice stress the ice will remain stationary and therefore be considered landfast.

The default model specifications are listed in Table 4.1. The internal ice strength constant, $P^* = 27500\,\mathrm{N\,m^{-2}}$, and initial ice thickness, $h = 1\,\mathrm{m}$, were kept constant and the Coriolis parameter is set to zero as it was not considered to be a dominant term. The width of the ice cover, L_y, was altered from $L_y = 150$ to 350 km in 50 km intervals, and the maximum wind stress (to 2 decimal places) under which the ice remained stationary was found.

The momentum equation for sea ice is

$$m\frac{\partial \vec{u}}{\partial t} = -mf\vec{k} \times \vec{u} - mg\nabla\zeta + \vec{\tau_a} + \vec{\tau_o} + \vec{\nabla}.\,\vec{\sigma}, \tag{4.1}$$

where m is the ice mass per unit area of ocean, $\vec{u}$ is the ice velocity, f is the Coriolis parameter, $\vec{k}$ is a unit vector pointing upwards, g is the acceleration due to gravity, ζ is the dynamic topography of the sea surface, $\vec{\tau_a}$ is the wind stress, $\vec{\tau_o}$ is the ocean stress, ∇ is the two dimensional nabla operator, and $\vec{\nabla}.\,\vec{\sigma}$ is the divergence of the internal ice stress tensor $\vec{\sigma}$. The divergence of the ice stress tensor describes the forces stemming from ice interactions such as rafting, ridging and fracturing. It has been documented that on timescales greater than weeks, the dominant terms are typically atmospheric and oceanic stresses and the internal ice stress (e.g. Steele et al., 1997; Feltham, 2008). The effects of ocean surface tilt and Coriolis have been shown to be of smaller magnitude than the other terms, but can become significant over longer time periods (Hibler, 1986). For simplicity we consider only the primary terms, so the simplified momentum equation governing sea ice motion is

$$0 = \vec{\tau_a} + \vec{\tau_o} + \vec{\nabla}.\,\vec{\sigma}. \tag{4.2}$$

The ocean is modelled as stagnant, and therefore there are no ocean currents. As such, the only stress imparted on the ice by the ocean is frictional drag. For simplicity we assume a linear drag law, $F_d = -Rv$, where F_d is the frictional drag and R is the constant drag coefficient. The model domain is set up so that the internal ice

stress is constant in x, and therefore the equation governing the momentum of the modelled sea ice becomes

$$0 = \tau_{ay} - Rv - \frac{\partial \sigma_{22}}{\partial y}. \tag{4.3}$$

Equation (4.3) is integrated over the width of the ice cover, L_y,

$$0 = \int_0^{L_y} \tau_{ay}\, dy - \int_0^{L_y} Rv\, dy - \int_0^{L_y} \frac{\partial \sigma_{22}}{\partial y}\, dy. \tag{4.4}$$

In Equation (4.4) $\int_0^{L_y} \tau_{ay}\, dy$ is the wind force per unit length in the x direction, $\int_0^{L_y} Rv\, dy$ is the frictional force per unit length in the x direction acting to resist ice motion and $\int_0^{L_y} \frac{\partial \sigma_{22}}{\partial y}\, dy$ is the internal ice stress per unit length in the x direction acting to resist motion. The chosen domain results in τ_{ay} being constant in x and y, and R and $\frac{\partial \sigma_{22}}{\partial y}$ being constant in x, therefore the momentum equation becomes

$$0 = \tau_{ay} L_y - R L_y \int_0^{L_y} v\, dy - (\sigma_c - \sigma_d), \tag{4.5}$$

where σ_c and σ_d are the internal ice stresses at the top and bottom boundaries respectively. If the ice is just on the point of motion, then along the closed top boundary the ice is being compressed, and σ_c will be equal to the maximum compressive strength. Along the bottom boundary the ice cover will be diverging. In CICE, the strength of the ice (P) is defined as

$$P = P^* h\, exp(-20(1 - A)), \tag{4.6}$$

where P^* is the compressive ice strength constant, h is the ice thickness, and A is the ice concentration. This definition causes the ice strength to increase exponentially as A tends to 1. In all of the considered scenarios $A = 1$. In sea ice modelling, the mechanical behaviour of the sea ice is described by a rheology, which defines the relationship between the internal ice stress tensor and the deformation of the ice

cover. If the sea ice in this problem were modelled to contain no tensile strength the maximum compressive strength of the ice would be as detailed in Equation (4.6), and $\sigma_c = P^* h \, exp^{-20(1-A)}$. The ice at the bottom boundary would diverge immediately, and $\sigma_d = 0$. However, if the ice was modelled to contain a degree of tensile strength then this is not the case. For example, Hunke (2001) showed that CICE's rheology is such that for ice undergoing one dimensional zonal flow under convergence, the internal ice stress is

$$\sigma_c = \frac{P^* h}{2}\left(\sqrt{1 + {}^1\!/\!_{e^2}} - 1\right). \tag{4.7}$$

Under divergence the internal ice stress is

$$\sigma_d = \frac{P^* h}{2}\left(-\sqrt{1 + {}^1\!/\!_{e^2}} - 1\right). \tag{4.8}$$

In Equations (4.7) and (4.8) the eccentricity of the elliptical yield curve, $e = 2$, determines the relative importance of the compressive and shear strength of the ice. For ice to be considered landfast it must be stationary, and therefore $v = 0$. The momentum equation is thus

$$0 = \tau_{ay} L_y - P^* h \sqrt{1 + {}^1\!/\!_{e^2}}. \tag{4.9}$$

From this, a non dimensional characteristic variable (α_{pc}) which includes the key parameters which determine ice motion can be defined. For the idealised 1D scenario where ice is acting under pure compression, the analytically identified principal parameters are the wind stress, τ_a, the width of the ice cover, L_y, the internal ice strength constant, P^*, and the thickness of the ice, h. Rearranging Equation (4.9) the non dimensional characteristic variable is defined,

$$\alpha_{\mathrm{pc}} = \frac{P^* h\sqrt{1+{}^1\!/_{e^2}}}{\tau_{ay} L_y} \geq 1 \text{ then the ice is stationary (landfast)}$$
$$< 1 \text{ then the ice is in motion}$$

If $\alpha_{\mathrm{pc}} \geq 1$ the ice will be stationary, or landfast, as the forces acting to set the ice into motion ($\tau_{ay} L_y$) are not strong enough to overcome the resistive forces ($P^* h\sqrt{1+{}^1\!/_{e^2}}$). When $\alpha_{\mathrm{pc}} < 1$ the ice will be in motion, as the forces acting to set the ice into motion are greater than the maximum resistive force that can be applied.

Results

Figure 4.3(a) shows the analytical and numerical solutions for the maximum wind stress under which the sheet of ice, of a given width, can remain motionless (both to 2 decimal places). In general, the numerical and analytical results compared well, with CICE able to reproduce the magnitude of the critical wind stress each width of ice was able to withstand. Although, for ice widths less than or equal to 200 km the numerical results are not identical to the analytical and CICE systematically holds ice motionless under stronger wind stresses, up to 6.7 % greater, than analytically suggested. The strong similarity between the analytical and numerical solutions suggests that the analytically derived characteristic variable, α_{pc}, contained all the principal parameters necessary to determine whether ice will be landfast or not in the model. When considering the solutions for the characteristic variable, Figure 4.3(b), the results suggest that there is a greater degree of error between the analytical and numerical solutions. This additional error comes from the numerical wind stress, used to find the numerical characteristic variable value, only being found to 2 decimal places while the analytical wind stress is not rounded to 2 decimal places.

There is a smooth monotonic inverse relation between the width of the ice cover and the maximum wind stress the ice is able to withstand, where $\tau_{ay} = {}^C\!/_{L_y}$ and $C = P^* h\sqrt{1+{}^1\!/_{e^2}}$. That is, as the width of the ice cover increased, the maximum wind stress under which it was able to remain motionless was consistently reduced.

This relation occurs because the wind stress is applied over the entire width of the ice cover, and so the smaller the sheet of ice, the smaller the area the wind stress can act upon.

These sensitivity experiments have shown that in this simple 1D pure compression scenario the occurrence of landfast ice is inversely related to the initial width of the ice cover. As such, it is increasingly less likely that ice will be landfast the wider the ice cover becomes, unless it in held in place by some additional resistive force. The analytically derived non dimensional characteristic variable, α_{pc}, included all the necessary sea ice and environmental parameters to determine whether the modelled ice cover will be fast or not.

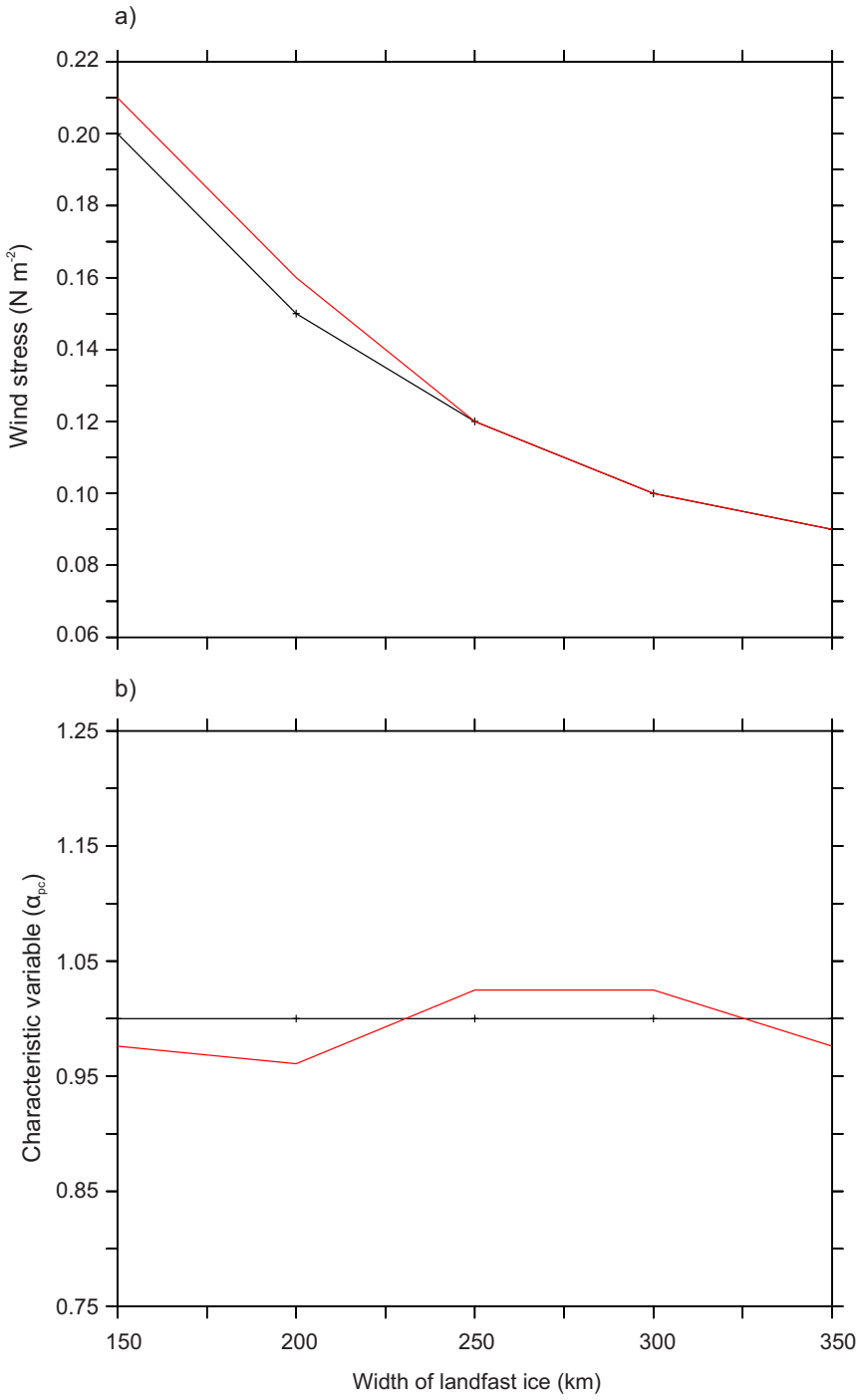

Figure 4.3: Analytical (black line) and numerical (CICE) (red line) solutions for (a) the maximum wind stress (Nm^{-2}) under which ice can remain stationary, and (b) the associated non dimensional characteristic variable, α_{pc}, for ice acting under pure compression.

Pure Shear

A periodic channel, completely covered by a homogeneous sheet of ice initialised at rest (Figure 4.2), is set-up in CICE using the default model specifications listed in Table 4.1. The channel is bound to the top and bottom by smooth closed boundaries (coastlines), and is open to the right and left with periodic boundaries. A constant alongshore wind stress (τ_{ax}) is applied over the whole domain. If the wind stress is sufficiently large to overcome the resistive internal ice stress then the ice will flow along the channel as a homogeneous sheet, exiting the channel through the periodic boundary. As such, it will not be considered landfast. If the wind stress is not sufficiently large to overcome the resistive internal ice stress the ice will remain stationary, and therefore be considered landfast.

In these sensitivity experiments the internal ice strength constant, $P^* = 27500\,\mathrm{N\,m^{-2}}$, and initial ice thickness, $h = 1\,m$, were kept constant throughout. The width of the ice cover, L_y, was altered from $L_y = 150 : 350$ km in 50 km intervals, and the maximum wind stress (to 2 decimal places) the ice of a given width was able to resist was found.

The motion of the modelled sea ice is described by the simplified momentum equation, Equation (4.2). As the ocean is modelled as stagnant, the only stress imparted on the ice by the ocean is frictional drag. For simplicity we assume a linear drag law, $F_d = -Ru$, where F_d is the frictional drag and R is the constant drag coefficient. The model domain is set up so that the internal ice stress is uniform in x, and therefore the equation governing the momentum of the modelled sea ice becomes

$$0 = \tau_{ax} - Ru - \frac{\partial \sigma_{12}}{\partial y}. \tag{4.10}$$

Equation (4.10) is integrated over the width of the ice cover, L_y, and the momentum equation becomes

$$0 = \int_0^{L_y} \tau_{ax}\, dy - \int_0^{L_y} Ru\, dy - \int_0^{L_y} \frac{\partial \sigma_{12}}{\partial y}\, dy, \tag{4.11}$$

where $\int_0^{L_y} \tau_{ax}\, dy$ is the wind force per unit length in the x direction, $\int_0^{L_y} Ru\, dy$ is the frictional force acting to resist ice motion force per unit length in the x direction and $\int_0^{L_y} \frac{\partial \sigma_{12}}{\partial y}\, dy$ is the internal ice stress acting to resist motion force per unit length in the x direction. The chosen 1D domain results in τ_{ax} being constant in x and y, and R and $\frac{\partial \sigma_{12}}{\partial y}$ being constant in x, therefore the momentum equation becomes

$$0 = \tau_{ax} L_y - R \int_0^{L_y} u\, dy - (\sigma_{s|_t} - \sigma_{s|_b}). \tag{4.12}$$

In Equation (4.12) $\sigma_{s|_t}$ and $\sigma_{s|_b}$ represent the shear stress between the ice and the coastline at the top and bottom channel boundaries respectively. The alternative sign convention for shear stress is used, that is counter-clockwise rotation (at top boundary) is considered positive and clockwise rotation (at bottom boundary) is considered negative. As the forces acting on the ice are constant, and the sheet of ice itself is homogeneous, the magnitude of the shear stress between the ice and the coast is the same at both boundaries. An eccentricity, $e = 2$ is used throughout, meaning the shear strength of the ice is $1/2e$ that of the compressive strength ($P = P^* h\, exp^{-20(1-A)}$). As $A = 1$ in the considered problem $|\sigma_{s|_{t,b}}| = {}^{P^* h}/_{2e}$. For ice to be considered landfast ice it must be stationary ($u = 0$), therefore the momentum equation is

$$0 = \tau_{ax} L_y - \frac{P^* h}{e}. \tag{4.13}$$

From Equation (4.13) a non dimensional characteristic variable (α_{ps}), which determines when ice will be stationary or not, can be defined. The analytically identified principal parameters which determine whether ice will move in the considered 1D pure shear scenario are the wind stress, τ_a, the width of the ice cover, L_y, the internal ice strength constant, P^*, and the thickness of the ice, h. Rearranging Equation (4.13), α_{ps} can be defined

$$\alpha_{\text{ps}} = \frac{P^* h}{e \tau_{ax} L_y} \geq 1 \text{ then the ice is stationary (i.e. landfast)}$$
$$< 1 \text{ then the ice is in motion}$$

If $\alpha_{\text{ps}} \geq 1$ the ice will be stationary, or landfast, as the forces acting to set the ice into motion ($\tau_{ax} L_y$) are not strong enough to overcome the resistive forces ($P^* h$). When $\alpha_{\text{ps}} < 1$ the ice will be in motion as the forces acting to set the ice into motion are greater than the maximum resistive force that can be applied.

Results

Figure 4.4(a) shows the analytical and numerical solutions for the maximum wind stress a sheet of ice, of a given width, can remain motionless under (both to 2 decimal places) when acting under pure shear stress. In general, the numerical and analytical results compared well, with CICE generally able to reproduce the wind stress each width of ice was able to withstand. Although, for an ice cover 100 km wide, the results were not identical, with CICE holding ice motionless under wind stresses up to 11% greater than analytically suggested. The strong similarity between the analytical and numerical solutions suggests the analytically derived characteristic variable, α_{ps}, contained all the principal parameters necessary to determine whether ice will be landfast or not within the model. When considering the solutions for the characteristic variable, Figure 4.4(b), the results suggest that there is a greater degree of error between the analytical and numerical solutions. This additional error comes from the numerical wind stress, used to find the numerical characteristic variable value, is only found to 2 decimal places, while the analytical wind stress is not rounded to 2 decimal places.

There is a smooth monotonic inverse relation between the width of the ice cover and the maximum wind stress the ice is able to withstand, where $\tau_{ax} = {}^{C}/_{L_y}$ and $C = {}^{P^* h}/_{e}$. That is, as the width of the ice cover increased, the maximum wind stress the ice was able to remain motionless under consistently reduced. This occurred

because the wind stress was applied over the entire width of the ice cover, and so the smaller the sheet of ice, the smaller the area the wind stress can act upon. This was also found in the 1D pure compression experiments.

From these sensitivity experiments it was found that in this simple one dimensional pure shear scenario, the occurrence of landfast ice was inversely related to the initial width of the ice cover. The sensitivity experiments showed that the wider the expanse of ice, the smaller the necessary forcing (in this case wind stress) needed to set the ice in motion. Therefore, it is increasingly less likely that ice will be fast the wider the ice cover, or channel, becomes unless it in held in place by some additional resistive force. The analytically derived non dimensional characteristic variable, α_{ps}, included all necessary sea ice and environmental parameters needed to determine whether the modelled ice cover will be fast or not.

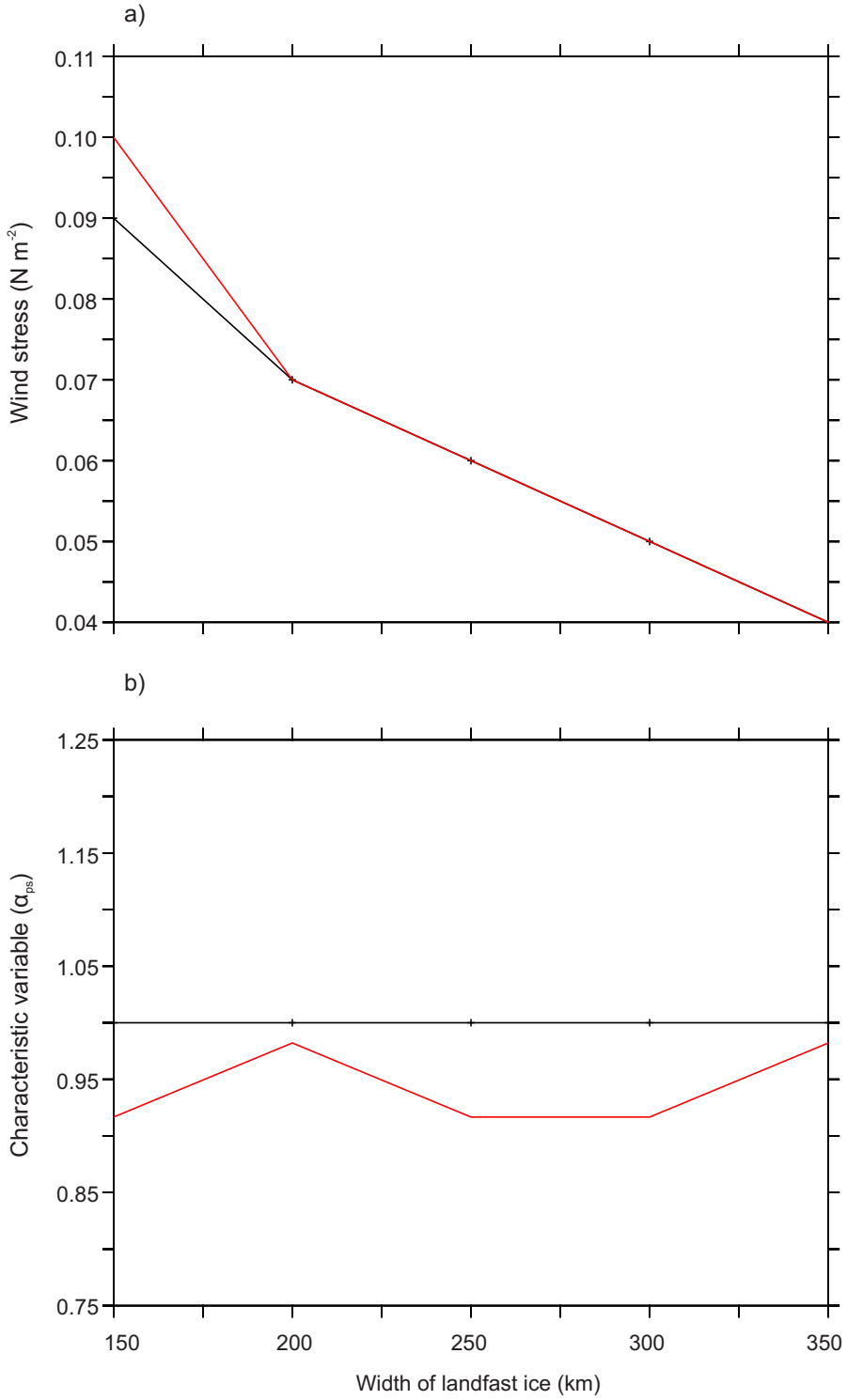

Figure 4.4: Analytical (black line) and numerical (CICE) (red line) solutions for (a) the maximum wind stress (Nm^{-2}) under which ice can remain stationary, and (b) the associated non dimensional characteristic variable α_{ps} for ice acting under pure shear.

Two Dimensional scenario

The results from the idealised one dimensional sensitivity experiments showed that the analytically derived non dimensional characteristic variables (α_{pc} and α_{ps}) were sufficient to determine the conditions under which landfast would form. This meant that the characteristic variables included all the necessary sea ice and environmental parameters that determine ice motion within the tested scenarios.

We now consider a more realistic, but still idealised, two dimensional domain, set up as shown in Figure 4.5. The default model specifications are detailed in Table 4.2. The domain is similar to that used for the one dimensional pure compression investigation (Figure 4.1), except that in these experiments the offshore boundary of the ice is anchored by a row of discontinuous grounded ridges (modelled as zero velocity ice points) instead of a continuous coastline. The row of grounded ridges essentially acts as a closed coastline, as the ice is not able to move past this point. There is an opening in the centre of the grounded ridges through which the ice is able to flow, if the forces acting on the ice are sufficiently large to initiate motion. This is similar to that observed in reality, where a sheet of landfast ice is discontinuously pinned along the offshore coast by thick grounded ice ridges. It is not possible to analytically solve the momentum equation for this scenario, and therefore an analytically derived non dimensional characteristic variable (α_{2D}) cannot be suggested. We investigate if, from the numerical solutions, the characteristic variable, or variables, can be determined. For α_{2D} to fully account for ice motion it must include all the sea ice and environmental parameters which determine ice motion as well as correctly determining the relationship between those variables.

From the one dimensional pure compression and pure shear experiments it was found that the key parameters determining sea ice motion were the width of the ice cover, referred to now as L_1, the thickness of the ice cover, h, the internal ice strength constant, P^*, and the wind stress, τ_a. It would be expected that these parameters will continue to be important in this 2D scenario. Additionally, the opening in the offshore boundary, L_2, introduces a new parameter. In order to suggest what the characteristic variable could be, we must first determine if L_2 is important in

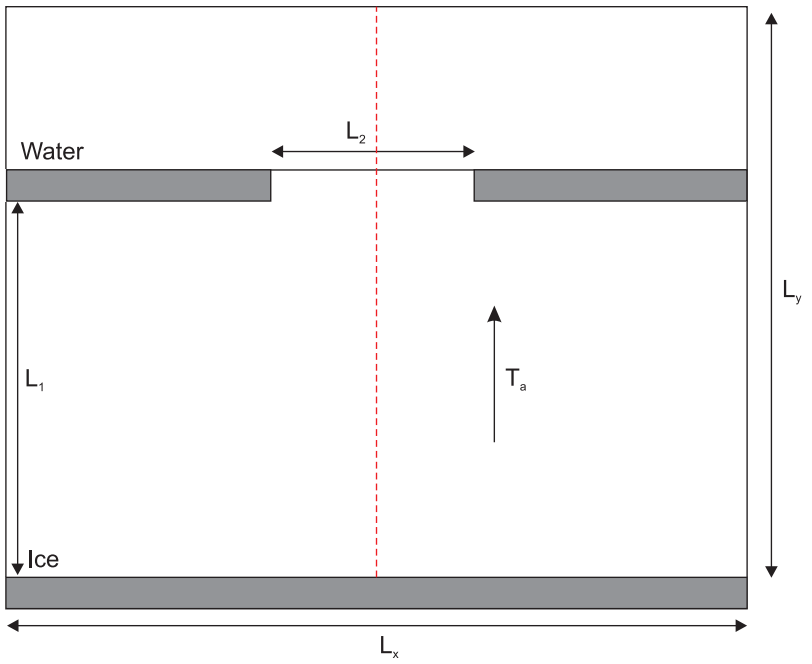

Figure 4.5: Schematic showing the model domain for the two dimensional scenario including compressive and shear stress. The central transect is indicated by the dashed red line.

controlling ice motion, and if so find its relation to the other variables.

In these sensitivity experiments the internal ice strength constant, $P^* = 27500\,\mathrm{N\,m^{-2}}$, and initial ice thickness, $h = 1\,\mathrm{m}$, were kept constant. Two distinct ice cover widths were tested, $L_1 = 200$ and 250 km. The width of the opening in the offshore grounded ridges was altered between $L_2 = 20$ to 90 km in 10 km intervals. The maximum wind stress (to 2 decimal places) under which the ice cover was able to remain stationary was found.

Ice was considered in motion, and therefore not landfast, if any section of the ice cover along the central transect from the closed bottom boundary, through the opening in the offshore grounded ridges, underwent a change in concentration greater than or equal to 20%. We assumed that if one section of the ice was in motion then all the ice shoreward of that section would eventually be in motion. There is the possibility that a stable ice bridge could form within the opening of the offshore grounded ridges, leeward of which an area of stationary, or landfast ice, could form.

Table 4.2: Model specifications for the 2D idealised model domain

Parameter	Symbol	Value (units)
Length of domain (X)	L_x	$10,000\,\mathrm{km}$
Length of domain (Y)	L_y	$10,000\,\mathrm{km}$
Resolution		$10\,\mathrm{km}$
Right domain boundary		Periodic
Left domain boundary		Periodic
Top domain boundary		Open
Bottom domain boundary		Closed
Initial ice width	L_1	200 and $250\,\mathrm{km}$
Initial ice thickness	h	$1\,\mathrm{m}$
Initial ice concentration	A	1
Initial ice velocity	U_i	$0\,\mathrm{m\,s^{-1}}$
Initial opening width	L_2	20 : 90 km in 10 km intervals
Ocean velocity	U_o	$0\,\mathrm{m\,s^{-1}}$
Wind stress	τ_a	- $\mathrm{N\,m^{-2}}$-
Empirical ice strength parameter	P^*	$27500\,\mathrm{N\,m^{-2}}$
Yield curve eccentricity	e	2
Coriolis	f	$0\,\mathrm{rad\,s^{-2}}$

Ice bridges form when the cohesive strength of the ice is able to withstand the external forces acting to set the ice into motion (Dumont et al., 2009). The eccentricity of the yield curve controls the cohesive strength of the ice (e.g. Hibler, 1979). Increasing/decreasing the eccentricity makes the yield curve more/less elongated, which in turn decreases/increases the cohesive strength of the ice. If the eccentricity is chosen to be very large, the yield curve is approximately a straight line, and the sea ice contains no, or very little, shear strength. Under these conditions the ice would flow like a cavitating fluid. Dumont et al. (2009) showed that CICE was able to form stable ice bridges, but only if the eccentricity was less than the standard value of 2.0. As the standard eccentricity value was used in these experiments we do not

anticipate the possibility of stable ice bridges, or the area of landfast ice shoreward of the ice bridge, to form. Nevertheless, ice bridges were observed to form under certain conditions after 5 days of simulation but these ice bridges were found to become unstable when the simulations were allowed to run for longer (20 days).

Results

The purpose of these sensitivity experiments was to understand what, if any, effect changing the width of the opening in the offshore grounded ridges had on the ability of landfast ice to form, and to suggest a non dimensional characteristic variable, or variables, (α_{2D}) which could be used to determine if landfast ice would form under the given conditions.

The numerical solutions for the defined 2D sensitivity experiments (Figure 4.6) suggest that there are two separate regimes operating, depending on the width of the opening in the offshore grounded ridges. Firstly, when the opening (L_2) was relatively wide, the ice behaved in line with expectations from the 1D investigations. That is, as L_2 increased, the critical wind stress the ice was able to withstand, and remain motionless under, gradually decreased. This scenario is similar to the 1D pure shear experiment, where ice was forced by a wind stress perpendicular to the channel opening. Here it was found that as the width of the channel opening (and the ice cover) increased, the ice cover became less able to remain fast. However, when the opening in the offshore grounded ridges was relatively narrow, the ice flow through the opening appeared more fluid. For these narrow openings, as the width of the opening decreased, the ice was able to outflow under increasingly weaker wind stresses. At very small opening widths, the ice flow was similar to that of a fluid, with very little landfast ice formed. Logically this behaviour does not seem realistic, as it would mean that in reality we would observe fast flowing ice in narrow channels under forcing conditions that would cause the ice to be stationary in a wider channel. This suggests that this 'fluid like' flow through narrow openings in the offshore grounded ridges is a numerical error, and therefore cannot be used to imply the behaviour of the landfast ice system. The point at which the ice transitions between the 'fluid

flow' to the more realistic flow is not constant. For an ice cover which was 250 km wide, 'narrow openings' included widths $\leq$ 40 km (or 4 grid cells), while for an ice cover 200 km wide, 'narrow openings' included widths $\leq$ 50 km (or 5 grid cells).

Similar behaviour was identified by Losch and Danilov (2012), who considered ice flow through a channel 40 km wide at a resolution of 5 km (equal to 8 grid cells). They compared the results from two distinct sea ice codes: CICE (which uses an elastic-viscous-plastic (EVP) rheology) and a sea ice code which used a viscous-plastic (VP) rheology. It was found that under certain conditions the VP code reported stationary ice in the modelled channel, while the EVP code (used in these experiments) simulated accelerated ice flow in comparison with surrounding regions. Losch and Danilov (2012) suggested that this behaviour, which was unique to the EVP code, was due to the lower ice viscosities allowed by the EVP rheology, producing 'weaker' ice. In CICE the dynamical calculations are completed on a separate, and much faster, timestep to the advective calculations, known as the elastic subcycling timestep. Losch and Danilov (2012) reported that by increasing the subcycling frequency, beyond the standard $1/30^{\text{th}}$ that of the advective timestep suggested by Hunke and Lipscomb (2010), the EVP solution converged to that of the VP code. However, in the experiments carried out in this analysis, the elastic subcycling timestep used was 0.04 that of the advective timestep, and the behaviour was still apparent. Increasing the number of subcycling iterations beyond this was found to greatly increase the computational time, and is unlikely to be realistic for large scale or fine resolution simulations.

Considering then only the results for 'wide openings' in the offshore grounded ridges, there is a monotonic, smooth inverse relation between the width of the opening in the offshore boundary and the maximum wind stress under which the ice can remain stationary. That is, for increasing L_2 the critical τ_a the ice can withstand decreased. This suggests that L_2 is an important parameter in determining whether ice will be fast or not, and should be included in any characteristic variable.

It should be noted that the numerical solution for the maximum τ_a under which the ice can remain motionless is likely to be an underestimate, as CICE is not able

to produce stable ice bridges under the current set-up. If CICE were able to produce a stable ice bridge then it is likely that an area of landfast ice would form windward of the bridge.

Suggested characteristic variables

As the problem posed cannot be solved analytically, here we try to infer what the non dimensional characteristic variable, or variables, (α_{2D}) could be from the numerical solutions. From the 1D pure shear and pure compression experiments it was found that the principal parameters determining ice motion are: the external forcing component, in this case the wind stress (τ_a), the width of the ice cover (L_1), the thickness of the ice cover (h) and the internal strength of the ice (P^*). For the posed 2D scenario these parameters remain important, but a new parameter, the width of the opening in the offshore grounded ridges (L_2), was introduced. Considering only the results for the 'wide' openings, and ignoring the results for the 'narrow' openings, where numerical error is thought to negatively affect the results, it was found that the critical τ_a the ice was able to withstand was inversely associated to L_2. From this, it can be taken that L_2 is important in determining whether ice will be landfast or not, and therefore should be included in any characteristic variable. It was also found that the width of the ice cover increased, the minimum width of the opening in the offshore grounded ridges necessary to allow ice motion under a given wind stress decreased, suggesting that L_1 and L_2 are not independent. However, the numerical results did not suggest what the relation between L_1 and L_2 should be. We now present a number of potential characteristic variables, and test their ability to determine the dynamical behaviour of the modelled ice cover.

The 2D domain considered here contains ice acting under both compression and shear, and can be thought of as a combination of the 1D pure compression and pure shear scenarios. As such, the characteristic variables derived for the pure compression and pure shear cases (Sections 4.3.1 and 4.3.1) are relevant here, although they may not fully describe the ice motion.

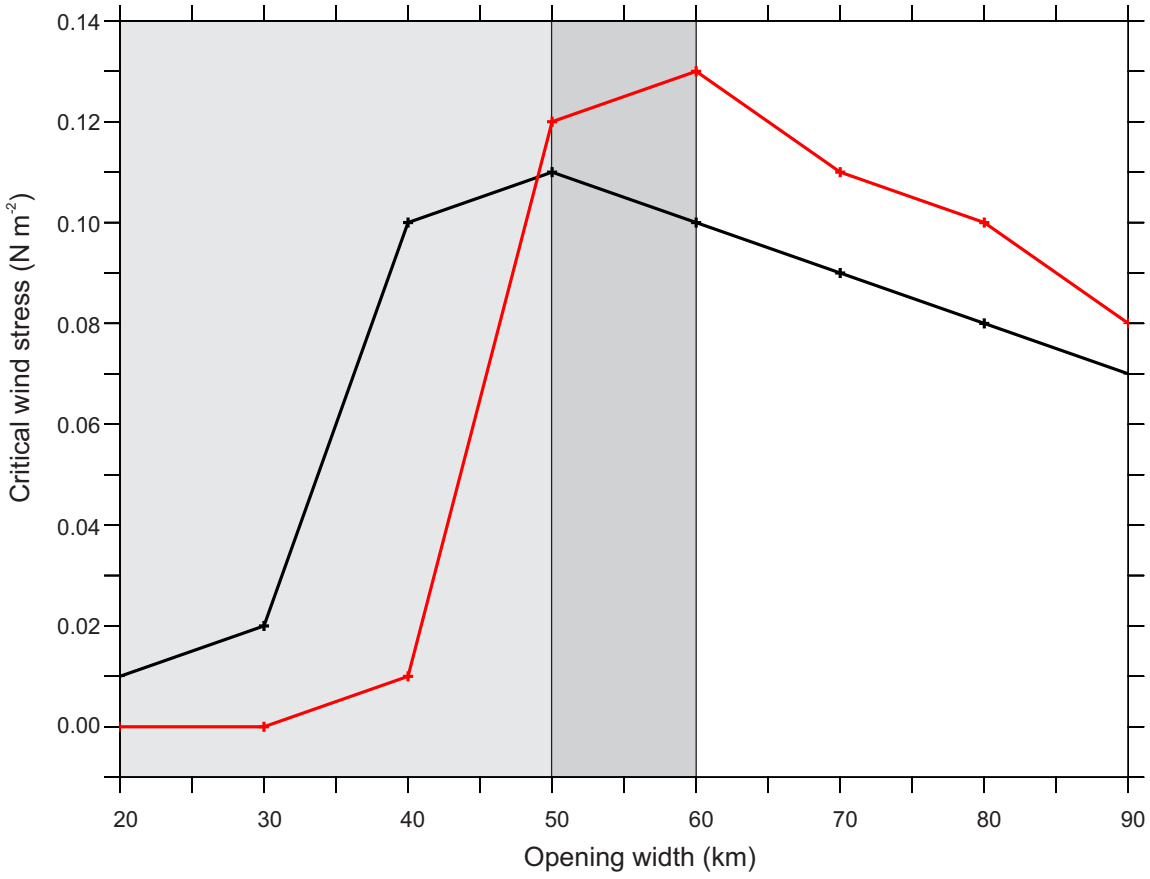

Figure 4.6: Maximum wind stress at which ice is considered motionless (i.e. landfast) for increasing opening widths in the offshore grounded ridges (L_2), for a sheet of ice 200 km wide (red line) and 250 km wide (black line) initialised at rest. The light and additional dark grey shaded areas illustrate the model results where are ignored due to unrealistic fluid like flow for $L_2 = 250$ and 200 km respectively.

For example, if there was no opening in the offshore grounded ridges ($L_2 = 0$) the 2D domain is comparable to the 1D pure compression domain. Creating an opening in the grounded ridges ($L_2 > 0$) means the ice is more susceptible to motion. As such, wind stresses which are able to cause ice motion when $L_2 = 0$ must also cause ice motion when $L_2 > 0$. Therefore, α_{pc} acts as a bounding limit for this 2D problem.

It would be expected that the ice which is situated within, and close to, the opening in the grounded ridges would act in the same way as ice flowing along a channel under pure shear, as the edges of the grounded ridges act like the walls of the channel. As such, wind stresses which result in ice motion in the 1D pure shear case should also result in the motion of ice within, and nearby, the opening in the grounded ridges.

For these reasons, we test the ability of α_{pc} and α_{ps} to describe ice motion in this 2D domain. We also consider a third characteristic variable, which is constructed as the minimum of the non dimensional pure compression and pure shear characteristic variables:

- $\alpha_1 \equiv \alpha_{pc} = \frac{P^* h_i \sqrt{1+1/e^2}}{\tau_a L_1}$
- $\alpha_2 \equiv \alpha_{ps} = \frac{P^* h_i}{e \tau_a L_2}$
- $\alpha_3 = \min(\alpha_{pc}, \alpha_{ps}) = \min\left(\frac{P^* h_i \sqrt{1+1/e^2}}{\tau_a L_1}, \frac{P^* h_i}{e \tau_a L_2}\right)$

Finally we also consider a characteristic variable based on a weighted linear combination of the pure shear and pure compression characteristic variables such that the solution tends to the pure compression case when the opening in the offshore ridges tends to 0:

- $\alpha_4 = \mu_1 \alpha_{ps} + (1 - \mu_1)\alpha_{pc} = \mu_1\left(\frac{P^* h_i}{e \tau_a L_2}\right) + (1 - \mu_1)\left(\frac{P^* h_i \sqrt{1+1/e^2}}{\tau_a L_1}\right)$
- $\alpha_5 = \mu_2 \alpha_{ps} + (1 - \mu_2)\alpha_{pc} = \mu_2\left(\frac{P^* h_i}{e \tau_a L_2}\right) + (1 - \mu_2)\left(\frac{P^* h_i \sqrt{1+1/e^2}}{\tau_a L_1}\right)$
- $\alpha_6 = \mu_3 \alpha_{ps} + (1 - \mu_3)\alpha_{pc} = \mu_3\left(\frac{P^* h_i}{e \tau_a L_2}\right) + (1 - \mu_3)\left(\frac{P^* h_i \sqrt{1+1/e^2}}{\tau_a L_1}\right)$

The values for $\mu_{1,2,3}$ used in these experiments are shown in Table 4.3. For all cases $\mu_{1,2,3} = 0$ when $L_2 = 0$, resulting in the solution being equal to pure compression when there is no opening in the offshore grounded ridges. As L_2 increases, the solution becomes a linear combination of the pure shear and pure compression cases. The weighting between the pure shear and pure compression depends on $\mu_{1,2,3}$, where $\mu_{1,2,3}$ increases at a constant rate with increasing L_2. $\Delta\mu_1$ was chosen so that $\mu_1 = 1$ when the opening in the offshore grounded ridges was equal to the width of the ice cover ($L_2 = L_1$). For a 10 km increase in L_2 $\Delta\mu_1 = 0.004$ and 0.005 when $L_1 = 200$ and 250 km respectively. $\Delta\mu_{2,3}$ were chosen arbitrarily and are independent of the width of the ice cover. For a 10 km increase in L_2 $\Delta\mu_2 = 0.01$ and $\Delta\mu_3 = 0.1$.

Table 4.3: Value of linear weighting for 2D characteristic variables

	μ_1		μ_2		μ_3	
L_2	$L_1 = 200$	$L_1 = 250$	$L_1 = 200$	$L_1 = 250$	$L_1 = 200$	$L_1 = 250$
0	0	0	0	0	0	0
10	.005	004	.01	.01	.1	.1
20	.010	008	.02	.02	.2	.2
30	.015	012	.03	.03	.3	.3
40	.020	016	.04	.04	.4	.4
50	.025	020	.05	.05	.5	.5
60	.030	024	.06	.06	.6	.6
70	.035	028	.07	.07	.7	.7
80	.040	032	.08	.08	.8	.8
90	.045	036	.09	.09	.9	.9

Values of the linear weighting variable (μ) for the tested 2D characteristic variables for each tested width of the ice cover (L_1) and opening in the offshore grounded ridges (L_2).

Figure 4.7 shows the modelled maximum wind stress under which the ice cover is able to remain stationary (i.e. landfast) for the proposed characteristic variables α_1, α_2

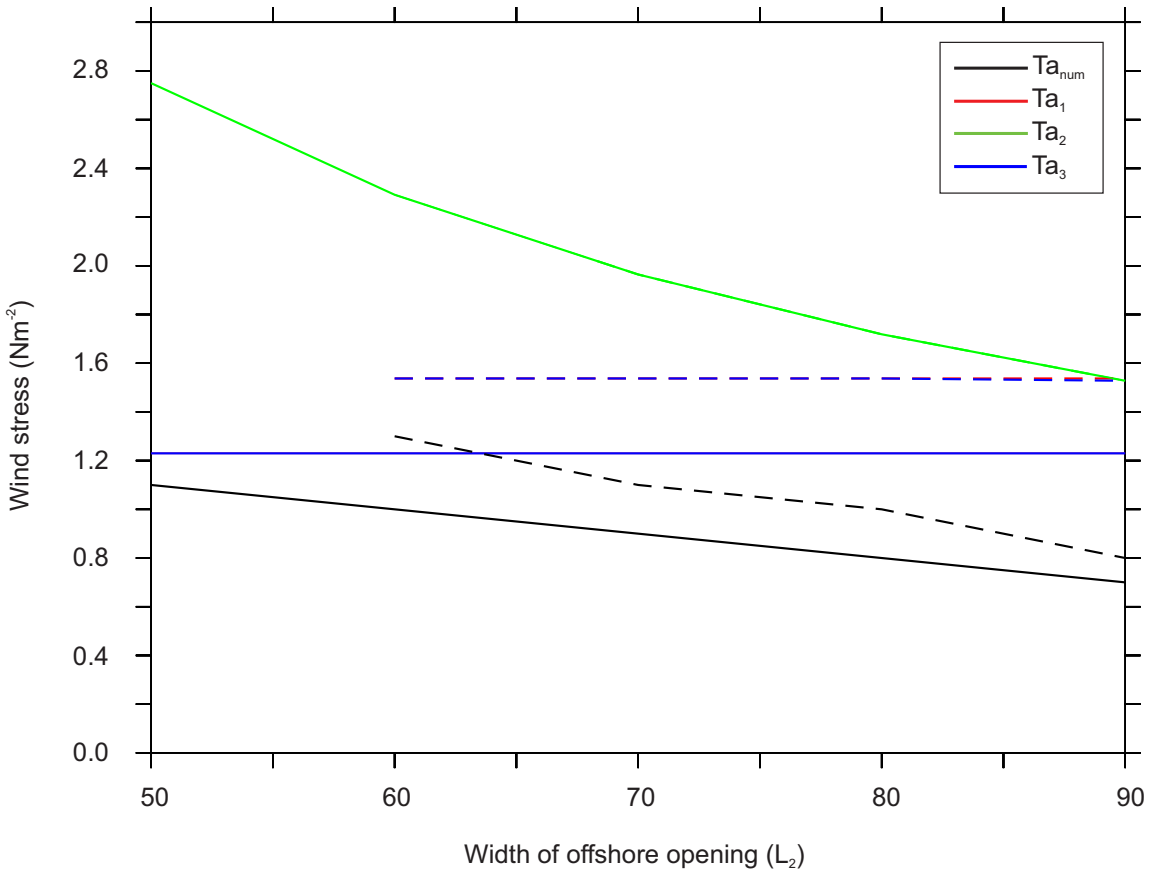

Figure 4.7: Maximum wind stress under which landfast ice can form as suggested by the proposed characteristic variables, $\tau_{a1} = \frac{P^* h \sqrt{1+1/e^2}}{L_1}$ (red line), $\tau_{a2} = \frac{P^* h}{e L_2}$ (green line) and $\tau_{a3} = \min(\tau_{a1}, \tau_{a2})$ (blue line) and the modelled solution (black line), for an ice cover 250 km wide (solid lines) and 200 km wide (dashed lines).

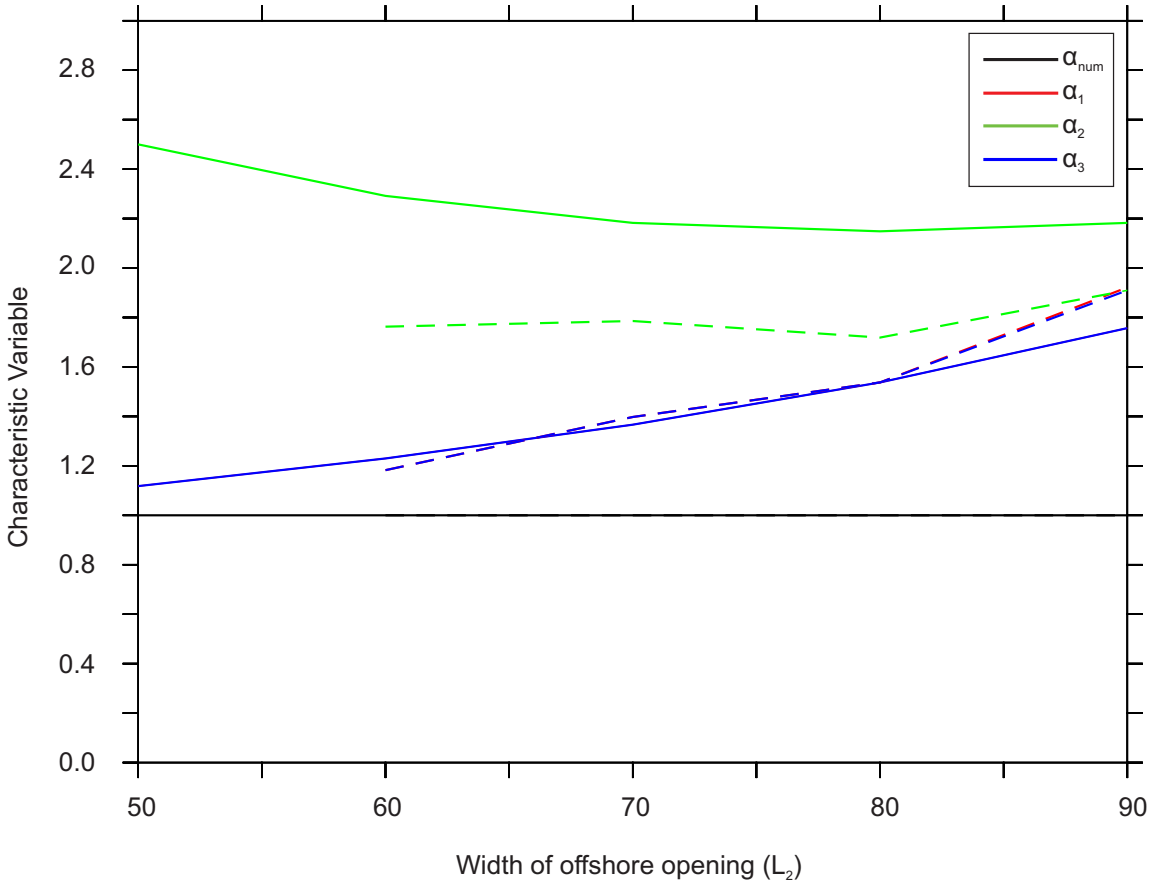

Figure 4.8: Value of proposed characteristic variables, $\alpha_1 = \frac{P^* h \sqrt{1+1/e^2}}{\tau_a L_1}$ (red line), $\alpha_2 = \frac{P^* h}{e \tau_a L_2}$ (green line) and $\alpha_3 = \min(\alpha_1, \alpha_2)$ (blue line) for an ice cover 250 km wide (solid lines) and 200 km wide (dashed lines). The analytically expected solution is shown by the black lines.

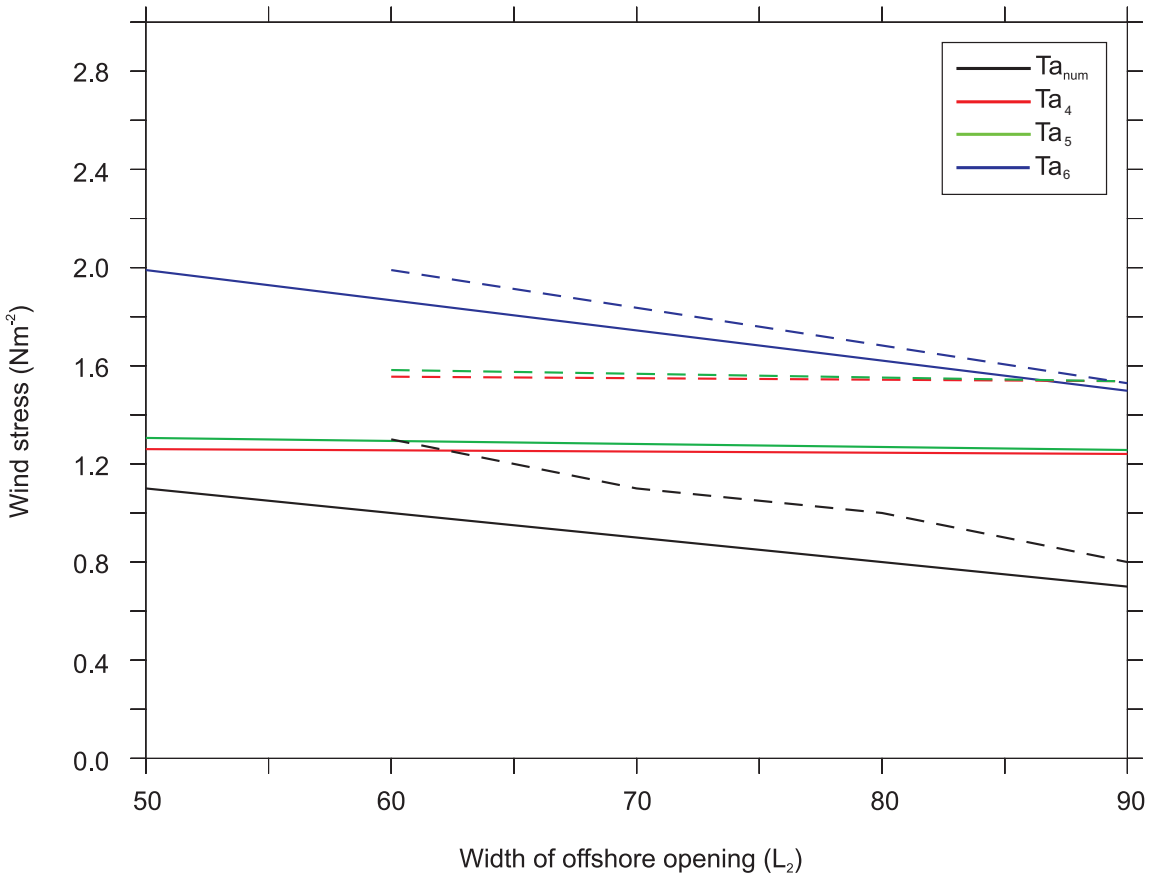

Figure 4.9: Maximum wind stress under which landfast ice can form as suggested by the proposed characteristic variables, $\tau_{a4} = \mu_1\tau_{aps} + (1-\mu_1)\tau_{apc}$ (red line), $\tau_{a5} = \mu_2\tau_{aps} + (1-\mu_2)\tau_{apc}$ (green line), $\tau_{a6} = \mu_3\tau_{aps} + (1-\mu_3)\tau_{apc}$ (blue line) and the modelled solution (black line), for an ice cover 250 km wide (solid lines) and 200 km wide (dashed lines).

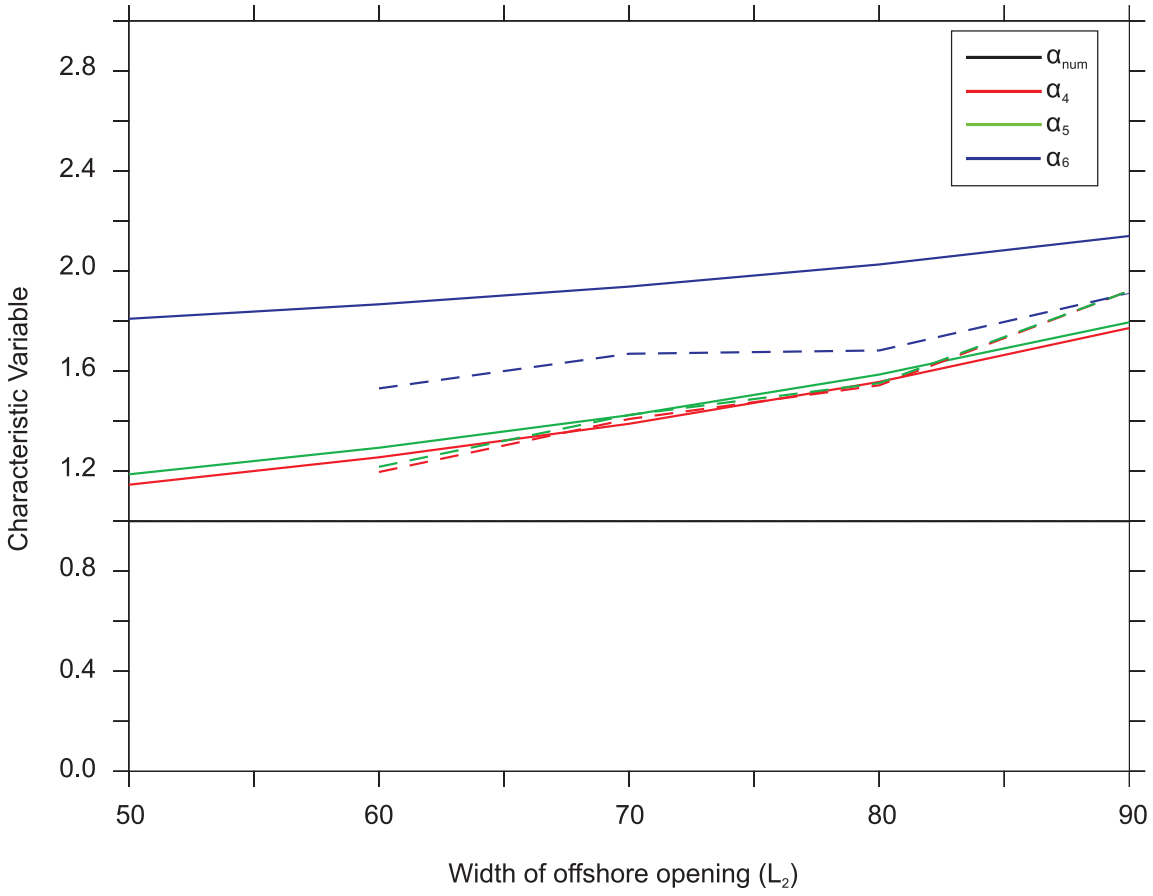

Figure 4.10: Value of proposed characteristic variables, $\alpha_4 = \mu_1\alpha_{ps} + (1-\mu_1)\alpha_{pc}$ (red line), $\alpha_5 = \mu_2\alpha_{ps} + (1-\mu_2)\alpha_{pc}$ (green line), $\alpha_6 = \mu_3\alpha_{ps} + (1-\mu_3)\alpha_{pc}$ (blue line) for an ice cover 250 km wide (solid lines) and 200 km wide (dashed lines). The analytically expected solution is shown by the black lines.

and α_3 and Figure 4.8 shows the associated characteristic variable solution. As α_1 is always less than α_2 the results from α_1 are obscured by those of α_3. The magnitude of the critical maximum wind stress under which ice should remain stationary as suggested from α_1 is comparable to the numerical solution. However, α_1 is not able to reproduce the variability in the critical wind stress caused by alterations in the width of the opening in the offshore grounded ridges, as α_1 does not include the parameter L_2. The characteristic variable based on the 1D pure shear experiments, α_2, was able to reproduce the variability in the critical maximum wind stress with changes in the opening width, as it included the parameter L_2. However, α_2 was not able to reproduce the changes in the magnitude of the critical wind stress caused by changes in the width of the ice cover, as it does not include the parameter L_1. As the critical wind stress produced by α_1 was always smaller than α_2, the results from α_3 are identical to α_1 and suffer from the same issues described.

Figure 4.9 shows the modelled maximum wind stress under which the ice cover is able to remain stationary (i.e. landfast) for the proposed characteristic variables α_4, α_5 and α_6 which are based on a linear weighting of α_{ps} and α_{pc}. Figure 4.10 shows the solutions for the associated characteristic variables. All proposed characteristic variables are able to reproduce the variability in the critical wind stress the ice is able to remain stationary under caused by alterations in the width of the opening in the offshore grounded ridges (L_2) and alterations to the initial width of the ice cover (L_1). The magnitude of the critical wind stress produced by α_4 and α_5 compare better with the numerical solution than α_6. However, α_6 is better able to reproduce the dependency on L_2.

The non dimensional characteristic variables proposed were able to reproduce some of the dynamical behaviour of the sea ice. However, none were able to fully describe the ice motion under the posed scenario. This implies that the tested characteristic variables either did not include all of the principal parameters necessary to describe ice motion, or did not properly describe the relationship between the parameters, or both.

Conclusion

In this Chapter we considered whether it was possible to produce a characteristic variable, or variables, which could fully account for the dynamics of sea ice, namely the ability of landfast ice to form, within a model simulation using idealised model domains and configurations. For the idealised 1D scenarios, where ice was acting under pure compression and pure shear stress, the analytically defined a non dimensional characteristic variable was sufficient to fully describe landfast ice occurrence within the model. However, for the idealised 2D scenario, which could not be solved analytically, the proposed characteristic variables were not sufficient to fully described the dynamics of the modelled landfast ice.

If a non dimensional characteristic variable for the 2D scenario was found, that was able to fully describe the dynamics of landfast ice within a model, that characteristic variable could then be tested in reality. To do this, regional observations of each of the principal parameters, and whether landfast ice formed or not, would be necessary. If the characteristic variable was able to describe the ability of landfast ice to form in reality, as well as within the model, this would suggest that the model is accurately representing the physics of the landfast ice. However, if the characteristic variable is not able to fully account for landfast ice formation in reality, this suggests that the model is not fully representing the physics of the landfast ice system. If this were the case, the characteristic variable could be updated to match the observational results, and could then be used as a simple improvement to landfast ice production within a sea ice model. The updated characteristic variable could be used to identify when landfast ice should form, and enforce its occurrence within the model through a mask. This could be used in place of a full landfast ice parameterisation based on ridge grounding, like that described in Chapter 2. This would be a more physical representation of landfast than simply prescribing the landfast ice cover based on bathymetry. For example, Lieser (2004) prescribed a mask for the landfast ice cover based on a relation between bathymetry and ice thickness. If the sea ice exceeded a certain thickness of the local ocean depth, it was classified as immobile landfast ice. From observations Lieser (2004) limited the occurrence of

landfast ice to waters of depth less than or equal to 30 m. This simple mask was found to reproduce the landfast ice cover reasonably well in some regions. However, defining landfast ice based only on bathymetry is an over simplification, as in this analysis it has been shown that the occurrence of landfast ice depends on a range of other factors. Prescribing the landfast ice cover based instead on the more physically representative characteristic variable could improve the ability of the model to reproduce the fast ice seasonal cycle. This would also lead to an improved representation of the processes which occur shoreward, or at the edge of the landfast ice cover, such as polynyas.

Appendix A

Defining the maximum and minimum area of landfast ice

A.1 Introduction

As discussed in Chapter 2, landfast ice formed as a result of the grounding of thick ice ridges can be parameterised in a relatively coarse resolution sea ice model by defining the sub-grid scale joint distribution of the two continuous random variables, draft ice thickness (h) and the local ocean depth (d). This allows the sub-grid scale distribution of the grounded, and the resultant landfast ice, to be found. As such, the method used to define the joint distribution of the variables will alter the resultant area of landfast ice. In Chapter 2, a parameterisation was developed that assumed an independent relation between ice draft and ocean depth, allowing the ice to occur, and ground, at any depth less than or equal to the draft ice thickness. A second parameterisation, which restricted the occurrence of erroneously thick grounded ice was also presented.

It may be desirable to define the maximum and minimum amount of landfast ice which can be formed. Although, in reality it is unlikely that the maximum or minimum will occur, defining the limiting bounds of the problem may help infer what a realistic distribution should be. To define the maximum and minimum amount of landfast ice the maximum and minimum anchoring strength produced by grounded

ice must be found. It is important to note that not all grounded ridges provide the same amount of anchoring strength to the landfast ice. Those ridges which are only just in contact with the seabed, where the draft thickness is just equal to the local ocean depth, provide significantly less anchoring strength than those ridges which gouge the seabed (Mahoney et al., 2007b). As such, it is not simply a case of finding the joint distribution of ice draft and ocean depth which results in the maximum and minimum amount of grounded ice. Instead, the joint distribution which results in the maximum and minimum anchoring strength, or frictional stress imparted on the ice cover by the grounded ridges must be found.

A.2 Method

We discuss a simple idealized scenario, where the maximum and minimum anchoring strength provided by the grounded ice within a grid cell can be determined if the distributions of the ice draft and ocean depth are known.

The anchoring strength of a grounded ridge is related to the depth to which the ice has gouged the sea, $h_g = h - d$. Positive values mean the ridge has gouged the seabed and is therefore relatively stable, positively contributing to the production and maintenance of landfast ice. Negative values mean that the ice is afloat, and not contributing to the formation of landfast ice. A value of zero means that the ice is aground, but it is only just in contact with the seabed. In this case, as the ridge and the seabed are not strongly coupled, the grounded ridge does not contribute to the formation of landfast ice. The total anchoring strength provided by the grounded ridges, I, is therefore defined by the sub-grid scale occurrence of grounded ridges and the strength to which those ridges are coupled with the seabed:

$$I = \int_0^\infty \mathrm{d}h \int_0^h \mathrm{d}d\, j(h,d)(h-d) \tag{A.1}$$

Where $j(h,d)$ is the joint distribution function of the ice draft (h) and ocean depth (d). To prevent negative contributions ocean depth is only integrated between 0 and

ice draft.

A.3 Idealised case

Considering an idealized scenario (illustrated in Figure A.1) where a grid cell is covered by bathymetry of two depth categories: shallow (d_1) and deep (d_2) water, where $d_1 < d_2$. The grid cell is completely covered by ice of two distinct thicknesses, h_1 and h_2, where $h_1 < d_1$ and $d_1 < h_2 < d_2$. In this scenario, only the thicker ice (h_2) has the ability to ground, as $h_1 < d_1 < d_2$. As the ice is homogeneous, the anchoring strength provided by the grounded ice will also be homogeneous. Therefore, the maximum and minimum anchoring strength that will be produced will be directly related to the maximum and minimum amount of ice aground.

A.3.1 Minimum

The minimum amount of grounded ice can be determined if the distributions of ice draft and ocean depth are known. The ice can be preferentially distributed so that only the necessary amount of ice is aground. In the considered grid cell, Figure A.1(a), the thin ice (h_1) was preferentially located over the shallowest water (d_1). By doing so, the amount of grounded ice, and the associated anchoring strength, is minimised. For this example, the minimum area of ice which necessarily must be aground is the difference between the area of shallow bathymetry and the area of thin ice, $A_{d1} - A_{h1}$, illustrated by the red line in Figure A.1(a). The anchoring strength provided by this grounded ice is related to the gouge depth, h_g, where $h_g = h_2 - d_1$. Therefore, the total minimum anchoring strength produced by the grounded ice is $\int_0^\infty \mathrm{d}h \int_0^h \mathrm{d}d\,(A_{d1} - A_{h1})(h_2 - d_1)$

A.3.2 Maximum

The maximum possible area of grounded ice, and the maximum anchoring strength produced by that grounded ice, can also be determined if the distributions of the

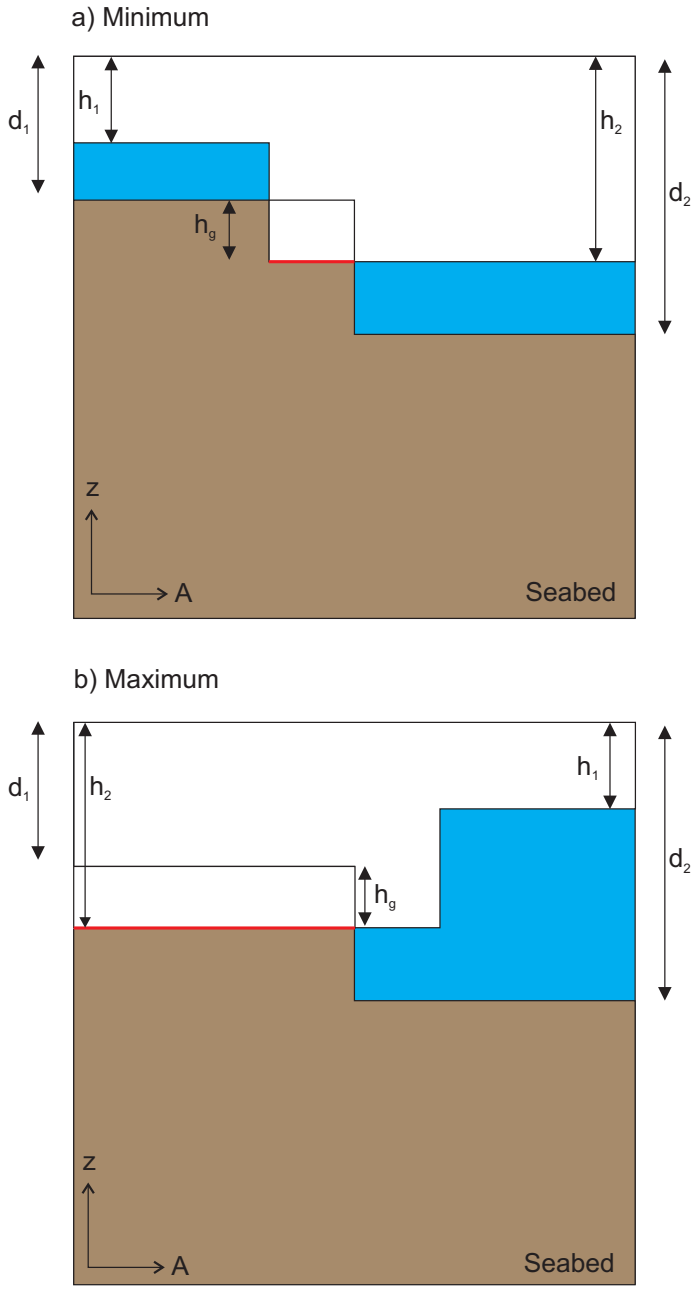

Figure A.1: Schematic showing ice draft and ocean depth versus cell fractional area (A), where A varies between 0 and 1. In (a) the minimum anchoring strength produced by the grounded ice is illustrated and (b) the maximum anchoring strength produced by the grounded ice is illustrated. Where $h_{1,2}$ are the minimum and maximum ice drafts, $d_{1,2}$ are the minimum and maximum ocean depths, h_g is the gouge depth and the red line indicates the area of grounded ice A_g.

ice and bathymetry are known, by preferentially distributing the ice so that the maximum possible area of ice is aground. In Figure A.1(b), the thick ice (h_2) was preferentially located over the shallowest water (d_1). By doing so, the area of grounded ice, and the associated anchoring strength, is maximised. For this example, the maximum area of ice which can be aground is equal to the area of shallowest bathymetry, A_{d1}, illustrated by the red line in Figure A.1(b). The anchoring strength provided by this grounded ice is related to the gouge depth, h_g, where $h_g = h_2 - d_1$. Therefore the total maximum anchoring strength produced by the grounded ice is $\int_0^\infty \mathrm{d}h \int_0^h \mathrm{d}d\, A_{d1}(h_2 - d_1)$.

A.4 Conclusion

We have shown here that in an idealised example the maximum possible and minimum necessary sub-grid scale anchoring strength produced by grounded ice can be determined from the ice draft and ocean depth distribution functions. Finding the extrema of the expression A.1 in the general case, where the number of ice draft and ocean depth categories are arbitrary, would require a variational problem to be formulated and solved, which is mathematically challenging and beyond the scope of this project.

An alternative method of finding the maximum and minimum anchoring strength would be to determine it numerically, where the ice draft is redistributed within a grid cell. The anchoring strength produced by the grounded ice would then be calculated for each tested distribution. For example, if one had N ocean depth categories and N ice draft categories then there would be $N!$ ways of distributing the ice within the grid cell. If N is large, then testing all possible distributions would be computationally very expensive. For example, when $N = 16$, as was the case for the CICE simulations presented in this thesis, then the total number of distributions to test would be close to 21 trillion. So, a more pragmatic approach would be to randomly distribute the ice draft a suitable number of times and select the maximum and minimum from the tested distributions. However, there is no guarantee that the absolute maximum or

minimum would be identified, only that of the random distributions tested. As you increase the number of tested distributions the numerical solution will converge to the actual, but the computational effort would also increase.

Bibliography

C. Amante and B.W. Eakins. ETOPO1 1 Arc-Minute Global Relief Model: Procedures, Data Sources and Analysis. NOAA Technical Memorandum NESDIS NGDC-24 19 pp, 2009.

J. Bareiss and K. Goergen. Spatial and temporal variability of sea ice in the Laptev Sea: Analyses and review of satellite passive-microwave data and model results. *Global and Planetary Change*, 48:28–54, 2005.

P.W. Barnes, D.M. Rearic, and E. Reiminitz. Ice gouge characteristics and their relation to ice gouging and ice dynamics in the Alaskan Beaufort Sea. In P.W. Barnes, D.M. Rearic, and E. Reiminitz, editors, *The Alaskan Beaufort Sea Ecosystems and Environment*, pages 185–212. Academic Press, 1984.

D. Barnett. Sea ice distribution in the Soviet Arctic. In L. W. Brigham, editor, *The Soviet Maritime Arctic*, pages 47–62. Belhaven Press,London, 1991.

P. Barrette. Offshore pipeline protection against seabed gouging by ice: An overview. *Cold Regions Science and Technology*, 69:3–20, 2011.

R.G. Barry, R.E. Moritz, and J.C. Rogers. Fast ice regimes of the Beaufort and Chukchi sea coasts, Alaska. *Cold Regions Science and Technology*, 1:129–152, 1979.

C.M. Bitz and W.H. Lipscomb. An energy-conserving thermodynamic model of sea ice. *Journal of Geophysical Research*, 104:15669–15677, 1999.

R.H. Bourke and R.P. Garrett. Sea ice thickness distribution in the Arctic Ocean. *Cold Region Science and Technology*, 13:259–280, 1987.

B. Cheng, M. Mäkynen, M. Similä, L. Rontu, and T. Vihma. Modelling snow and ice thickness in the coastal Kara Sea, Russian Arctic. *Annals of Glaciology*, 54: 105–113, 2013.

D.M. Cole, H. Eicken, K. Frey, and L.H. Shapiro. Observations of banding in first-year Arctic sea ice. *Journal of Geophysical Research*, 109:C08012, 2004.

K.E. Conlan, H.S. Lenihan, R.G. Kvitek, and J.S. Oliver. Ice scour disturbance to benthic communities in the Canadian High Arctic. *Marine Ecology*, 166:1–16, 1998.

K.G. Dean, W.J. Stringer, K. Ahlns, C. Searcy, , and T. Weingartner. The influence of river discharge on the thawing of sea ice, Mackenzie River Delta: Albedo and temperature analysis. *Polar Research*, 13:83–94, 1994.

A. Defant. Die Gezeiten des Atlantischen Ozeans und des Arctischen Meeres. *Ann. Hydr. Mar Met.*, 52(8-9):153–166,177–184, 1924.

D. Dethleff. Polynyas as a Possible Source for Enigmatic Bennett Island Atmospheric Plumes. In O.M Johannessen, R.D. Muench, and J.E. Overland, editors, *The Polar Oceans and their Role in Shaping the Global Environment*, pages 475–483. AGU, 1994.

D.V. Divine, R. Korsnes, and A.P. Makshtas. Temporal and spatial variations of shore-fast ice in the Kara Sea. *Continental Shelf Research*, 24:1717–1736, 2004.

D.V. Divine, R. Korsnes, A.P. Makshtas, F. Godtliebsen, and H. Svendsen. Atmospheric-driven state transfer of shore-fast ice in the northeastern Kara Sea. *Journal of Geophysical Research*, 110:C09013, 2005.

I.A. Dmitrenko, V.A. Gribanov, D.L. Volkov, H. Kassens, and H. Eicken. Impact of river discharge on the fast ice extension in the Russian Arctic shelf area. In *15th*

International Conference on Port and Ocean Engineering under Arctic Conditions (POAC99), volume 1, 1999.

M.L. Druckenmiller, H. Eicken, and L. George, J.C. Brower. Assessing the shorefast ice: Iupiat whaling trails off Barrow, Alaska. In I. Krupnik, C. Aporta, S. Gearheard, L. Kielsen Holm, and G. Laidler, editors, *SIKU Knowing our ice - Documenting Inuit sea ice knowledge and use*, pages 202–228. Springer-Verlag, New York, 2000.

J.A. Dumas, G.M. Flato, and R.D. Brown. Future projections of landfast ice thickness and duration in the Canadian Arctic. *Journal of Climate*, 19:5175–5189, 2006.

D. Dumont, Y. Gratton, and T.E. Arbetter. Modeling the Dynamics of the North Water Polynya Ice Bridge. *Journal of Physical Oceanography*, 39:14481461, 2009.

G.D. Egbert and S. Erofeeva. Inverse Modeling of Barotropic Ocean Tides. *Journal of Atmospheric and Oceanic Technology*, 19:183–204, 2002.

G.D. Egbert, A.F. Bennett, and M.G.G. foreman. TOPEX/POSEIDON tides estimated using a global inverse model. *Journal of Geophysical Research*, 99:24821–24852, 1994.

H. Eicken, I. Dmitrenko, K. Tyshko, A. Darovskikh, W. Dierking, U. Blahak, J. Groves, and H. Kassens. Zonation of the Laptev Sea landfast ice cover and its importance in a frozen estuary. *Global and Planetary Change*, 48(1/3, Sp.Iss.): 55–83, 2005.

H. Eicken, L. Shapiro, A.G. Gaylord, A. Mahoney, and P.W. Cotter. Recurring spring leads and landfast ice in the Beaufort and Chukchi Seas, 1993-2004, 2009. URL `http://dx.doi.org/10.7265/N5SB43P0`. Boulder, Colorado USA: National Snow and Ice Data Center.

D.L. Feltham. Sea Ice Rheology. *Annual Review of Fluid Mechanics*, 40:91–112, 2008.

F. Fetterer, K. Knowles, W. Meier, and M. Savoie. Sea Ice Index. [indicate subset used], 2002, updated 2009. Boulder, Colorado USA: National Snow and Ice Data Center. http://dx.doi.org/10.7265/N5QJ7F7W.

G.M. Flato and R.D. Brown. Variability and climate sensitivity of landfast Arctic sea ice. *Journal of Geophysical Research*, 101:25767–25777, 1996.

A.D. Fraser, R.A. Massom, K.J. Michael, B.K. Galton-Fenzi, and J.L. Lieser. East Antarctic Landfast Sea Ice Distribution and Variability. *Journal of Climate*, 25: 1137–1156, 2012.

R.J. Galley, B.G.T. Else, S.E.L. Howell, J.V. Lukovich, and Barber. D.G. Landfast Sea Ice Conditions in the Canadian Arctic: 1983 2009. *Arctic*, 65:133–144, 2012.

S. Gerland, A.H.H. Renner, F. Godtliebsen, D. Divine, and T.B. Loyning. Decrease of sea ice thickness at Hopen, Barents Sea, during 1966-2007. *Geophysical Research Letters*, 35:L06501, 2008.

A.B. Giles, R.A. Massom, and V.I. Lytle. Fast-ice distribution in East Antarctica during 1997 and 1999 determined using RADARSAT data. *Journal of Geophysical Research*, 113, 2008.

B. Gjevik and T. Straume. Model simulations for the M2 and K1 tide in the Nordic Sea and Arctic Ocean. *Tellus*, 41:73–96, 1989.

B. Gjevik, E. Nost, and T. Straume. Model simulations of tides in the Barents Sea. *Journal of Geophysical Research*, 99:3337–3350, 1994.

C.G. Hannah, F. Dupont, and M. Dunphy. Polynyas and Tidal Currents in the Canadian Arctic Archipelago. *Arctic*, 62:83–95, 2009.

A. Hequette, M. Desrosiers, and P.W. Barnes. Sea ice scouring on the inner shelf of the Southeastern Canadian Beaufort Sea. *Marine Geology*, 128:201–219, 1995.

W. Hibler, III and E. Schulson. On modeling the anisotropic failure and flow of flawed sea ice. *Journal of Geophysical Research*, 105:17105–17120, 2000.

W.D. Hibler. A Dynamic Thermodynamic Sea Ice Model. *Journal of Physical Oceanography*, 9:815–846, 1979.

P.R. Hill, S.M. Blasco, J.R. Harper, and D.B. Fissel. Sedimentation on the Canadian Beaufort Shelf. *Continental Shelf Research*, 11:821–842, 1991.

D. M. Holland, R. G. Ingram, L. A. Mysak, and J. M. Oberhuber. A numerical simulation of the sea ice cover in the northern Greenland Sea. *Journal of Geophysical Research*, 1995:4751–4760, 1995.

P. R. Holland, N. Bruneau, C. Enright, M. Losch, N.T. Kurtz, and R. Kwok. Modeled Trends in Antarctic Sea Ice Thickness. *Journal of Climate*, 27:3784–3801, 2014.

G. Holloway and A. Proshutinsky. Role of tides in Arctic ocean/ice climate. *Journal of geophysical research*, 112:C04S06, 2007.

M.A. Hopkins, W.D. Hibler III, and G.M. Flato. On the Numerical Simulation of the Sea Ice Ridging Process. *Journal of Geophysical Research*, 96:4809–4820, 1991.

N.H. Hughes, J.P. Wilkinson, and P. Wadhams. Multi-satellite sensor analysis of fast-ice development in the Norske Øer Ice Barrier, northeast Greenland. *Annals of Glaciology*, 52:151–160, 2011.

E.C. Hunke. Viscous-plastic sea ice dynamics with the EVP model: Linearization issues. *Journal of Computational Physics*, 107:18–38, 2001.

E.C. Hunke. Thickness sensitivities in the CICE sea ice model. *Ocean Modelling*, 34:137–149, 2010.

E.C Hunke and W.H. Lipscomb. CICE: the Los Alamos Sea Ice Model Documentation and Software User's Manual Version 4.1, LA-CC-06-012, 2010. Los Alamos National Labratory, Los Alamos, New Mexico.

S.S. Jacobs, H. Hellmer, C. Doake, and R. Frolich. Melting of ice shelves and the mass balance of Antarctica. *Journal of Glaciology*, 38:375–387, 1992.

O. M. Johannessen, L. Bengtsson, M. W. Miles, S. I. Kuzmina, V. A. Semenov, G. V. Alekseev, A. P. Nagurnyi, V. F. Zakharov, L. P. Bobylev, L. H. Pettersson, K. Hasselmann, and H. P. Cattle. Arctic climate change: observed and modelled temperature and sea-ice variability. *Tellus A*, 56:328341, 2004.

M. Koentopp, O. Eisen, C. Kottmeier, L. Padman, and P. Lemke. Influence of tides on sea ice in the Weddell Sea: Investigations with a high-resolution dynamic-thermodynamic sea ice model. *Journal of Geophysical Research*, 110:C02014, 2005.

C. König Beatty and D.M. Holland. Modeling Landfast Sea Ice by Adding Tensile Strength. *Journal of Physical Oceanography*, 40:185–198, 2010.

A. Kovacs and M. Mellor. Sea ice morphology and ice as a geological agent in the southern Beaufort Sea. In J.C. Reed and J.E. Sater, editors, *The Coast and Shelf of the Beaufort Sea*, pages 113–161. Arctic Institute of North America, Arlington, Va, Jan 1974a. Proceedings symposium on Beaufort Sea Coast and Shelf Research.

A. Kovacs and M. Mellor. Sea ice morphology and ice as a geological agent in the southern Beaufort Sea. In J.C. Reed and J.E. Sater, editors, *The Coast and Shelf of the Beaufort Sea*, pages 113–161. Arctic Institute of North America, Arlington, Va., 1974b.

Z. Kowalik. Modeling of topographically amplified diurnal tides in the Nordic Seas. *Journal of Physical Oceanography*, 24:1717–1731, 1994.

Z. Kowalik and A.Yu. Proshutinsky. The Arctic Ocean tides. In O.M Johannessen, R.D. Muench, and J.E. Overland, editors, *The Polar Oceans and their Role in Shaping the Global Environment*, pages 137–158. AGU, 1994.

Z. Kowalik and A.Yu. Proshutinsky. Topographic enhancement of tidal motion in the western Barents Sea. *Journal of Geophysical Research*, 100:2613–2637, 1995.

N.T Kurtz and T. Markus. Satellite observations of Antarctic sea ice thickness and volume. *Journal of Geophysical Research*, 117:C08025, 2012.

R. Kwok and G.F Cunningham. ICESat over Arctic sea ice: Estimation of snow depth and ice thickness. *Journal of Geophysical Research*, 113:C08010, 2008.

R. Kwok, G.F. Cunningham, Wensnahan M., I. Rigor, H.J. Zwally, and D. Yi. Thinning and volume loss of the Arctic Ocean sea ice cover. *Journal of Geophysical Research*, 114:C07005, 2009.

S.W. Laxon, K.A. Giles, A.L. Ridout, D.J. Wingham, R. Willatt, R. Cullen, R. Kwok, A. Schweiger, J. Zhang, C. Haas, S. Hendricks, R. Krishfield, N. Kurtz, S. Farrell, and M. Davidson. CryoSat-2 estimates of Arctic sea ice thickness and volume. *Geophysical Research Letters*, 40:732–737, 2013.

M. Lepparanta. The dynamics of sea ice. In M. Lepparanta, editor, *Physics of Ice Covered Seas, Vol 1*, pages 305–342. Helsinki Univeristy Press, 1998.

M. Lepparanta. *The Drift of Sea Ice*. Springer, 2011.

M. Lepparanta and R. Hakala. The structure and strength of first-year ice ridges in the Baltic Sea. *Cold Regions Science and Technology*, 20:295–311, 1992.

M. Lepparanta, M. Lensu, P. Kosloff, and B. Veitch. The life story of a first-year sea ice ridge. *Cold Regions Science and Technology*, 23:279–290, 1995.

J.L. Lieser. A numerical model for short-term sea ice forecasting in the Arctic. *PhD Thesis, University of Bremen*, 2004.

M. Losch and S. Danilov. On Solving the Momentum Equations of Dynamic Sea Ice Models with Implicit Solvers and the Elastic-Viscous-Plastic Technique. *Ocean Modelling*, 41:42–52, 2012.

R.W. Macdonald, D.W. Paton, E.C. Carmack, and A. Omstedt. The freshwater budget and under-ice spreading of Mackenzie River water in the Canadian Beaufort Sea based on salinity and 18O/16O measurements in water. *Journal of Geophysical Research*, 100:895–919, 1995.

A. Mahoney, H. Eicken, L. Shapiro, and A. Garves. Defining and locating the seaward landfast ice edge in northern Alaska. In *18th International Conference on Port and Ocean Engineering under Arctic Conditions*, June 2005.

A. Mahoney, H. Eicken, A.G. Gaylord, and L. Shapiro. Alaska landfast sea ice: Links with bathymetry and atmospheric circulation. *Journal of Geophysical Research*, 112:C02001, 2007a.

A. Mahoney, H. Eicken, and L. Shapiro. How fast is landfast sea ice? A study of the attachment and detachment of nearshore ice at Barrow, Alaska. *Cold Regions Science and Technology*, 47:233–255, 2007b.

R.A. Massom, K.L. Hill, V.I. Lytle, A.P. Worby, M.J. Paget, and I. Allison. Effects of regional fast-ice and iceberg distributions on the behaviour of the Mertz Glacier polynya, East Antarctica. *Annals of Glaciology*, 33:391–398, 2001.

G.A. Maykut and M.G. McPhee. Solar heating of the Arctic mixed layer. *Journal of Geophysical Research*, 100:24691–24704, 1995.

G.A. Maykut and N. Untersteiner. Some results from a time dependent thermodynamic model of sea ice. *Journal of Geophysical Research*, 79:1550–1575, 1971.

H. Melling, R.A. Lake, D. Topham, and D. Fissel. Oceanic thermal structure in the western Canadian Arctic. *Continental Shelf Research*, 3:223–258, 1984.

M.A Morales-Maqueda, A.J. Willmott, and N.R.T Biggs. Polynya Dynamics: A review of observational and modelling. *Reviews of Geophysics*, 42:1717–1731, 2004.

T.S Murty. Modification of hydrographic characteristics, tides, and normial modes by ice cover. *Marine Geodesy*, 9:451–468, 1985.

NIC. National Ice Center Arctic sea ice charts and climatologies in gridded format, 2006, updated 2009. URL `http://dx.doi.org/10.7265/N5X34VDB`. Edited and compiled by F. Fetterer and C. Fowler. Boulder, Colorado USA: National Snow and Ice Data Center.

M.C. O'Brien, R.W. Macdonald, H. Melling, and K. Iseki. Particle fluxes and geochemistry on the Canadian Beaufort Shelf: Implications for sediment transport and deposition. *Continental Shelf Research*, 26:41–81, 2006.

Ö. E. Ólason. Dynamical Modelling of Kara Sea Land-fast Ice. *PhD Thesis, Univeristy of Hamburg*, 2012.

L. Padman and S. Erofeeva. A barotropic inverse tidal model for the Arctic Ocean. *Geophysical Research Letters*, 31, 2004.

A.C. Palmer and C.Y. Tung. Reducing the cost of protecting Arctic marine pipelines against ice gouging. In *Proceedings of the Twenty-second International Offshore and Polar Engineering Conference*, pages 1300–1303. International Society of Offshore and Polar Engineers, 2012.

A.C. Palmer, I. Konuk, A.W. Niedoroda, K. Been, and K.R. Croasdale. Arctic seabed ice gouging and large sub-gouge deformations. In Mark Cassidy and Susan Gourvenec, editors, *1st International Symposium on Frontiers in Offshore Geotechnics*, pages 645–650. Taylor and Francis, 2005.

R. Phillips, J.I. Clark, and S. Kenny. PRISE Studies on Gouge Forces and Subgouge Deformations. In *International Conference on Port and Ocean Engineering Under Arctic Conditions, POAC 05*, pages 75–84. Clarkson University, Potsdam, NY, 2005.

C.F. Postlethwaite, M.A. Morales Maqueda, V. le Fouest, G.R. Tattersall, J. Holt, and A.J Willmott. The effect of tides on dense water formation in Arctic shelf seas. *Ocean Science*, 7:203–217, 2011.

S.J. Prinsenberg. The circulation pattern and current structure of Hudson. In E.P Martini, editor, *Canadian Inland Seas*, pages 187–203. Elsevier, 1986.

S.J. Prinsenberg. Seasonal Current Variations Observed in Western Hudson Bay. *Journal of Geophysical Research*, 92:10756–10766, 1987.

A.T. Proshutinsky. Tidal water an ice dynamics in the Arctic Ocean. In *Proceedings from the International Conference on the Role of the Polar Regions in Global Change*, pages 296–303. Geophysical Institute, University of Alaska Press, Fairbanks, 1991.

A.Yu. Proshutinsky. Generation of eddy structures in the Faroe-Shetland Strait by tidal currents. *Oceanology*, 28:567–571, 1988.

D.T. Pugh. *Tides, surges and mean sea-level*. John Wiley and Sons Ltd, 1996.

J.G.L Rae, H.T. Hewitt, A.B. Keen, J.K. Ridley, J.M. Edwards, and C.M. Harris. A sensitivity study of the sea ice simulation in the global coupled climate model, HadGEM3. *Ocean Modelling*, 74:60–64, 2014.

E. Reimnitz. Interactions of river discharge with sea ice in proximity of Arctic deltas: a review. *Polarforschung, Bremerhaven, Alfred Wegener Institute for Polar and Marine Research and German Society of Polar Research*, 70:123–134, 2000.

E. Reimnitz and P. Barnes. Sea Ice as a Geologic Agent on the Beaufort Sea Shelf of Alaska. In J.C. Reed and J.E. Sater, editors, *The Coast and Shelf of the Beaufort Sea (Proceedings of a Symposium on Beaufort Sea Coast and Shelf Research)*, pages 301–353. Arctic Institute of North America, Arlington, Va., 1974.

E. Reimnitz, P. Barnes, T. Forgatsch, and C. Rodeick. Influence of grounding ice on the arctic shelf of Alaska. *Marine Geology*, 13:323–334, 1972.

D. A. Rothrock. The energetics of the plastic deformation of pack ice by ridging. *Journal of Geophysical Research*, 80:4514–4519, 1975.

D.A Rothrock, J. Zhang, and Y. Yu. The Arctic ice thickness anomaly of the 1990s: A consistent view from observations and models. *Journal of Geophysical Research*, 108:C33083, 2003.

F.J. Saucier, S. Senneville, S. Prinsenberg, and F. Roy. Modelling the sea ice-ocean seasonal cycle in Hudson Bay, Foxe Basin and dson Strait, Canada. *Climate Dynamics*, 23:303–226, 2004.

U. Schauer and E. Fahrbach. A dense water plume in the Western Barents Sea: Downstream modification an interannual variability. *Deep Sea Research Part I*, 46:2095–2108, 1999.

A. Schweiger, R. Lindsay, J.L. Zhang, M. Steele, H. Stern, and R. Kwok. Uncertainity in modelled Arctic sea ice volume. *Journal of Geophysical Research*, 116:C00D06, 2011.

M.C. Serreze, J.A. Maslanik, T.A. Scambos, F. Fetterer, J. Stroeve, K. Knowles, C. Fowler, S. Drobot, R.G. Barry, and T.M. Haran. A record minimum Arctic sea ice extent and area in 2002. *Geophysical Research Letters*, 30:1110, 2003.

L. Shapiro and P. Barnes. Correlation of nearshore ice movement with seabed ice gouges near Barrow, Alaska. *Journal of Geophysical Research*, 96:16979–16989, 1991.

L. Shapiro and R. Metzner. Coefficients of friction of sea ice on beach gravel. *Journal of Offshore Mechanics and Arctic Engineering*, 109:388–390, 1987.

J.H. Simpson and J. Sharples. *Introduction to the Physical and Biological Oceanography of Shelf Seas*. Cambridge University Press, Cambridge, 2012.

M. Steele. Sea ice melting and floe geometry in a simple ice-ocean model. *Journal of Geophysical Research*, 97:17729–17738, 1992.

M. Steele and T. Boyd. Retreat of the cold halocline layer in the Arctic Ocean. *Journal of Geophysical Research*, 103:10419–10435, 2012.

M. Steele, J. Zhang, D. Rothrock, and H. Stern. The force balance of sea ice in a numerical model of the Arctic Ocean. *Journal of Geophysical Research*, 102:21061 – 21079, 1997.

W.J. Stringer. Morphology of the Beaufort Sea shorefast ice. In J.C. Reed and J.E. Sater, editors, *The Coast and Shelf of the Beaufort Sea (Proceedings of a Symposium on Beaufort Sea Coast and Shelf Research)*, pages 165–172. Arctic Institute of North America, Arlington, Va., 1974.

W.J. Stringer, S.A. Barrett, and L.K. Schreurs. *Nearshore Ice Conditions and Hazards in theBeaufort, Chukchi and Bering Seas*. Geophys. Inst. Univ. of Alaska, Fairbanks, 1980.

J. Stroeve and C. Shuman. Historical Arctic and Antarctic Surface Observational Data [station 043160, on 8/01/2000], Boulder, Colorado USA: National Snow and Ice Data Center., 2004. URL `http://nsidc.org/data/nsidc-0190.html`.

J.C. Stroeve, M.C. Serreze, F. Fetterer, T. Arbetter, W. Meier, J. Maslanik, and K. Knowles. Tracking the Arctic's shrinking ice cover: another extreme September minimum in 2004. *Geophysical Research Letters*, 32:L04501, 2005.

J.C. Stroeve, M. C. Serrese, M.M. Holland, J.E. Kay, J. Malanik, and A.P. Barrett. The Arctic's rapidly shrinking sea ice cover: A research synthesis. *Climate Change*, 110:1005–1027, 2012.

G.W. Timco and R.P Burden. An analysis of the shapes of sea ice ridges. *Cold Regions Science and Technology*, 25:65–77, 1997.

L.-B Tremblay and M. Hakakian. Estimating the sea ice compressive strength from satellite-derived sea ice drift and NCEP reanalysis data. *Journal of Physical Oceanography*, 36:2165–2172, 2006.

N. Untersteiner. Calculations of temperature regime and heat budget of sea ice in the Central Arctic. *Journal of Geophysical Research*, 69:4755–4766, 1964.

V. I. Vladimir, A.A. Vladimir, I. Repina, N.V. Koldunov, and A. Smirnov. Tracing Atlantic Water Signature in the Arctic Sea Ice Cover East of Svalbard. *Advances in Meteorology*, 2012:201818, 2012.

V.A. Volkov, O.M. Johannessen, V.E. Borodachev, G.N. Voinov, L.H. Pettersson, L.P. Bobylev, and A.V. Kouraev. *Polar Seas Oceanography: An integrated case study of the Kara Sea*. London: Springer, 2002.

P. Wadhams. *Ice in the Ocean*. Gordon and Breach Science Publishers, 2000.

K. Wang. Observing the yield curve of compacted pack ice. *Journal of Geophysical Research*, 112:C05015, 2007.

W.F. Weeks. *On Sea Ice*. University of Alaska Press, 2010.

P. Winsor and G. Bjork. Polynya activity in the Arctic Ocean from 1958-1997. *Journal of Geophysical Research*, 105:8789–8803, 2000.

WMO. WMO sea-ice nomenclature, 1970. Secretariat of the World Meteorological Organization, Geneva, Switzerland.

A.P. Worby, C.A. Geiger, M.J. Paget, M.L. Van Woert, S.F. Ackley, and T.L. DeLiberty. Thickness distribution of Antarctic sea ice. *Journal of Geophysical Research*, 113:C05S92, 2008.

H. Yndestad. The influence of the lunar node cycle on Arctic climate. *Journal of Marine Science*, 63:401–420, 2006.